# ACTIVE-SCREEN PLASMA REDUCTION AND MULTI-FUNCTIONALISATIONS OF GRAPHENE OXIDE

*by*

ZHIYUAN JING


A thesis submitted to

the University of Birmingham

for the degree of

DOCTOR OF PHILOSOPHY

School of Metallurgy and Materials

College of Engineering and Physical Sciences

University of Birmingham

April 2021

# Abstract

Graphene is a young but popular carbon material due to its attractive properties for various applications. As a derivative of graphene, graphene oxide (GO) is often used as the precursor of graphene due to its low cost, hydrophilicity and capability for modifications. Notwithstanding the fact that some methods have been explored for GO reduction, nitrogen doping or hybridisation with metal nanoparticles, each of these methods has its own limitations and none of them could fulfil all these three functions together. Therefore, a novel active-screen plasma (ASP) technique has been developed from this research by combining GO reduction, nitrogen doping and hybridising with metal nanoparticles in one treatment. The morphology, micro-structure, element composition as well as chemical bond of GO were fully characterised, and the electrical and electrochemical properties were evaluated.

The results have shown that ASP treatment using argon as a working gas was superior to annealing treatment in terms of GO reduction, lower sheet resistance and better super-capacitive performance. When a gas mixture of nitrogen and hydrogen was used in ASP, GO was reduced and nitrogen doped simultaneously, and the optimal ratio of nitrogen to hydrogen is 1:3, with the nitrogen doping configurations of pyridinic N, pyrrolic N and graphitic N. On the other hand, ASP using a gas mixture of nitrogen and argon deteriorated the electrical property.

Apart from reduction and nitrogen doping, metal nanoparticles from the active screen were sputtered and deposited on ASP treated GO at the same time when an additional noble metal lid was placed on top of the stainless-steel screen. Iron and chromium sputtered from the stainless steel were mainly in oxidised states, whilst noble metals were mainly in the form of pure metals, except for a minority of metal oxides in the cases of palladium and platinum.

With the noble metal deposition, the electrical and electrochemical properties of ASP treated GO were greatly influenced. The sheet resistances of ASP treated GO hybridised with platinum and gold were further reduced dramatically, and the super-capacitive performance of the ASP treated GO hybridised with platinum nanoparticles is the best among all the samples. However, silver nanoparticles aggregated and formed into large particles when deposited on GO surfaces, and palladium was chemically bonded with carbon, so that in these two cases, the metal hybridisation could not contribute to the improvement of electrical or electrochemical properties of GO.

It is expected that the novel ASP technology combining surface modification and metal hybridisation could open the way towards new applications of multi-functionalised GO such as GO-Ag for anti-bacterial materials, GO-Au and GO-Ag for surface-enhanced Raman scattering and GO-Pt, GO-Pd and GO-Au for catalysts.

# Acknowledgements

First of all, I would like to give my sincere gratitude to my supervisors, Prof. Hanshan Dong and Dr. Xiaoying Li for the opportunity they offered me to study under them, and their invaluable supervision throughout my PhD study. It is indeed an honour for me to be one of the members of the Surface Engineering group.

I would also like to thank Prof. Wei Zhang and Dr. Helong Yu from the National Key Laboratory for Remanufacturing, China, and Prof. Yulin Qiao from the National Engineering Research Center for Mechanical Product Remanufacturing, China, for their support in my study.

I must also extend my appreciation to the staff in the School of Metallurgy and Materials for their support: namely Dr. Daniel Reed and Miss Amy Newell for their assistance in Raman spectroscopy and XRD, Mr. Paul Stanley and Mrs. Theresa Morris for their guidance in SEM and TEM, Prof. Jon Binner and Mr. Tailin Zhang for thermal annealing treatment, and Mr. Frank Biddlestone for TGA measurements. My appreciation also goes to Mrs. Weiling Guo from the National Key Laboratory for Remanufacturing, China, for her assistance in XPS.

I would also like to express my special thanks to all the members, past and present, of the SE group, especially Dr. Zhenxue Zhang, Dr. Yangchun Dong, Dr. Shaojun Qi, Dr. Xiao Tao, Dr. Xiaochao Ji, Dr. Valter Luiz Jantara Junior, Dr.

Behnam Dashtbozorg, Miss Yana Liang, Mr. James Alexander, Miss Yingdi Feng, Mr. Thomas Collins, Miss Chang Che, Mr. Xinhe Xiong and Mr. Fangzhou Shi, for both their help in my study and their friendship during my life in the UK.

Finally, I would like to give my deepest love and thanks to my family and friends, as well as my girlfriend Yu Tian, for their support and care all the time, especially in the challenging times.

# Publication

- **Jing Z**, Qi S, Tao X, et al. Active-screen plasma multi-functionalization of graphene oxide for supercapacitor application[J]. Journal of Materials Science, 2021, 56(4): 3296-3311.

# Table of Contents

# List of Figures

# List of Tables

# List of Abbreviations

| | |
|---|---|
| AC | alternating current |
| AFM | atomic force microscope |
| ASP | active-screen plasma |
| CV | cyclic voltammetry |
| DC | direct-current |
| DFT | density functional theory |
| DOS | density of states |
| EDS | energy dispersive x-ray spectroscopy |
| EMI | electromagnetic interference |
| EIS | electrochemical impedance spectroscopy |
| ESFDA | electrostatic force directed assembly |
| FET | field effect transistors |
| FTO | florine-doped tin oxide |
| GCD | galvanostatic charge/discharge |
| GO | graphene oxide |
| ITO | indium tin oxide |
| LIB | lithium-ion battery |
| MA | microwave absorption |
| N-doped | nitrogen-doped |
| PIII | plasma-immersion ion implanter |
| rGO | reduced graphene oxide |
| RF | radio frequency |
| SC | supercapacitor |

| | |
|---|---|
| SEM | scanning electron microscopy |
| TCF | transparent conductive film |
| TEM | transmission electron microscopy |
| TGA | thermal gravimetric analysis |
| XPS | x-ray photoelectron spectroscopy |
| XRD | x-ray diffraction |

# Chapter 1 Introduction

Graphene material is a new and advanced carbon material, with many extraordinary characteristics in different aspects, including mechanical, electrical, optical, and thermal properties, and hence it is an excellent candidate for many applications, especially electronic and optoelectronic devices, such as field effect transistors, supercapacitors, sensors and transparent conductive electrodes for solar cells [1].

Graphene oxide (GO) is a type of graphene material decorated with oxygen functional groups, mainly hydroxyl, epoxide, carbonyl, and carboxyl, etc. Due to the presence of these oxygen functional groups, GO is hydrophilic, so that it can be dispersed in liquid solutions stably without any modification, whilst graphene, which is hydrophobic, requires surfactants to disperse stably in solutions [2, 3]. Therefore, GO is an attractive precursor material for the fabrication of graphene-based films [4]. However, these oxygen functional groups, on the other hand, have a negative effect on the properties. For example, graphene is electrically conductive while GO is an insulator [5]. Consequently, a reduction process is usually required for GO applications[6]. Additionally, nitrogen doping of graphene materials is often associated with significant performance enhancements for graphene-based applications [7, 8].

For the reduction of GO and nitrogen doping of graphene materials, various

methods have been developed, and these two processes can be realised simultaneously. The methods can be mainly categorised into two routes [7, 9]. One is via thermal method, and the other is wet-chemical method. However, these two major methods both have their own limitations. Thus, apart from these two methods, some advanced techniques have been explored, with plasma techniques being a promising approach [10, 11].

Moreover, hybridisation with metal nanoparticles is another common approach investigated to broaden the applications of graphene materials [12]. With regards to hybridisation with metal nanoparticles, the dominant route is *in-situ* reduction of metal precursors and GO mixture [12]. Plasma techniques have also managed to be applied for this purpose [13]. However, the use of metal precursors is still not an ideal method for hybridisation due to the involvement of chemical reaction with harmful by-products.

Active-screen plasma (ASP) is an advanced novel plasma technique with a modification of setup based on conventional direct-current (DC) plasma. In ASP technique, a mesh (active screen) is incorporated in the furnace chamber, thereby overcoming drawbacks of DC plasma, such as edge effects, hollow cathode formations, and sample damage caused by ion bombardment. Also, as a remote plasma, ASP technique can be applied on non-conductive materials.

Originally, ASP technique was mainly used on metal alloys for nitriding and carburising [14, 15]. Recently, it has also found potential uses for the treatment

of carbon materials, such as carbon fibres, whereby metal nanoparticles from the active screen can be sputtered and deposited on the carbon fibres during the treatment [16, 17]. Based on this, it can be theoretically deduced that ASP can be applied on GO materials for a simultaneous reduction, nitrogen doping and hybridising with metal nanoparticles, without the use of chemicals or high temperatures. However, only limited work has been reported on this topic thus far.

Therefore, the aim of this present work was to apply ASP technique on GO material, and examining its effects on GO reduction, nitrogen doping and hybridisation. Specifically, the research objectives were the following:

- To explore GO reduction, nitrogen doping and metal hybridisation via ASP technique for the multi-functionalisation of GO.
- To study the effects of ASP technique on the functionalisation of GO in terms of working gas type and ratio for GO modification, active-screen noble metal type for metal sputtering and deposition, and treatment duration and gas pressure for optimal condition.
- To characterise the morphology, micro-structure, chemical composition, and chemical bonding of ASP treated GO, using SEM/EDS, Raman spectroscopy, TEM, and XPS.
- To evaluate the electrical and electrochemical properties of GO after ASP treatment.

- To understand the mechanism involved in ASP processing GO and the property improvement.

# Chapter 2 Literature review

## 2.1. Graphene and Its Derivatives

### 2.1.1 Graphene

#### 2.1.1.1 General introduction

There are many allotropes of carbon, among which graphite and diamond are two typical ones, representing two types of carbon hybridisations: $sp^2$ and $sp^3$, respectively. The $sp^2$ carbon hybridisation involves one “s” orbital and two “p” orbitals of the carbon atom mixing into three equivalent orbitals, which is linked to three other carbon atoms and forms into a trigonal symmetry with an angle of 120° in one plane. The $sp^3$ carbon hybridisation, on the other hand, involves one “s” orbital and three “p” orbitals of the carbon atom mixing into four equivalent orbitals, which is linked to four other carbon atoms and forms into a tetrahedron with an angle of 109.5°. The sketches of these two carbon hybridisations are shown in Fig. 2-1. With the development of research on carbon materials, more types of elementary substances of carbon have been found, as shown in Fig. 2-2.

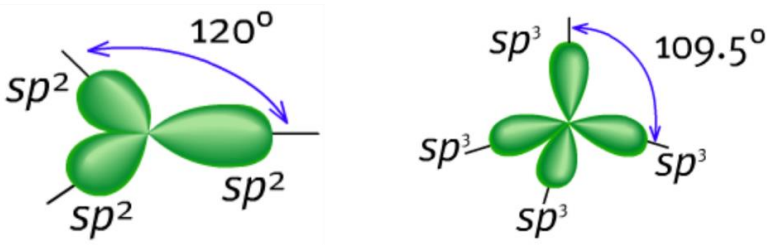


Fig. 2-1 $sp^2$ and $sp^3$ carbon hybridisations [18]

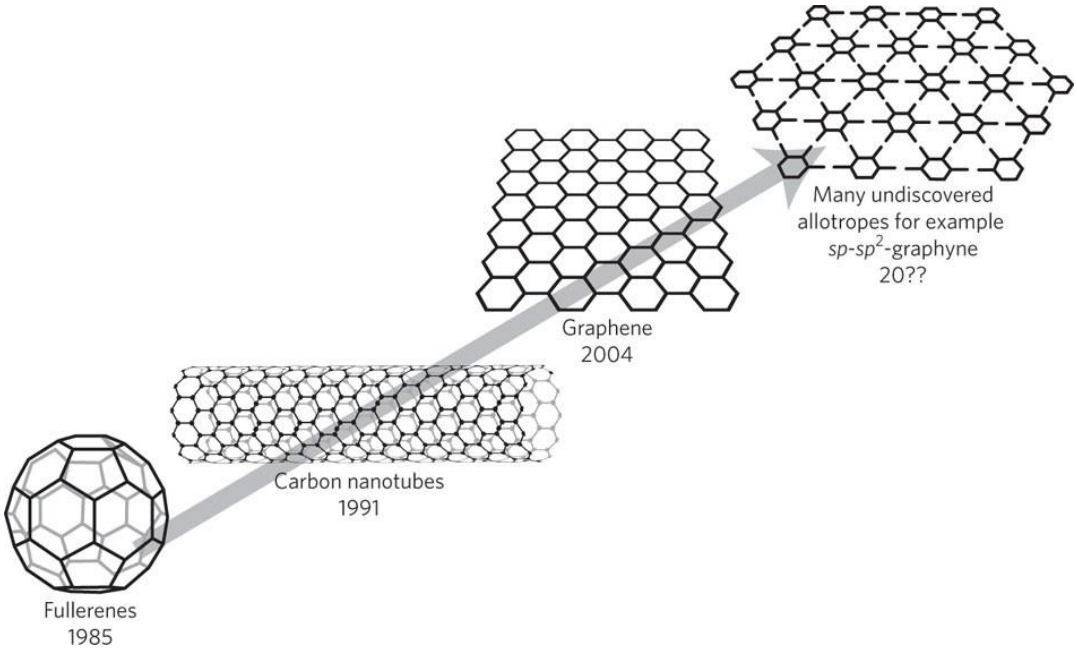


Fig. 2-2 New types of carbon allotropes: fullerenes, carbon nanotubes and graphene [19].

Fullerenes like $C_{60}$ and many other types in the form of a ball-like shape were discovered or produced in 1980s [20], and in 1991, Japanese scientist Iijima discovered carbon nanotubes, which once again attracted significant interest in the relevant research due to its curious characteristics and broad potential applications [21].

More recently, research on carbon materials has once again gained widespread attention following the successful discovery of graphene in the lab. This tremendous achievement was made in 2004, by Andre Geim and Kostya Novoselov, two researchers from University of Manchester, using simple mechanical exfoliation method to peel off the graphene layer from highly oriented pyrolytic graphite [22]. Although the preparation process is extremely inefficient, this achievement still became a milestone in the research field of

carbon materials, proving the existence of graphene and its practical feasibility for production, which had only existed in academic theory beforehand. Afterwards, many other methods and techniques have been developed to produce graphene, such as Hummer's method [23, 24] and CVD [25], either in large scale or in perfect quality .

The international research attention regarding graphene materials results from its unique structure and properties suitable for wide-ranging applications. The structure, properties and applications of graphene and its derivatives will be introduced in the following chapter.

#### 2.1.1.2 Structure of graphene

As a core, graphene is a single layer of graphite (monolayer graphene), but in practice, double layers, as well as few layers (three to ten layers), of graphite are also referred to graphene (bilayer graphene and few-layer or multi-layer graphene, respectively) in the research. Carbon atoms in graphene are all in $sp^2$ hybridisation, forming a hexagonal structure, like a honeycomb pattern. Each carbon atom is connected to three other carbon atoms, forming three σ-bonds in one plane. The bond length between two connected carbon atoms is 0.142 nm and the binding energy is 615 kJ/mol. In addition to the three σ-bonds, a π-bond is made by the extra *p* orbital electron, which orients perpendicular to the graphene plane, and all adjacent π-bonds hybridise into delocalised π and π* bands, giving rise to the electronic properties of graphene.

In the graphene plane, there are two types of edges: armchair edges and zigzag edges, as shown in Fig. 2-3 (a) [26]. Also, a single lattice unit of graphene is a rhombus containing two carbon atoms, denoted as A and B in black and white, respectively, in Fig. 2-3 (a) [26]. The reciprocal lattice of graphene is shown in Fig. 2-3 (b) [26], and the hexagonal in grey is the first Brillouin zone. The high symmetry points are Γ, M, K and K′, and among them, K and K′ are the Dirac points. An ideal graphene with a perfect structure without any defect is believed to be a semi-conductor with a zero band-gap, or a semi-metal, since the conduction bands and valence bands touch at the Dirac points, with zero electronic density of states (DOS).

Due to this unique structure, graphene exhibits some intriguing properties, and can be applied into some potential applications that are discussed below.

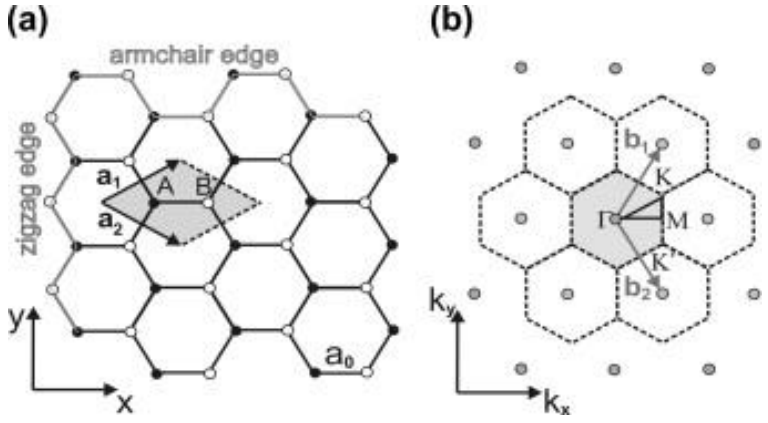


Fig. 2-3 Crystal structure of graphene: (a) 2D hexagonal lattice of graphene in real space with basis vectors a1 and a2. The unit cell is highlighted in grey. It contains two nonequivalent carbon atoms A and B, each of which span a triangular sublattice as indicated with black and white atoms, respectively. An armchair and a zigzag edge are highlighted in grey. (b) Reciprocal lattice (dashed) with reciprocal lattice vectors b1 and b2. The first Brillouin zone is marked grey and the high symmetry points Γ, M, K and K′ are indicated [26].

#### 2.1.1.3 Properties of graphene

The structure of graphene give rise to a unique combination of properties not observed in other materials, including the mechanical, thermal, electrical/electronic, and chemical properties.

(1). Mechanical properties

Due to the large binding energy of the σ-bonds between carbon atoms in $sp^2$ hybridisation, graphene materials are considered as one of the strongest materials in the world. The Young's modules, Poisson's ratio and strength of graphene have been tested using both theoretical calculations and experimental measurements.

Taking the thickness of 0.334 nm, Liu et al. [27] calculated that the Young's modules of graphene is 1050 GPa and the Poisson ratio is 0.186, using the plane wave density functional theory. The maximum Cauchy stresses for uniaxial tension in the direction of zigzag and armchair are 110 GPa and 121 GPa, respectively.

However, it is difficult to accurately measure the mechanical properties of graphene via direct experimental tests, due to different graphene samples prepared and various methods applied in different studies, and thus the results vary. Lee et al. [28] measured the elastic properties of free-standing monolayer graphene membranes by nanoindentation in an atomic force microscope, and the Young's modulus was measured to be 1000 ± 100 GPa, while the intrinsic

stress were 130 ± 10 GPa. In the measurement of Gómez-Navarro et al. [29], the graphene monolayer with defects were synthesised via chemical reduction, and a similar method of using an atomic force microscope (AFM) tip were applied to measure the elastic modulus, and a mean elastic modulus of only 250 GPa was obtained. Moreover, it was measured that the bending rigidity and tension of graphene materials measured in AFM depend on the thickness [30], and in the studies of Frank and Tanenbaum [31], the Young's modulus was extracted to be 500 GPa for suspended graphene sheets with less than 10 nm thickness.

Even with different measured results, it is evident that graphene is one of the strongest materials in the world.

(2). Thermal properties

Graphene is highly thermal conductive at room temperature, with thermal conductivity (K) measured up to (5.30 ± 0.48) × $10^3$ W/mK, using an optothermal Raman technique developed by Balandin et al. [32]. However, the values of thermal conductivity of graphene varies in different research studies due to different measuring setups, with K being measured at only ~600 W/mK by Faugeras et al. when the absorbed laser power was much lower than the previous studies [33]. Despite of the uncertainty of the exact value of thermal conductivity, graphene is competitive to conventional thermal conductive metal material, e.g., bulk copper, whose thermal conductivity is around 400 W/mK.

(3). Electrical/electronic properties

As mentioned in Section 2.1.1.2, the π-bonds from the extra electron in *p* orbits of carbon atoms result in delocalised π (valence) and π* (conduction) bands. In the band structure of a pristine graphene as shown in Fig. 2-4, the valence and conduction bands meet at the Dirac points, where the Fermi level is situated. At Dirac point, the DOS is zero, and the energy gap is zero as well.

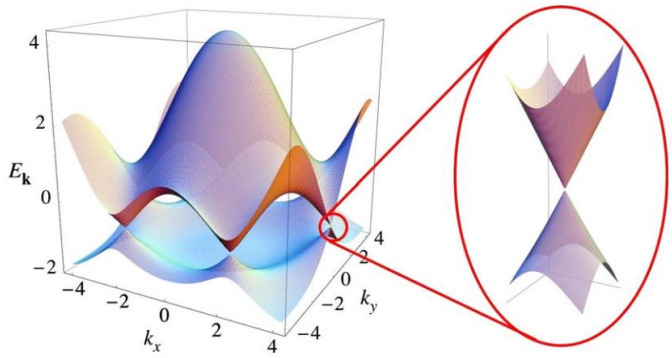


Fig. 2-4 Band structure of graphene showing the conductance and valence bands meeting at the Dirac points [34].

The electrical conductivity of graphene can be determined by the carrier mobility, and according to the studies of Morozov et al. [35], the intrinsic mobility of monolayer or bilayer graphene with eliminated disorders can be up to approximately 200 000 $cm^2/Vs$.

(4). Chemical properties

Due to the stable atomic structure of graphene for the strong bonding between carbon atoms in the graphitic plane via σ-bonds, graphene is essentially inert with high chemical stability. The chemical properties of graphene materials are mainly reflected in the functionalisations of graphene, which offer a chance for graphene materials to participate in chemical reactions. The functionalisation

can be divided into covalent and non-covalent functionalisations, differing in whether σ-bonds break and reconnect to other atoms.

The non-covalent functionalisation is realised due to the π-π stacking between the graphitic plane and the other molecules containing aromatic rings via weak Van der Waals forces. Molecules doped non-covalently do not interfere with the pristine lattice, but only adhere to the graphene surface. Nevertheless, electrons can still transfer between the doped molecules and the graphene, and the Dirac point of graphene can be altered from 0 V after the non-covalent functionalisation [36].

The covalent functionalisation results from the chemical reactions of graphene with other substances, and the doped substances can be either atoms or radical groups. The binding in covalent functionalisation is stronger than the counterpart non-covalent ones, and thus more intense condition is required for the reaction to occur.

#### 2.1.1.4 Applications of graphene

Due to its unique and extraordinary properties, graphene is a promising material for many applications, especially electronic devices. In this section, some typical examples of the applications of graphene are briefly introduced.

(1). Field effect transistors (FETs)

Due to the high field-effect mobility, graphene materials are promising candidates to fabricate FETs. Also, with the bipolar feature of graphene, both

*n*-and *p*-type doping can be realised by controlling the carrier type, and thus a p-n junction can be prepared using graphene materials alone [37, 38]. As to the requirement of high $I_{on}/I_{off}$ ratio for logic FETs, various methods of opening the bandgap at the Dirac point have been investigated [39].

(2). Sensors

The adsorption ability, as well as the change of the electrical properties after adsorption, enables graphene to be a competitive candidate as a sensor for certain types of gases, organic molecules, and biomaterials, such as carbon dioxide, ammonia gas, dopamine, ascorbic acid, and NADH [40-43]. The good sensitivity is attributed to the large specific area and the high carrier mobility as charge transfers between graphene and the adsorbed substances, resulting in the change of Fermi level, carrier density and conductance.

(3). Optoelectronic devices

For optoelectronic devices such as solar cells and LEDs, graphene is also a promising material to replace the conventional indium tin oxide (ITO) and fluorine-doped tin oxide (FTO) to fabricate transparent conductive films (TCFs) [44, 45]. This is owing to both its high electrical conductivity and carrier mobility, and its high optical transmittance.

(4). Energy storage devices

Because of the high specific surface area, good electrical conductivity, and superior chemical stability, graphene has been extensively applied as an

electrode material or additive in energy storage devices such as supercapacitors (SCs), lithium-ion batteries (LIBs), fuel cells and hydrogen storage devices [46-50].

## 2.1.2 Graphene Oxide

### 2.1.2.1 General introduction

Graphene oxide (GO) is a derivative of graphene, containing various oxygen functional groups, and is often used as a precursor for the synthesis of graphene through reduction methods. The oxygen functional groups are mostly epoxy and hydroxyl groups on the basal plane, with carboxyl, carbonyl and phenol groups at the edge or defect areas [51]. However, due to the difference of synthesis protocols applied and reactions extents, the oxygen functional groups vary in each GO sheet, and it is not realistic for GO to have a consistent stoichiometry. The models of the GO structure is reviewed in [52], as shown in Fig. 2-5.

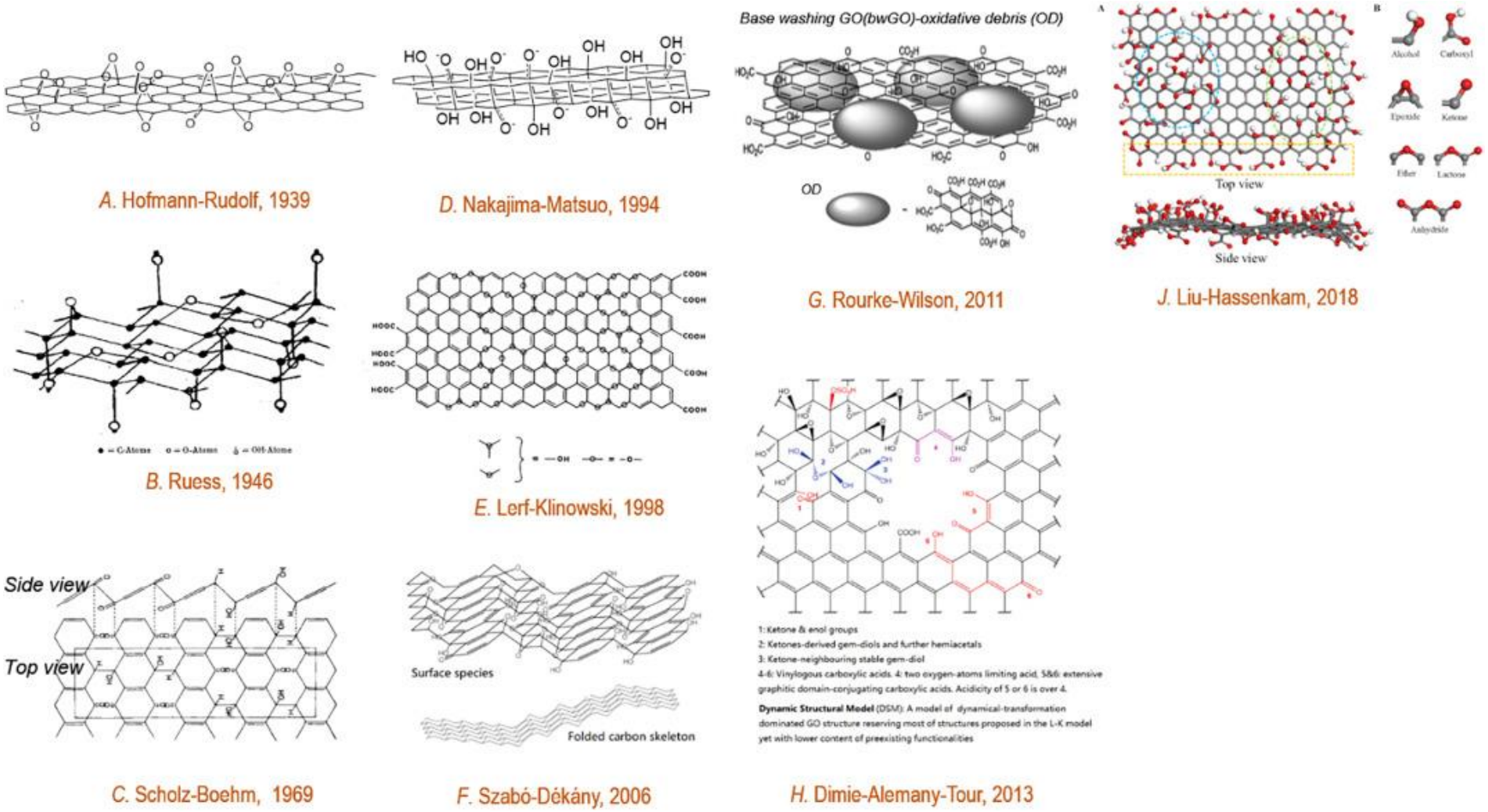


Fig. 2-5 Theoretical models for structures of graphite or GO [52].

The oxygen functional groups on GO inevitably affect the unique properties of pristine graphene, with a typical change being decreased electrical conductivity. On the other hand, these hydrophilic oxygen functional groups enable GO dispersion in aqueous and organic solvents, making it convenient for GO to deposit directly onto substrates via drop-casting, spin-coating and spraying in large scale, so that the step of graphene transfer for applications can be bypassed [53, 54]. Moreover, the oxygen functional groups, as well as the possible defects in GO, are active sites in the graphitic structure, which is advantageous to the functionalisation of graphene materials for more specific applications [55].

#### 2.1.2.2 Properties of graphene oxide

The oxygen functional groups, as well as the defects that are highly likely to exist in GO, have a great impact on its properties and chemical stability [55]. In this section, the mechanical and electrical properties, as well as the chemical stability of GO, are introduced.

(1). Mechanical properties

As Paci et al. investigated in a Monte Carlo based scheme, the theoretical mechanical properties significantly decrease due to holes in GO sheets [56]. Alternatively, the mechanical properties have also been measured experimentally using various methods. Under AFM imaging in the contact mode, and with finite element analysis, the effective Young's modulus and pre-stress of individual platelets of GO has been found to be 207.6 ± 23.4 GPa and 76.8

± 19.9 MPa, respectively [57]. Using a nanoindentation system on a dynamic contact module, the mechanical properties of free-standing GO films produced via electrophoretic deposition were measured [58]. The effective Young's moduli were 695 ± 53 GPa and 697 ± 15 GPa, for 50- and 60-nm-thick GO films, respectively, with ultimate tensile strength of 3-33 GPa and crack initiation arising at loads of 65 and 72 μN, respectively. Theoretically, using first-principles computations, Liu et al. compared the mechanical properties of GO in ordered and amorphous structural models, with different coverage of oxygen functional groups ($sp^3$ hybridised carbon bonded with hydroxyl or epoxy) [59]. The results showed that the Young's modules and intrinsic strength of ordered GO are higher than those of amorphous ones, and an increasing oxidation coverage decreased these parameters.

(2). Thermal properties

The thermal conductivity of GO is significantly reduced, compared to pristine graphene, which is mainly considered attributed to an enhanced phonon scattering and the shortened phonon mean free path. Based on the molecular dynamic method, many researchers simulated and calculated the thermal conductivity of GO with different oxidation degree or vacancy degree [60-62] [63]. Mu et al. investigated the relationship between oxygen coverage and thermal conductivity, finding that the thermal conductivity decreased by 50 % with only 0.5 % oxygen coverage, and even by 90 % with 5 % oxygen coverage [60]. Chen and Li also investigate the effect of oxidation degree on thermal

conductivity, and the thermal conductivity is around 72 and 670 W/mK at an oxidation degree of 0.35 and 0.05, respectively [61, 62]. Besides, Yang, et al. further consider the effect of vacancy defect in GO on thermal conductivity, as vacancy defects are commonly exist in GO, and found it playing a more significant role in decreasing thermal conductivity, as oxidation degree on longer dominant the thermal conductivity when the vacancy defect exceeds 2 % [63].

(3). Electrical properties

In contrast to pristine graphene, GO is generally an electrically insulating material. It is proposed by Mattevi el al. [64] that the electrical conductivity (charge transportation) is determined by the $sp^2$ bonding fraction in graphitic structure where π electrons can move freely. The oxygen functional groups create $sp^3$ C-O bonding, which prevent the electrons from freely moving in the basal plane, and form a transport barrier for the charge carriers [55, 4]. To obtain graphene sheets with low resistance, GO is usually reduced to rGO with fewer oxygen functional groups or defects [65, 66]. Kang et al. deposited GO films via electrophoretic deposition, and then transferred them to polydimethylsiloxane substrates with low oxygen concentrations, and measured the sheet resistance to be approximately 276–2024 Ω/sq [67].

(4). Chemical stability

Although the graphitic structure is chemically inert, the oxygen functional

groups and disorders are active sites that lower the criteria for the modification and functionalisation, making GO more chemically active. Also, these reactive oxygen functional groups can interact with other molecules, broadening the applications of graphene materials [68].

For comparison, a table below summarises the properties of graphene and GO, as shown in Table 2-1.

#### 2.1.2.3 Applications of GO

Since GO is the precursor for the synthesis of graphene through reduction methods, it has potential for use in all the applications of graphene that have previously been mentioned in Section 2.1.1.4 (FETs, sensors optoelectronic devices and energy storage devices).

Moreover, GO can be seen as a kind of functionalised graphene material with oxygen functional groups decorated on the basal plane, which modify the electronic structure and properties of GO, and further broaden its applications [55, 68]. Some literature reviews have summarised the applications of GO [69-71]. Except for those applications mentioned above, other applications such as catalysts, biomaterials, drug delivery, and membranes have also been widely studied using GO as, at least one of, the components [72].

With plentiful types of applications of GO, it is impossible to cover all of them in detail within this section. Thus, only some of the applications described in Section 2.2.1 are described in more detail.

Table 2-1 Comparison between properties graphene and GO

| | Graphene | | | GO | | |
|---|---|---|---|---|---|---|
| | | Results | Ref. | | Results | Ref. |
| **Mechanical properties** | Young's modules<br>Poisson ratio | 1050 GPa<br>0.186 | [27] | Young's modulus<br>pre-stress | 207.6 ± 23.4 GPa<br>76.8 ± 19.9 MPa | [57] |
| | Young's modules<br>Intrinsic stress | 1000 ± 100 GPa<br>130 ± 10 GPa | [28] | Young's modulus | 695 ± 53 GPa | [58] |
| | elastic modulus | 250 GPa | [29] | Young's modulus | 697 ± 15 GPa | |
| | Young's modulus | 500 GPa | [31] | | | |
| **Thermal property** | Thermal conductivity | $(5.30 \pm 0.48) \times 10^3$ W/mK | [32] | Thermal conductivity | 72 W/(mK)<br>(oxygen degree 0.35)<br>670 W/(mK)<br>(oxygen degree 0.05) | [61][62] |
| | | ~600 W/mK | [33] | | | |
| **Electrical /electronic properties** | Carrier mobility | 200 000 $cm^2/Vs$ | [35] | Hole mobility (in air) | 0.25 $cm^2/Vs$ | [73] |
| | Electron mobility (number of carbons along the edge N=3k) | ~ $10^6$ $cm^2/Vs$ | [74] | Hole mobility (in vacuum) | 0.59 $cm^2/Vs$ | |
| | Hole mobility (number of carbons along the edge N=3k) | ~ $10^4$ $cm^2/Vs$ | | | | |
| | Electron mobility (number of carbons along the edge N=3k±1) | ~ $10^4$ $cm^2/Vs$ | | | | |
| | Hole mobility (number of | 4-8 × $10^5$ $cm^2/Vs$ | | | | |

| | | | | | | |
|---|---|---|---|---|---|---|
| | carbons along the edge N=3k±1) | | | | | |
| | Sheet resistance | 100 Ω/sq | [75] | Sheet resistance | 276–2024 Ω/sq | [67] |
| **Chemical properties** | Chemical stability | stable | | Chemical stability | active | |

## 2.2. Potential Applications and Challenges

As introduced in Section 2.1, the unique properties of graphene and GO enable this type of carbon material to have potential for various applications. However, it is also a practical issue that, in many cases, graphene and GO cannot be directly used without modifications. Thus, in this section, some of the applications and the functionalisations approaches of graphene materials are introduced.

### 2.2.1 Potential Applications

#### 2.2.1.1 Transparent conductive films

Transparent Conductive films (TCFs) as electrodes are fundamental components for several electronic and optoelectronic devices, such as FETs, organic light-emitting diode (OLEDs), and solar cells. Conventionally, the mostly used TCFs are made of ITO and FTO films, but these materials are expensive due to the precious elements they contained. Graphene has been promoted as a future substitute for ITO and FTO based on its high conductivity and high transparency.

Bae et al. reported a roll-to-roll production approach of graphene sheets in large scales of 30 inches, followed by transfer to polyethylene terephthalate substrates as transparent electrodes, which could then be fabricated into a four-wire touch-screen panel [76]. The sheet resistance of the stacked layers of the graphene film were as low as 125 Ω/sq with a transmittance of 97.4%, with the

properties to be further improved after doping.

Han et al. also fabricated flexible OLEDs, in which the modified graphene was used as anodes [77]. The sheet resistance of the modified graphene-based anode decreased to approximately 30 Ω/sq, and showed higher current efficiency and luminous efficiency of both fluorescent and phosphorescent OLEDs than conventional ITO-based anode counterparts.

Gomez De Arco et al. synthesised graphene films using a chemical vapour deposition (CVD) technique, which showed superiority to the ITO counterpart in terms of retaining the conductance following bending [78]. The organic photovoltaic cells fabricated based on this graphene electrode showed a sheet resistance of 3.5 kΩ/sq with a transparency of 89 %, and exhibited comparable performance to the ITO counterparts.

#### 2.2.1.2 Energy storage devices

The huge consumption of, and high demand for, energy in the development of society calls for high-performance energy storage systems. Lithium-ion batteries and supercapacitors are two types of electrical energy storage devices that draw worldwide attention for their impressive abilities to store energy.

(1). Lithium-ion batteries (LIBs)

LIBs are advanced rechargeable batteries that feature with high energy density and nominal voltages. The mechanism of energy storage is based on the intercalation of lithium ions in the electrodes, and the schematic principle of a

LIB charging/discharging process is shown in Fig. 2-6 [79]. The anode material of LIBs is mainly graphite, whilst the cathode material is lithium-containing material, typical consisting of lithium cobalt oxide [80].

Since graphite is still the most widely used material as the anode of LIBs for its high coulombic efficiency and high capacity to intercalate lithium ions, research for further improvements is always ongoing. Graphene as single layer, or few layers, of graphite is inevitably studied as an alternative anode material. Guo et al. synthesised graphene nanosheets from artificial graphite and measured the electrochemical properties in a three-electrode system using lithium sheets as reference and counter electrodes [48]. The results showed an enhancement of the electrochemical properties of the graphene-based electrodes, as the reversible capacity was almost twice that of the electrodes based on artificial graphite.

As for the cathode material of LIBs, the performances of typical materials such as $LiCoO_2$, $LiMnO_2$ and $LiFePO_4$ are hindered by their poor electrical conductivity, and thus, graphene has also been explored as an additive for the cathode material for the purpose of improving the rate capability for a faster charging/discharging process [81, 82].

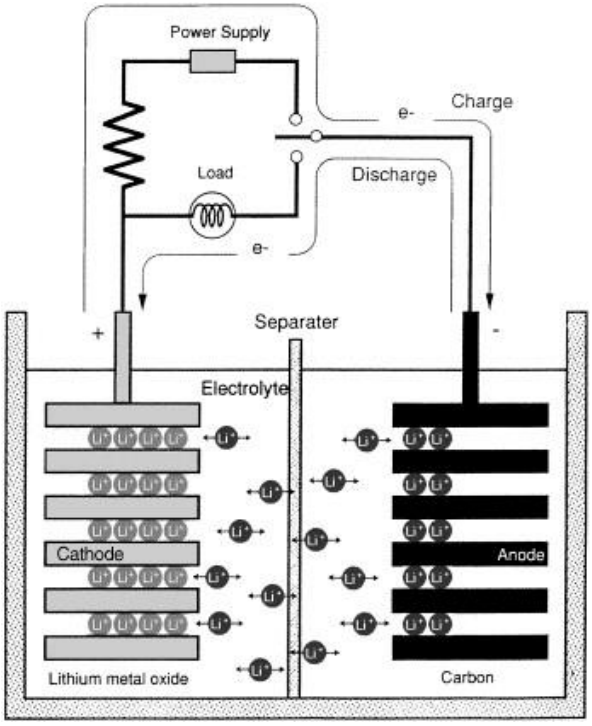


Fig. 2-6 Principle of lithium ion battery [79].

(2). Supercapacitors (SCs)

SCs, also named electrochemical capacitors, have lower energy density than that of secondary batteries, but possess higher power density and longer cyclic stability [83]. According to the mechanism of energy storage, SCs can be divided into three categories: electric double-layer capacitors (EDLCs), pseudo-capacitors, and hybrid SCs [84]. EDLCs store the electrical energy electrostatically by non-faradaic adsorption of charges at the electrode/electrolyte interface, while pseudo-capacitors rely on the faradic redox reaction. Hybrid SCs combine both EDLC and pseudo-capacitor mechanisms. These three types of SCs are shown in Fig. 2-7.

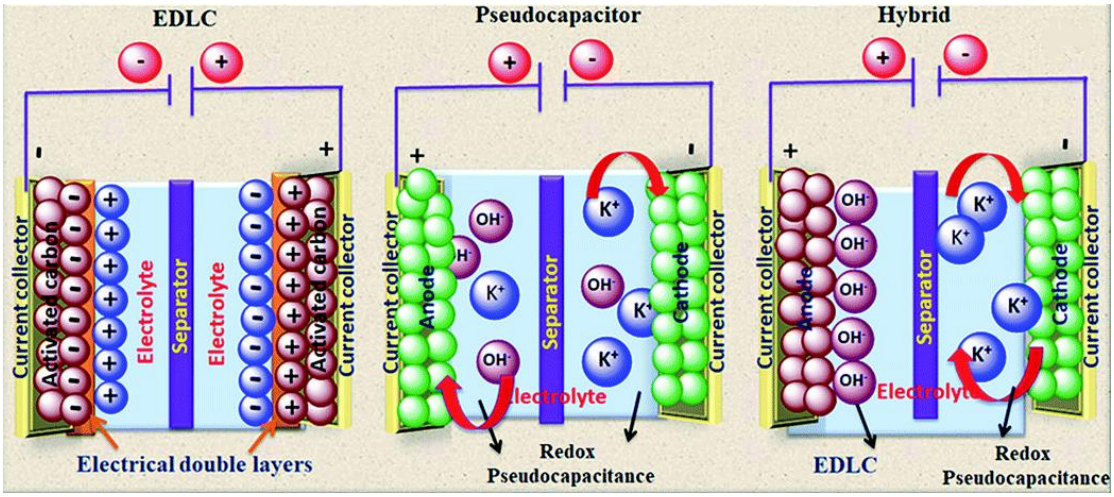


Fig. 2-7 Type of supercapacitors: EDLC, pseudo-capacitor and hybrid SC [85].

As for EDLCs, the material for the electrode is required to be electrically conductive, with a high specific surface area and chemical stability, so that more charges can be adsorbed and accumulated on the capacitor for a higher energy density. Graphene is a perfect candidate material for the requirements as the nominal carrier mobility exceeds 200,000 $cm^2/Vs$ [35] and the theoretical specific surface area reaches 2630 $m^2/g$ [86]. A significant amount of research has been carried out with a focus on the graphene-based SCs [87, 88]. For example, Yang et al. synthesised a porous graphene via hydrogen annealing, and the SC based on the synthesised graphene electrode showed outstanding electrochemical performance, with power densities of 41 kW/kg and energy densities of 148.75 Wh/kg [89].

In regard to pseudo-capacitors, transition metal oxides are popular electrode materials, such as ruthenium oxide ($RuO_2$), and manganese dioxide ($MnO_2$) for their high conductivity, as well as, their redox reaction capability [90]. Consequently, the composites of graphene materials with these transition metal

oxides have been explored to increase the capacity through the combination of both double electrical layer capacitance and pseudo-capacitance [91].

#### 2.2.1.3 Other applications

In addition to the two major applications mentioned above, there are many other applications in which graphene materials have found potential as functional or smart materials, such as electromagnetic interference (EMI) shielding or microwave absorption (MA) materials, hydrogen storage materials, sensor materials, de-icing materials, etc.

EMI shielding or MA materials are of wide applications in healthcare, electronic safety and national defence security, and graphene materials are competitive for their low density, high specific surface area, and high electrical conductivity. Li et al. fabricated graphene sheets/polyacrylate composites containing segregated graphene sheet architecture stacked within a polymer matrix, and measured excellent EMI shielding efficiency of around 66 dB over a frequency of 8.2-12.4 GHz when 6 wt% of graphene was added. This was attributed to the high electrical conductivity, ~190 S/m, with a low percolation threshold [92]. Zhang el al. synthesised a macroscopic 3D free-standing graphene foam which possessed an outstanding MA performance, across a wide frequency bandwidth of 60.5 GHz, covering 93.8 % of the entire bandwidth at 90 % of the compressing strain, with a specific MA of $2.2 \times 10^5$ dB $cm^2/g$ [93].

In regards to the applications for hydrogen storage, Kumar et al. reported

designing a nanohole-structured and palladium-embedded 3D porous graphene for hydrogen storage, with a maximum uptake of 5.4 wt% hydrogen [94]. The graphene functioned as a nanohole donor for the distribution of Pt nanoparticles and adherence of H atoms.

In freezing environments, a light-weight de-icing coating is pursued for applications such as aerospace and cold climate situated wind turbines, to prevent the negative influence from ice accretion [95]. Graphene films, due to their incredible thermal, electrical and mechanical properties, as well as their light weight, have become an attractive candidate for electro-thermal heaters. Karim et al. designed highly conductive graphene-based glass fibre rovings with low electrical resistance of approximately 1.7 Ω/cm, which was found to be suitable for de-icing applications [96]. Additionally, the conductive layer of graphene embedded also has great potential to act as a protective layer against lightning strikes, as an alternative to metal materials, therefore reducing the weight and hence cost and power consumption [97].

In addition, graphene materials are also investigated as filler materials in reinforced composites to improve the mechanical performances due to their fantastic mechanical properties [98-102]. Song et al. reported the addition of graphene sheets in polypropylene latex as a nanofiller, and the yield strength and Young's modules of the polymer matrix was found to increase by approximately 75 % and 74 %, respectively [103]. However, despite the

numerous studies already conducted, more work is needed to fully understand the mechanism of the improvement of mechanical properties of the graphene-based reinforced composites [98, 100, 101].

### 2.2.2 Reduction of GO and Functionalisation of Graphene Materials

Given the fact that graphene materials have great potential in various applications, the reduction of GO and functionalisation of the graphene materials is critical in practical use for better performance in specific applications. Mainly, the functionalisation of graphene materials can be divided into the heteroatom doping and hybridisation with other materials. In this section, nitrogen doping as the major type of heteroatom doping, and the metal/metal oxides as one of the typical types of material hybrids with graphene materials, are introduced.

#### 2.2.2.1 Reduction of GO

Due to the oxygen functional groups decorated on the graphitic basal plane, the properties of the graphene materials are heavily affected, such as GO being an electrical insulator, while graphene is a super-conductor. To restore the properties of graphene, a reduction process is carried out on GOs [104]. However, it should be noted that regardless of how the reduction reaction is carried out, the oxygen functional groups can never be fully eliminated, and thus, the final production after reduction treatment is denoted as reduced GO

(rGO) to distinguish it from the pristine graphene. Mostly, the C/O ratio of GO falls into the range of 2:1 and 4:1, while the ratio typically increases to around 12:1 for rGO, or even higher, depending on the methods and degree of the reduction process [9, 105]. There are various methods developed to reduce GO, with the main approaches being thermal annealing and chemical reactions using reduction agents [106].

(1). Thermal annealing reduction

GO reduction, using thermal annealing method, is usually conducted in vacuum [107], or in inert gas such as argon [108], or in reducing gases such as hydrogen [109]. The reduction degree is mainly influenced by thermal annealing temperature, as the removal of the different types of oxygen functional groups starts at different temperatures [110], and expectedly, higher annealing temperature result in further reduction of GO, with higher C/O ratio, and hence higher electrical conductivity. According to relevant studies, the reduction starts in the region of 100 ℃, [110] but temperatures exceeding 1000 ℃ are required for maximum oxygen reduction [111]. According to a study by Sengupta, the optimal thermal annealing temperature is found at approximately 350 ℃, at which the highest carbon content and the minimum defects were achieved [112]. The mechanism of this method relies on the control of thermal radiation that cuts off the bonding between carbon basal plane and oxygen functional groups.

Zhao et al. investigated the temperature effect ranging from 150 to 900 ℃ on

the properties and super-capacitive performance of thermally-reduced rGO [113]. The rGO exhibited the highest Brunauer–Emmett–Teller surface area and electrical conductivity at a temperature of 500 ℃, but they both were found to decrease at higher temperatures, likely resulting from the overlap and coalescence of graphene sheets and smaller dimensions of graphene. However, the highest specific capacitance was achieved at a temperature of only 200 ℃. This is due to the oxygen functional groups, though negatively influencing the electrical conductivity, acting as channels for ions to move into internal surfaces, and to increase the pseudo-capacitance by redox reaction during the charging/discharging process. Based on these results, it should be noted that for specific applications of graphene materials, there are both advantages and limitations for the oxygen functional groups, and the optimal degree of reduction should be determined following experimental trials, as it is not always the case that maximum reduction degree gives the most desirable outcomes.

Thermal annealing methods are commonly used in GO reduction due to their simplicity in operation and for not requiring harmful chemicals. However, this method is restricted in cases where GO is deposited on temperature-sensitive substrates. Moreover, high-temperature thermal annealing is energy-consuming, which also results in higher costs.

(2). Chemical reaction using reducing agents

GO reduction using chemical agents is advantageous due to the mild conditions of room temperature, or low temperature heating, and large-scale production. The commonly used reagents in GO reduction are hydrazine [114, 115], sodium borohydride [116, 117], and hydroiodic acid [118, 119].

Stankovich et al. measured the conductivity of rGO following reduction using hydrazine hydrate, which is about 5 orders of magnitude higher than that of GO [120]. Also, Park et al. analysed the structure of rGO after hydrazine reduction, and found the removal of epoxy and hydroxyl groups, as well as the restoration of the basal plane, and the insertion of aromatic nitrogen moieties in a five-membered ring at the edges [121].

Guex et al. explored the effect of reduction time using 300 mM sodium borohydride at 80 ℃, and found the reduction rate was initially fast, with the C/O ratio increasing from 2:1 to around 6:1 in about 1 h, but then remaining in the range of 6:1 and 7:1 at longer reaction times. The highest conductivity was achieved after reduction for 1440 minutes, which reached to around 1500 S/m [122].

Pei et al. compared the reduction effect of hydroiodic acid with hydrazine and sodium borohydride on GO films, and found that hydroiodic acid can not only remove the oxygen functional groups and restore the defects of the carbon structure, but also maintain the flexibility and integrity of GO films, whereas GO

films broke up after sodium borohydride reduction or were distorted and rigid after hydrazine vapour reduction [123].

However, it should be noted that the reducing agents mentioned above are known to be dangerous and harmful to the operators. Ascorbic acid, as a mild reducing agent, has attracted attention for its non-toxicity, and is a potential substitute for the strong reducing agents [124, 125]. Fernández-Merino et al. compared several reducing agents, and found that the highest electrical conductivity of GO reduced using ascorbic acid reached 7700 S/m when the reductant concentration was 2 mM, which is comparable to the GO reduced by hydrazine [126]. Gasnier et al. prepared graphene paste electrodes using ascorbic acid-reduced graphene composited with graphite and mineral oil, which was successfully applied for sensing ascorbic acid and determining the quantity of NADH in the presence of ascorbic acid [6].

(3). Other methods

Except for thermal annealing and chemical reaction using reducing agents, there are many other methods that have been investigated for the reduction of GO, such as microwave irradiation, photo reduction, electrochemical reaction, and plasma reduction.

GO reduction via microwave irradiation is hypothesised to result from the rapid heating caused by microwave irradiation and is advantageous for its mild environment and short processing time [127]. Voiry et al. applied microwaves

of 1 to 2 second pulses to reduce GO, and before applying, the GO was first slightly reduced via thermal annealing to increase the conductivity for higher absorption of microwave [128]. The rGO obtained exhibited excellent transport properties for FETs, with high mobility values over 1000 $cm^2/Vs$, and demonstrated potential as a catalyst support in oxygen evolution reactions.

Photo reduction has been explored as an environmentally friendly and ultrafast method for GO reduction at ambient conditions, and various photo source have been investigated, such as flash light, and femtosecond laser pulses or other ultraviolet irradiation [129-131].

In regards to electrochemical reduction, the GO can either be in suspension as a component of electrolyte, or deposited on electrodes before the electrochemical reaction [132]. In both approaches, the final production of rGO can be formed on the substrate (the electrode), which is convenient for direct usage. Furthermore, this method is superior for its low cost, fast speed, zero hazardous chemicals involvement, and controllability. Electrochemical reduction process can be conducted in cyclic voltammetry, linear sweep voltammetry, or a constant potential mode. Lindfors et al. applied an electrochemical method to reduce poly(3,4-ethylenedioxythiophene)-GO composite films, the redox capacitance of which increased, showing potential for electrochemical devices [133].

In addition, plasma reduction of GO is introduced in detail in Section 2.3.

#### 2.2.2.2 Nitrogen doping of graphene materials

Chemical doping can be described as a covalent functionalisation of graphene materials that can, not only tune their Fermi level, but also open their bandgap, and hence, modulate the electronic properties of graphene [134, 135]. One of the common chemical doping methods is substitutional doping with one or more hetero atoms, such as boron, nitrogen, phosphorus, sulphur and halogen elements (e.g., chlorine). Among these, nitrogen is the most common dopant, due to its similar atomic size with carbon and strong valence bonding with carbon [7]. Thus, this section focuses on nitrogen-doped (N-doped) graphene.

N-doped graphene is mainly in three configurations: pyridinic N, pyrrolic N and graphitic N (also commonly referred to as quaternary N in the literature) [7], which are shown in Fig. 2-8 [136]. Pyridinic N is a nitrogen atom that connects with two carbon atoms at edges or vacancy defects in $sp^2$ hybridisation, forming two σ-bonds, and contributes one electron to the π bonding, leaving two electrons as a lone pair. Pyrrolic N also represents the nitrogen atom at the edges or defects, but with bonding with two other carbon atoms in $sp^3$ hybridisation, and thus a five-membered ring is formed with two electrons offered to the π bonding. Graphitic N consists of nitrogen atoms that are substituted for carbon atoms in the basal plane, and thus connects with three carbons in $sp^2$ hybridisation, forming three σ bonds, with the other two electrons devoted to π and π* bonds.

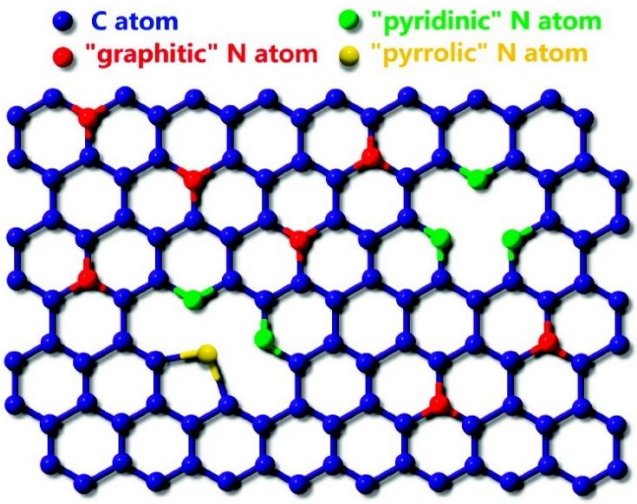


Fig. 2-8 Schematic bonding configurations of N-doped graphene. The blue, red, green, and yellow spheres represent the C, “graphitic” N, “pyridinic” N, and “pyrrolic” N atoms in the N-doped graphene, respectively [137].

These different configurations of nitrogen doping have different effects in tuning the electric properties on the N-doped graphene. Studies [138, 139] have found that the pyridinic N are electron acceptors from graphene due to the adjacent vacancy defects, showing lower binding energy of DOSs (Dirac point shifts towards lower binding energy) as *p*-type characteristics, as well as increased work functions. On the contrary, graphitic N donates electrons, resulting in the Dirac point shifting to higher binding energies of *n*-type doping and an increase in charge density. The opposite doping behaviours of pyridinic N and graphitic N may weaken their integrated modulation effects when the two configurations co-exist, as the DOS versus energy for N-doped graphene with different configurations shown in Fig. 2-9 [139]. Pyrrolic N is mainly considered as *p*-type doping[140, 141], but is possibly due to two adjacent pyridinic N [142]. However, it is believed that graphitic N is the only one of the three configurations that

contributes to increasing the electrical conductivity of graphene.

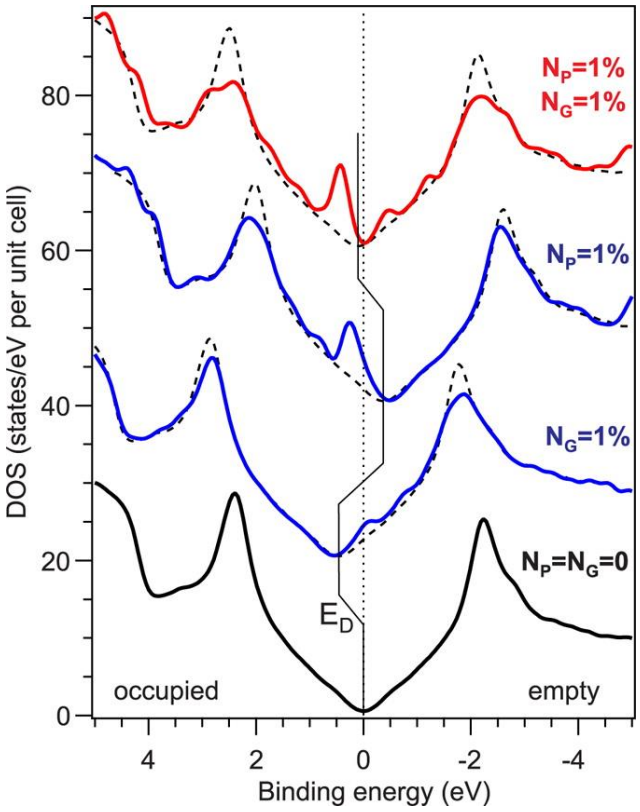


Fig. 2-9 Total DOS versus energy for N-graphene with different concentrations of pyridinic and graphitic N. $N_P$ refers to pyridinic N and $N_G$ is the graphitic N. The solid zigzag line shows the positions of the Dirac point, which was determined by shifting the pure graphene DOS (dashed lines) in energy scale to fit the DOS of each calculated system [139].

1. Applications

Since the electronic properties can be tuned by nitrogen doping, N-doped graphene has potential to improve the performances of graphene materials in applications, such as FETs, LIBs, SCs, electrocatalysts of oxygen reduction reaction (ORR) for fuel cells, and electrochemical sensors.

(1). Field effect transistors (FETs)

As mentioned above in Section 2.1.1.4, the band gap opening of graphene is

needed for the usage of FETs. Studies have shown an obvious band gap in N-doped graphene, which can still maintain most of the superior carrier mobility and electrical conductivity of the undoped graphene. Li et al. prepared N-doped GO through irradiation in ammonia gas atmosphere and fabricated *n*-type graphene FET based on the N-doped GO, whose Dirac point was around -8 V and electron mobility was about 7.08 $cm^2/Vs$ [143]. In the study of Chang et al., the FET based on N-doped graphene nanoplatelets synthesised using a wet-chemical reaction, followed by thermal annealing, exhibited hole and electron mobilities of up to 11.5 and 12.4 $cm^2/Vs$ with Dirac point shifted to -16 V [144].

(2). Lithium-ion batteries (LIBs)

N-doped graphene, compared to pristine graphene, has an increased capacity, especially at high charge/discharge rates [145]. Wu et al. fabricated a LIB based on N-doped graphene, and the capacities at both slow and fast charge rates (1043 mAh/g at charge rate of 50 mA/g and ~199 mAh/g at 25 A/g) were higher than those of pristine graphene-based equivalents. According to their analysis, the increased capacities of N-doped graphene were attributed to higher electrical conductivity and electrochemical activity, thermal stability, defects formed with the doping that store Li, better wettability for ion diffusion, and the preserved basic properties of graphene [146]. Wang et al. prepared a N-doped holey graphene monolith with a volumetric capacity of 1052 $mAh/cm^3$ and a long cycle lifespan of over 1200 cycles that are superior to all other previously reported Si-based and carbon/sulphur hybrid electrodes [147].

(3). Supercapacitors (SCs)

As to SCs, the N-doped graphene also shows an improvement in capacity, and studies believed that the mechanisms differ according to the nitrogen configurations. Mainly, pyridinic N and pyrrolic N enhance the pseudo-capacitance while graphitic N increases the electrical conductivity [148, 149]. Additionally, the protruding nitrogen in the graphitic structure also facilitates increased accumulation of charges on the electrodes, and prevents the stacking of graphene layers, enhancing super-capacitive performances. Sahu et al. synthesised a N-doped graphene with a high nitrogen content of 15 % from a non-mulberry silk cocoon membrane, which exhibited a high specific capacitance of 631 F/g from CV experiments [150]. Balaji et al. also fabricated N-doped graphene-based SCs synthesised via supercritical fluid assisted processing using dimethyl glyoxime, which showed a specific capacitance of 286 F/g from galvanostatic charge-discharge tests at a current density of 0.5 A/g in aqueous 1 M $H_2SO_4$ electrolyte media [151]. Currently, there is still significant research being conducted on N-doped graphene synthesised through various processes for SCs applications [152, 153].

(4). Electrocatalysts of oxygen reduction reaction (ORR) for fuel cells

Widespread research has been dedicated to examining N-doped graphene for the application of electrocatalysts for ORR activities as an attractive alternative to conventionally used platinum [154-156]. This is largely due to the nitrogen doping opening the band gap of graphene, and the doped nitrogen atoms, as

well as the defects induced with the doping, which affect the electronic structure (electron density and spin density), acting as active sites for reactions. This is also explained by the higher electronegativity of nitrogen atoms inducing more electrons when modifying the electronic structure. However, details of how the three different bonding configurations affect the electrocatalytic properties are still not fully understood, as inconsistent results have been found in different studies [157]. Many studies believe that graphitic nitrogen is the dominant factor contributing to the improved performance [158], however, the other bonding configurations, such as the pyridinic nitrogen, may also influence the properties. It is worth noting that it is not always the case that the addition of more nitrogen will improve the performance [159].

(5). Sensors

The nitrogen doping of graphene has the effect of increasing sensitivity for detecting molecules, this is due to improved electron transfer ability and electrocatalytic properties, which allows for N-doped graphene to be considered for applications as electrochemical sensors. Studies have found it effective in detecting various materials, examples of which include, but are not limited to, biomaterials such as ascorbic acid, dopamine, uric acid [160], dangerous chemicals such as Bisphenol A [161], molecules such as Rhodamine B [162], and pH [163].

## 2. Synthesis methods

Methods of N-doped graphene synthesis can be divided into two categories: *in-situ* growth and post-treatment. CVD technique is the most common approach to *in-situ* growth of N-doped graphene [164, 165]. Additionaly, segregation growth [166, 167], solvothermal [168, 169] and arc discharge [170, 171] approaches can also been utilised to synthesise N-doped graphene directly. Post-treatment on graphene materials is usually conducted by: hydrothermal chemical reactions [172, 173], thermal annealing [174, 175], and plasma treatment.

### (1). CVD synthesis

CVD synthesis of N-doped graphene is comparable to pristine graphene, with the only difference being that nitrogen-containing precursors are added as a nitrogen source. Wei et al. reported being the first to experimentally synthesise N-doped graphene using a CVD technique [137]. It was conducted by heating the substrate rapidly with a copper film on it as a catalyst, and ammonia was simultaneously added with methane as the nitrogen and carbon sources, respectively. Other than the commonly used gas mixture of methane and ammonia, other carbon and nitrogen sources can also be used in CVD synthesis of N-doped graphene. Cui et al. applied ethanal and methylamine in CVD to synthesise N-doped graphene, which is found to predominantly contain graphitic N, and shows even lower sheet resistance than CVD-synthesised pristine graphene [176]. Also, Shinde et al. managed to synthesise N-doped

graphene via atmospheric pressure CVD using camphor and melamine as a solid type of carbon and nitrogen sources [177].

(2). Hydrothermal synthesis

Hydrothermal synthesis are mainly carried out using GO aqueous dispersion and chemicals containing nitrogen, such as ammonia [178, 179], organic amine [180, 181], and urea [173, 182], at an elevated temperature in the range of 100-200 ℃ for a duration of several hours. GO is selected as the precursor of N-doped graphene for its hydrophilicity. During the hydrothermal process, chemical reactions occur between GO and nitrogen-containing chemicals, which result in both GO reduction and nitrogen doping. Zhang et al. compared the reduction and doping effects, as well as the super-capacitive performances based on the N-doped graphene/cobalt oxide composites using urea, ammonia and hydrazine hydrate as different reducing agents and nitrogen sources in hydrothermal reactions [183]. Results showed the approaches using urea exhibited the best super-capacitive performances, which may be attributed to its superior reduction degree and the resulting nitrogen configuration type.

(3). Thermal annealing approach

Similar to hydrothermal synthesis, thermal annealing synthesis of N-doped graphene is also realised via chemical reactions between graphene materials and nitrogen-containing chemicals but they are both in solid phase [175]. Mostly, graphene or GO is mixed with melamine or urea and thermal annealed at a high

temperature in the range of 350-800 ℃ [184, 185]. Compared to hydrothermal synthesis, the thermal annealing is conducted at much higher temperatures but for shorter durations of about 1 h or less. Li et al. synthesised N-doped graphene using GO and urea, and then investigated the effects of nitrogen precursors using other nitrogen-containing chemicals (cyanamide, melamine, ammonium nitrite and ammonium chloride). The comparison results showed that the urea treated samples contained the highest nitrogen content (18.7%) with the lowest oxygen levels (4.9%), and exhibited the best catalytic oxidation activity [186].

As to all the methods mentioned above, CVD synthesis, as an *in-situ* synthesis method, is limited for its low productivity, while post-treatments involve chemicals waste throughout the process, hydrothermal synthesis requires long durations, and high temperatures are required in thermal annealing synthesis. Plasma treatment, as another post-treatment method, has the potential to overcomes some of these drawbacks. The details of synthesising N-doped graphene via plasma treatment are specially introduced in Section 2.3.3.2.

#### 2.2.2.3 Hybrids with metal/metal oxide nanomaterials

Functionalisation of graphene materials through being combined with other nanoparticles, especially transition metal or metal oxide nanoparticles, and forming into a graphene-based composites, is another approach to broadening their applications due to the synergetic effects in property improvements as well as hindering aggregation of the nanomaterials [12, 187]. Due to the wide variety

of the metal and metal oxide nanoparticles, the hybrids of graphene materials and metal/metal oxide nanoparticles were applied in many fields, such as energy storage and conversion, catalysis, sensing, and biological applications, and each of the applications has their preferred metal/metal oxides types. However, given the wide variety of the metal/metal oxide types of the composites, it is hard to fully cover all the types of composites for all the applications in detail here, and a certain type of graphene-based composites is not limited in only one kind of applications. Based on this consideration, herein, this section only focuses on the relevant research progress of hybrids of graphene and metal/metal oxide nanoparticles applied on SCs as an example for the introduction of their applications, as the corresponding properties and super-capacitive performances of the samples were evaluated in this thesis. Readers who are interested in more of the applications of the graphene-based composites can refer to an review article [12], and some more applications are also exemplified in Section 5.4.

1. Application of SCs

As to SCs, transition metal oxides are mainly selected to composited with graphene materials, such as ruthenium oxides, manganese oxides, iron oxides, nickel oxides, molybdenum oxides, and cobalt oxides [91]. These transition metal oxides are electrochemically active on their own, suitable as SCs electrode materials for increasing pseudo-capacitance, and can prevent the stacking of graphene sheets, ensuring the high specific surface area of

graphene materials. In return, graphene with high electrical conductivity overcomes the poor electrical properties of the metal oxides, and acts as barriers to prevent the aggregation of metal oxide nanoparticles.

Ruthenium oxide ($RuO_2$) is of good super-capacitance due to its electrical conductivity and electrochemical reversibility, and graphene- $RuO_2$ composites can further enhance the performance of SC applications [188]. Soin et al. sputtered nanocrystalline $RuO_2$ on few-layer graphene, and due to the synergetic effect between graphene and $RuO_2$, the specific capacitance of the hybrids reached about 650 F/g, twice as much as that of $RuO_2$ alone [189].

Manganese oxide ($MnO_2$), an abundant material in nature with environmental friendliness, shows potential as electrode material for SCs but is restricted for its poor electrical conductivity. Graphene-$MnO_2$ composites avoid the drawbacks of the individual component in the application, as $MnO_2$ nanoparticles reduce the diffusion length of alkali metal cations in the electrolytes for a rapid intercalation via chemical reactions, and graphene provides extra rapid electron transfer channels for the reaction to occur, in addition to their own contributions to the double-layer capacitance [190]. Singu et al. produced hybrids of graphene and $MnO_2$ in a one-pot hydrothermal chemical reaction method using GO solution with $MnCl_2$ in $NH_3$ solution, which exhibited an excellent super-capacitive performance as energy and power densities reached 23.3 Wh/kg and 2001 W/kg, respectively, with a capacitance

of 398.8 F/g, due to the synergetic effects of the graphene and $MnO_2$ [191].

Analogous with $MnO_2$, iron oxides (both $Fe_3O_4$ and $Fe_2O_3$) are also appealing as components in graphene-based SC electrodes for their low cost and non-toxicity. Shi et al. synthesised hybrids of rGO sheets and $Fe_3O_4$ nanoparticles and deposited them on carbon papers as SC electrodes. With an optimised ratio of $Fe_3O_4$ and rGO, better super-capacitive performances were achieved, compared to the pure $Fe_3O_4$ or rGO ones [192]. Ma et al. also fabricated a SC electrode using N-doped graphene with $Fe_2O_3$ nanoparticles, and the specific capacitance increased to 267 F/g at a current density of 0.5 A/g [193].

Apart from the metal oxides, pure noble metal nanoparticle hybridisation with graphene materials have also been studied as SC electrode materials, such as silver, gold, palladium and platinum, etc. These noble metals, although being expensive, can be additives in composites for SC electrodes due to their high electrical conductivity. The pseudo-capacitance can therefore be improved as rapid and effective electrons transport in reduction and oxidation reactions are promoted [194].

Silver is the noble metal with the highest electrical conductivity. When compositing with graphene materials, the supercapacitors fabricated using the graphene/silver hybrids show an improved performance, as confirmed by numerous studies [195-201]. Khamlich et al. used a microwave-assisted method to grow silver nanoparticles on graphene networks, and the

nanocomposites were applied as SC electrodes [199]. The nanomaterials showed a better super-capacitive performance in comparison with that of graphene alone, as the specific capacitance reached 528 F/g. Jiao et al. added silver in the composites of graphene and polyaniline, and evaluated the super-capacitive performance of the ternary composite on filter paper, and a specific capacitance of 437.3 F/g was achieved, with energy and power densities of 1133.5Wh/kg and 88.8 kW/kg, respectively [201].

Similarly, gold incorporated in graphene materials as SC electrodes can also enhance the super-capacitive performances [202-205]. Sahoo et al. prepared a nano-gold decorated rGO wrapped polymethyl methacrylate nanohybrids and investigated the super-capacitive performances of a symmetric cell based on the nanohybrids [204]. The addition of gold in the nanohybrids greatly increased the energy density to 29.46 Wh/kg at a power density of 235 W/kg, and 19.20 Wh/kg at the power density of 598 W/kg, resulting from the synergetic effect of rGO and gold, due to the high electrical conductivity of gold that improves the overall electrical conductivity of the hybrids and facilitates the adsorption of electrolyte. Bahar et al. synthesised hollow porous gold nanoparticle decorated rGO nanocomposites via chemical method using hydroquinone as the reducing agent [205]. The improvement of adding gold in rGO was confirmed, and the effect of gold nanoparticle size was also investigated by adjusting the concentration of hydroquinone. The results demonstrated that decreasing the particle size contributed to a higher specific capacitance, which may be

attributed to an increase of particle number or density.

Palladium nanoparticles integrated with graphene materials are mainly applied in applications of catalysis and sensing, but in recent years studies on graphene-palladium composites were also carried out for the applications of SCs [206-209]. Dar et al. combined palladium nanoparticles and graphene nanosheets together via chemical reactions from palladium chloride and GO, and at a current density of 1.25 A/g, the specific capacitance, energy density and power density increased to 637 F/g, 56 Wh/kg and 1166 W/kg, respectively, compared to pure graphene nanosheets [206]. Kalambate et al. evaluated the performance of a SC based on a ternary composite containing N-doped graphene, palladium nanoparticles and porous polyaniline [209], and the incorporation of palladium nanoparticles contributed to the enhanced specific capacitance to 931 F/g due to its high electrical conductivity.

Platinum and graphene hybrids are mainly explored for applications of electrocatalysis due to the high catalytic properties [210], but also show potential for application as SCs [211-215]. Zhang et al. decorated platinum nanoparticles on graphene and explored the performance of the hybrids as SC electrodes [212]. The specific capacitance of the Pt/rGO hybrids was enhanced to 154 F/g at a current density of 0.1 A/g, with a much better capacity retention compared to rGO. Comparable with the other noble metals mentioned above, the improvement of the performance is deduced from being an intercalator to

increase the interlayer spacing for larger surface area and a bridge for electron transportation at defects, given the high electrical conductivity of platinum. The uniform distribution of the platinum nanoparticles without agglomeration was also noted for an effective enhancement. Sha et al. also fabricated platinum nanoparticles decorated graphene-polyaniline composites, which exhibited a specific capacitance of 922.5 F/g at a current density of 1 A/g as SC electrodes, higher than that without platinum [215].

2. Synthesis approaches

The synthesis of the graphene-based composites with metal/metal oxide nanoparticles are mainly carried out in two ways: *ex-situ* hybridisation and *in-situ* reduction, as shown in Fig. 2-10 [12]. *Ex-situ* hybridisation describes the approach of preparing graphene materials and metal/metal oxide nanoparticles separately before mixing together. For a better compositing effect, modifications of both, or either, graphene materials and nanoparticles are needed [216-221]. This is a complicated and time-consuming technique, and thus in most cases, *in-situ* reduction is carried out instead. *In-situ* reduction is conducted through simultaneous reduction of the mixture of GO suspension with metal precursors (mostly metal salts) via various reduction methods, resulting in a one-pot synthesis. Many reduction methods have been applied for the preparation of graphene-based metal/metal oxide nanocomposites, such as chemical reaction, hydrothermal (solvothermal) reduction, and electrochemical reduction.

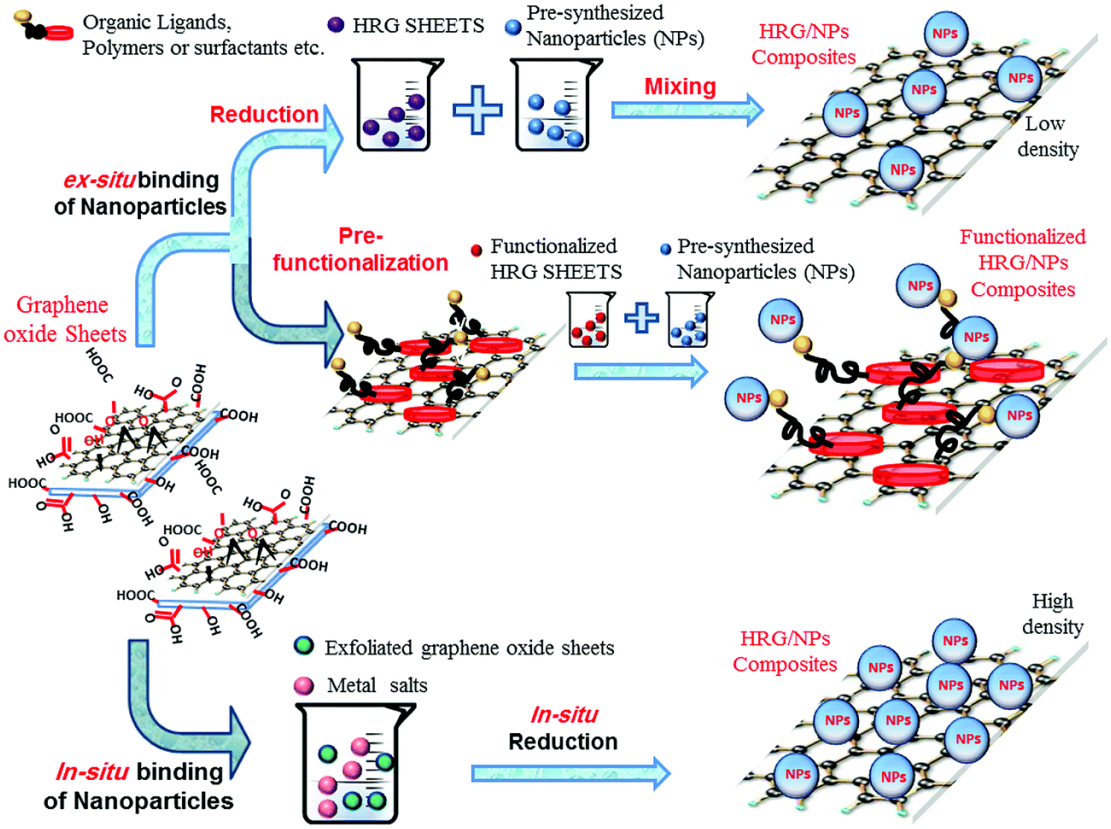


Fig. 2-10 Schematic illustration of the hybridising graphene and nanoparticles [12].

Still, due to extensive work having already been carried out on the methods for various graphene-metal/metal oxide hybrids, it is not realistic to fully cover all the research and studies within this review. Thus, iron oxides, and four typical noble metals (Ag, Au, Pd, and Pt) are taken as examined in more detail.

Shen et al. synthesised magnetic nanocomposites of graphene and $Fe_3O_4$ in a one-pot solvothermal method using GO and iron acetylacetonate as raw materials in ethylene glycol. Hydrazine hydrate was added if GO reduction was needed [222]. For chemical reaction of preparing graphene/$Fe_3O_4$ composites, iron precursors of two valence states ($Fe^{2+}$ and $Fe^{3+}$), such as $(NH_4)_2Fe(SO_4)_2 \cdot 6H_2O$ together with $NH_4Fe(SO_4)_2 \cdot 12H_2O$, or $FeCl_3 \cdot 6H_2O$ plus $FeCl_2 \cdot 4H_2O$, were applied slowly with ammonia solution under alkaline

conditions for precipitation of $Fe_3O_4$ on graphene [223-225]. If only $Fe^{3+}$ solution was applied, $Fe_2O_3$ would then be composited [226]. Other iron salts such as $FeSO_4 \cdot 7H_2O$ [193], $Fe(NO_3)_3 \cdot 9H_2O$ [227], can also be use as precursors. Additionally, Ghasemi et al. applied an electrophoretic approach to fabricate nanocomposites of $Fe_3O_4$ anchored on graphene sheets, with iron salts $FeCl_3$ and $FeCl_2$ being used as the positively charged metal cations migrating and depositing with GO to the cathode [228].

Similarly, for pure noble metal nanoparticles (Au, Ag, Pt and Pd), the protocol for hybridisation with graphene materials is the simultaneous reduction of the corresponding metal salts and GO. The main precursors for the four corresponding noble metals are chloroauric acid ($HAuCl_4$) [229-234], silver nitrate ($AgNO_3$) [235-238], chloroplatinic acid ($H_2PtCl_6$) [239-241] and palladium chloride ($PdCl_2$) [242, 243], palladium acetate [$Pd(OAc)_2$] [244, 245], or palladium nitrate [$Pd(NO_3)_2$] [246], respectively. The reducing agents and stabilising agents are hydrazine hydrate [247], sodium borohydride[248-251], sodium citrate [252-254], or ascorbic acid [255, 256]. The chemical reactions are carried out in alkaline solution by modifying the pH value with ammonia solution or sodium hydroxide. Other than direct chemical reduction, annealing approaches [257, 258], electrochemical [259-261] or electrodeposition methods [262-264], photochemical reduction [265-268, 246], reduction assisted by ultrasound irradiation [269], or microwave irradiation [270-275] with mild reducing agents such as ethylene glycol have all been applied for the synthesis

of graphene/metal hybrids [276]. Some examples are introduced below.

Liu et al. coated graphene sheets on Cu or Zn foils via immersion and subsequent drying, and the graphene coated Cu or Zn foils were re-immersed into metal ion solutions ($H_2PtCl_4$, $HAuCl_4$, $H_2PdCl_4$ and $AgNO_3$) for a period of time [277]. These Cu or Zn substrates functioned as reducing agents and the noble metals (Pt, Au, Pd, and Ag) were reduced and distributed on graphene sheets homogeneously. The procedure is shown in Fig. 2-11. Giovanni et al. mixed GO solutions with noble metal salts via ultrasonication and then dried the solution in a vacuum oven, before thermal annealing in nitrogen or hydrogen at 1000 ℃ to yield the noble metal doped graphene hybrid [278]. This process is shown in Fig. 2-12.

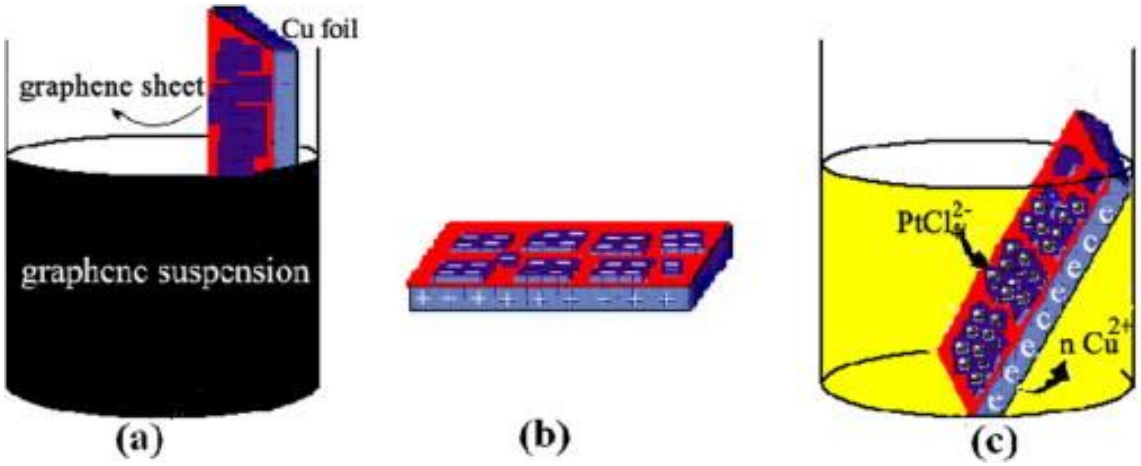


Fig. 2-11 Schematic illustration for (a) preparing Cu foil-supported GS substrate, (b) charge redistribution on Cu foil-supported GS substrate, and (c) Pt nanoparticle deposition process [277].

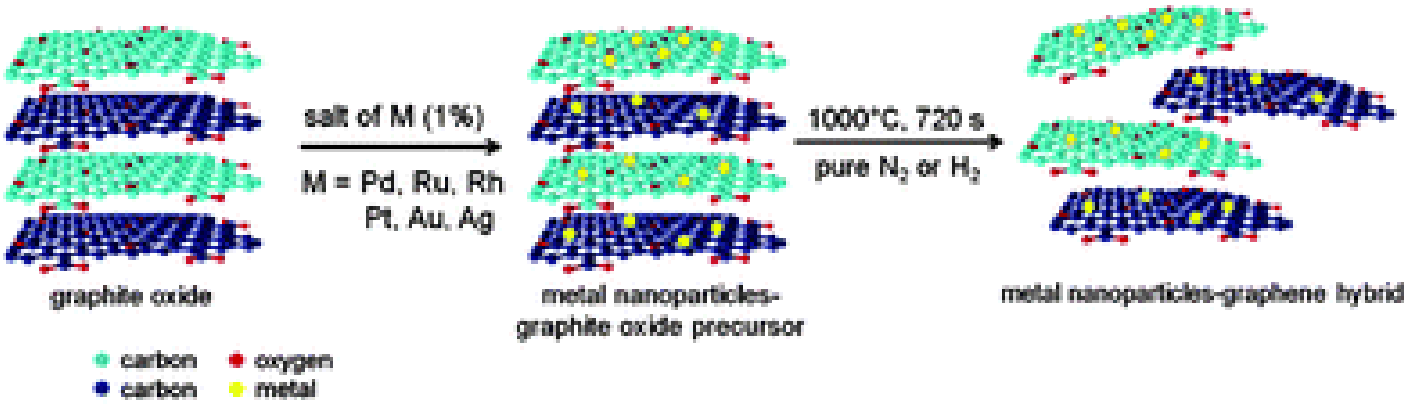


Fig. 2-12 The production route of noble metal doped-graphene hybrid materials [278].

Recently, Park et al. employed a galvanic reaction to deposit gold on graphene [279]. A reductant/graphene/oxidant sandwich structure was designed as $AuCl_4^-$ was dropped on graphene previously formed on a germanium wafer or copper foil substrates, and the gold ion acted as the reductant, while the graphene substrate was the oxidant. Electrons could transfer across graphene, hence enabling the redox reaction to occur. Grag et al. explored the potential of peroxidase-like and carbocatalytic properties of GO in oxidising silver nitrate [280]. The peroxidase-like and carbocatalytic properties were triggered in the presence of $H_2O_2$, $NH_3$ in $Na_2HPO_4$ or in deionised distilled water. The outcomes indicated successful conversion of $AgNO_3$ to Ag nanoparticles with GO alone. Abdolhosseinzadeh et al. reported an ultraprecise photocatalytic method of a scalable synthesis for platinum/rGO composites, as partially reduced GO and $H_2PtCl_6$ were mixed with methanol as hole-scavengers and were then exposed to ultraviolet illumination for a specific time period, with the subsequent addition of ascorbic acid and heat treatment for 1 h at 90 ℃ [281]. Tang et al. synthesised a Pd precursor: Pd(bipyridine)(pyrene)$_2$, whereby Pd

nanoparticles could be decorated on graphene without introducing defects, as graphene could establish π-π bonds with this Pd precursor when immersed in the precursor solution, and this Pd precursor reduced to $Pd^0$ after annealing in $H_2$/Ar at 300 ℃ for 40 min, therefor decorating graphene with Pd in a simple and cost-effectively approach. [282]

Based on the introductions above, graphene materials functionalised via reducing, nitrogen doping and hybridising with metal/metal oxide nanoparticles can effectively broaden their potentials for various applications. Various methods have been explored and investigated in functionalising graphene materials. Among these, plasma treatment, as an effective technique in surface engineering, has been applied in GO reduction and nitrogen doping of graphene. Therefore, the section below gives a specific introduction on plasma technology and its relevant application in functionalisation of graphene materials.

# 2.3. Plasma Technology

## 2.3.1 Introduction of Plasma Physics

### 2.3.1.1 Basic knowledge of plasma

Plasma is a mixture of charged particles, active species and neutral atoms, and is therefore more than just ionised molecules. It is referred to as the fourth state of matter to distinguish from state of gas, whose basic constitution unit is molecular. Plasma is electrically conductive due to individual mobile charged

particles, but is yet neutral as a whole for equal ratio of positively and negatively charged particles.

Plasma can be generated from heating gas to extremely high temperatures or by applying strong electromagnetic fields, so that some of the gas molecules are ionised into electrons, ions, protons, or disassociated into neutral radicals, with the unionised gas molecules and atoms being also found in excited states. The thermal method needs to be applied at an extremely high temperature for the ionisation, which results in extreme working conditions and high energy consumption. Thus, in most cases, electromagnetic fields are applied to generate plasma [283].

Due to the characteristics of plasma, it is fundamental to firstly understand electrical discharge, with DC glow discharge being one of the most common forms.

#### 2.3.1.2 Glow discharge

When applying a voltage in a low-pressure tube to generate electrical discharge and the corresponding plasma, the current follows nonlinearly with the voltage, as shown in the curve in Fig. 2-13 [284]. According to the curve, there are mainly three regimes of electrical discharge: dark discharge, glow discharge, and arc discharge. This curve is introduced from left to right in detail as follows.

Background ionisation regime (A-B). This section is mainly caused by ions and electrons from cosmic rays, so the current increase slowly at a slow rate with a

low voltage.

Saturation regime (B-C). With the increase of voltage, all the electrons and ions from the background radiation are consumed to form the discharge, but no new electrons are created *in-situ*.

Townsend regime (C-E). The applied voltage is large enough that secondary electrons gain sufficient energy to ionise neutral gases, and therefore molecules are ionised directly, increasing the current exponentially. Between D and E is unipolar corona discharge, where local electric field concentrations at sharp sites reaches the breakdown strength of the neutral gases. At point E, the voltage reaches the value where the electrical breakdown occurs.

The three regimes above are categorised as dark discharge, due to being invisible to the eye (dark) except the individual corona discharges between D and E. When the electrical breakdown occurs, the plasma becomes visible, and the discharge regime comes into glow discharge.

Normal glow (E-G). Due to the ionisation, charges building on the electrodes are dissipated, resulting in a reduction of voltage at first between E to F, with the voltage remaining stable with an increase of current from F to G when the plasma increasingly occupies the cathode until it fully covers the cathode at the saturation point at G. During this section, the current is independent from the voltage. If starting reversely from G, as current decreasing, the normal glow

follows the curve from G to F’ and to D, due to the hysteresis from the plasma being already ignited.

Abnormal glow (G-H). The voltage increases with increasing current due to more charges building up at the cathode. It is worth noting that glow discharge plasma treatments are conducted within this region.

Glow-to-arc transition (H-I). Incandescence is achieved in this section from the high current density on the cathode, with a drop of voltage and increase of current, as the glow discharge transforms into arc discharge.

Non-thermal arc regime (I-J). The voltage continues to decrease with the increase of current, and the temperature of the electrons, ions and gases are unequal.

Thermal arc regime (J-K). The voltage once again increases with the current, and the temperature of the electrons, ions and gases are almost equal, achieving a thermodynamic equilibrium state.

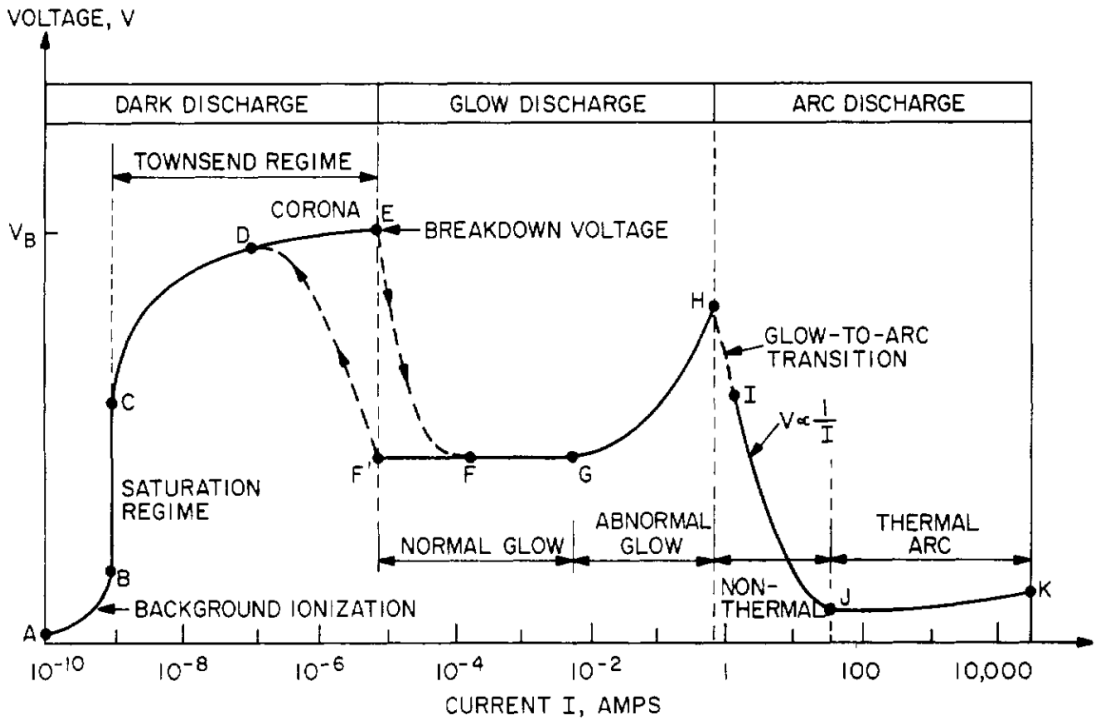


Fig. 2-13 Voltage-current characteristic of the DC low pressure electrical discharge tube [284].

When plasma is formed in the normal glow regime of low-pressure DC electrical discharge, it appears as a stratified phenomenon as shown in Fig. 2-14 [284], with characteristics axial profiles described below. The plasma between the cathode and anode can be divided into different zones, and in the sequence from cathode to anode, they are: Aston dark space, cathode glow, Crookes dark space, negative glow, Faraday dark space, positive column, anode glow, and anode dark space.

Aston dark space. A very thin region next to the cathode with strong electrical field but low electron density or energy that cannot initiate gas excitation.

Cathode glow. The region with high ion density, as atoms are sputtered off the cathode and ions excite more atoms, emitting luminescence.

Crookes dark space. Also named cathode dark space, is a region with high ion density but lower electrical field than the Aston dark space.

These three spaces above belong to cathode region, as electrons accelerate and gain energy.

Negative glow. The region where gas ionisation and excitation occur, as electrons with the highest energy produce positively charged species and excitation events, hence lowering the local electrical field and emitting the brightest light in the discharge region.

Faraday dark space. A region where the energy of electrons, the electron density and net charges reduce after the ionisation and excitation.

Positive column. A quasi-neutral space with low electrical field only to maintain the ionisation at the cathode region. The glow in this zone is weak but uniform, and it stretches with the discharge tube given a constant pressure.

Anode glow. A brighter zone than the positive column, as the boundary of anode sheath.

Anode dark space. The anode sheath negatively charged due to electrons attracted.

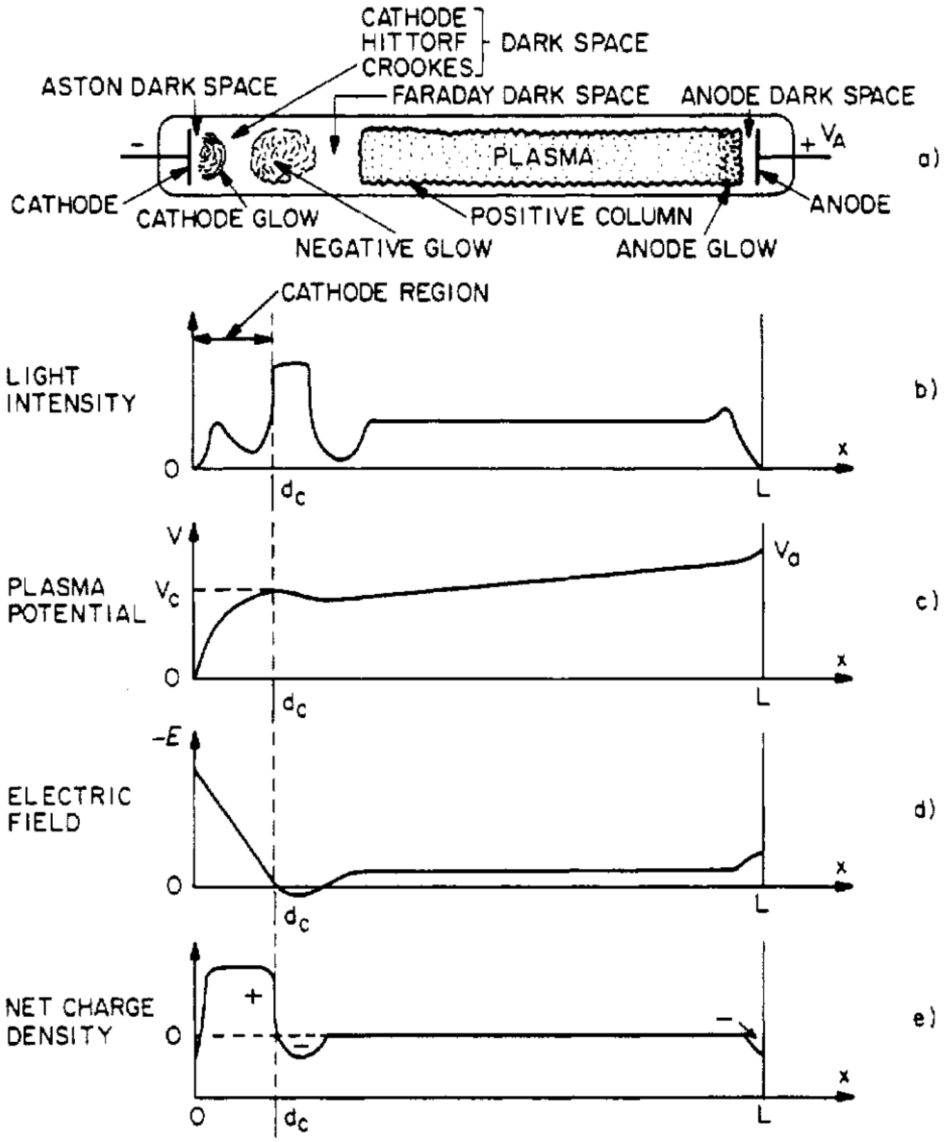


Fig. 2-14 Axial variation of the characteristics of the normal glow discharge [284].

After plasma fully covers cathode, the increase of current requires further increase of voltage, and it comes into abnormal glow discharge. In this regime, the structure is almost the same as normal glow discharge, only except for being more luminous.

#### 2.3.1.3 Interactions between ions and material surface

Plasma treatment in material processing is a technique which utilises plasma to achieve material surface engineering. Active species of plasma from different

processing gases have different treatment effects. During plasma treatment processing, these ionised particles and active species interact with the to-be-treated material surface directly, or collide with each other and produce secondary, short-lived precursors needed for interactions with the surface, overcoming their internal energy, breaking bonds on the material surface to remove surface contamination or other unwanted components, and alternatively forming new bonds to modify the surface or grow a new layer or coating.

The interaction effects of plasma treatment can be sputtering, heating, implantation, diffusion, cleaning, defect formation, etching, and chemical reaction acceleration [285]. For plasma sputtering, ions strike the target materials at the cathode, and the atoms from the target are then sputtered (dislodged) out and deposited on the workpiece held nearby. As to heating, the ion bombardment to the surface acts to transfer kinetic energy to the target, causing the temperature to increase. For implantation, the ions become embedded onto the surface during the bombardment, forming an implantation layer as a coating on the surface. Diffusion means that the substances from either the plasma or atoms deposited from sputtering travel through the surface of the heated workpiece. Cleaning, defects formation and etching are all caused by the ion bombardment to the cathode but with different degrees. Cleaning is the elimination of contaminants on the surface, such as the oil or oxidation layers, as these contamination on the surface are sputtered away; defects are

formed when some of the atoms from the surface material being sputtered out, leaving the crystalline structure with vacancies or dislocations; etching occurs when the atoms of the surface layer being sputtered out, leaving with an elimination of an area macroscopically. Chemical reaction acceleration represents the utilisation of plasma for an acceleration or promotion of a chemical reaction, stimulated by the active species present in the plasma.

### 2.3.2 Categories of Plasma techniques

There are a variety of plasma treatment categories, based on different characteristics of plasma [286]. According to operating pressure, there is low pressure plasma and atmospheric pressure plasma [287]; in terms of processing temperature, there is low temperature plasma and high temperature plasma; as to the thermodynamic state, plasma can be divided into equilibrium plasma and non-equilibrium plasma. Equilibrium plasma is also called thermal plasma, where the kinetic energy of the electrons are nearly the same as the ions and gases, while for non-equilibrium plasma, which is also named non-thermal plasma or cold plasma, the kinetic energy of the electrons is much higher than that of the ions or gases [288]. Generally, plasma treatment is named after the energy supply type for the generation of plasma or the nature of discharge, for example, plasma generated using electron beam is called electron beam plasma [289, 290]. According to the frequency of electric power supply, plasma can be classified into DC plasma, radio-frequency (RF) plasma

(usually at 13.56 MHz), and microwave plasma (mainly at 2.45 GHz). Based on the discharge characteristics and form, there are corona discharge plasma, glow discharge plasma, arc discharge plasma, dielectric barrier discharge (DBD) plasma, and hollow cathode discharge (HCD) plasma. Apart from above, there are also two coupling types for the energy generating the plasma: inductive and capacitive coupling. All these different plasma categories make plasma treatment an intriguing technique in materials engineering [291, 292]. Therefore, this review selectively introduces some interesting types of plasma techniques and their unique structures below.

#### 2.3.2.1 DBD plasma

DBD, short as barrier discharge, or named silent discharge, features its configuration with one or more insulators acting as the dielectric material between the discharge gap. Fig. 2-15 shows two basic configurations of DBD reactors [293]. Alternating voltage is applied so that displacement current can pass through the dielectric barrier, the amount of which is determined by the constant and thickness of the dielectric material, and the time derivative of the applied voltage. Very strong electric fields are required in the discharge gap to enable the current to pass through the barrier, as electrical breakdown typically occurs in gases. When the pressure is in the range of $10^5$ Pa, numerous micro-discharges can be observed [294]. The dielectric works as a ballast to limit the average current density in the gas and ensures that the micro-discharges are distributed evenly. Due to the principles of discharge, DBD plasma belongs to

non-thermal and atmospheric pressure plasma. It is advantageous, compared to other conventional plasma techniques, because of a higher efficiency and a lower energy consumption. It does not require a vacuum system, and the temperature during its use remains at room temperature, and therefore, it is suitable for temperature-restricted working environments and materials. DBD plasma technique has been applied in industry for large-scale treatment due to its simple configuration.

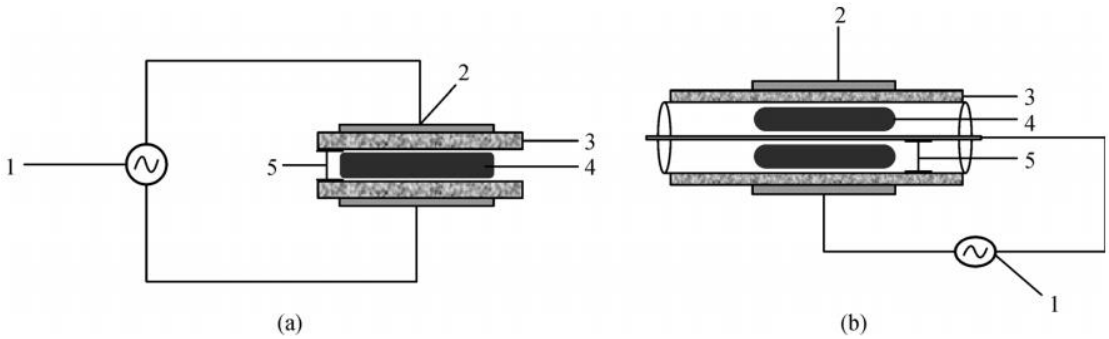


Fig. 2-15 Configurations of dielectric barrier discharge (DBD) reactors, where 1 is the alternating current (AC) at high voltage; 2 is the electrode; 3 is the dielectric barriers; 4 is the discharge zone; 5 is the discharge gap. (a) Planer DBD configuration; (b) Cylindrical DBD configuration [293].

#### 2.3.2.2 Atmospheric pressure plasma jet (APPJ)

APPJ is a unique technique in atmospheric pressure plasma that has attracted extensive research interest. After plasma generation, this technique ejects the plasma gases through a jet or nozzle via strong flow rates, usually inert gases such as He or Ar are used. This is a type of non-equilibrium plasma technique that does not require any vacuum system, so it is cost-effective, convenient and flexible. The first use of APPJ can be dated back to 1960s, and after many years of development, it has evolved into several different schemes and devices [295].

Plasma source of APPJs can be DC, pulsed DC, alternating current, RF or microwave, and the configuration can vary from coaxially or rectangular geometries, as shown in Fig. 2-16. The use of the nozzle for the jet of the plasma limits its use for large-area processing, but using array of jets and scanning strategies can solve this problem [296]. Thus, APPJs have also found industrial use. This technique has been employed in a number of applications, including but not limited to surface modification, deposition of coatings and biomedical applications [297].

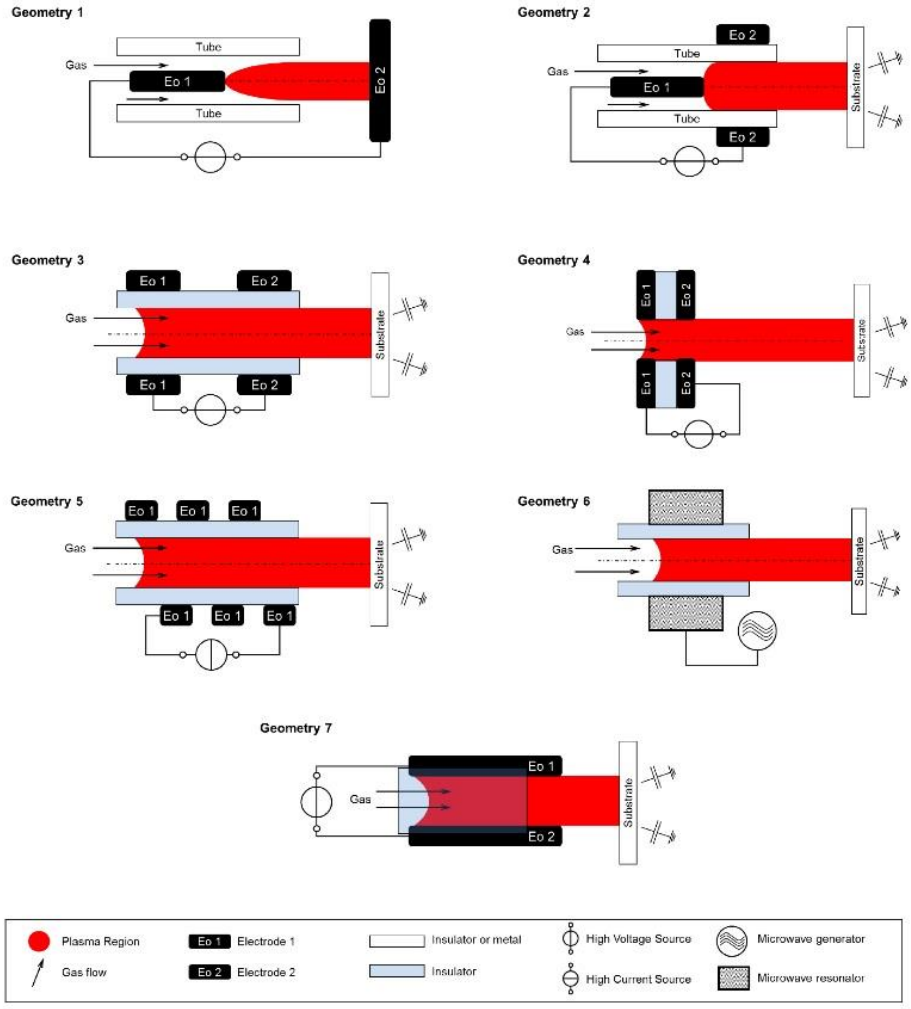


Fig. 2-16 Cross sectional views of the basic geometries of coaxially (geometry 1–6) and rectangular (geometry 7) arranged plasma jets [295].

#### 2.3.2.3 HCD plasma

HCD is a kind of discharge where the negative glow from nearby surfaces from overlapping regions (hollow cathodes), resulting in secondary electrons being trapped, and hence a dense plasma with high current density being produced. The hollow structure can be in a parallel plane, cylinder or other cavity-like shape. This phenomenon is referred as the hollow cathode effect [298]. In HCD plasma, the electron density and discharge current are high due to the large number of secondary electrons produced and maintained. Mechanisms explain that this is due to the pendulum effect of electrons with high energy in the discharge. These high-energy electrons are generated from the bombardment of, and photoemission from, the cathode surface or ionisation events following gas collisions, which are then accelerated due to the cathode sheath potential, and lead to the electrons passing through the negative glow region to the opposite cathode sheath, and are then reflected back, the trajectory of which is similar to a pendulum. With each pendulum trajectory, increasing the ionisation of neutral gases can occur. Moreover, a larger number of photons and excited neutral atoms enhance the electron emission, which also contributes to a higher local plasma current density. However, a different perspective developed, where it is the quasi-resonant generation of doubly-charged gas ions within the central negative glow region of the discharge that give rise to the hollow cathode effect [299]. Regardless of the fundamental mechanism involved, HCD plasma characteristically involves high current density plasma, and therefore,

is suitable for applications like thin film preparation.

#### 2.3.2.4 Active-screen plasma

Active-screen plasma (ASP) is based on conventional DC plasma with a configuration modification that an active screen is applied on the cathode plate. The active screen is made of a mesh cage, that houses the workpiece that is positioned on an insulated worktable at a floating potential. The configuration of ASP is shown in Fig. 2-17(a,b) [300]. As shown in the diagram (Fig. 2-17(a,b)), the plasma is distributed around the cathode. In conventional DC plasma configuration, the samples are positioned on the cathode plate, and thus the samples themselves are cathode as well, so that the plasma directly functions on the samples. In comparison, samples are positioned on a plate at a floating potential housed in the active screen in ASP configuration, and thus only the active screen is the cathode, so that plasma is mainly distributed around the active screen without reaching the samples. Therefore, ASP is a type of remote plasma or post-plasma technique, as during the ASP process, positively charged ions are mainly attracted to and bombard to the active screen, whilst radicals are the predominant species that reach and interact with the workpiece, minimising the damage that may be caused by the ion bombardment. Also, sputtering occurs in ASP process, and metal nanoparticles from active screen are sputtered off and deposited on the sample, as shown in Fig. 2-17 (c). Due to the modification of the setup, ASP can avoid the formation of edge effects and hollow cathodes, resulting in more uniform and homogeneous treatments

[301]. The isolation of the workpiece from cathode also enables ASP to treat electrically non-conductive materials.

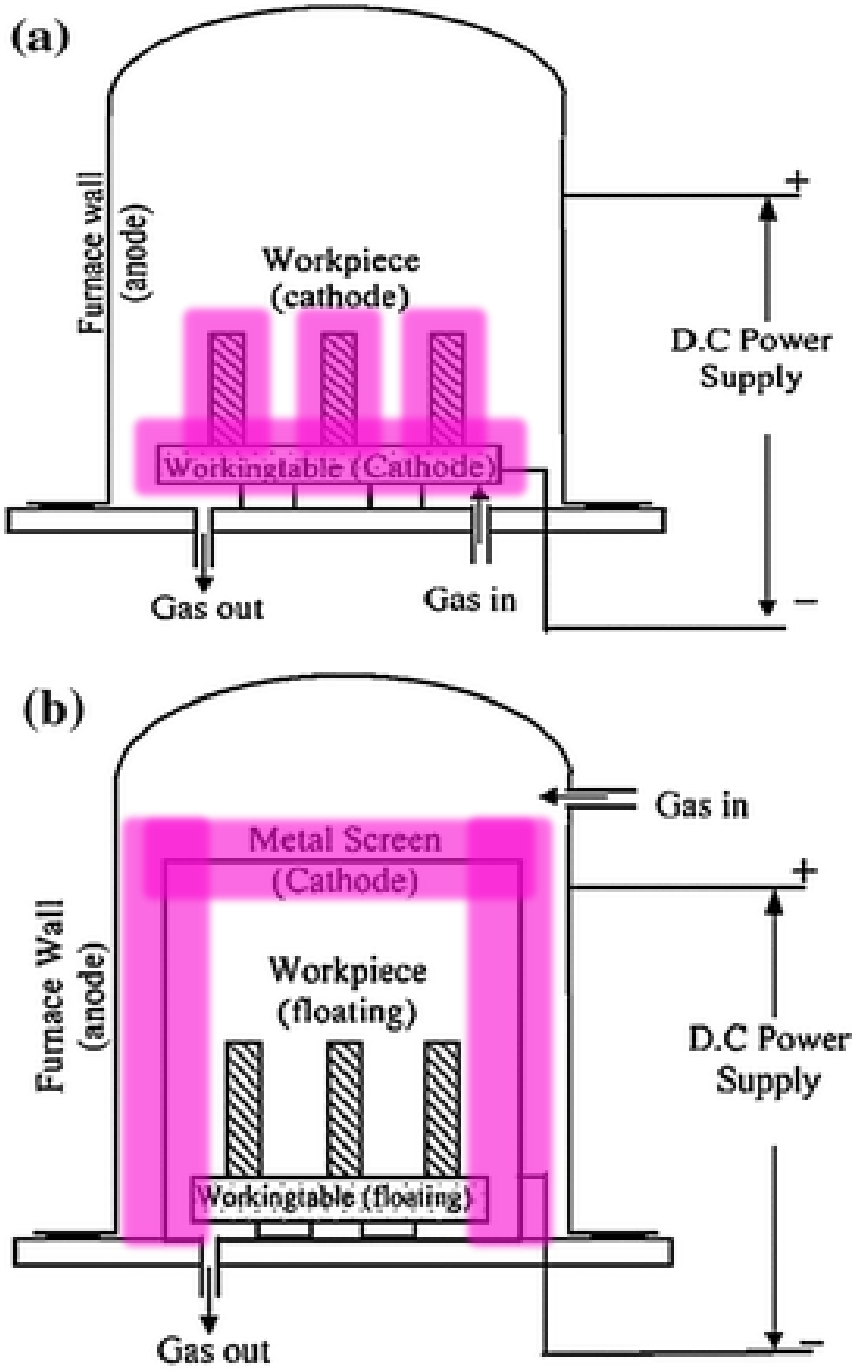

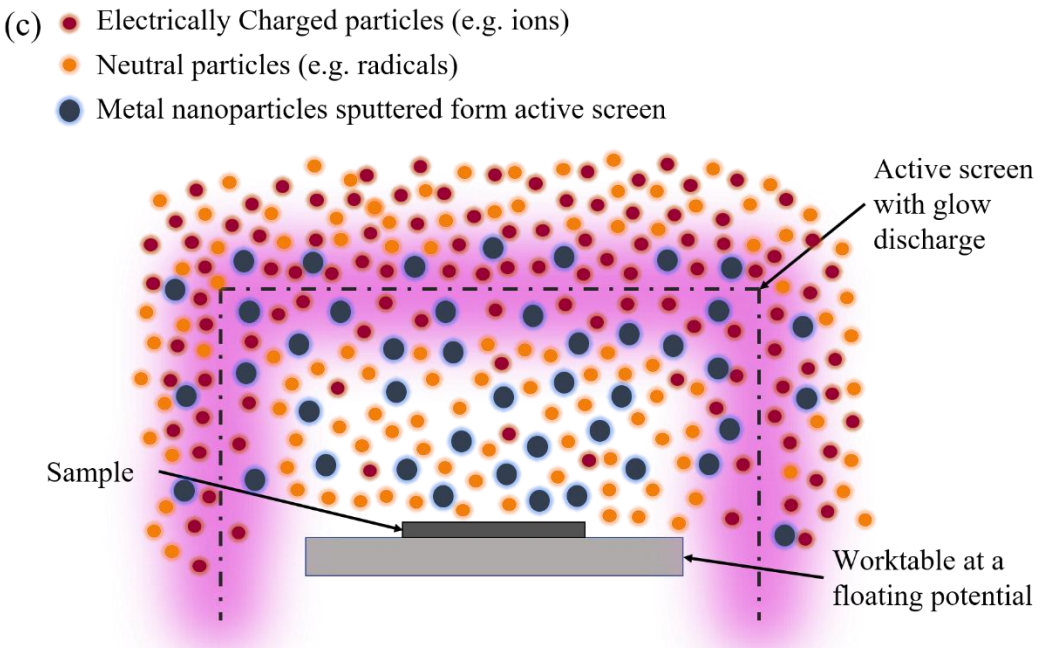


Fig. 2-17 Comparison of setup of (a) conventional DC plasma and (b) ASP [300] (modified with the addition of plasma distribution in purple). (c) Illustration of ASP process.

ASP technique was originally intended for metal nitriding or carburising processes [15], to form nitrides or carbides, respectively on the alloys. Recently, ASP has also been applied to modify carbon materials [302]. Santiago et al. successfully doped nitrogen on carbon fibres using ASP [303], and via the addition of specific metal target plates on the active screen, different target metals could be deposited on carbon fibre surfaces, which has been shown to be beneficial for their application as SCs [16]. Based on this finding, Zelun et al. compared different metals (Ag, Pt, Pd) used in ASP treatment, and the performances of SCs based on the ASP-treated carbon fibres deposited with these different metals were found to vary, potentially due to the different sizes of the metal nanoparticles [17].

## 2.3.3 Plasma Functionalisation on Graphene Materials

### 2.3.3.1 Plasma reducing GO

The first reported GO reduction using a plasma technique was by Navarro et al., in which GO samples were exposed to hydrogen plasma [304]. They applied two methods: a chemical approach using strong chemical reducing agent (hydrazine) and a plasma technique to reduce GO. The hydrogen plasma treatment lasted for only 5-10 s, which was much shorter than that of the hydrazine reduction process (24 h). The plasma treatment was conducted at room temperature, even lower than that of 80 ℃ used for hydrazine reduction. The degree of GO reduction using plasma, compared to the chemical method, was discovered to be superior. Since then, plasma has attracted attention and been explored for the reduction of GO.

The first two studies specifically on GO reduction using plasma approaches were published almost simultaneously in 2010, by Baraket et al. and Lambert et al., respectively. In Baraket's method, a uniform electron beam was generated using a -2 kV pulse applied in the linear hollow cathode, two grounded anodes (one with a slot for the electron beam to pass through, while the other one as the termination anode), with a 150 G magnetic field, to produce plasma. The schematic of the facility is shown in Fig. 2-18 [305]. This design produces plasma with low electron energies, thus low temperature and low potential, hence low kinetic energies and low density of ions impacting with sample surface, so that etching effect can be effectively avoided, which enabled

this process to be suitable for GO materials. Lambert et al. used aerosol-through-plasma process to thermally exfoliate and reduce graphite oxide, in which plasma is generated by 900 W microwave [306]. The microwave atmospheric plasma torch system is shown in Fig. 2-19. Graphite oxide, which was vibrated and aerosolised in a carrier gas (Ar), was heated by plasma discharge (~2500 K) during the travel through the plasma discharge zone. The rGO produced by this plasma process showed a significantly lower oxygen content than that produced by chemical and thermal reduction methods. Following these studies, an increasing number of studies were dedicated to using various plasma techniques on GO reduction, such as RF plasma [307, 308], DC plasma [309], DBD plasma [310, 311], and APPJ [296] for their advantages of low temperature, quick processing time, clean processing conditions, low energy consumption, and high efficiency, compared to conventional thermal or chemical reduction methods.

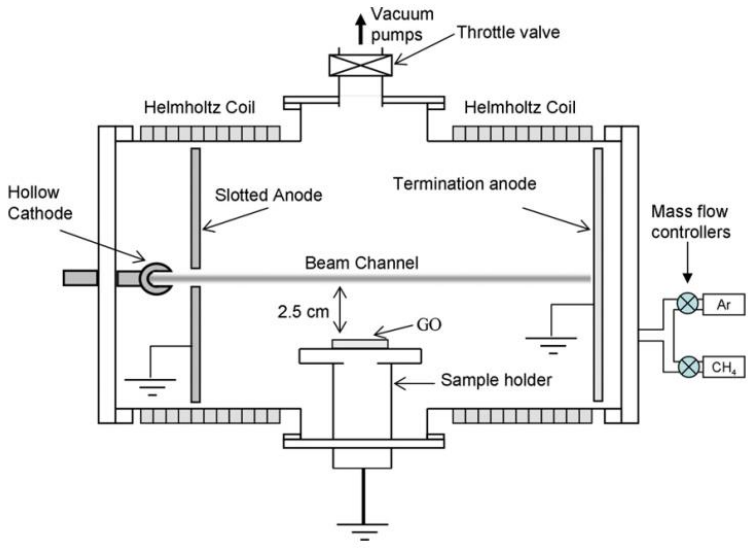


Fig. 2-18 A schematic of the experimental apparatus used to reduce GO [305].

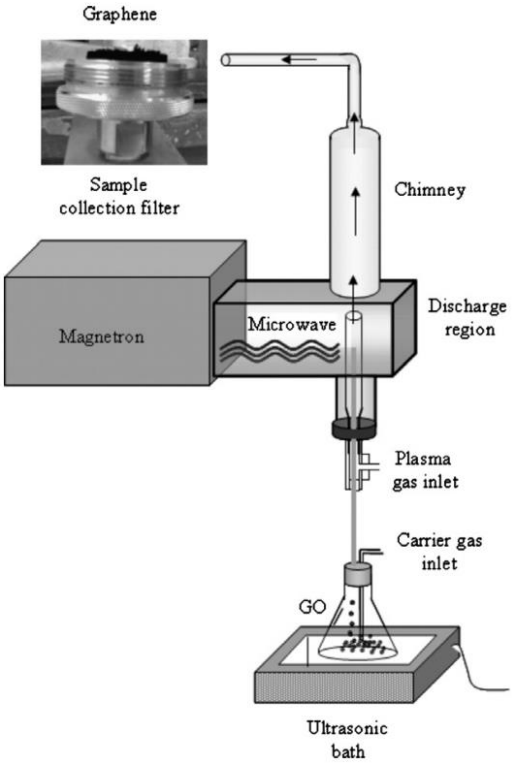


Fig. 2-19 Schematic of the microwave atmospheric plasma torch system used to exfoliate and reduce GO into PRGO [306].

Various types of plasma techniques that have been used for GO reduction are displayed in Table 2-2, as well as their relevant process conditions, including gas type and flux, pressure, processing temperature, and exposure duration. Mostly, plasma technique should be applied in a vacuum atmosphere for the input of specific plasma gas and ionisation. However, vacuum systems are not readily suitable for large-scale industrial application. Thus, atmospheric pressure plasma techniques have been explored in the GO reduction. Kim et al. applied atmospheric pressure DBD plasma reactor to reduce GO, with the process lasting 4 h [310], and Bodik et al. reduced the process time down to 10 s using diffuse coplanar surface barrier discharge (DCSBD) generated plasma at atmospheric pressure [311]. Losic et al. applied APPJs to generate arc

discharge plasma within atmospheric environments, and the scanning system managed it for a rapid, cost-effective and simple approach to treat GO films on a large scale, with few limitations on size and shape of samples and substrates [296]. Dey et al. combined APPJ with inkjet printing techniques to realise the simultaneous reduction and inkjet printing of GO. The plasma was generated in DBD configuration and interacted with aerosolised GO ink during the inkjet process, so that the GO ink deposited were reduced from carboxylic acid functionalities to phenol groups, and an extended plasma jet exposure further reduced GO in healing the graphitic structure [312]. For the general plasma reduction process, GO samples are in solid state either as powders or as dried films, but GO in liquid phase was also successfully reduced via plasma methods. In Chandana's study, GO samples were dispersed in water and a plasma jet was used to generate the plasma [313]. The setup is shown in Fig. 2-20. AC voltage was applied to ignite the plasma between the stainless working electrode (6 mm) above the dispersion, and the ground electrode of a wire mesh, on which the reaction flask containing dispersed GO was placed. Ar plasma from the jet induced water to disassociate into energetic hydrogen and hydroxyl radicals, which were responsible for GO reduction in water. In the study by Yoshimura et al., etched tungsten needle point high-voltage electrodes and Pt sheet planar ground electrodes were both immersed in GO/aminopyridine isopropanol solution [314]. In this way, liquid plasma was directly generated as electron bombardment with isopropanol produced

hydrogen radicals and ions, removing oxygen functional groups in GO. The schematics of this plasma processing technique are shown in Fig. 2-21. The liquid plasma setup, compared to gaseous plasma, is advantageous not only for vacuum-free configuration, but also for reducing damage due to the milder reaction conditions, since no localised heating effects can arise that would damage the GO structure [313].

Typically, the gas for plasma GO reduction are mainly inert gases like Ar or He, $H_2$, or mixtures of them, with some using $CH_4$ as an additional gas, as shown in Table 2-2. For the mechanism of plasma reduction of GO, it is mainly believed that the flux of reactive species, such as energetic radicals and electrons within the plasma, impinge on the GO surface, interacting with the $sp^3$ domain of the carbon structure where oxygen functional groups exist. The polar chemical bonds of C-O can be distorted and broken easily during the electron/ion bombardment during the process [315]. Through interactions, volatile products are produced and are removed from the GO surface, therefore removing oxygen functional groups, and achieving GO reduction [305]. In pure argon plasma, there are energetic electrons, active atomic argon radicals and reactive argon ions, and the physical electron/ion bombardment plays a key role in the removal of oxygen functional groups; in pure hydrogen plasma, there are electrons, protons (hydrogen ions), and atomic hydrogen radicals, as well as neutral hydrogen gas molecules, and the interactions between the plasma and the GO surfaces are dominated by the chemical reactions of hydrogen radicals

and neutral gas with GO, hence reducing GO [309]. The mixture of argon and hydrogen plasma has a synergetic effect on the reduction of GO, as ion bombardment can assist the reactions [316]. Some researchers attribute the synergy to the Penning ionisation as the yield of hydrogen radicals is improved in the chain reactions [310]. In addition, during the plasma process, the collisions of reactive species can increase the temperature, which also contributes to further GO reduction [309, 317].

Based on the mechanism of GO reduction during plasma treatment, the resulting reduction of GO is mainly incfluenced by the flux of active species generated in the plasma, and since they are mainly charged particles, the discharge current can be an indicator of the flux. Therefore, the parameters of plasma treatment that have an influenced on the discharge current, such as power, temperature, and pressure, depending on the plasma technique applied, as well as treatment time and gas ratio if it is gas mixture as working gas, need to be optimised for an optimal result [305, 316, 318-321]. Notably, extended durations of the ion bombardment during plasma processing, as well as an excessively high power and temperature, is considered to cause damage to the GO structure, leaving more defects [315, 10].

Apart from argon and hydrogen, methane plasma is able to restore the defects and disorders of GO structure during the reduction process [322], due to the hydrocarbon radicals and ions produced within plasma [323]. However, the

plasma restoration duration should be limited as disorders may grow when there is few oxygen-containing functional groups remaining after the reduction process, while excessive hydrocarbon radicals and ions still exist [324]. Moreover, the addition of Cu as a catalyst can enhance the restoration of graphene, as Obata et al. experimented with the use of a Cu pad in the plasma treatment on GO at 550 ℃, and the Raman spectra following the plasma treatment showed a much sharper G band with a small D band and a larger 2D band, which is comparable to the CVD-synthesised graphene at 1000 ℃ [325].

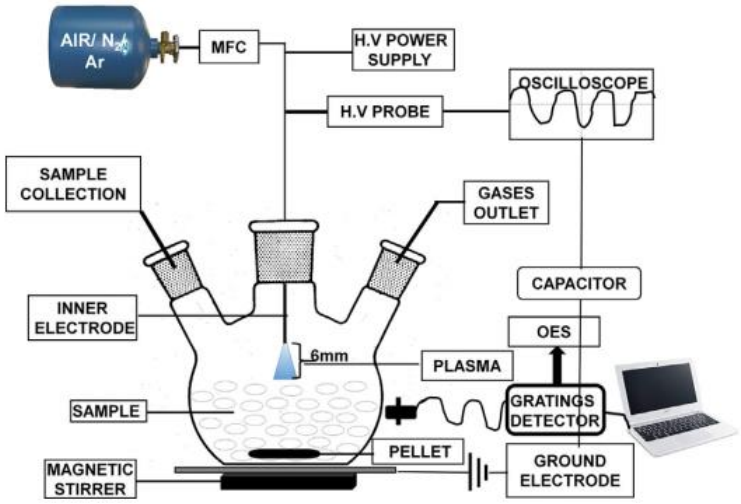


Fig. 2-20 Schematic of the experimental set-up [313].

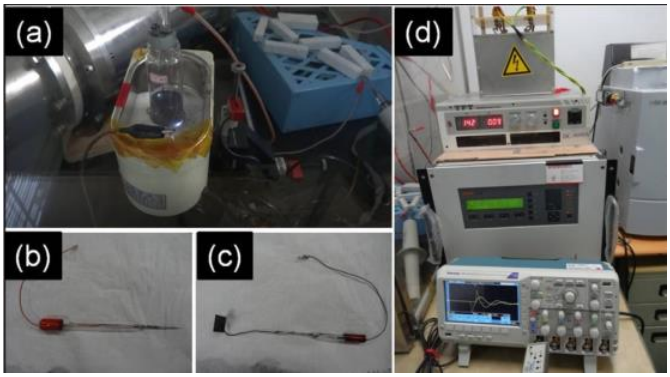


Fig. 2-21 (a) Plasma reactor with three stage assemble control (b) an etched tungsten needle (c) Pt ground electrode (d) pulse generator connected to high-voltage amplifier [314].

Table 2-2 Review of generation and other parameters of plasma reducing GO

| Generation | Voltage /Power /Frequency | Species | Total flow rate | Pressure | Temperature | Treatment time | Reference |
|---|---|---|---|---|---|---|---|
| Electron beam plasma | -2 kV, pulse width 2 ms, period 20 ms | $CH_4$+Ar | 180 sccm | 90 mTorr | / | 30 s | [305] |
| Microwave plasma | 900 W | Ar | / | / | ~2500 K (only discharge region) | <1 s | [306] |
| DC microplasma | ~2 kV | Ar/Ar+$H_2$ | / | Atmospheric | 70 ℃ | 30 min | [309] |
| DC glow discharge plasma | -10 kV | He | / | Atmospheric | Room temperature | 2 s | [317] |
| DC glow discharge plasma | ~-10 kV | Ar | 7 ml/min | 240 mTorr | / | 4-8 min | [315] |
| DC plasma | 15, 30 W | $H_2$ | / | ~50 Pa | Room temperature-120 ℃ | 10 s-5 min | [10] |
| RF plasma | 25 W, 13.56 MHz | Ar | 20 sccm | ~2×$10^{-2}$ Torr | 25 ℃ | 5-40 min | [307] |
| RF plasma | 60 W | $H_2$ | | Atmospheric | Room temperature | 30 min | [321] |
| RF plasma | 10 W, 13.56 MHz | $H_2$+$CH_4$ | 35+35 sccm | 9.7-9.8 Pa | 550 ℃ | 10-120 min | [325] |
| RF plasma | 60 W | $H_2$ | / | / | Room temperature | 30 min | [308] |

| Generation | Voltage /Power /Frequency | Species | Total flow rate | Pressure | Temperature | Treatment time | Reference |
|---|---|---|---|---|---|---|---|
| Inductively coupled RF plasma | 20-100 W, 13.56 MHz, | $H_2$+Ar | / | / | No obvious heating | 3-10 min | [316] |
| Inductively coupled RF plasma | 100 W, 13.56MHz | $CH_4$+Ar | 30 sccm | 50 mTorr | Room temperature | 1-10 min | [324] |
| PECVD RF plasma | 200 W, 13.56MHz | $H_2$ | 300 sccm | 20 mTorr | 150 ℃ | 18 s | [318] |
| PECVD RF plasma | 100 W | $CH_4$ | / | 0.20 Torr | 575 ℃ | 3-10 min | [322] |
| PECVD RF plasma | 100 W, 13.56 MHz | $H_2$/$CH_4$/$H_2$+$CH_4$ | 100 sccm | 400 mTorr | 240 ℃ | 5-30 min | [323] |
| PECVD RF plasma | 10 W, 13.56 MHz | $H_2$ | 50, 20 sccm | 0.3-0.8 mbar | 27±1 ℃ | 20-40 s | [319] |
| DBD plasma | 16-20 kV, 400 Hz | Ar+$H_2$ | 60+15 sccm | Atmospheric | / | 4 h | [310] |
| DCSBD plasma | 40 $Wcm^{-3}$ | $H_2$ | / | Atmospheric | / | 1-64 s | [320] |
| DCSBD plasma | 1.9 W $cm^{-2}$ | $H_2$/$CH_4$/$H_2$+$CH_4$ | 0.2 ml/min | Atmospheric | / | 1-5 s | [311] |
| APPJ: arc discharge plasma | 300 W, 20 kHz, ~10 kV | Air | / | Atmospheric | / | 10-120 s | [296] |
| APPJ, DBD configuration | 1-15 kV | He+$H_2$ | 1600+100 sccm +500 sccm(carrier gas) | Atmospheric | / | 1 min | [312] |

| Generation | Voltage /Power /Frequency | Species | Total flow rate | Pressure | Temperature | Treatment time | Reference |
|---|---|---|---|---|---|---|---|
| APPJ (sample in liquid phase) | 20 kV, 1 W, 50 Hz | Ar+liquid | 300 sccm | Atmospheric | / | 3-12 h | [313] |
| Discharge plasma (submerged liquid plasma) | ~4.0 kV, 10 kHz, pulse delay 500 μs, pulse width 5 ms | Liquid | / | Liquid | / | 30 min | [314] |

#### 2.3.3.2 Plasma nitrogen doping graphene materials

Plasma techniques have also been successfully and widely applied to nitrogen doping graphene materials, modifying their electronic properties to increase their potential use for fabricating FETs, sensors, optoelectronic, and other electronic devices with improved efficiency. Usually, pure nitrogen gas or ammonia gas or gas mixtures containing one of these two types of gas is used as the working gas during plasma treatment aimed at nitrogen doping graphene materials.

1. Properties improvement and relevant applications

McManus et al. [326] compared the electrical characteristics of plasma-treated graphene using different gases, and the transfer characteristic of FETs made from Ar plasma treatment remained as *p*-types, while the materials were switched to *n*-type following nitrogen doping plasma treatment with $NH_3/H_2$ as working gases.

The electronic properties of N-doped graphene materials via plasma treatment have also been explored in the aspect of work function, as it represents the difference between the vacuum level and the Fermi level. The work function of graphene depends on the DOS of graphene; thus, the configuration of doped nitrogen influences the increase/decrease of work function. Akada et al. [327] reported that graphitic N reduces the work function while pyridinic and pyrrolic N increase the work function, and thus it can be controlled to decrease at the

start of plasma process when graphitic N is dominated, and to increase when pyridinic and pyrrolic N start to form with an extented plasma process. Zeng and Lin [328] explored the relationship between power condition of RF plasma and the work function, and concluded that an increase of RF power leads to the reduction of work function, attributing it to the formation of more graphitic N as the electron donors to increase the electron concentration.

The modulation of charge transfer characteristics and the change of DOS near the Fermi level of N-doped graphene materials also enhance the electrochemical properties, enabling the applications for electrocatalysis, energy storage, and sensors.

Regarding nitrogen doping of graphene materials via plasma techniques, the most extensively studied application is for catalysts. Among them, catalysts for fuel cells using graphene materials have attracted wide attention, and plasma-assisted nitrogen doping on graphene materials has been found to further enhance the electrocatalytic performance of graphene-based materials in both the reactions that are involved in fuel cells, such as oxygen reduction reaction (ORR) [329, 330], hydrogen peroxide ($H_2O_2$) reduction reaction [331], oxygen evolution reaction (OER) [332], as well as other reactions, such as hydrogen evolution reaction (HER) [333] for hydrogen production, or for bio-applications [334, 335].

Plasma techniques have also played a role in nitrogen doping of graphene

materials for the application as SCs [336, 337]. Jeong et al. [338] reported high-performance ultracapacitors made of N-doped graphene via plasma processes with capacitances reaching approximately 280 F/g, about 4 times larger than that of pristine graphene. Jeong et al. [338] explored the features of N-configuration and their evolution during plasma process, and pyridine-like N at basal planes was found to be the predominant cause for the enhancement of super-capacitive performances due to the largest binding energy difference, based on the first-principles density functional theory calculations, whilst negatively-charged pyrrole-like N also contributed to the enhancement of capacitance, but could, on the other hand, have a negative effect in reversibility of charging/discharging processes due to the potentially excessively strong ionic bonding. The nitrogen doping effect and super-capacitive performance have also been studied for different processing times [339], scan times [340], as well as different temperatures (by adjusting the flow rate and jet-substrate distance using APPJ) [341].

Except for SCs, nitrogen doping on graphene materials has also been explored for other devices such as batteries [342], sensors [343-346]. In addition to enhancing electrochemical properties, plasma nitrogen doping of graphene materials has been investigated as a means to improving other properties, such as field emission characteristics [347, 348], adsorption properties [349], and ferromagnetism [350].

2. Plasma designing and modifying

With the potential to modify a wide variety of properties and performances of N-doped graphene materials for different applications, the plasma process approach can be designed and controlled in different ways to achieve desirable doping adjustments for targeted properties and application performances. Physical masks containing holes with varying sizes were placed on graphene to investigate the effects on plasma treatment [351]. Since only ions and active species that penetrate the holes can function on graphene, the masks with different thicknesses and hole sizes can be used as a tool to model the spatial nitrogen-doping distribution, and to manipulate the targeted properties in localised regions. On the other hand, plasma is known to easily etch target samples, causing damage to fragile graphene materials through ion bombardment. An aluminium oxide buffer layer was deposited on graphene before a remote plasma nitriding, which acted to block the Ar ions from damaging the graphene during the plasma igniting process, but still allowed nitrogen doping on graphene [352]. Neustroev et al. [353] used a plasma etching system and applied inductively coupled nitrogen plasma on rGO, and compared two different sample locations, as shown in Fig. 2-22. It is found that rGO films facing downwards, on the surface not facing towards the inductor, can avoid the etching damage, while still being nitrogen doped effectively, with an improvement in photosensitivity.

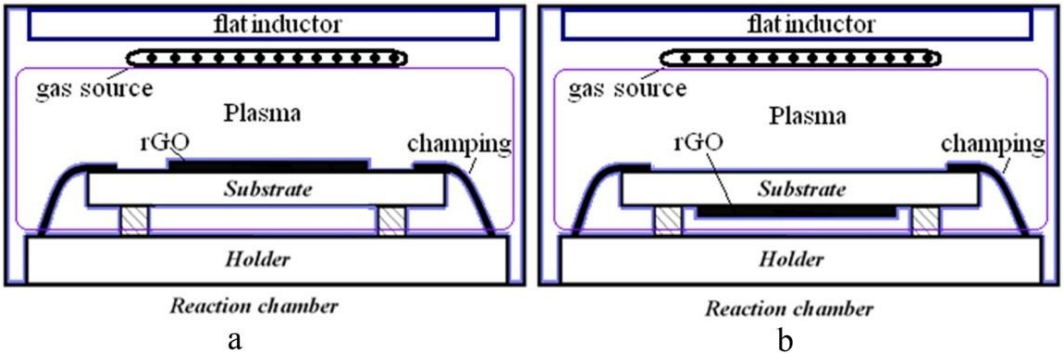


Fig. 2-22 Methods for locating the samples in the reaction chamber: (a)—graphene oxide film is located toward the electrode of the reaction chamber, (b)—the graphene oxide film is turned to the opposite side from the electrode [353].

Nitrogen content determines the degree of doping, and the different bonding configurations of nitrogen doping in graphene materials show quite different behaviours, as pyridinic N is *p*-type while graphitic N is *n*-type. Meanwhile, the nitrogen content and types of doping configurations are related to the defect sites on graphene materials. Thus, studies have shown that it is possible to control the nitrogen content and dominant configurations of doping via plasma process under different conditions, during which the defect sites are formed as reactive regions. Plasma source, power and bias, process duration, plasma working gas, as well as other parameters, all have an impact on the doping content and configuration type, as energies vary during the plasma process.

Lin et al. [11] compared two different modes of plasma sources: an ion mode containing both ions and natural thermalised species at both high and low ion energies, and an atom mode with only thermalised atoms emitted, while ions are trapped. It was believed that high ion energy is needed to knock carbon atoms out of graphene for nitrogen atom to form graphitic N, as it was only

found to be dominant in graphene following treatment of plasma at ion modes with higher incident energies. Moreover, pyridinic N formed at pre-existing defects is favoured at low-energy atom mode. Lin et al. [354] also tried an electron cyclotron resonance enhanced microwave plasma gun and an RF plasma-immersion ion implanter (PIII) on pristine graphene materials for nitrogen doping. The microwave plasma gun emitted $N^+$ ions and N atoms at 850 ℃, while the RF PIII mainly generated $N_2^+$ ions at room temperature. In the comparison, the higher dissociation efficiency of microwave plasma guns and the higher temperatures as a healing process introduced a higher nitrogen content to bi-layer graphene, mainly in the graphitic N configuration. Sakulsermsuk et al. [355] compared self-made RF plasma and PIII on nitrogen doping of graphene, and pyrrolic N was the major configuration after RF plasma treatment while pyridinic N was dominant for PIII. It was proposed to be linked to the vacancy types formed during these treatments. RF plasma with energy range of tens of eV tends to form divacancies, while PIII with energy of the order of 4 keV is more likely to form monovacancies. It was calculated that pyrrolic N configuration is favourably located next to divacancy while pyridinic N prefers to be next to monovacancy, and it is found to correlated with the experimental results. Meanwhile, a longer implantation duration or a higher implantation energy can potentially convert pyrrolic N to pyridinic N. Bigras et al. [356] compared graphene exposed to different regions of remote plasma by controlling the gas flow rate: the late afterglow and the early afterglow, as shown

in Fig. 2-23. Mainly, late afterglow is relatively mild as it mainly contains a high density of reactive nitrogen atoms, while early afterglow is relatively harsh as metastable $N_2$ states, positive ions and nitrogen atoms coexist. Due to the highly energetic species, multi-vacancies were created in the early afterglow-treated graphene, with an increase of nitrogen content of up to 49 %, compared to only 18 % in late afterglow-treated one.

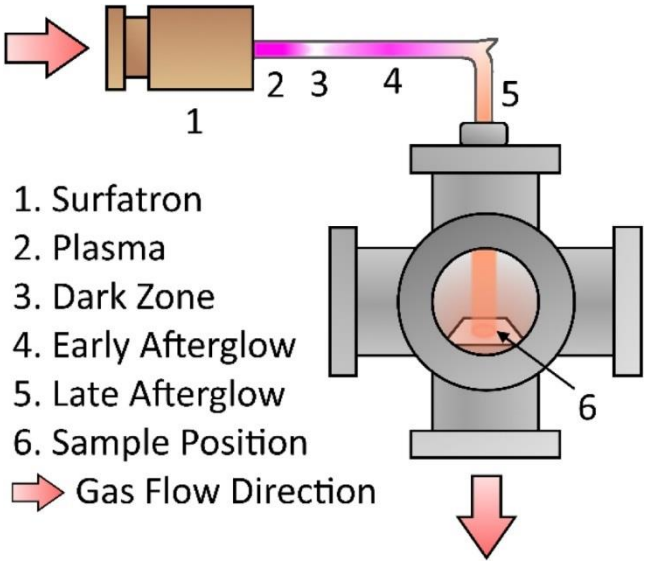


Fig. 2-23 Treatment of graphene films in the flowing afterglow of microwave N2 plasmas created by the propagation of an electromagnetic surface wave. Schematic of the plasma system, where 2–5 show the location of the different zones of the discharge and afterglow regions and 6 is the position of the graphene sample in the downstream flow. When the N2 flow rate is increased, the early afterglow is shifted towards the sample [356].

Since power and bias determine the plasma energy, a higher power or bias applied in plasma leads to a higher degree of nitrogen doping, and formation of specific configuration types, but an exceedingly high energy or long duration can also cause damage to the graphitic lattice. Studies show that in RF nitrogen plasma, the covalent bonding of nitrogen in multilayer graphene only exist on

existing defect-sites at bias lower than 50 V, and pyridinic and pyrrolic nitrogen components show at increasing higher bias [357]. Similar results were also found in GO reduction and nitrogen doping, such that plasma reactions only occur at the present reactive sites in GO until higher bias (> 50 V) with ion energies greater than 50-100 eV are achieved, when then enable new reactive sites to be created during the GO reduction for further nitrogen doping, with pyridinic rings and pyrrols or diazine rings in $sp^2$ structures being the dominant types [358]. Rybin et al. [359] investigated the effect of time and power on nitrogen doping of graphene using ammonia RF plasma, and found less time was required at a higher powers for effective nitrogen doping, with the maximum nitrogen doping of 3 at% occurring at the lower power of 10 W for an extended time of 20 min, compared to 2.2 at% at 20 W for 10 min. A longer time resulted in an increase of pyrrolic N but a decrease of pyridinic N and graphitic N. Dias et al. [360] reported nitrogen doping on graphene using a microwave apparatus as the graphene was exposed to the remote regions of $N_2$-Ar plasma for 5 and 10 minutes. The study showed that the $sp^2/sp^3$ ratio increased in the plasma process in the short term due to the etching of $sp^3$ structures and doping, but reversely decreased with the nitrogen and carbon contents in prolonged processing. The decrease in the long run was ascribed to the chemical sputtering that created atoms with dangling bonds, and an increase in N-Q structure in $sp^3$ hybridisation. Chi et al. [361] studied the effect of graphene defects and plasma power on doping content and configuration type, using

graphene with different defect densities and thicknesses, and nitrogen plasma treatment with different microwave power (400 and 1300 W). The results displayed a higher nitrogen content at higher plasma power, especially at graphene sheets with high defect density, with pyridinic N as the major configuration. It was suggested that damages in graphene sheets play a role in the nitrogen doping process, so that only plasma at high powers can create sites at basal planes for quaternary nitrogen configuration doping. However, it was found by Yanilmaz et al. [362] that the pyridinic N failed to form when plasma power decreased and time increased, but pyrrolic N and graphitic N increased, with pyrrolic N being the dominant one.

Based on relevant studies, the selection of working gases and the ratio of gases in cases of gas mixtures being used have an impact on nitrogen doping content and configuration of graphene. Bundaleska et al. [363] synthesised nitrogen doped graphene using the remote region of microwave plasma, and compared three different ratios of nitrogen and argon mixture: 5%–95%, 30%–70% and 40%–60%, respectively. The increase of nitrogen content led to the increase of nitrogen ions density in the plasma and resulted in the increase of nitrogen doping content from only 2.4 at% for the plasma of 5 % nitrogen to 12.5 at% and 25 at% for the plasma of 30 % and 40 % nitrogen, respectively. Moreover, except for the imide groups, graphitic bonds and some C-N bonds in $sp^3$ structures for the 5 % nitrogen plasma, the increase of nitrogen content at higher nitrogen ratios was found mainly in the $sp^3$ structure, assumed to be

similar to β-$C_3N_4$. Santhosh et al. [364] investigated the influence and mechanism of nitrogen incorporation in the plasma treatment of graphene nanowalls using two types of nitrogen-containing gases: ammonia and nitrogen. An RF inductively coupled plasma system at a power of 300 W was used and the graphene nanowalls were placed in the post-glow region, under a temperature lower than 50 ℃. Both these plasmas included the process of defect generation and interaction of plasma species with defects. The differences were demonstrated by the nitrogen bonding configurations on the defects. Ammonia plasma containing $NH_x$ (where x = 1, 2, 3) species formed graphitic N at single vacancy defect sites, pyrrolic N at double vacancy defect sites, and pyridinic N, pyrrolic N and amines at the edges. The pyrrolic N at double vacancies tended to convert to pyridinic N with longer plasma exposure. However, nitrogen plasma formed graphitic N at single vacancy defect sites, pyridinic N at double vacancy defects, and pyridinic N, oxides of pyridinic N and pyrrolic N at edges, and the formation of pyrrolic N at edges increased with pyridinic N transforming to graphitic N at double vacancy sites.

#### 2.3.3.3 Plasma hybridising graphene materials with metals

For hybridising nanocrystals on graphene materials, electrostatic force directed assembly (ESFDA) technique using an arc plasma source were applied to synthesise nanocrystals, which are shown in Fig. 2-24 [365]. In this method, an arc plasma was applied between a tungsten cathode and a graphite anode, and a silver wire was physically vapourised to form nanocrystals in the arc plasma,

being partially electrical. Due to being electrically charged, these nanocrystals were carried by a DC electrical field force in inert gases, and assembled onto the GO sheets. This process was specifically designed for hybridising, and thus graphene materials were not involved in the reactions in the process, only being the substrate.

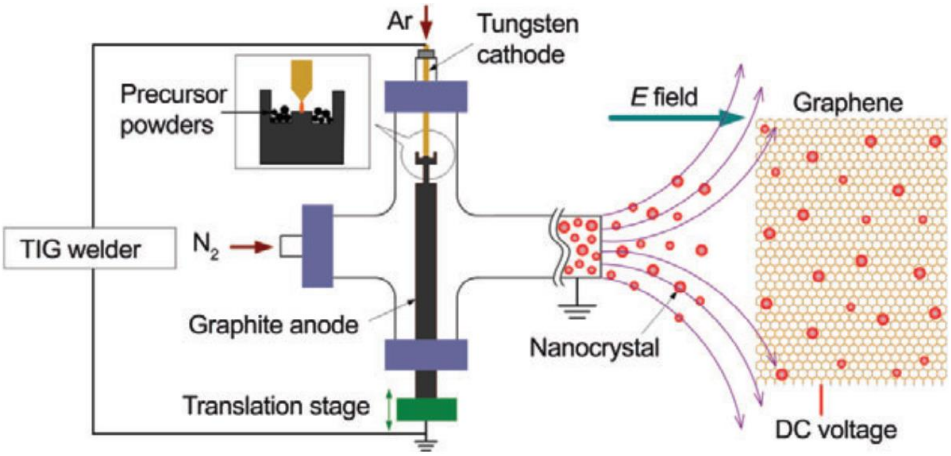


Fig. 2-24 Schematic diagram of Ag nanocrystal synthesis using a mini-arc plasma reactor and the subsequent deposition of as-produced nanocrystals onto a graphene oxide sheet through ESFDA [365].

Sputtering is also an approach for synthesising nanoparticles, and Yamazaki et al. applied sputtering in plasma to deposit Pt nanoparticles on graphene [366]. Atomic Pt was identified at the very start of sputtering for only 1 s, and with increasing sputtering time, Pt atoms were found to grow into two-dimensional clusters, and saturated and formed three-dimensional structures when sputtering time reached 10 s. The dispersed Pt atoms were mainly anchored at the step edges between the graphene layers, and were theoretically confirmed to be bonded to three carbon atoms as Pt-C.

However, as mentioned in Section 2.2.2.3, hybridisation of graphene materials

with metal/metal oxide nanoparticles are mainly carried out in two ways: *ex-situ* hybridisation and *in-situ* reduction, and in the *in-situ* reduction, various reducing methods, such as hydrothermal reduction, thermal annealing reduction and electrochemical reduction have been explored, in which both the metal materials and the graphene materials are involved in the reduction process. In relation to this type of approach, plasma reduction has also been applied for synthesising hybrids of graphene and metal materials.

Xu et al. employed a DBD plasma to simultaneously reduce graphite oxide and $PdCl_2$ so that Pd nanoparticles were well dispersed on graphene sheets in one step, and the preparation process is shown in Fig. 2-25 [367]. The Pd precursor and graphite oxide were first well-mixed in ethanol with a pH value of 10, followed by a centrifugation and drying process before plasma processing, which is different from hydrothermal reduction that is processed directly in liquid phase. They also proposed the possible mechanism of the process, which is briefly introduced as follows. In the alkaline solution of the mixture of graphite oxide and $PdCl_2$, ionised oxygen functional groups facilitate the adsorption of palladium ions on the graphene sheets homogeneously to form complexes via electrostatic bonding, and during the plasma processing, the charged particles in the plasma react with both the oxygen functional groups and $Pd^{2+}$, resulting in the reduction and exfoliation of graphene sheets through forming and expansion of gaseous product, as well as $PdCl_2$ reduction via chemical bond splitting by electrons in the plasma. The reduced Pd nanoparticles are then

attached firmly on the graphene sheets due to the interaction states and transmission channels generated between them.

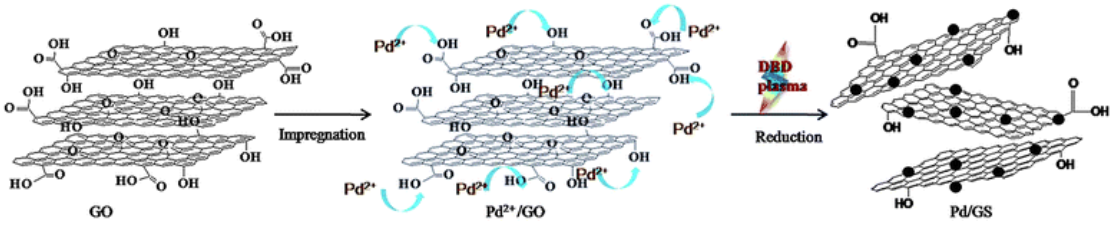


Fig. 2-25 Schematic representation of the preparation of Pd/GS composites [367].

Similarly, this process has also been applied for hybridising graphene with Pt, Ag, Au and Fe nanoparticles through various plasma techniques [13, 368-373]. Yang et al. investigated the relationship between size and density of nanoparticles, the plasma treatment time, and the precursor concentration [371]. They found that the particle size decreased while density increased with increasing plasma treatment time. However, an extended plasma treatment would remove the oxygen functional groups on GO, so that the metal nanoparticles would lose anchoring sites, causing an aggregation of nanoparticles. Also, an increase of metal precursor concentration would facilitate the formation of larger particle sizes, but also lead to aggregation when the concentration reached a critical limit.

For plasma hybridisation of graphene with metal nanoparticles, apart from both reduction of GO and metal precursors, the graphene materials can also be nitrogen doped simultaneously using nitrogen or ammonia as the working gases [374, 375].

From the reviews above about the plasma hybridising of graphene materials with metal nanoparticles, the approaches can still be divided into two categories. The first is synthesising metal nanoparticles via plasma and deposition of them on graphene, as the ESFDA technique and sputtering in the first two examples displayed. The second is the *in-situ* reduction as most cases applied, but chemicals of metal salts are required as the precursors.

## 2.4. Summary

Graphene materials, with unique electrical, thermal, mechanical properties, demonstrate great potential for many applications, such as FETs, optoelectronics, sensors and energy storage devices. GO is a derivative of graphene that is commonly used as the raw material to synthesise graphene. Due to the oxygen functional groups in GO, the superior properties of pristine graphene are affected, but these functional groups also enable GO to be hydrophilic and available for functionalisation.

Before being applied into practical use, graphene materials usually need to undergo functionalisation to improve their performance for a better suitability for each specific application. Reduction of GO is a common approach to increase the electrical conductivity. Nitrogen doping is a typical covalent modification of graphene materials that can tune their Fermi level, open their bandgap, and modulate the electronic properties of graphene, so that graphene materials can be better used in FETs, LIBs, SCs, sensors, as well as other

future applications. Hybridising with metal/metal oxide nanoparticles is another approach to functionalisation so that a composite is formed that possesses the properties from both components, and even with potential synergetic effects of enhancing the performance, which broadens the applications of the composite.

For all these functionalisation methods mentioned above, various techniques have been explored, such as thermal annealing and wet-chemical methods. However, these methods are limited either by the high temperatures required or by the toxic chemicals involved in the preparation process. Plasma treatment, as an advanced technique, has been found effective in all previously mentioned functionalisation approaches of graphene materials, and can potentially overcome some disadvantages associated with the other approaches.

However, in most cases of plasma hybridisation of graphene materials, metal salts are required as the precursors for metal nanoparticles. ASP, as an advanced plasma technique, has been found able to deposit metal nanoparticles directly onto carbon fibres during the process. Therefore, within this study, ASP is applied for the functionalisation of GO, and is explored for its potential to simultaneously reduce GO, nitrogen dope, and hybridise with metal nanoparticles. The electrical and electrochemical properties of GO after AS plasma treatment are investigated, and the mechanisms involved are discussed.

# Chapter 3 Experimental procedures

## 3.1 Materials & Sample Preparation

### 3.1.1 Graphene oxide

Graphene oxide (GO) was supplied by Sigma-Aldrich Company Ltd. (Dorset, UK; Product number: 777676) as a dispersion in $H_2O$ with a concentration of 4 mg/mL. The GO dispersion was first diluted to 0.8 mg/mL with deionised water in an ultrasonic bath for 10 min. This diluted GO dispersion is for the preparation of GO samples for active-screen plasma (ASP) treatments and further characterisations, as well as property tests. In addition, GO sheets provided by the same supplier (Product number: 763713) in the form of solid flake were directly used for thermal gravimetric analysis (TGA) test.

### 3.1.2 Substrate materials

Three types of substrate materials were used for the sample preparation.

(1). Silicon wafers

Silicon wafers supplied by MCL Electronic Materials, Ltd. (Specification Number: HBEVXQ0C) were cut using a glass knife into small pieces as rectangle-like shapes with lengths of around 8-10 mm. GO samples on silicon wafer were prepared for SEM/EDS and Raman spectroscopy characterisations.

(2). Silicate glass pieces

Silicate glass pieces were microscope slides supplied by Thermo Scientific -

Menzel-Glaser and were cut into small pieces with lengths of 12. 5 mm × 12. 5 mm. This substrate was for GO samples testing the sheet resistance.

(3). Fluorine-doped tin oxide (FTO) coated glass

FTO coated glass with a thickness of 2.2 mm was supplied by Sigma-Aldrich Company Ltd. (Dorset, UK) (Product number: 735167) and was cut into square pieces with a length of 1.5 cm × 1.5 cm for electrochemistry testing and 1.0 cm × 1.0 cm for XPS characterisation.

### 3.1.3 Sample preparations

Substrates were first cleaned in acetone for 10 minutes in an ultrasonic bath and dried with hot air. Diluted GO dispersions were drop cast on using a syringe. Amount of GO dispersion differed for different substrates according to their sizes, ensuring to prevent overflowing. One drop of GO dispersion for each silicon wafer substrate; 0.2 ml for 12. 5 mm × 12. 5 mm silicate glass pieces; 0.3 ml for 1.5 cm × 1.5 cm FTO coated glass while 0.1 ml for the 1.0 cm × 1.0 cm one. These GO sample on silicate glass pieces and FTO coated glass were dried at 85 ℃ for 1 h while those on silicon wafer were dried in air at room temperature.

## 3.2 Treatments on graphene oxide

### 3.2.1 Active-screen plasma treatment

DC plasma furnaces were used for ASP treatments (Klöckner Ionon GMBH,

Bergisch Gladbach, Germany). The setups of the ASP treatments are demonstrated in Fig. 3-1 in two modes. To investigate the effect of ASP on GO, as well as the gas effect (results reported in Sections 4.2 to 4.4), the DC plasma furnace was modified with a mesh cylindrical cage made of AISI 316 stainless steel which acted as the so-called active-screen to house the samples. The samples were positioned on an insulated worktable at a floating potential, and the distance between the samples and cage lid was approximately 15 mm, as shown in Fig. 3-1(a). When it came to exploring the hybrid effect of ASP combining both gas modification of, and metal deposition on, GO (results reported in Sections 4.5 to 4.7), a noble metal plate was incorporated by directly placing them on the stainless-steel cage, as shown in Fig. 3-1(b). All the ASP treatments were conducted at 100 ℃.

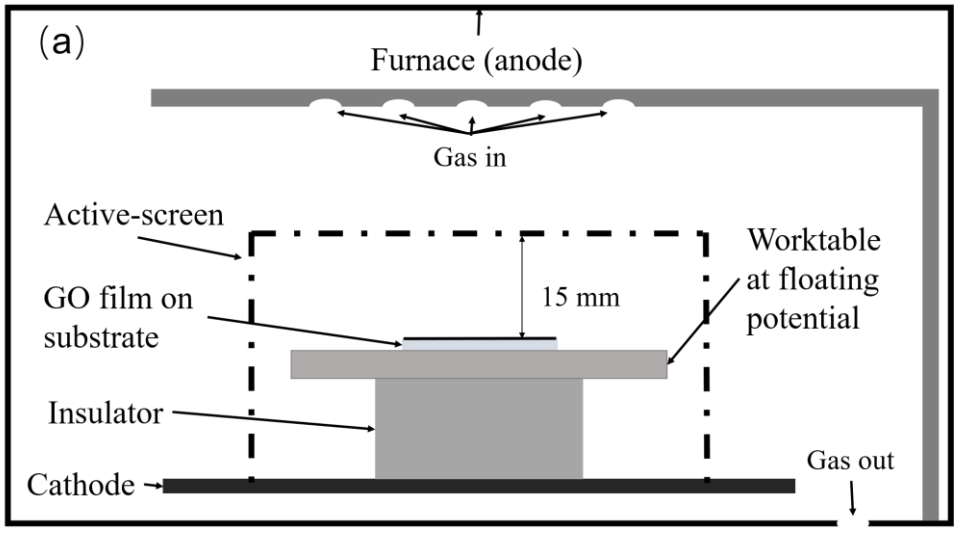

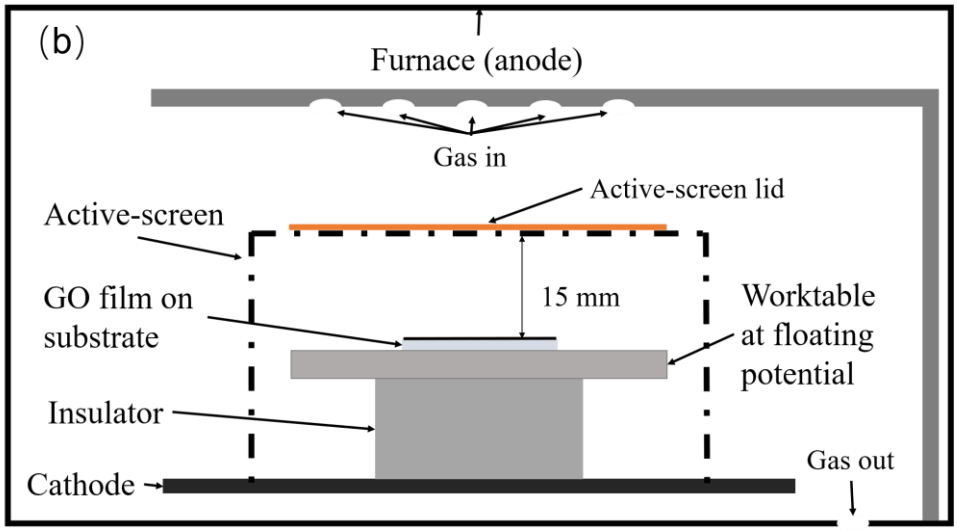


Fig. 3-1 Schematic of active-screen plasma treatment (not to scale). Two modes are displayed as (a) and (b), with the difference of an extra precious metal plate as lid positioning on the active-screen cage in (b).

### 3.2.2 Annealing treatment

To investigate the effect of ASP on GO, an annealing treatment was conducted for comparison with ASP treatment, to evaluate the temperature effect on GO reduction. GO samples were annealed in a tube furnace (GHA 12/450, Carbolite Gero Ltd, UK) at a temperature of 100 ℃ for 1 h in argon at atmospheric pressure. During the annealing process, the samples were wrapped in aluminium foil to prevent contamination.

## 3.3 Characterisation techniques

### 3.3.1 Scanning electron microscopy (SEM)

The surface morphologies of the GO samples were examined using a Philips XL-30 field emission environmental scanning electron microscope (FE-ESEM) in secondary electron mode. When examining the metals deposited on GO

samples (in Sections 4.5-4.7), a JSM-7610FPlus FE-SEM was used.

### 3.3.2 Energy dispersive X-ray spectroscopy (EDS)

The elemental distributions of the GO samples were measured using energy dispersive X-ray spectroscopy associated with SEM. Respectively, Oxford Inca Energy was used with the FE-ESEM and EDAX Octane Elect Super was utilised with the JSM-7610FPlus.

### 3.3.3 Transmission electron microscopy (TEM)

(1). For raw GO

The micro-structure of raw GO was studied on a Jeol JEM-1400 TEM at a voltage of 80 kV to avoid possible damage to the GO sheets [376, 377]. The electron micrographs were recorded using a Morada 3.0 soft imaging system.

To prepare TEM samples of raw GO, GO dispersion was first further diluted in ethanol to semitransparent, and the Cu grid with a holey carbon film was then immersed in the diluted GO suspension for 5 seconds to collect the GO sheets. Later, Cu grid was taken out for drying in ambient environment. Due to the nano-scale thickness of GO sheets, the sample was then prepared for TEM observation.

(2). For ASP treated GO

Observations of the ASP treated GO samples were operated on a FEI Tecnai G2 F20 TEM, with an accelerating voltage of 200 kV. High-resolution TEM

(HRTEM) images and selected area electron diffraction (SAED) patterns were also obtained.

To prepare TEM sample of ASP treated GO, the films were exfoliated from the FTO coated glass substrates, and milled in agate mortar with agate pestle. The milled film was then sonicated in ethanal bath so that the treated GO with metals could disperse homogeneously for the Cu grid to collect in the same way mentioned above.

### 3.3.4 X-ray diffraction (XRD)

The crystallisation status of the GO was obtained using an AXRD benchtop powder diffraction system from Proto Manufacturing with Cu Kα radiation (λ =0.154 nm) and nickel Kβ absorber (0.02 mm; Kβ = 1.392250 Å). Angles (2θ) were collected in the range of 5° and 80°, with a step length (△2θ) of 0.015°. The dwell time at each step for collection was 1.0 s.

### 3.3.5 Raman spectroscopy

Raman spectroscopy is a useful tool to explore the structure and electronic states of carbon materials. Raman spectra of GO samples were recorded using a confocal Raman microscope (Renishaw in Via Reflex). The laser wavelength was 488 nm and the power was limited to 3.5 W. The target areas of GO samples were focused under an optical microscope of 20 X. Five acquisition scans were accumulated for each measurement. The baseline of the spectra

line was subtracted using the WiRE software (version 4.2).

### 3.3.6 X-ray photoelectron spectroscopy (XPS)

XPS was employed in the analysis of the composition and the binding states of GO before and after the ASP treatments using Thermo Scientific ESCALAB 250Xi facility. An Al Kα (1486.8 eV) source with a binding step size of 0.05 eV was applied on a spot size of 500 μm. To obtain the original surface status of the samples maintained in the ambient environment and a real content ratio of the metal deposited on the GO surface, measurements were both conducted before and after etching. The etching was done by argon ion sputtering using a medium current with a 2k eV voltage and a 0.18 nm/s step for 56 s.

For analysis, the peaks of the element spectra were deconvoluted using the associated Avantage software with the XPS instrument.

### 3.3.7 Thermal gravimetric analysis (TGA)

In order to investigate the effect of GO weight with reduction process and temperature, thermal gravimetric analysis was conducted using a thermal analyser (NETZSCH STA 449 C), in an argon atmosphere with a heating rate of 10 K/min. A small piece of GO sheet in solid state weighing 2.49 mg was used for the measurement.

## 3.4 Electrical property measurements

To investigate the electrical property of the GO samples before and after

treatments, sheet resistance was measured using a four-point probe measurement system (Ossila, UK) (Fig. 3-2). The measurements were repeated 5 times, and the average and standard deviation are reported.

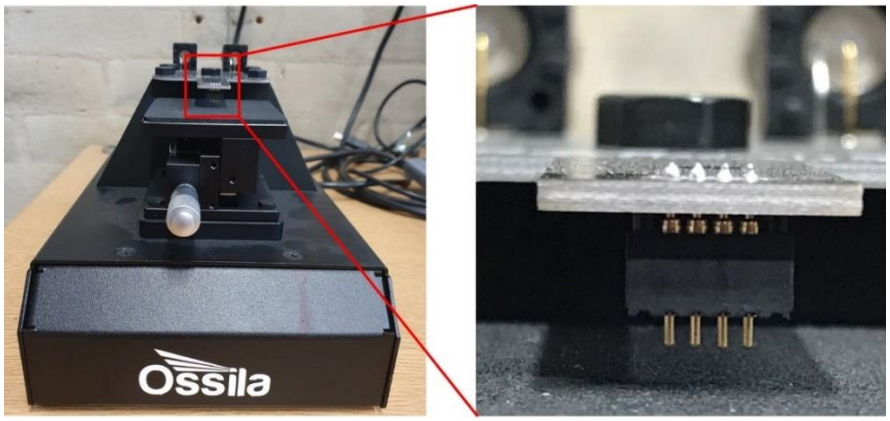


Fig. 3-2 The four-point probe measurement system, with the four probes circled in red square enlarged on the right side.

## 3.5 Electrochemical tests

The electrochemical measurements were carried out to test the super-capacitive performances of the GO samples, as a half-cell in a three-electrode configuration, using a Gamry Interface 1000 potentiostat. A 3.5 % NaCl aqueous solution was used as the electrolyte for a higher ionic conductivity than organic electrolyte or ionic liquids. The sample acted as working electrode, and was exposed to the electrolyte with a surface area of 0.503 $cm^2$ to participate in the electrochemical testing, and silver tape was used to stick on the FTO coated glass and GO unexposed to the electrolyte, connecting the GO to the lead to the potentiostat. The counter electrode was a platinum-coated rod of 6 mm in diameter, and the reference electrode was a saturated calomel electrode. Cyclic voltammetry (CV), electrochemical impedance spectroscopy (EIS) and

galvanostatic charge/discharge (GCD) tests were performed at room temperature. The diagrammatic setup of the three-electrode configuration used for the electrochemical tests is shown in Fig. 3-3.

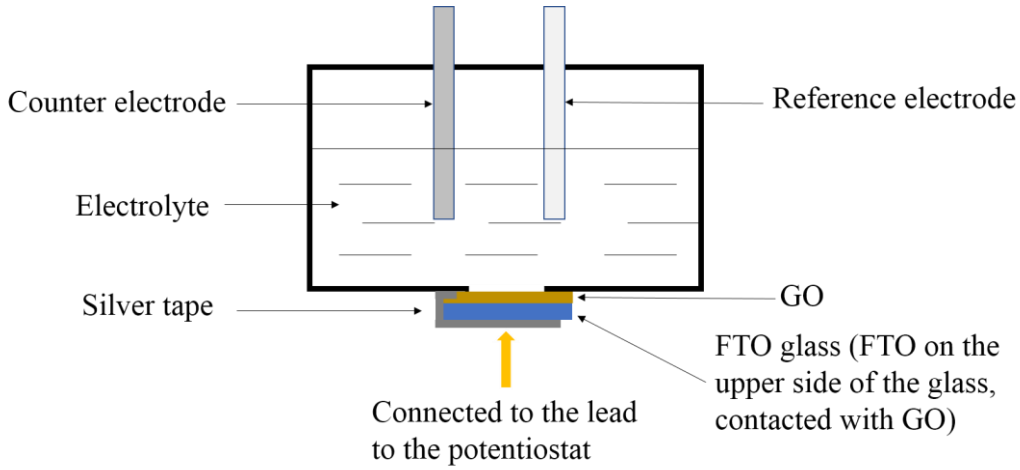


Fig. 3-3 Diagrammatic setup of the three-electrode configuration used for the electrochemical tests (not to scale).

### 3.5.1 Cyclic voltammetry (CV)

The CV tests were conducted between -0.1 V and +0.9 V, both vs. the reference electrode, and the scan rate differed at 100, 50, 20, 10 and 5 mV/s. The CV curves obtained were analysed using the built-in Echem Analyst, Gamry Instruments software. To calculate the capacitance, data from the CV curves were selected from 0.35 V to 0.45 V on both the positive and negative sides. The capacitances were calculated by Equations 1, where *C* is capacitance, *Q* is the charge accumulated during the cycle period, *I* is the instantaneous current, *U* is the applied potential, and *v* is the scan rate.

$$C = \frac{Q}{2\Delta U} = \frac{\int I\, dU}{2v \times \Delta U} \quad (1)$$

### 3.5.2 Electrochemical impedance spectroscopy (EIS)

After the CV test, a step of conditioning, followed by an open circuit potential measurement was conducted before the EIS test. Conditioning is a step where potential was applied statically for a certain length of time to insure a certain state of the electrode for the later measurement. The conditioning potential is 0 V and the conditioning time is 200 s. The EIS tests were performed at frequencies between 0.1 MHz and 0.01 Hz with a sinusoidal perturbation of 10 mV. The points/decade parameter was set as 10, so that 71 points were recorded during the EIS test.

Nyquist plots were produced based on the EIS data using the built-in Echem Analyst, Gamry Instruments software, and the equivalent Randles circuit model shown in Fig. 3-4 was established using a built-in fitting module of “CPE with Diffusion”. In this model, ESR is Equivalent Series Resistance, representing the sum of electrolyte resistance, electrode resistance and contact resistance between the electrode and the current collector; $C_{dl}$ is the double layer capacitance, as ions form the electrolyte adsorb onto the electrode surface and form a double layer, which behaves as a capacitor due to the charges separated by an insulator, and however, due to being an imperfect capacitor, this double layer capacitance is seen as a constant phase element $Y_o$ in the results interpretation; $R_{ct}$ is the charge transfer resistance, which is formed by a single, kinetically-controlled electrochemical reaction; $Z_w$ is Warburg impedance

created by diffusion.

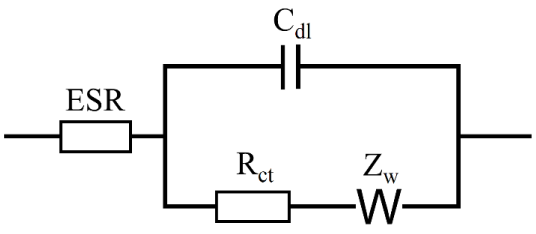


Fig. 3-4 Randles circuit model.

### 3.5.3 Galvanostatic charge/discharge (GCD)

The GCD measurement was also conducted after the conditioning step which is the same as the one mentioned in the EIS test. In the GCD test, the samples were tested at a constant current of 100 mA within the potential range from -0.1 V to 0.9 V.

# Chapter 4 Results and Discussions

This chapter is divided into three parts: the first part is about ASP reduction of GO, including the microstructure and TGA result of raw GO material and the comparison of ASP reduction of GO with thermal reduction of GO (Section 4.1 to 4.3); the second part reports the results of GO after ASP modification (Section 4.4 to 4.6); and the third part explores the hybrid effects of ASP on GO in modification and metal deposition (Section 4.7 to 4.10).

## Part I: ASP Reduction of GO

## 4.1 GO raw materials

### 4.1.1 Morphology of GO film and sheet

Before studying the effects of ASP treatment on GO, the GO raw material was first characterised using SEM and TEM to observe the morphology of GO before treatments.

1. SEM observation on GO

Fig. 4-1 (a, b) show the dried GO film drop casting on silicon wafer in different magnifications. It is clear to observe many wrinkles in bright or light colour of different lengths and directions. These are believed to be the GO films corrugated on the substrate. This morphology is characteristic of GO film, as it is similar with the ref [378, 379]. The wrinkles are likely to be formed due to the water drainage between GO and substrate during the drying process, as well

as the stresses from the interaction with anchorage on surfaces [380].

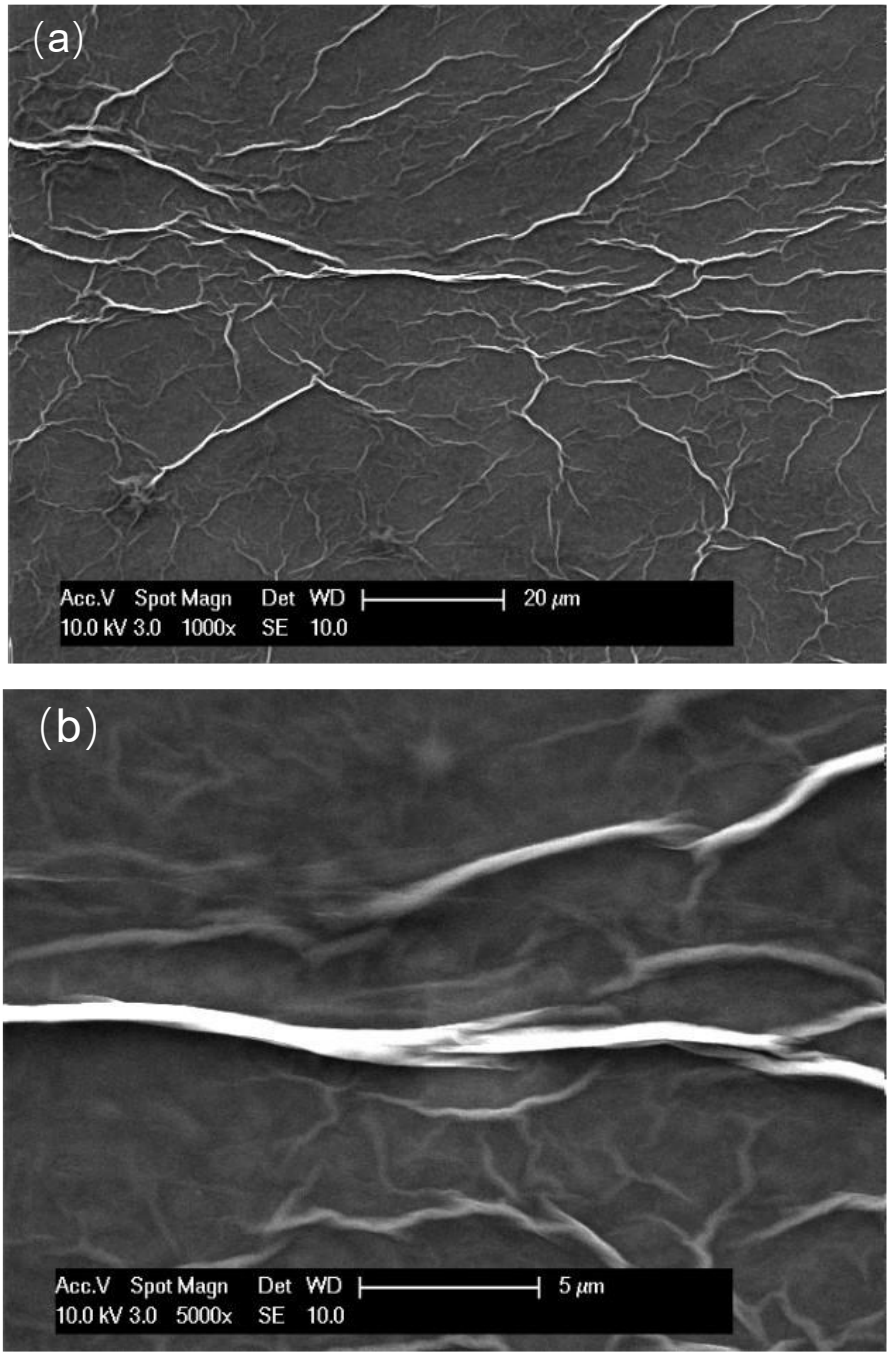


Fig. 4-1 (a, b) SEM images of GO film on silicon wafer at two magnifications.

2. EDS results of GO

Fig. 4-2 is the EDS result of GO film. As expected, it shows the presence of carbon, oxygen, silicon and sulphur. Silicon is from the silicon wafer substrate

as the basic constituent element, and carbon is from GO. Oxygen comes from both GO and substrate, and sulphur is considered the species from the residuals left on GO during its synthesis. Due to the large interaction volume for X-ray generation, which is in the micron range, the peak of Si signal (coming from the underlying silicon wafer) is relevantly strong as shown in Fig. 4-2.

Table 4-1 exhibits the percentages of element compositions from spectra of two different sites on the GO film sample. These two sites are red circled as shown in Fig. 4-3, as Spectrum 1 is on the bright site of the wrinkle, whilst Spectrum 2 is on the relevantly dark area. Although EDS results cannot be used for quantitative determination because of the high deviation, the results tested at different sites in the same sample at the same time are still roughly comparable. It is clear to see a drop of carbon and oxygen contents but an increase of silicon content in Spectrum 2 compared to Spectrum 1. This can confirm that the bright wrinkles are GO bulged out of the plane substrate.

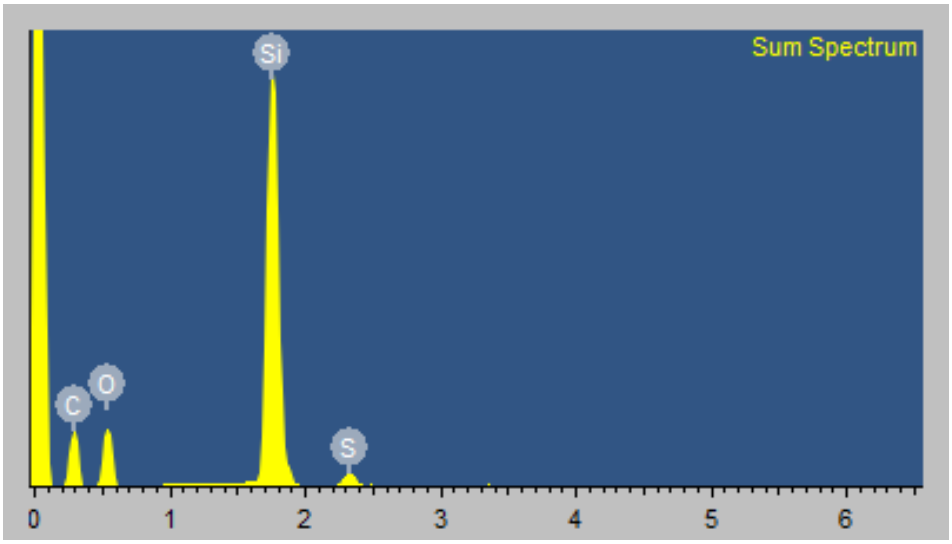


Fig. 4-2 EDS result of GO film on silicon wafer.

Table 4-1 Element percentages (wt.%) of GO film on silicon wafer of two sites in Fig. 4-3.

| | C | O | Si | S |
|---|---|---|---|---|
| **Spectrum 1** | 46.92 | 27.02 | 22.22 | 3.84 |
| **Spectrum 2** | 38.68 | 14.91 | 43.97 | 2.44 |

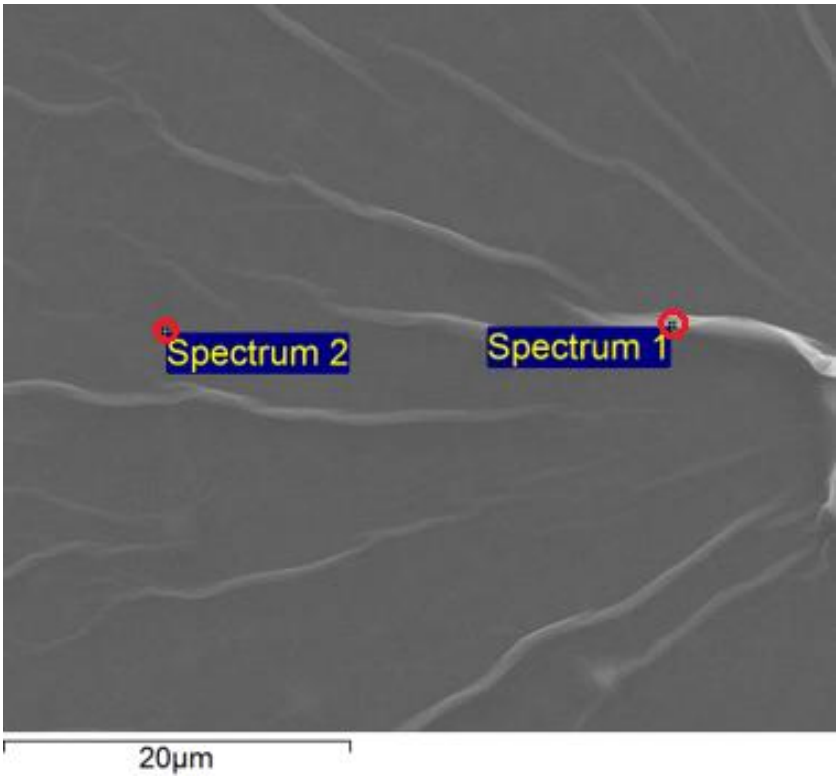


Fig. 4-3 Two different test sites of EDS on GO film.

3. TEM observation of GO sheets

Fig. 4-4 are the TEM images of two individual GO sheets in different sizes and shapes. The lateral size of GO in Fig. 4-4(a) is approximately 2 microns while the one in Fig. 4-4(b) is larger, with more obvious crumples. These two TEM images imply that the shapes of GO sheets are irregular and the sizes are in several microns.

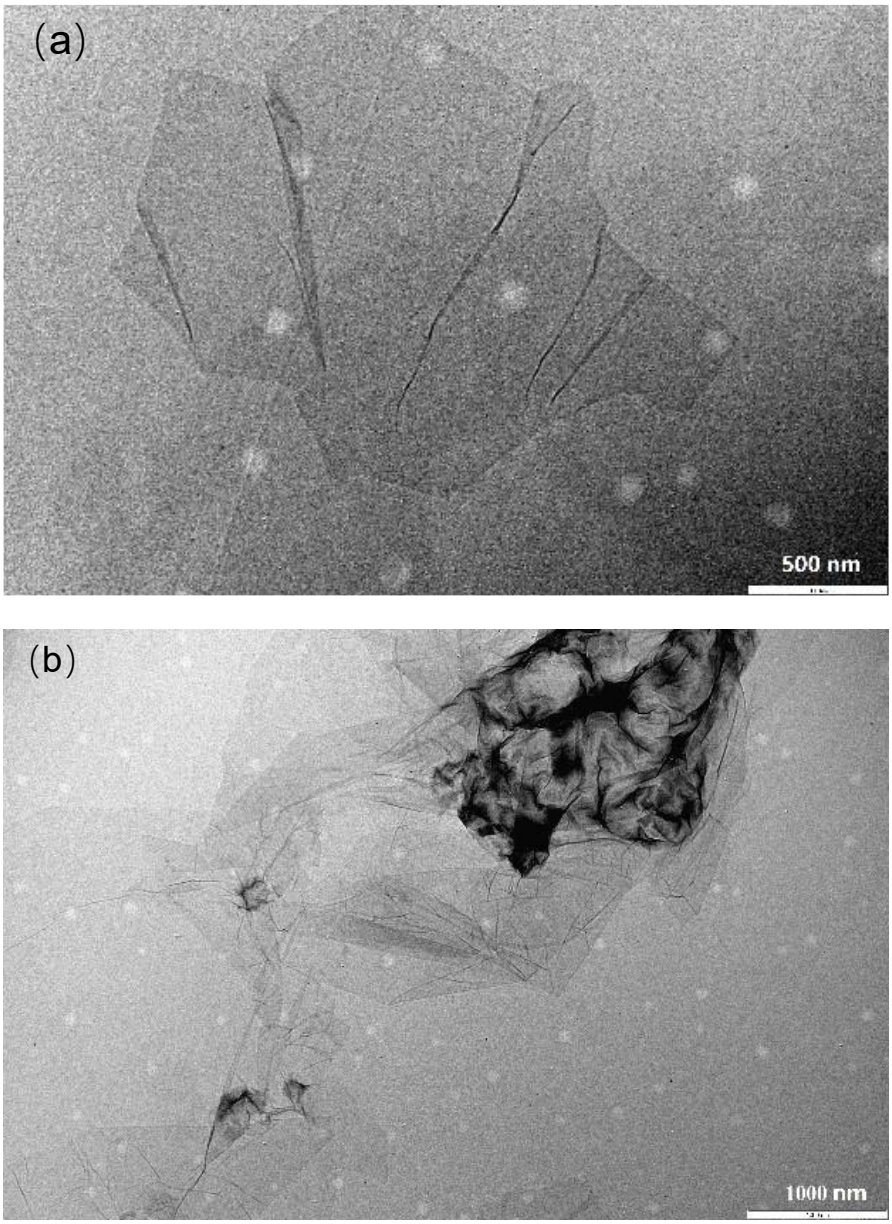


Fig. 4-4 (a, b) TEM images of GO at two magnifications.

## 4.1.2 Structure of GO

1. XRD patterns of GO

Fig. 4-5 shows the XRD patterns of FTO coated glass with and without GO film on it. In Fig. 4-5(a) where 2 theta ranges from 10° to 80°, characteristics peaks of FTO are shown in both two, with each index labelled above, which match well with those of $SnO_2$ of tetragonal phase [381, 382]. In comparison, a broad

peak at around 12° is evident for GO sample, while the one for FTO is around 13° but not that evident, and this difference is shown specifically in Fig. 4-5(b). The broad peak around 12° is supposed to be the integration a characteristic peak of GO for its (0 0 1) crystal plane near 11°, and the broad peak of FTO at 13° [383, 384].

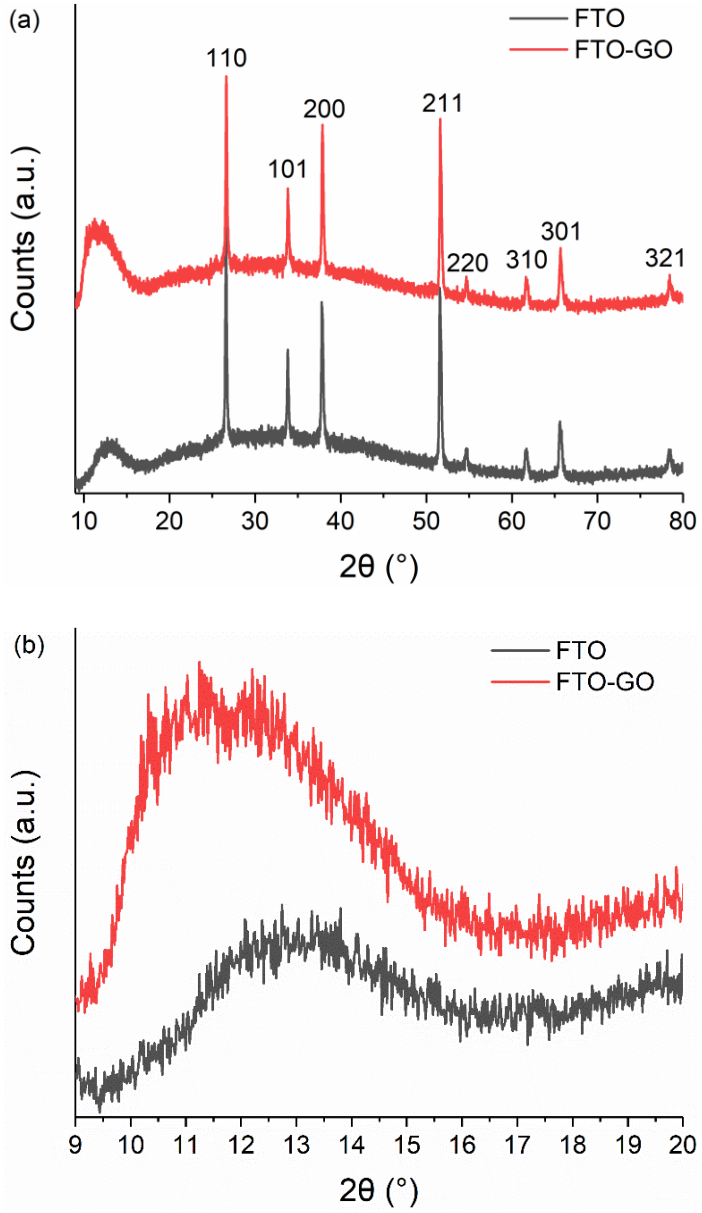


Fig. 4-5 XRD patterns of FTO coated glass with and without GO film, (a) 2θ ranges from 10° to 80°, (b) 2θ ranges from 9° to 20°.

2. Raman spectrum of GO

Raman spectrum is a versatile tool for analysis of carbon materials. However, the data interpretation is difficult because various factors can influence the spectrum. This thesis will try to interpret the Raman spectra of GO samples to evaluate the effects of ASP treatment on GO materials.

Fig. 4.6 is the Raman spectrum of raw GO film sample. Two dominant peaks: D peak and G peak, as well as three relatively small peaks: 2D peak, D+D' peak and 2D' peak, are present in the Raman spectrum of GO film. G peak at around 1580 $cm^{-1}$ corresponds to the high-frequency $E_{2g}$ phonon at Brillouin zone centre Γ of graphene, which makes it the most prominent and characteristic peak of graphene. D peak at around 1360 $cm^{-1}$ is associated with the defects and disorders of graphene structure. The high intensity of D peak here indicates that there are large amounts of defects in GO, due to oxygen functional groups and vacancies [385].

D+D' peak comes from two-phonon defect-assisted processes. 2D peak and 2D' peak are the second order (also known as overtone) of D peak and intra-valley D' peak, respectively, but D' peak is not prominent here in this Raman spectrum. 2D peak can be used to determine the layer number of graphene materials. However, these three tiny peaks between 2700 $cm^{-1}$ and 3200 $cm^{-1}$ are not discussed here, due to the extreme low intensities.

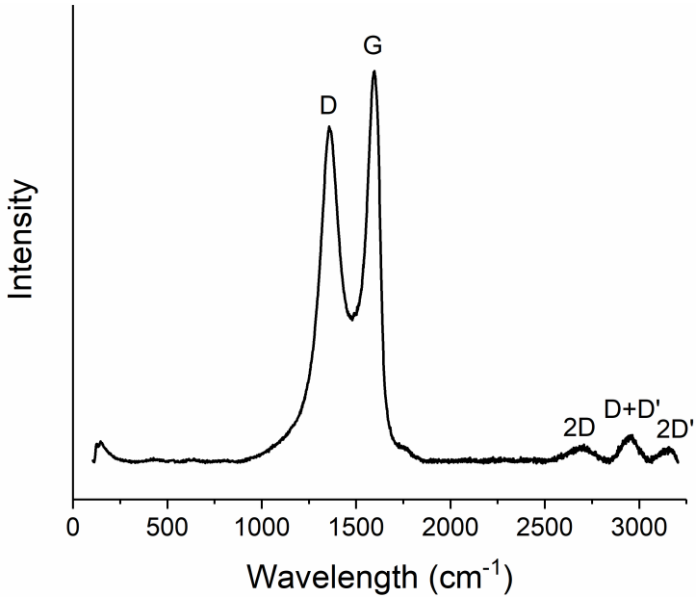


Fig. 4-6 Raman spectrum of GO.

3. XPS of GO

Fig. 4-7 is the spectra survey of GO before and after etching, inset with the element atomic percentages. Both show the presence of carbon, oxygen, nitrogen and sulphur, which is different from EDS result in the presence of nitrogen and the absence of silicon. It is because the depth of XPS measurement is only approximately 10 nm so that only the signals from the very surface of the sample can be detected. As stated before, carbon and oxygen are from GO, and sulphur is from the residuals during GO preparation. Nitrogen could also be the dopant atoms of GO incorporated during the synthesis. As to the atomic percentage of the element, it is found that after etching, oxygen content drops sharply, whilst carbon content increases, suggesting that GO got reduced after etching, with a large proportion of the oxygen functional groups removed.

Fig. 4-8 shows the high-resolution XPS spectra of C1s after deconvolution, inset with the lists of basic information of each peak, including the corresponding chemical states, binding energies and atomic percentages. (This is followed by all the figures of XPS spectra deconvolution throughout the thesis). Before etching, as shown in Fig. 4-8(a), the C1s spectrum features two dominant peaks, and can be decomposed into three peaks: Peak A, Peak B and a small Peak C at 284.6, 286.8 eV and 287.9 eV, representing C-C, C-O and C=O, respectively [386]. C-C here represents mainly the aromatic graphitic-like structure of $sp^2$ hybridisation which is the basic structure of GO. C-O includes both hydroxyl C-OH and epoxy C-O-C. C=O includes both carbonyl and carboxyl, with carbonyl the dominant one [387]. Thus, the GO raw material contains the basic graphitic structure, with various oxygen functional groups (hydroxyl, epoxy, carbonyl and carboxyl) decorated, and the C/O ratio is about 2:1.

After etching, the high-resolution XPS C1s spectrum alters significantly, with only one dominant peak left, as shown in Fig. 4-8(b). the spectra can also be decomposed into three peaks (still denoted as Peak A, Peak B and Peak C) at 284.6, 285.7 and 289.2 eV, respectively. Peak A at 284.6 eV and Peak C at 289.2 eV represent C-C and C=O, respectively, but in this case, carboxyl dominates Peak C, as it shifts to a higher binding energy [387], which is probably because carbonyl groups got eliminated during the etching. As to the Peak B at 285.7 eV, however, given extremely low content of nitrogen and

oxygen in GO, it is likely to be ascribed to C-C $sp^3$ hybridisation [387], which are the disorders caused by etching.

Etching process in XPS measurement is conducted via argon ion beam, which is supposed to have a huge impact on the GO structure [306, 357].Comparing the high-resolution C1s spectra of GO before and after etching, it is found that GO undergoes significant reduction and structure reconstruction, as a majority of oxygen functional groups are removed, with C-C $sp^3$ hybridisation structure formed. Thus, to properly evaluate the structure information of GO in ASP treatment, the XPS measurements are all conducted without etching process in the following investigations.

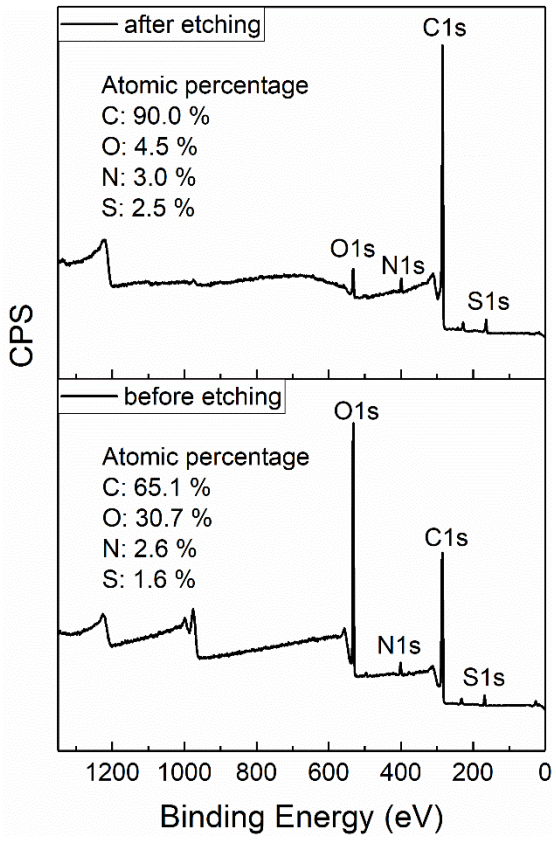


Fig. 4-7 XPS spectra survey of GO before and after etching (inset with atomic percentage of detected elements).

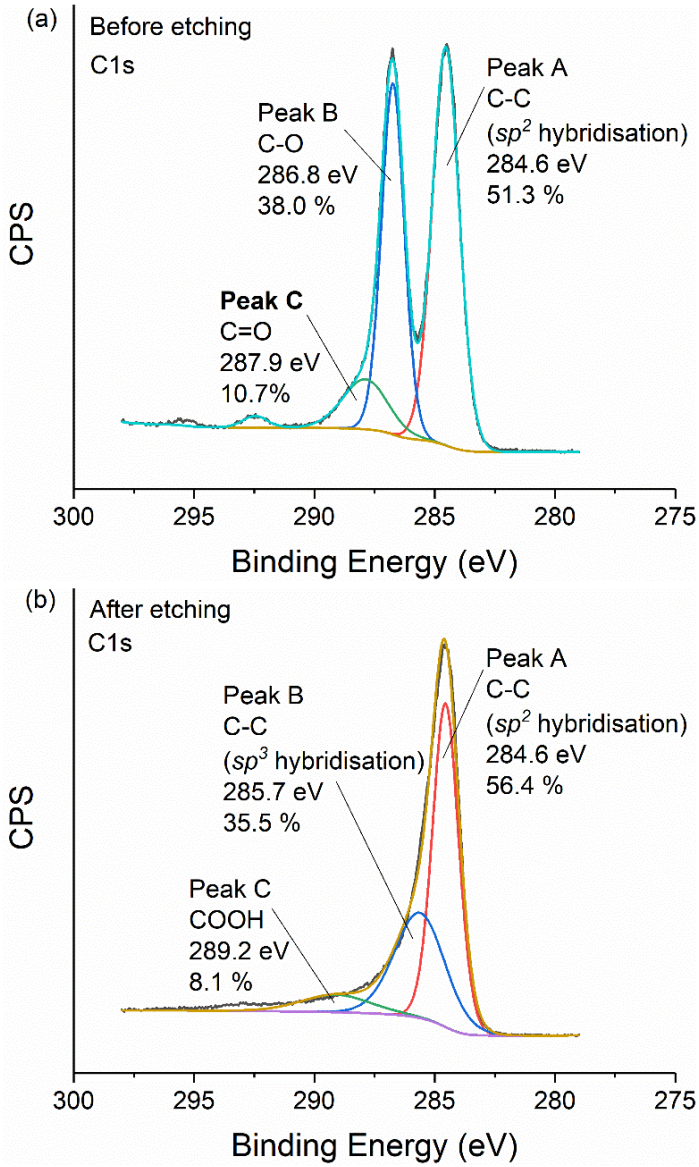


Fig. 4-8 Deconvoluted C1s spectra (a) before etching, (b) after etching.

### 4.1.3 TGA of GO

TGA is a measurement of the mass change with the temperature to determine thermal stability of the sample. TGA measurement on GO can be used for analysis of the GO reduction process with the change of temperature. Fig. 4-9 is the TGA result of GO. As shown, with the increase of temperature, the mass loss of GO can be divided into four phases, in which the rates of mass loss are different. In Phase 1, the mass loss of GO starts at the beginning of the

temperature increase and about 92 % of the mass remains at around 140 ℃. Then it gets into Phase 2, in which the rate of mass loss gets much faster, until at around 216 ℃, when only about 66 % of GO remains. The mass loss rate gets slow in Phase 3 with about 58 % of GO left at a temperature of around 320 ℃, and the rate becomes even slower in Phase 4.

These four phases with different mass loss rate indicate four different thermal decomposition phases of GO during TGA process (i.e., loss of different oxygen functional groups in GO). According to ref. [110], the decomposition temperature of oxygen groups in GO with different layers is not exactly the same, but follows the same rule. In summary, as to multilayer GO (over five layers), hydroxyls decompose first, initiated at around 75 ℃, follows with epoxides and carboxyl, at around 150 and 175 ℃, respectively. Ketones are the last one to decompose at around 225 ℃. Based on this, the TGA results can be explained: in Phase 1, the residual water removes, and hydroxyls starts to decompose; in Phase 2, all the residual water has been eliminated, and epoxides and carboxyl groups are decomposing, as well as hydroxyls; in Phase 3 and Phase 4, although ketones begin to decompose, some certain oxygen functional groups have been eliminated or become the minor ones, decreasing the mass loss rate.

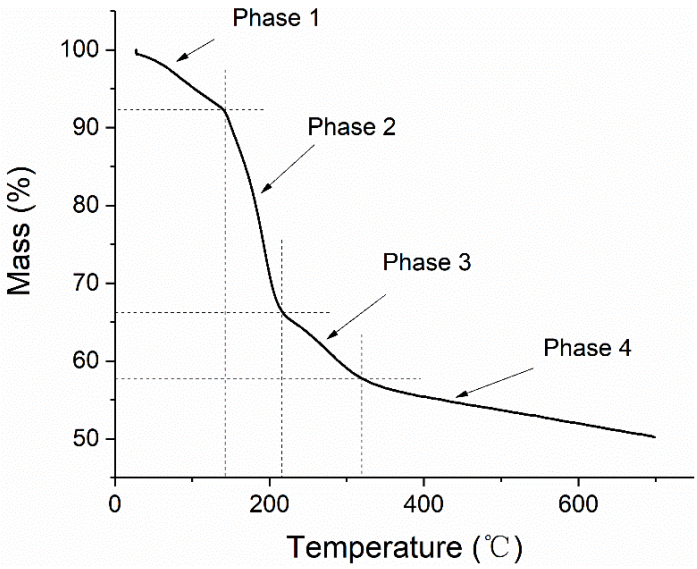


Fig. 4-9 TGA result of GO.

## 4.2 Results of ASP Reduction on GO

In this section, the effects of ASP on GO are investigated via comparison with annealing treatment on GO reduction. To compare with annealing treatment, ASP treatments were conducted using argon as the working gas, and annealing is also carried out in argon atmosphere, both at a temperature at 100 ℃ for a duration of 1 h.

### 4.2.1 Micro-structure

1. SEM observation and EDS results

For comparison, the untreated GO film was characterised again here. Fig. 4-10 shows the SEM images of untreated, annealed and ASP treated GO films at two different magnifications. However, there is no specific difference among these three samples, all showing the wrinkles of the GO film. The EDS results are exhibited in Table 4-2. Due to the difference in element content at different

detecting positions, as discussed in Section 4.1.1 (Table 4-1 and Fig. 4-3), the areas with wrinkles were selected for EDS analysis, as circled in green rectangle in Fig. 4-10. Although not quantitively accurate, the subtle decrease of oxygen content for annealed and ASP treated samples may possibly be an implication of GO being partially reduced during the treatments, which is consistent with the TGA result that the mass loss of GO starts to decrease before 100 ℃.

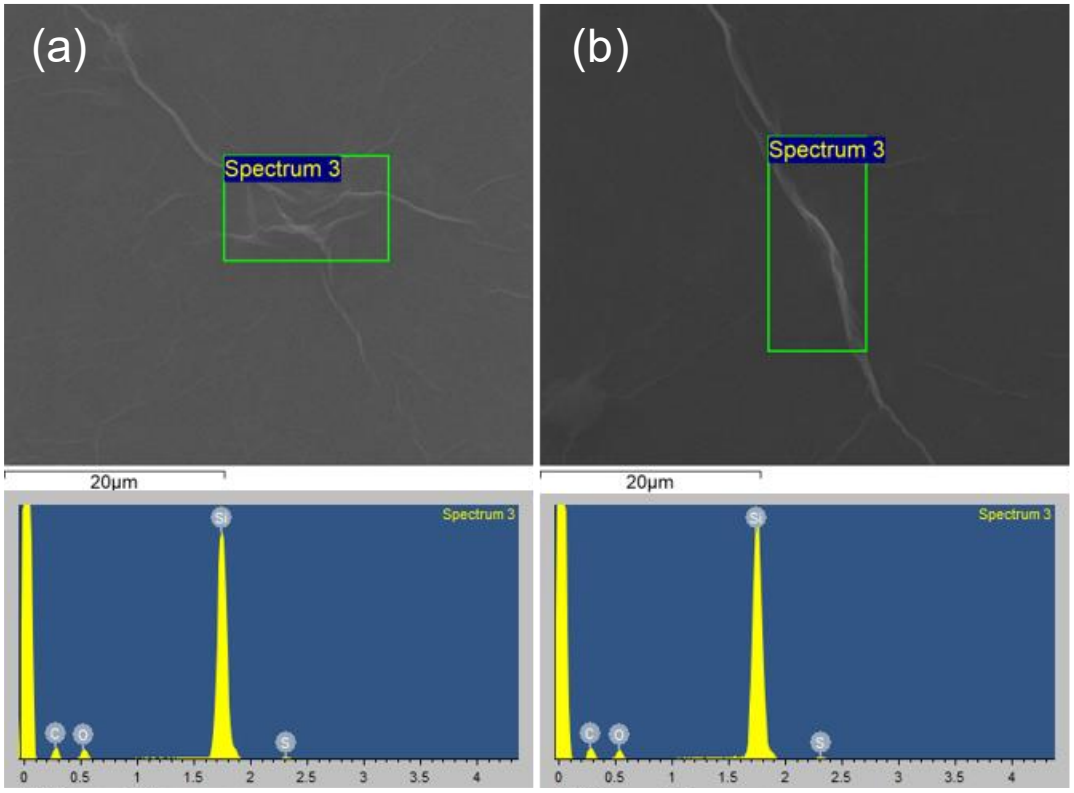

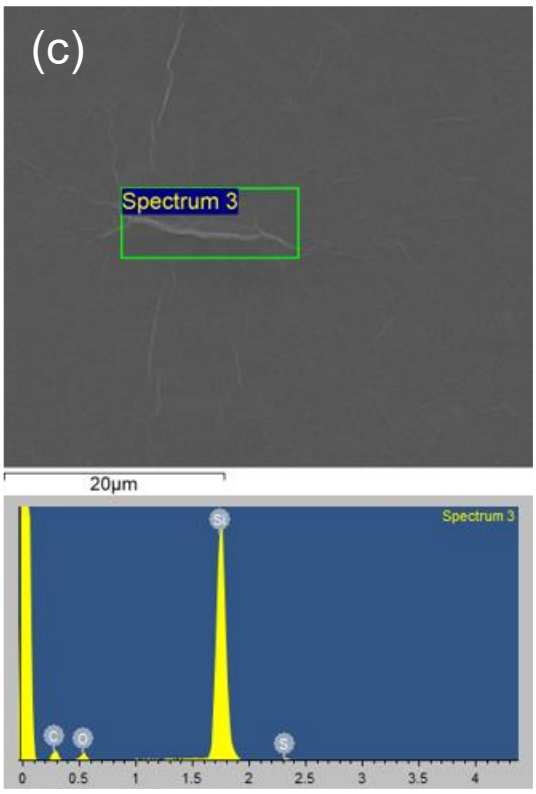


Fig. 4-10 SEM and EDS images of (a) untreated, (b) annealed and (c) ASP treated GO films.

Table 4-2 Element content (wt.%) of GO samples before or after treatments

| | C | O | Si | S |
|---|---|---|---|---|
| **Untreated GO** | 41.15 | 17.13 | 41.26 | 0.46 |
| **Annealed GO** | 41.52 | 14.98 | 43.11 | 0.39 |
| **ASP treated GO** | 39.91 | 13.36 | 46.17 | 0.56 |

2. Raman spectra

Fig. 4-11 is the Raman spectra of untreated, annealed and ASP treated GO, in the wavelength range between 1000 $cm^{-1}$ and 2200 $cm^{-1}$. Two characteristic peaks: D peak and G peak, are prominent in all these three Raman spectra of GO samples, and the corresponding parameters are shown in Table 4-3.

Usually, the intensity ratio of D peak and G peak ($I_D/I_G$) is widely used to determine the graphene structure in terms of the defects and disorders that

result from its oxidation and vacancies, and a smaller $I_D/I_G$ suggests fewer defects of the graphene structure [388]. However, according to Andrea C. Ferrari [389, 390], three stages are defined in his amorphisation trajectory: stage (1) from graphite to nanocrystalline graphite, stage (2) from nanocrystalline graphite to low $sp^3$ amorphous carbon, stage (3) from low $sp^3$ amorphous carbon to high $sp^3$ amorphous carbon. Since D peak arises from the breathing modes of six-atom rings, only the defects in crystalline region of $sp^2$ hybrid graphitic carbon in stage (1) can cause the increase of $I_D/I_G$, whilst in stage (2), the formation of amorphous carbon in $sp^3$ hybrid cannot contribute to a higher $I_D/I_G$.[385] Thus, $I_D/I_G$ may decrease with a rise in defects when crystalline graphite turns to an amorphous carbon structure, as $sp^2$ rings of graphitic structure are damaged, impairing the intensity of D peak [391]. Therefore, an increase in $I_D/I_G$ may suggest that the average size of $sp^2$ cluster decrease that occurs in stage (1), or the number of the $sp^2$ aromatic rings increased upon reduction in stage (2) [390, 9]. Based on all this analysis, it is hard to judge the structure transformation of GO simply by the change of $I_D/I_G$.

Here, the $I_D/I_G$ increased from 0.858 to 0.882 for the annealed one and decreased to 0.836 for the ASP treated one. Both the two $I_D/I_G$ of treated GO are close to the that of untreated GO. The subtle differences can be owing to one of the two reasons. One is the integration effect of the transformation in both stage (1) and stage (2). The other is because of the deviation that there is no evident structure transformation of GO after these treatments, possibly due

to the mild treatment conditions.

Apart from $I_D/I_G$, the information of graphitic structure can also be deduced from other information, such as the full-width at half-maximum of G peak (FWHM(G)) and the position of G peak. FWHM(G) always increases with an increase of disorders, and G peak would shift from 1580 $cm^{-1}$ to 1600 $cm^{-1}$ in stage (1), and from 1600 $cm^{-1}$ to 1510 $cm^{-1}$ in stage (2) [392]. Here, the three positions of G peak are still close to each other. However, the FWHM(G) of annealed GO decreases from 92 $cm^{-1}$ to 84 $cm^{-1}$ whilst that of ASP treated GO increases from 92 $cm^{-1}$ to 98 $cm^{-1}$.

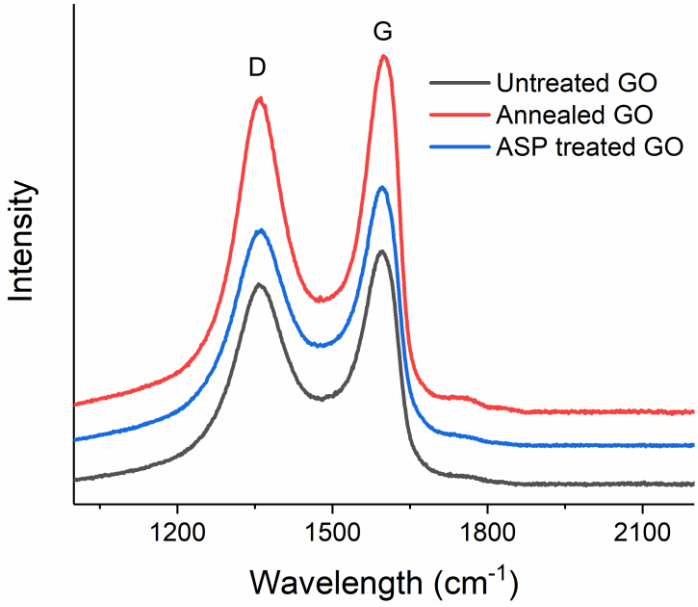


Fig. 4-11 Raman spectra of untreated, annealed and ASP treated GO.

Table 4-3 Raman spectra details of GO samples after different treatments in argon

| | D peak | | G peak | | $I_D/I_G$ |
|---|---|---|---|---|---|
| | Wavelength/$cm^{-1}$ | FWHM/$cm^{-1}$ | Wavelength/$cm^{-1}$ | FWHM/$cm^{-1}$ | |
| **Untreated GO** | 1357 | 139 | 1597 | 92 | 0.858 |
| **Annealed GO** | 1361 | 122 | 1598 | 84 | 0.882 |
| **ASP treated GO** | 1363 | 152 | 1595 | 98 | 0.836 |

Based on all these results, it can be explained that GO was partially reduced in both annealed and ASP treatments. However, more defects are formed during the ASP process, possibly because of the ion bombardment in the plasma [315].

### 4.2.2 Electrical and electrochemical properties

1. Sheet resistance measurement

Fig. 4-12 is the sheet resistance of untreated GO, annealed GO and ASP treated GO. The sheet resistance of untreated GO is the highest, of approximately $5.2\times10^6$ Ω $sq^{-1}$, while both annealed and ASP treated GO exhibit lower sheet resistances. The sheet resistance of annealed GO is decreased to around $1.8\times10^6$ Ω $sq^{-1}$, and that of ASP treated GO is decreased further to only about $0.75\times10^6$ Ω $sq^{-1}$. Since the annealed GO is only treated by an increase of temperature to 100 ℃, the sheet resistance of annealed GO can be seen as the sheet resistance of GO at the temperature of 100 ℃.

The drop of sheet resistance of annealed GO can be attributed to GO reduction. Since a higher temperature leads to a higher degree of reduction if no extra damage was caused, the sheet resistance of GO will decrease at a higher temperature. The sheet resistance of ASP treated GO is lower than that of annealed GO, which indicates that the effect of decreasing sheet resistance of GO can be realised by ASP treatment with a lower temperature than by annealing treatment.

Given the analysis of Raman spectroscopy that the graphitic structure of ASP

treated GO was damaged and amorphous $sp^3$ domain forms, which should lead to a higher sheet resistance. The lower sheet resistance of ASP treated GO can be explained in a more effective reduction, which is further discussed in Section 4.3.

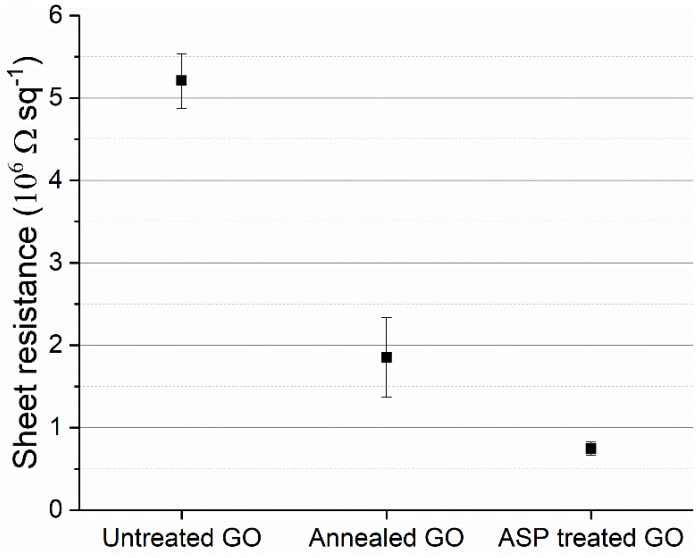


Fig. 4-12 Sheet resistance of untreated, annealed and ASP treated GO.

2. Electrochemistry tests

(1). CV test

The electrochemical performances of untreated GO, annealed GO, and ASP treated GO samples were evaluated in CV test, and the results are shown in Fig. 4-13. Among these figures, Fig. 4-13(a-c) are the curves of the samples at different scan rates, while Fig. 4-13(d) compares the CV curves of these samples at a scan rate of 100 mV $s^{-1}$.

All the CV curves at low scan rates exhibit quasi-rectangular shapes, indicating a capacitive behaviour [152]. In comparison, untreated GO curves show the

smallest area, while ASP treated GO curves possess the largest area (Fig. 4-13(d)). The larger area of the treated GO samples, particularly the ASP treated one, suggests their better capacitive performances. Two broadenings of the capacitive current can be found near 0.6 and 0.8 V of ASP treated GO only, which may come from the Faradaic redox responses, which means that a pseudocapacitive charging might occur during the voltammetry cycle. This could be ascribed to the incorporation of transition metal oxides during the ASP treatment (which will be investigated later in Section 4.7) [150].

Fig. 4-13(e) displays the capacitances of these GO samples calculated at different scan rates. All the capacitances increase with the decreasing scan rates. This is because more charges can be allowed to penetrate electrode materials at slower scan rates, so that the inner surface of the electrode materials can be utilised for adsorption in the process. At a scan rate of 5 mV $s^{-1}$, the capacitance of ASP treated GO reaches around 930 μF, nearly 3.5 times that of untreated GO, and higher than that of annealed GO, which was around 710 μF.

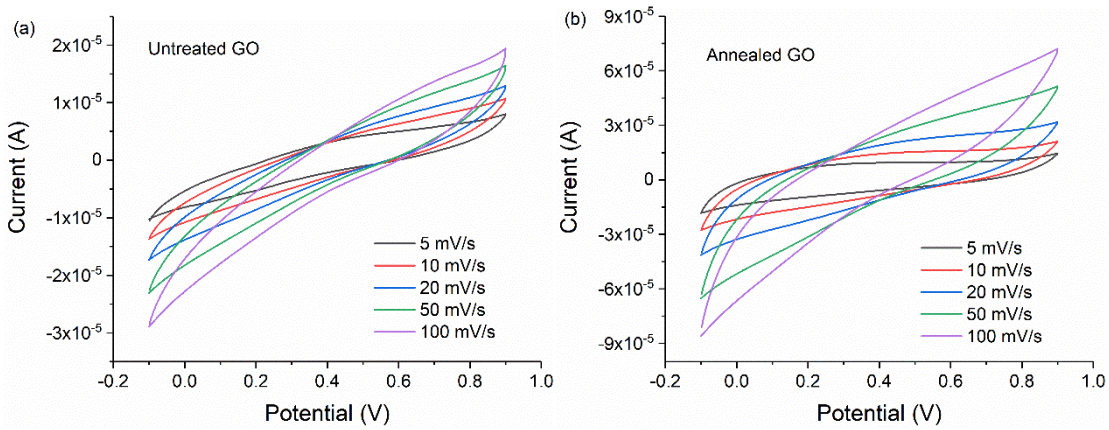

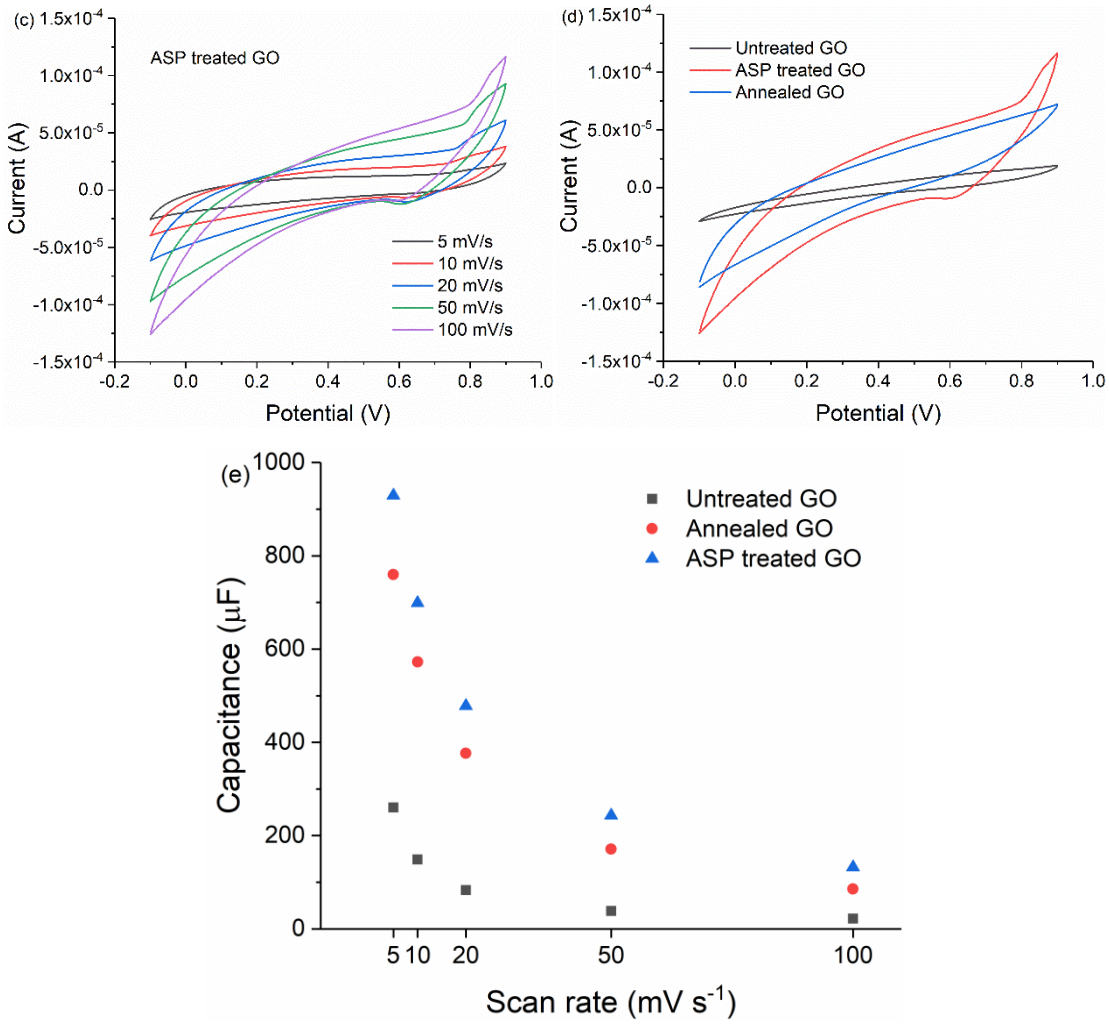


Fig. 4-13 CV curves of (a) untreated GO (b) annealed GO (c) ASP treated GO, (d) comparison of CV curves at 100 mV $s^{-1}$, and (e) capacitances at different scan rates.

(2). EIS test

EIS tests were conducted to further investigate the electrochemical performance of these GO samples. Fig. 4-14 shows the Nyquist plots of the EIS result. Table 4-4 exhibits some of the parameters of the equivalent circuit fit of the EIS results.

Nyquist plot for a SC can be divided into two parts. The straight segment at low frequencies is related to the Warburg finite-length diffusion stage, while the

diameter of semi-circle at high frequency region indicates the charge transfer resistance ($R_{ct}$) [393]. The smallest semi-circle of ASP-GO implies the fastest charge diffusion in the charging/discharging process. An ideal SC should show a small $R_{ct}$, i.e., a small semi-circle. Equivalent series resistance (ESR) includes electrolyte resistance, electrode resistance, and contact resistance between the electrode and the current collector [394], and can be obtained from the intercept of the plot to the x-axis. The $R_{ct}$ and ESR of ASP treated GO are 3.02 kΩ and 0.16 kΩ, respectively, both much lower than those of untreated GO (15.82 kΩ and 0.64 kΩ) and annealed GO (5.70 kΩ and 0.25 kΩ). This also agrees with the sheet resistance measurement results (Fig. 4-12), indicating a better effect on improving the electrical properties of GO by ASP treatment than by annealing treatment. In addition, in the low frequency region, the vertical lines that parallel to the imaginary axis of both annealed GO and ASP treated GO also indicate a capacitive characteristic [395].

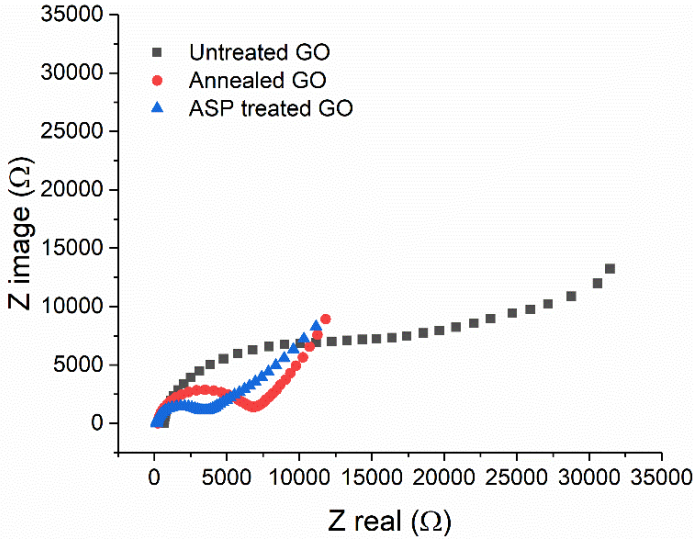


Fig. 4-14 Nyquist plots of untreated GO, annealed GO and ASP treated GO.

Table 4-4 Parameters of the equivalent circuit fit of the EIS results

| | ESR (kΩ) | $R_{ct}$ (kΩ) | $Y_o$ ($S \cdot s^{\alpha}$) | α* | $W_d$ ($S \cdot s^{1/2}$)** | Goodness |
|---|---|---|---|---|---|---|
| **Untreated GO** | 0.64 | 15.82 | $5.60\times10^{-4}$ | 0.89 | $1.26\times10^{-4}$ | $2.70\times10^{-3}$ |
| **Annealed GO** | 0.25 | 5.70 | $4.22\times10^{-4}$ | 0.96 | $4.01\times10^{-4}$ | $1.07\times10^{-3}$ |
| **ASP treated GO** | 0.16 | 3.02 | $4.50\times10^{-4}$ | 0.95 | $3.42\times10^{-4}$ | $0.17\times10^{-3}$ |

* α is an exponent 0<α<1, and α=1 for a capacitor. This is applied through the thesis.

** $W_d$ is the reciprocal of Warburg coefficient σ, and σ can determine Warburg impedance by $Z_w=\sigma(\omega)^{-1/2}(1-j)$. This is applied through the thesis.

(3). GCD test

Further comparison was conducted by GCD test, and the results are shown in Fig. 4-15. The IR (Ohmic) drop obviously reduces after both treatments, with the ASP treated GO showing the smallest one, of approximately 0.09 V, only half of untreated GO. Since IR drop is an indication of the energy loss caused by internal resistance [396], the smallest IR drop value for ASP treated GO suggests that its internal resistance is the smallest and the energy lost during the charge-discharge process is the least. This is consistent with the EIS results. In addition, the charge and discharge lines are nearly symmetrical, indicating the feasibility for SC application. However, the charge/discharge plots are not exactly isosceles triangles, suggesting some pseudocapacitive characteristics in the electrodes [150]. The charge/discharge time of ASP treated GO is the longest, almost twice that of annealed GO, and more than eight times longer than the untreated GO, indicative of the highest capacitance. This is consistent with the CV results. The smallest IR drop and the longest charge/discharge time both suggest that ASP treated GO is more promising than the annealed GO for SC applications. Also, the GCD curves are cycled for three times, and the

charge/discharge time is not shortened significantly, indicating a good cyclic performance as well.

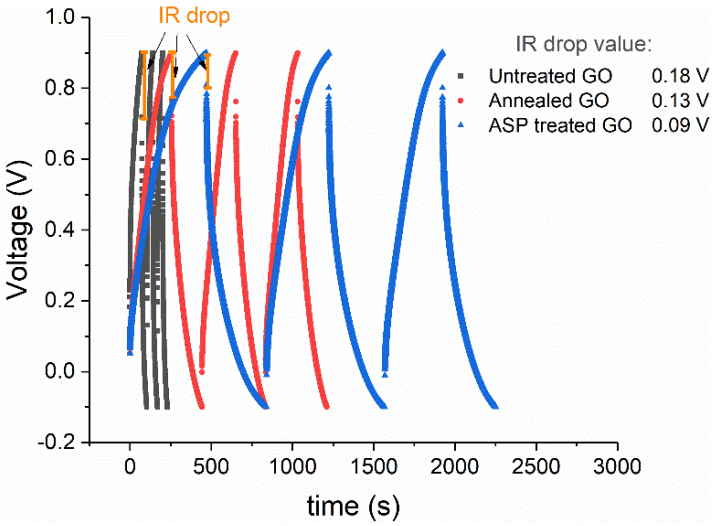


Fig. 4-15 GCD plot of untreated GO, annealed GO and ASP treated GO.

According to the CV, EIS and GCD tests, the ASP treated GO exhibits the best super-capacitive performances. This is likely to be ascribed to the best electrical properties of the ASP treated GO, which results from a more effective reduction, as well as the deposited transitional metal oxide nanoparticles. Furthermore, these metal oxide nanoparticles can also contribute to the pseudo-capacitance.

## 4.3 Mechanism of ASP GO Reduction

As described in Sections 4.2, ASP treated GO using argon showed an increase in electrical and electrochemical properties (Fig. 4-12 to Fig. 4-15), compared to the untreated GO, which implies the reduction of GO during ASP treatment. This has been strongly supported by the characterisation of the ASP treated GO. The reduction of GO can be ascribed to two reasons.

As reviewed in Section 2.2.2.1, the reduction of GO could be achieved through thermal reduction such as vacuum annealing at high temperature [111]. This has also been supported by the reduction of thermally annealed GO in this research (Section 4.2).

During ASP treatment, plasma is formed in the electrical field through ionisation of gas molecules. The negative-charged particles (ions) move to the cathode (active screen) so that ion bombardments occur as the ions collide with the active screen. During this process, the active screen is heated by the thermal energy transferred from the kinetic energy of the energetic ions, thus leading to a temperature increase of the active screen. The thermal energy will then be transferred to the worktable where the GO samples are placed through thermal reradiation. Since the transfer of energy is through photons, no medium for the energy to transfer is required, and therefore the transfer is efficient regardless of the treatment pressure or environment [397]. Consequently, the temperature of the worktable, and any materials placed on it, will increase.

The radiation-induced temperature increase of the GO samples was controlled to approximately 100 ℃ in the present study, as measured using a thermo-couple placed on the same worktable as the GO samples. Although thermal reduction of GO is normally conducted at a high temperature of around 1000 ℃ [111], GO can be partially reduced at lower temperatures [398] since the decomposition of hydroxyls starts at about 100 ℃ [110]. This agrees with the

TGA result in Section 4.1.3 that the mass loss of GO started before 100 ℃.

However, ASP treatment is shown to be much more effective than thermal annealing in reducing GO, as reported by Chen et al. [399]. Also, as discussed in Section 2.2.2.1, the optimal annealing temperature for GO reduction is 350 ℃ [112], and GO reduced for application as a supercapacitor (SC) is conducted at a temperature of at least 200 ℃ for an obvious removal of oxygen functional groups and a significant electrical property enhancement [111, 113], while in some cases, the temperature for thermal reduction is even higher [109, 400]. Moreover, as reported in Section 4.2, the electrical and electrochemical properties of ASP treated GO are better than those of annealed GO under the same processing conditions (Fig. 4-12 to Fig. 4-15). Therefore, a more effective reduction should play the main role in enhancing the properties.

The superiority of the ASP treatment to the thermal annealing in reducing GO suggests that there must be other more important reducing mechanisms involved in ASP reduction of GO. As discussed in Section 2.3.3.1, plasma reduction of GO is mainly based on the interactions between the plasma flux of active species and the C-O bonds in GO. When using argon, argon ions and activated argon atoms are the main active species in the plasma that collide with the GO to remove the oxygen functional groups. These active species can interact with the oxygen functional groups to form molecules that escape from the graphene lattice, thus leading to the reduction of GO [310].

However, it should be indicated that conventional plasma techniques such as DC plasma that directly forms on GO will cause damage to the graphene lattice due to the strong ion bombardment [10]. In contrast, ASP is a type of remote plasma or post-plasma technique [401, 402], because GO is placed on an insulating worktable at a floating potential and is away from the plasma formed on the active screen.

The active screen that connects with the cathode plate shares the same potential with the cathode, and thus it attracts the positively charged particles in plasma to move towards itself. As a result, the majority of positively charged particles (ions) bombard, react with and implant into the active screen, without reaching the GO samples. However, the neutral radicals generated during the ASP treatment could reach the GO samples placed on the worktable without significant effect from the electric field, as is illustrated in Fig. 2-17(c). During the ASP treatment, the active species that finally interact with GO samples are mostly neutral radicals with only limited number of ions, thus the damage from direct ion bombardment which could occur during DC plasma treatment is minimised [302].

# Part II: ASP Modification of GO

## 4.4 Results of Gas Effect on ASP Treatment

Section 4.2 has shown that ASP treatment is superior in improving the super-capacitive performances of GO. In this section, the effects of gas used in ASP

treatments were explored and compared, as different working gases: pure argon, pure hydrogen, gas mixture of nitrogen and argon, and gas mixture of nitrogen and hydrogen, were applied in ASP treatments. The percentage of nitrogen in both gas mixtures is 25 %. All the other conditions were the same, as all the ASP treatments were conducted at a total gas pressure of 0.75 mbar, at a temperature of 100 ℃ for a duration of 1 h. The samples are denoted as Ar-GO, $H_2$-GO, $N_2$Ar-GO and $N_2H_2$-GO, respectively, according to the working gas used in the ASP treatments.

### 4.4.1 Micro-structure

1. SEM observation and EDS results

The SEM images of GO after ASP treatments using different gases are shown in Fig. 4-16. Similarly, the SEM images of these GO samples show no specific difference, with wrinkles on all the samples. The EDS results are obtained from the areas circled in green rectangles in Fig. 4-16. In EDS results, still, the four elements: carbon, oxygen, silicon and sulphur are detected, and the elemental contents are displayed in Table 4-5, and are similar as well. Oxygen contents of all these four ASP treated GO again show a subtle decrease compared to untreated GO, implying that all the GO after ASP treatments get reduced. However, nitrogen element is not exhibited in GO samples after ASP treatments using the mixture gases containing $N_2$. It is supposed that nitrogen doping would occur, according to literature [403]. The absence of nitrogen in EDS result

may be due to a too low content of nitrogen doped in GO to be detected.

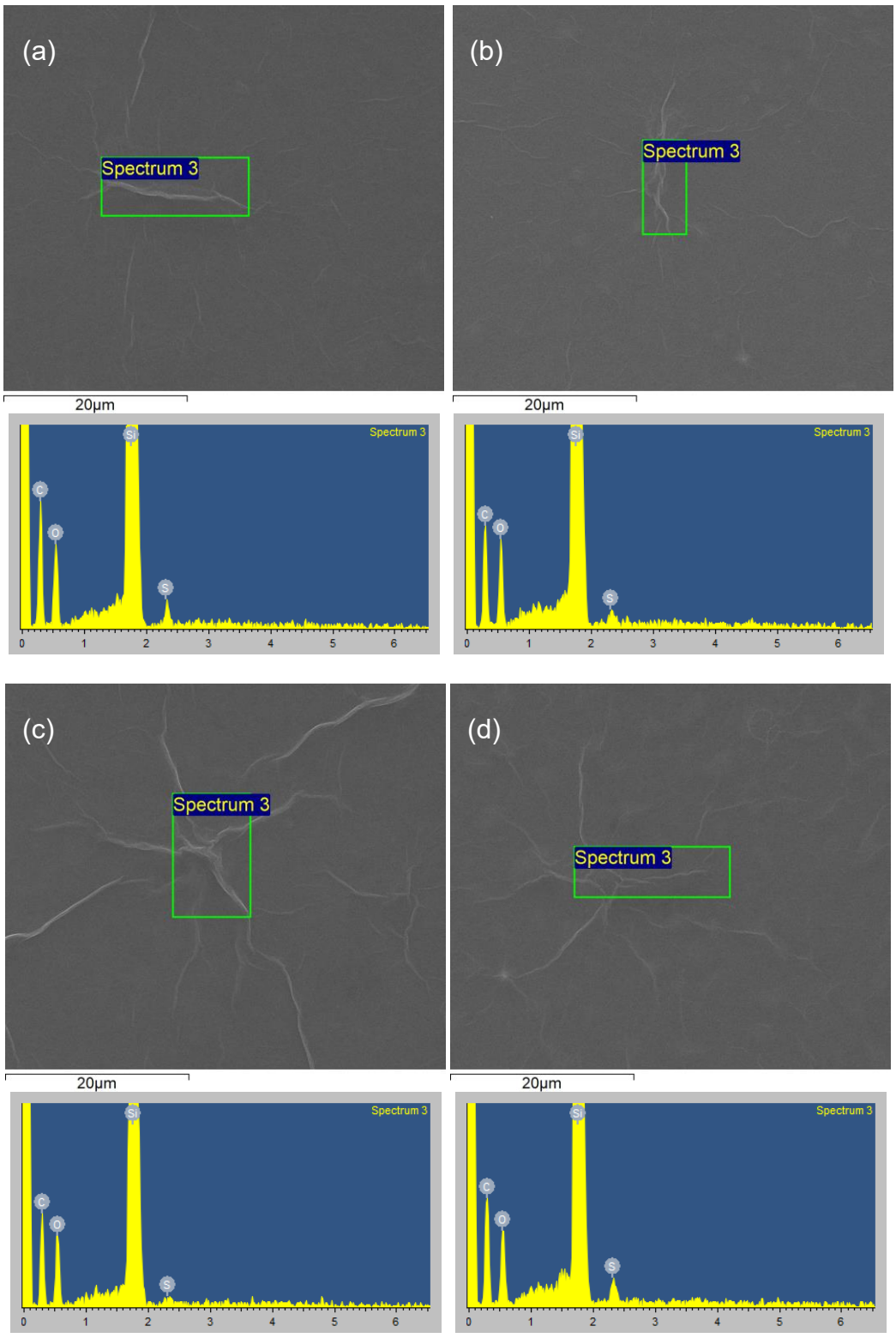


Fig. 4-16 Selected areas for EDS in SEM images, with the corresponding EDS images of (a) Ar-GO (b) $H_2$-GO (c) $N_2$Ar-GO and (d) $N_2H_2$-GO.

Table 4-5 Element content of ASP treated GO samples using different gases

| | C | O | Si | S |
|---|---|---|---|---|
| **Untreated GO** | 41.15 | 17.13 | 41.26 | 0.46 |
| **Ar-GO** | 39.91 | 13.36 | 46.17 | 0.56 |
| **$H_2$-GO** | 37.03 | 11.79 | 50.89 | 0.3 |
| **$N_2$Ar-GO** | 39.36 | 14.33 | 46.08 | 0.22 |
| **$N_2H_2$-GO** | 39.97 | 10.78 | 48.69 | 0.56 |

2. Raman spectra

The Raman spectra of untreated GO and other GO samples treated by ASP treatment using different gases are shown in Fig. 4-17. The dominant D peak and G peak still feature in all the Raman spectra, and the corresponding parameters are displayed in Table 4-6.

According to the parameters, all the Raman spectra of the ASP treated GO except $N_2H_2$-GO are similar, as the $I_D/I_G$ in the range of 0.836 to 0.875, the positions of G peak in the range of 1593 $cm^{-1}$ to 1598 $cm^{-1}$, and FWHM(G) in the range of 96 $cm^{-1}$ to 98 $cm^{-1}$. This means that the graphitic structures of Ar-GO. $H_2$-GO and $N_2$Ar-GO are similar, as GO are likely to get reduced, but more disorders are formed as well due to the possible ion bombardment in ASP plasma, based on the increase of their FWHM(G).

However, the FWHM(G) of $N_2H_2$-GO is 91 $cm^{-1}$, which is close to that of untreated GO. This smaller FWHM(G) than its three counterparts is possibly caused by the nitrogen doping [392]. As to $N_2$Ar-GO, the effect of nitrogen is not the same as that of $N_2H_2$-GO, and the difference are discussed in Section 4.6.

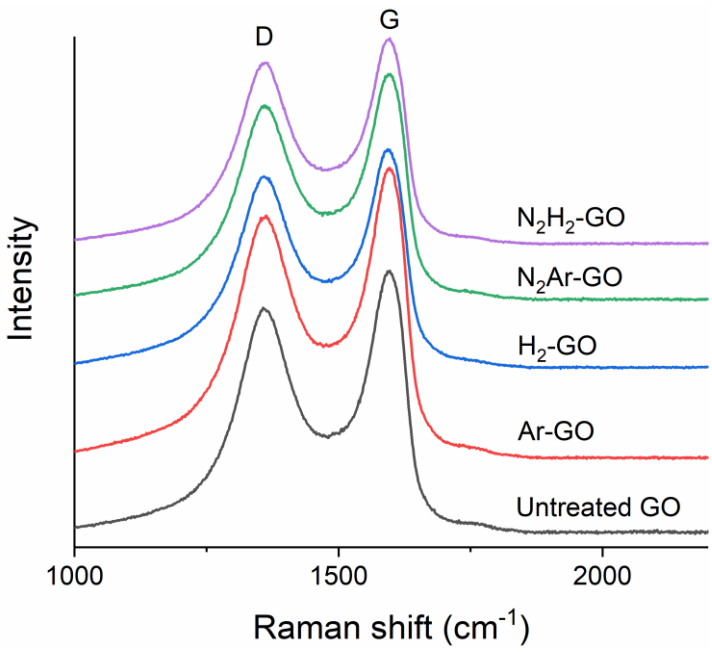


Fig. 4-17 Raman spectra of untreated and ASP treated GO using different gases.

Table 4-6 Raman spectra details GO samples before and after ASP treatment using different gases

| | D peak | | G peak | | $I_D/I_G$ |
|---|---|---|---|---|---|
| | Wavelength/$cm^{-1}$ | FWHM/$cm^{-1}$ | Wavelength/$cm^{-1}$ | FWHM/$cm^{-1}$ | |
| **Untreated GO** | 1357 | 139 | 1597 | 92 | 0.858 |
| **Ar-GO** | 1363 | 152 | 1595 | 98 | 0.836 |
| **$H_2$-GO** | 1359 | 146 | 1593 | 98 | 0.875 |
| **$N_2$Ar-GO** | 1360 | 146 | 1598 | 96 | 0.859 |
| **$N_2H_2$-GO** | 1364 | 133 | 1597 | 91 | 0.881 |

## 4.4.2 Electrical and electrochemical properties

1. Sheet resistance measurement

Fig. 4-18 shows the sheet resistances of untreated GO and ASP treated GO using different gases. It can be observed that the sheet resistances of all ASP treated GO samples, except $N_2$Ar-GO, decreased in comparison to untreated GO, which should be due to the contribution from the removal of oxygen functional groups.

As a comparison, both sheet resistances of Ar-GO and $N_2H_2$-GO are lower than that of $H_2$-GO. Since it has been deduced in Section 4.2.2 that the superiority of the ASP treated GO partly results from the sputtering of transition metal nanoparticles, the lower sheet resistance of Ar-GO than that of $H_2$-GO is likely due to higher sputtering, as argon is heavier than hydrogen so that more metallic nanoparticles are deposited on GO, contributing to lower sheet resistance [399]. In regard to $N_2H_2$-GO, the addition of $N_2$ to $H_2$ would induce nitrogen doping in GO, resulting in a better electrical property [404], and the best effect of ASP treatment on $N_2H_2$-GO is discussed in particular in Section 4.6.1.

However, $N_2$Ar-GO exhibits a poor electrical property, as its sheet resistance is even higher than that of untreated GO. This negative effect of ASP treatment using gas mixture of nitrogen and argon is discussed in Section 4.6.2.

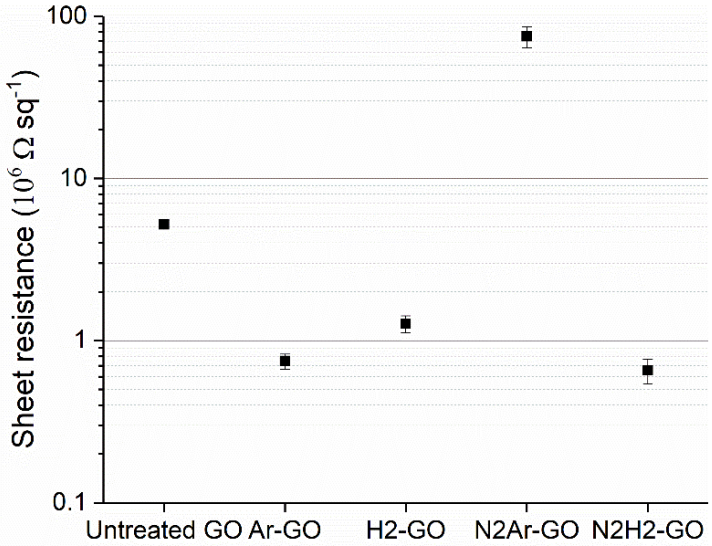


Fig. 4-18 Sheet resistance of untreated and ASP treated GO using different gases.

2. Electrochemistry tests

(1). CV test

The electrochemical performances of ASP treated GO samples using different gases were evaluated in CV test at different scan rates. Due to the similarity of CV curves, the results are shown in Appendix (Fig. A-1). All the CV curves at low scan rates show the quasi-rectangular shapes which indicate their capacitive behaviour [152]. Meanwhile, a broadening of the capacitive current can be found near 0.8 V of all these ASP treated GO, implying that it comes from the ASP treatments, regardless of the working gas used in the plasma treatment. As discussed in Section 4.2.2, it could be ascribed to the incorporation of transition metal oxides during the ASP treatment.

Fig. 4-19(a) compares the CV curves of these samples at a scan rate of 100 mV $s^{-1}$. The area of the CV curve indicates the capacitance, and all these CV curves of four ASP treated GO have a larger area than that of untreated GO, with $N_2H_2$-GO the largest whilst $N_2$Ar-GO the smallest.

Fig. 4-19(b) displays the capacitance of these GO samples calculated at different scan rates. The capacitances decrease with the increasing scan rates for all the samples tested. The capacitance of $N_2H_2$-GO is the highest among all, which reaches around 1148 μF at a scan rate of 5 mV $s^{-1}$, nearly 4.4 times that of untreated GO. Moreover, the sequence of the capacitances of ASP treated GO accords with that of sheet resistances, as the GO with lower sheet

resistance possesses higher capacitance. This agrees with the idea that better electrical property of electrode material is beneficial to the super-capacitive performance. However, it is also noticeable that the capacitance of $N_2$Ar-GO is also higher than that of the untreated GO, despite the higher sheet resistance. This means that the improvement of super-capacitive performance is not related to the electrical property only. This agrees with the idea that pseudo-capacitance was involved, as the nitrogen doping and the deposition of transitional metal nanoparticles still occur on $N_2$Ar-GO.

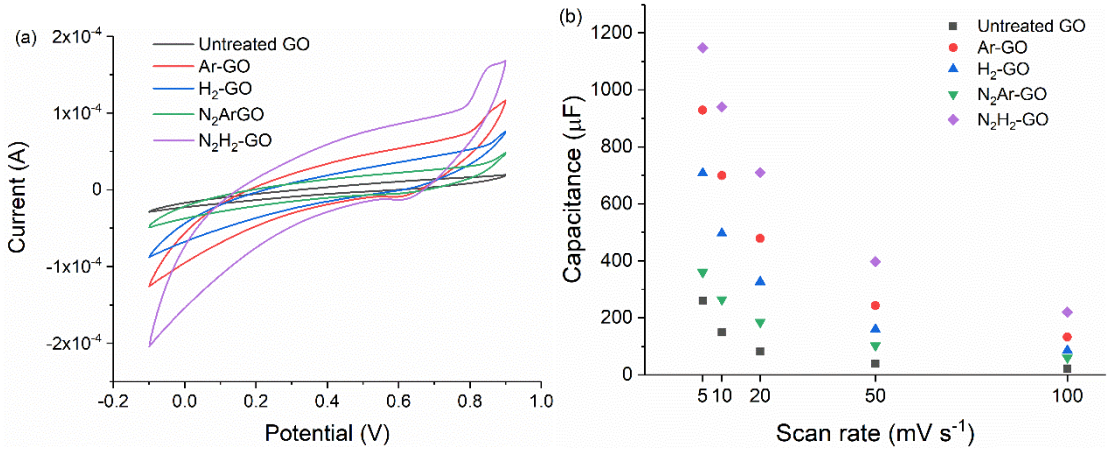


Fig. 4-19 (a) Comparison of CV curves of ASP treated GO using different gases at 100 mV $s^{-1}$, and (b) capacitances at different scan rates.

(2). EIS test

Fig. 4-20 shows the Nyquist plots of the EIS result, and Table 4-7 exhibits some of the parameters of the equivalent circuit fit of the EIS results. For these four ASP treated GO, the $R_{ct}$ are all smaller than that of untreated GO and follow the same trend as the capacitance calculated in CV curves, as the smallest $R_{ct}$ belongs to $N_2H_2$-GO to around 2.55 kΩ. However, this is not the same as ESR,

which may be due to the various resistances involved in, and the electrode resistance cannot be concluded from this ERS results.

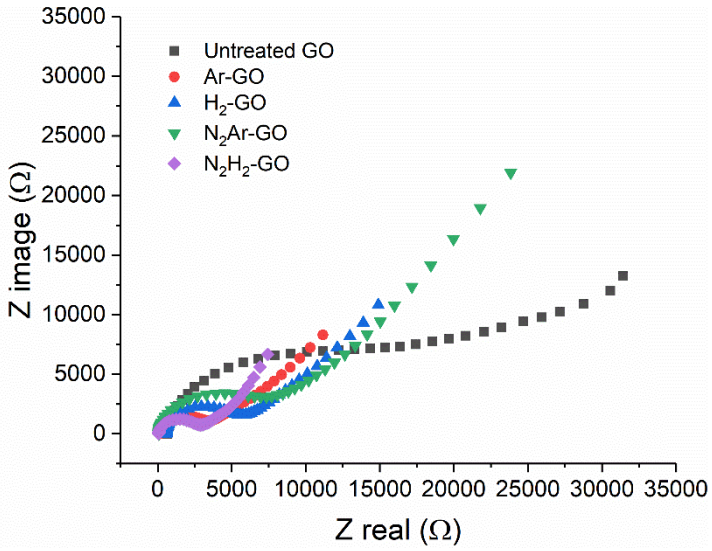


Fig. 4-20 Nyquist plots of untreated GO and ASP treated GO using different gases.

Table 4-7 Parameters of the equivalent circuit fit of the EIS results

| | ESR (kΩ) | $R_{ct}$ (kΩ) | $Y_o$ ($S \cdot s^{\alpha}$) | α | $W_d$ ($S \cdot s^{1/2}$) | Goodness |
|---|---|---|---|---|---|---|
| **Untreated GO** | 0.64 | 15.82 | $5.60\times10^{-4}$ | 0.89 | $1.26\times10^{-4}$ | $2.70\times10^{-3}$ |
| **Ar-GO** | 0.16 | 3.02 | $4.50\times10^{-4}$ | 0.95 | $3.42\times10^{-4}$ | $0.17\times10^{-3}$ |
| **$H_2$-GO** | 0.56 | 4.50 | $3.57\times10^{-4}$ | 0.97 | $2.77\times10^{-4}$ | $0.13\times10^{-3}$ |
| **$N_2$Ar-GO** | 0.07 | 6.27 | $4.04\times10^{-4}$ | 0.96 | $1.50\times10^{-4}$ | $0.44\times10^{-3}$ |
| **$N_2H_2$-GO** | 0.06 | 2.55 | $4.25\times10^{-4}$ | 0.95 | $5.13\times10^{-4}$ | $0.76\times10^{-3}$ |

(3). GCD test

GCD results are shown in Fig. 4-21. Still, the charge and discharge lines are nearly symmetrical for all the GO samples, but the charge/discharge plots are not exactly isosceles triangles, indicating the feasibility for SC applications with some pseudo-capacitive characteristic in all these GO electrodes. The sequence of charge/discharge time length of all the GO samples follows the same sequence of capacitance, and all the IR drop of ASP treated GO decrease,

with one of $N_2H_2$-GO the smallest. Still, these ASP treated GO samples exhibit good cyclic performances.

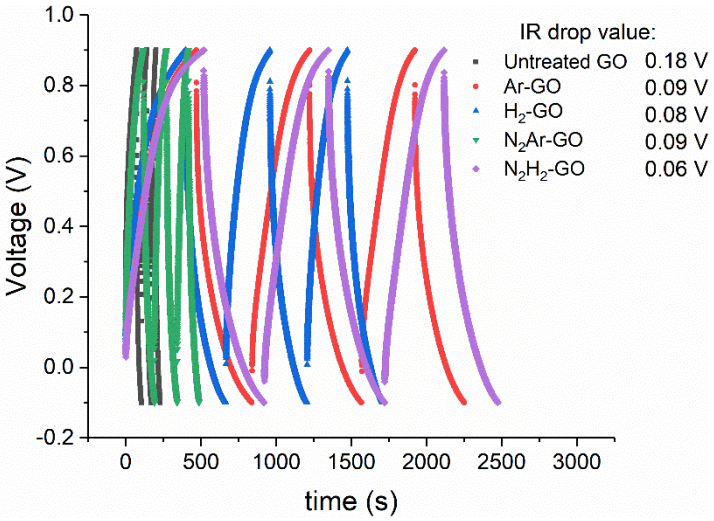


Fig. 4-21 GCD plots of untreated GO and ASP treated GO using different gases.

Based on these property tests, it is found that GO ASP treated using gas mixture of nitrogen and hydrogen, the one with the lowest sheet resistance, is the most promising one for SC applications, possibly due to nitrogen doping. On the other hand, ASP treatment using gas mixture of nitrogen and argon has a negative effect on the electrical property of GO, but still contribute to the electrochemical property, possibly due to the nitrogen doping.

## 4.5 Results of $N_2/H_2$ Ratio Effect on ASP Treatment

Section 4.4 shows that the ASP treatment on GO using gas mixture of nitrogen and hydrogen results in the best super-capacitive performances. Therefore, this section explores how the ratio of nitrogen and hydrogen affects the performances. The gas mixtures of nitrogen and hydrogen are in ratio of 1:3,

1:1 and 3:1, and the corresponding ASP treated GO samples are designated NH13, NH11, NH31. The other conditions were all the same, with a total gas pressure of 0.75 mbar, and a temperature of 100 ℃, for a duration of 1 h.

### 4.5.1 Micro-structure

1. XPS survey spectra and element contents

Fig. 4-22 shows the XPS survey spectra of untreated and ASP treated GO using gas mixture of nitrogen and hydrogen in different ratios, and the atomic percentage of each detected element, as well as content ratio of nitrogen to carbon, is listed in Table 4-8. The basic elements of carbon and oxygen, as well as nitrogen and sulphur are detected in all the GO samples, and it is evident that iron and chromium are detected in all the ASP treated GO samples, which are two of the main element compositions of stainless steel, confirming that the transition metal nanoparticles are sputtered and deposited on GO in ASP treatments.

As to the oxygen content of ASP treated GO, it can be noticed that for NH13, the oxygen content is higher than that of untreated GO, which is opposite to the expected GO reduction process. This increase of oxygen content comes from the compensation of metal oxides that deposit on the GO samples. Noting in advance that transition metals sputtered are in the form of oxides. The decreased oxygen for NH11 is attributed to the GO reduction, and the oxygen compensation from metal oxide cannot cover the decrease from GO reduction,

due to a lower content of transition metal. However, the oxygen content increases in NH31, which is probably caused by the contamination, since the content of sulphur in NH31 is unexpectedly higher than those of the other GO samples.

Regarding the nitrogen content, due to the large difference of carbon content among all the GO samples, the ratio of nitrogen to carbon (N/C) is calculated and listed for comparison. The increased N/C indicate that GO get nitrogen doped, and the highest ratio belongs to NH31, whilst the lowest to NH11. This means that the nitrogen doping efficiency is related to the ratio of nitrogen to hydrogen of the working gas.

Finally, the contents of iron and chromium are compared, and it is evident that the metal content is the highest in NH13, second in NH11, and the lowest in NH31. This can be deduced that the sputtering yield is related to the gas used in plasma treatment, and in this case of gas mixture of nitrogen and hydrogen, the sputtering yield is inversely proportional to the nitrogen concentration in the gas mixture.

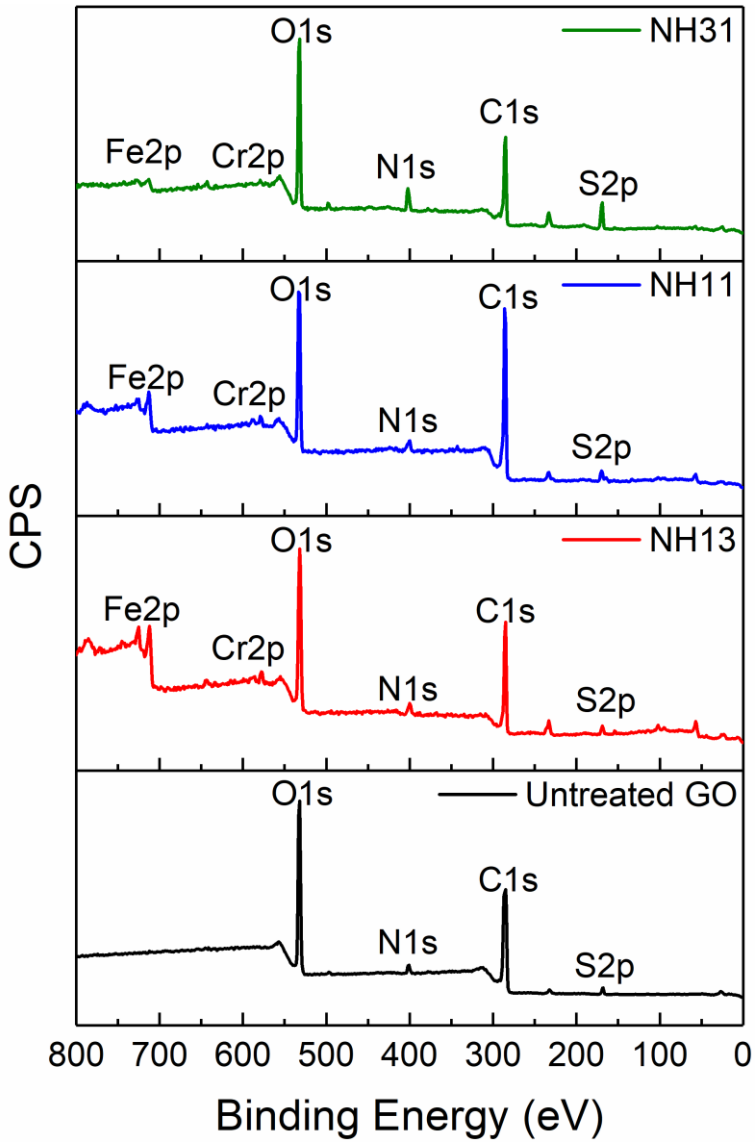


Fig. 4-22 XPS spectra surveys of untreated GO, NH13, NH11 and NH31.

Table 4-8 Atomic percentage of elements detected in untreated GO, NH13, NH11 and NH31.

| | Untreated GO | NH13 | NH11 | NH31 |
|---|---|---|---|---|
| **C1s** | 65.1 | 49.98 | 64.8 | 46.04 |
| **O1s** | 30.7 | 34.38 | 25.36 | 36.26 |
| **N1s** | 2.6 | 4.44 | 2.84 | 8.49 |
| **S2p** | 1.6 | 2.67 | 2.99 | 7.52 |
| **Fe2p** | / | 7.39 | 3.42 | 1.41 |
| **Cr2p** | / | 1.14 | 0.59 | 0.28 |
| **N/C** | 0.04 | 0.09 | 0.04 | 0.18 |

2. C1s spectra

Fig. 4-23(a) compares the high-resolution C1s XPS spectra of all the GO samples. It is shown that one of the dominant peaks in the untreated GO at 286.8 eV (Fig. 4-8(a)), which is assigned to C-O, is suppressed in the three ASP treated GO samples. This confirms that GO is reduced in ASP treatments, regardless of the gas ratio.

For further comparing the three ASP treated GO, the C1s XPS spectra are decomposed into three peaks: Peak A, Peak B, and Peak C, and the details are also listed in Fig. 4-23(b-d). Peak A is attributed to C-C; Peak B represents both C-O and C-N, based on the non-negligible presence of both oxygen and nitrogen elements in GO [405, 406]; and Peak C is assigned to C=O. Given a much lower content of nitrogen than that of oxygen, the percentage of Peak B can be an implication of C-O content and a lower percentage of Peak B then indicates a better reduction effect. Here, NH13 has the lowest content of Peak B, suggesting the best reduction effect of NH13.

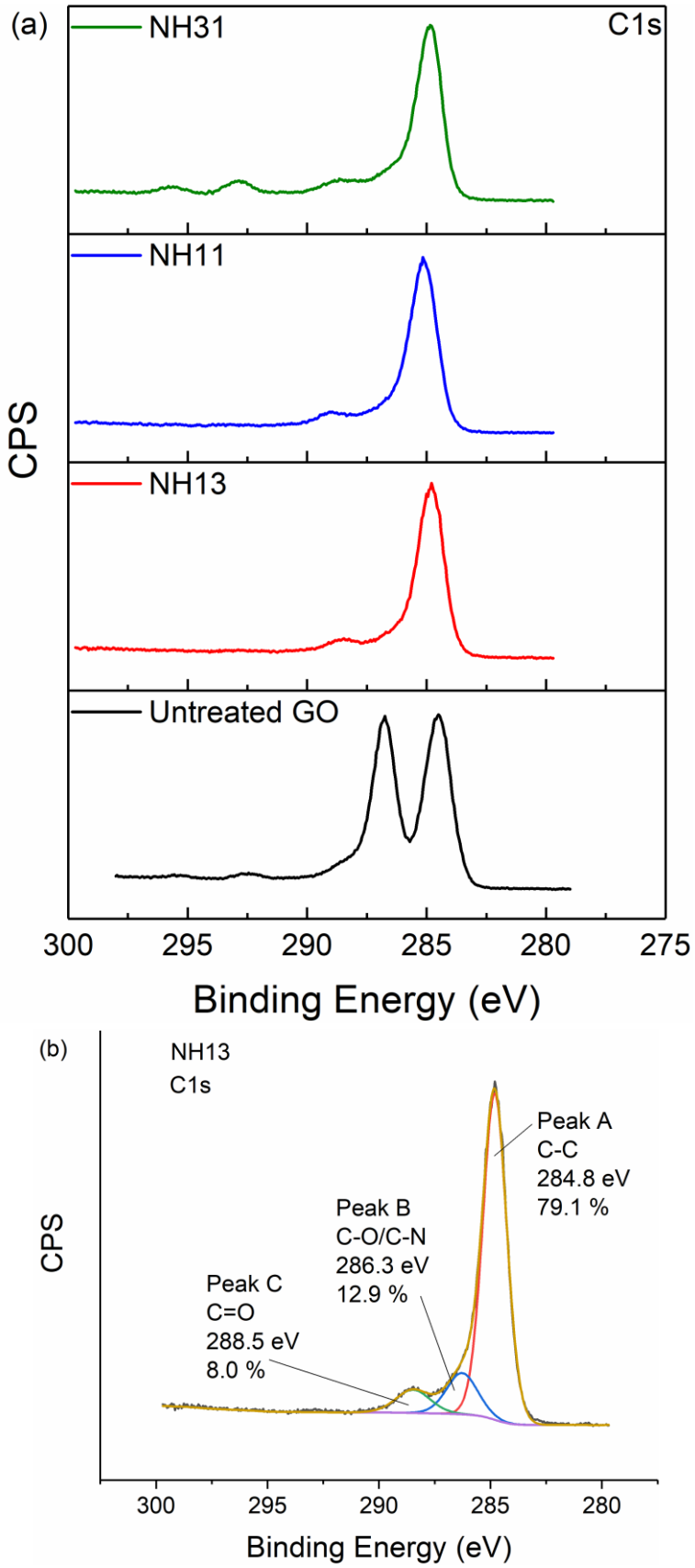
(a)
NH31
C1s
NH11
NH13
Untreated GO
CPS
300
295
290
285
280
275
Binding Energy (eV)
(b)
NH13
C1s
Peak A
C-C
284.8 eV
79.1 %
Peak B
C-O/C-N
286.3 eV
12.9 %
Peak C
C=O
288.5 eV
8.0 %
CPS
300
295
290
285
280
Binding Energy (eV)

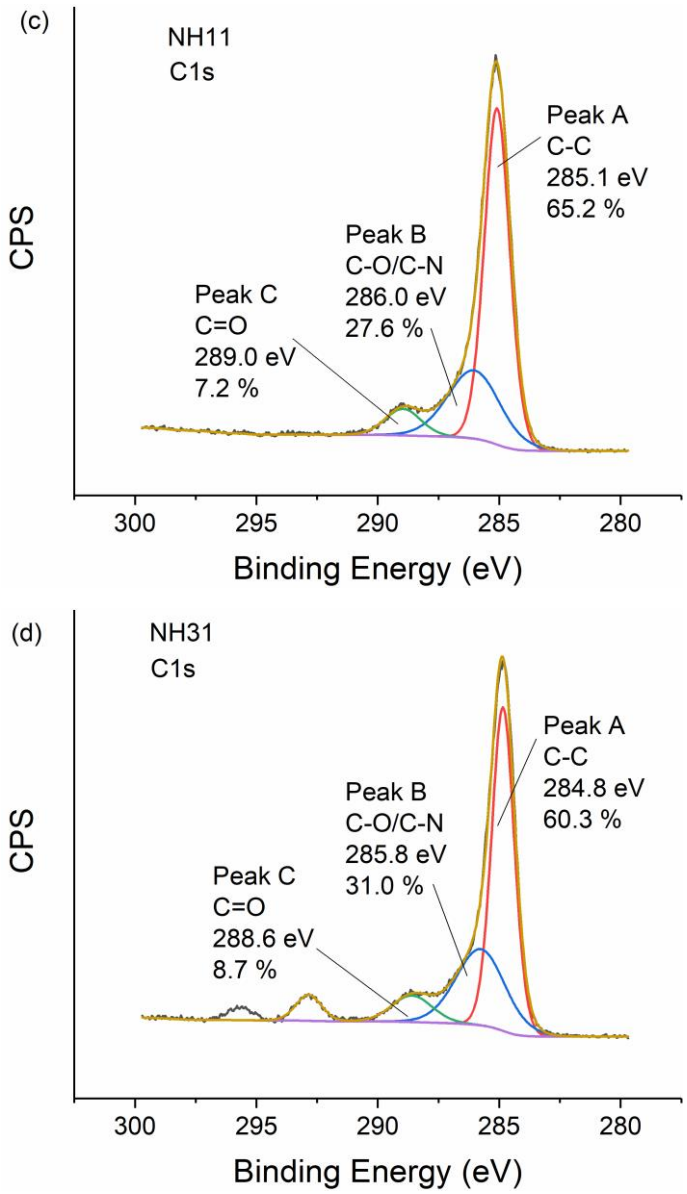


Fig. 4-23 (a) Comparison of high-resolution C1s XPS spectra of GO samples and the deconvoluted spectra of (b) NH13 (c) NH11, and (d) NH31.

3. N1s spectra

High-resolution XPS spectra of N1s are compared as well, as shown in Fig. 4-24(a). It is found that the dominant peak shifts to lower binding energy with an increased proportion of hydrogen in the gas mixture, which means the gas ratio of nitrogen and hydrogen has an influence on the nitrogen doping configuration in GO, and the configuration with lower binding energy is

preferred to form in gas mixture with higher proportion of hydrogen. The N1s spectra can be deconvoluted into two peaks: Peak D and Peak E, as shown in Fig. 4-24(b-d). Peak D represents Pyrrolic N for NH11 and NH31, and the integration of Pyridinic N and Pyrrolic N for NH13 due to a lower binding energy, while Peak E stands for Graphitic N [8].

As compared, NH31 is dominant in Graphitic N, accounting for about two thirds of the total nitrogen, and the left one third is Pyrrolic N. With an increasing proportion of hydrogen in the gas mixture, the content of Pyrrolic N increases and become the dominant configuration, accounting for over four fifths of the total nitrogen dopants. When the proportion of hydrogen increases to 75 % in gas mixture, the configuration of the lowest binding energy: Pyridinic N, starts to form, and the content of Graphitic N is less than 5 %.

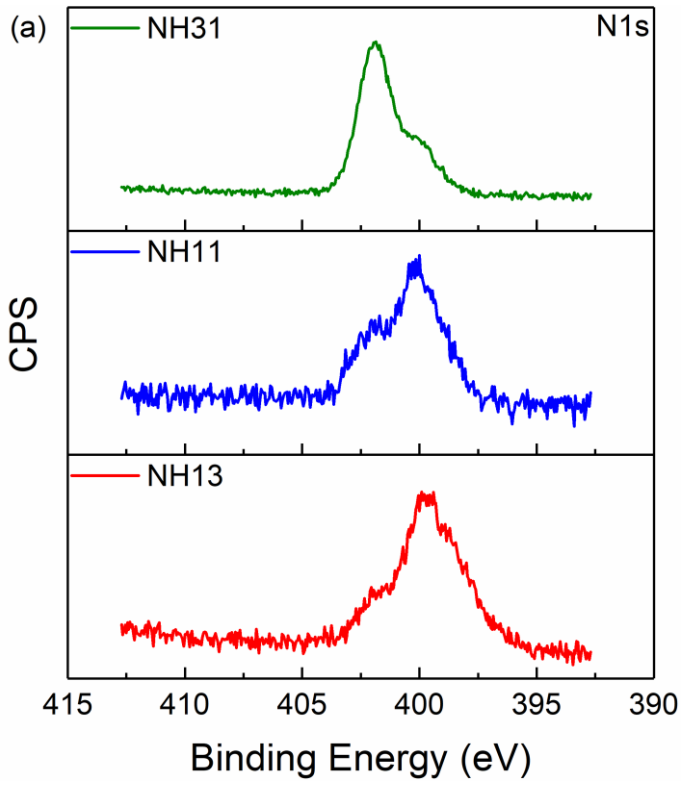

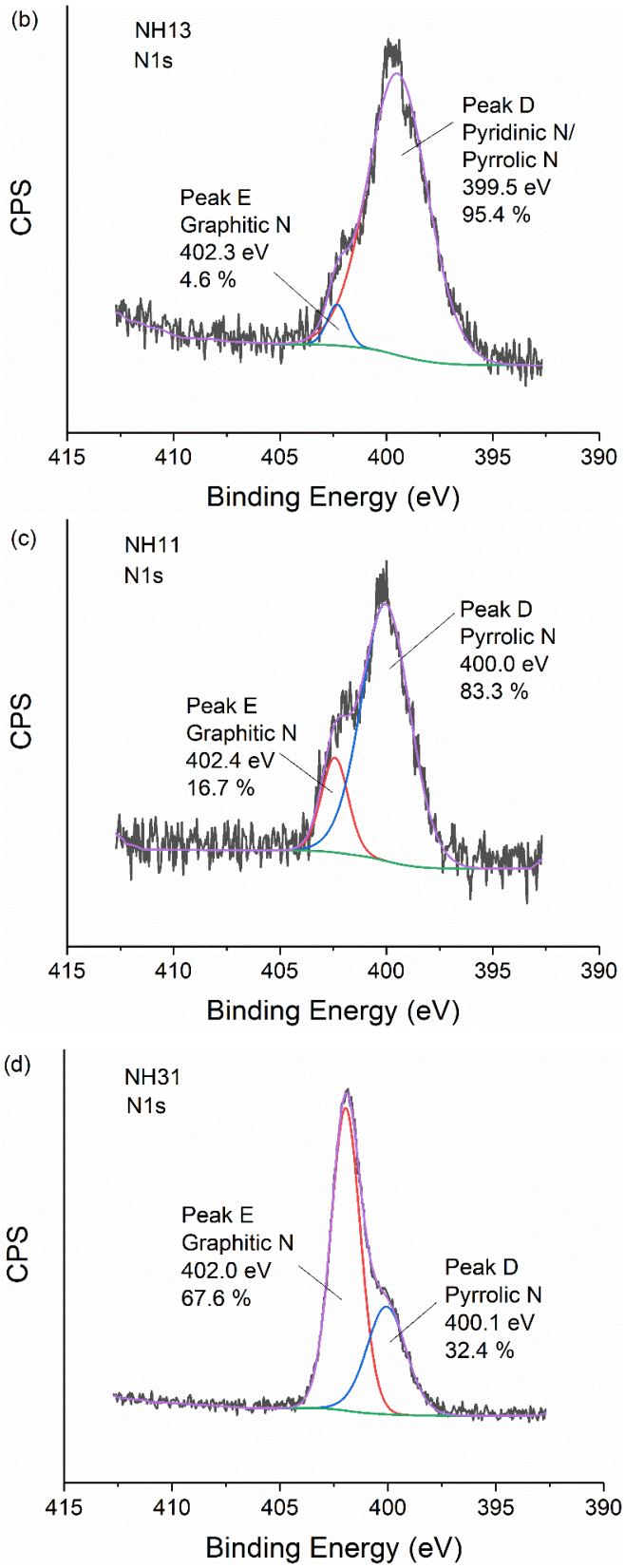


Fig. 4-24 (a) Comparison of high-resolution N1s XPS spectra of GO samples and the deconvoluted spectra of (b) NH13 (c) NH11, and (d) NH31.

4. O1s spectra

Likewise, high-resolution O1s XPS spectra of GO samples before and after ASP treatment using gas mixture of nitrogen and hydrogen with different ratios are compared, as shown in Fig. 4-25(a). For NH13, there appears an extra peak at around 530 eV, which is not observed in NH31.

These spectra are then decomposed into two peaks: Peak F and Peak G, as shown in Fig. 4-25(b-d). Peak F represents metal oxides, which comes from the transition metal sputtered from active screen [407, 408], and Peak G is assigned to the organic C (containing both C-O and C=O) from GO [111, 409]. Peak F takes 22.0 % in NH31, decreases to only 3.7 % in NH11, and even disappears in NH31, which means that the content of metal oxides decreases with the decreasing proportion of hydrogen in the gas mixture, which agrees with the content of the metals (iron and chromium) detected in ASP treated GO: the highest metal content in NH13, but lowest in NH31.

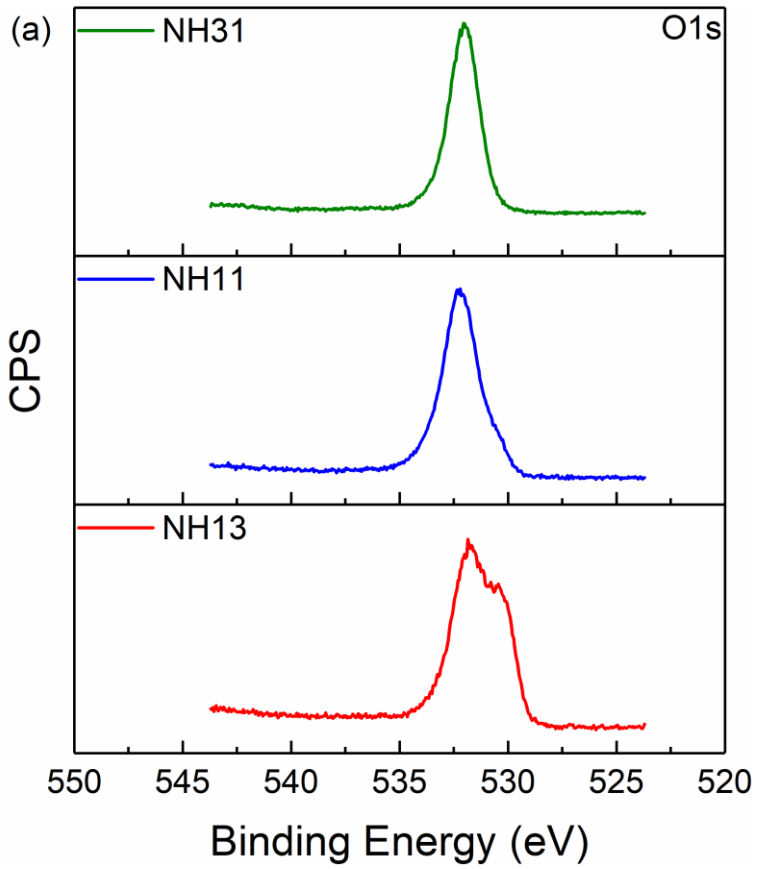
(a)
NH31
O1s
NH11
NH13
CPS
550
545
540
535
530
525
520
Binding Energy (eV)

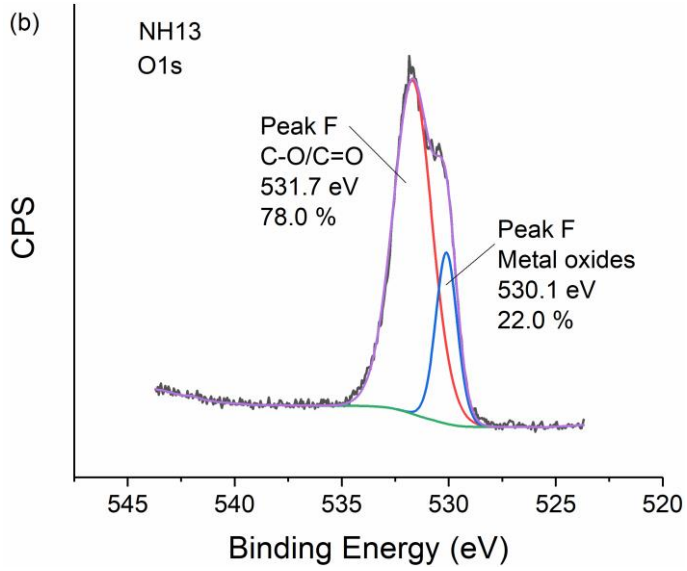
(b)
NH13
O1s
Peak F
C-O/C=O
531.7 eV
78.0 %
Peak F
Metal oxides
530.1 eV
22.0 %
CPS
545
540
535
530
525
520
Binding Energy (eV)

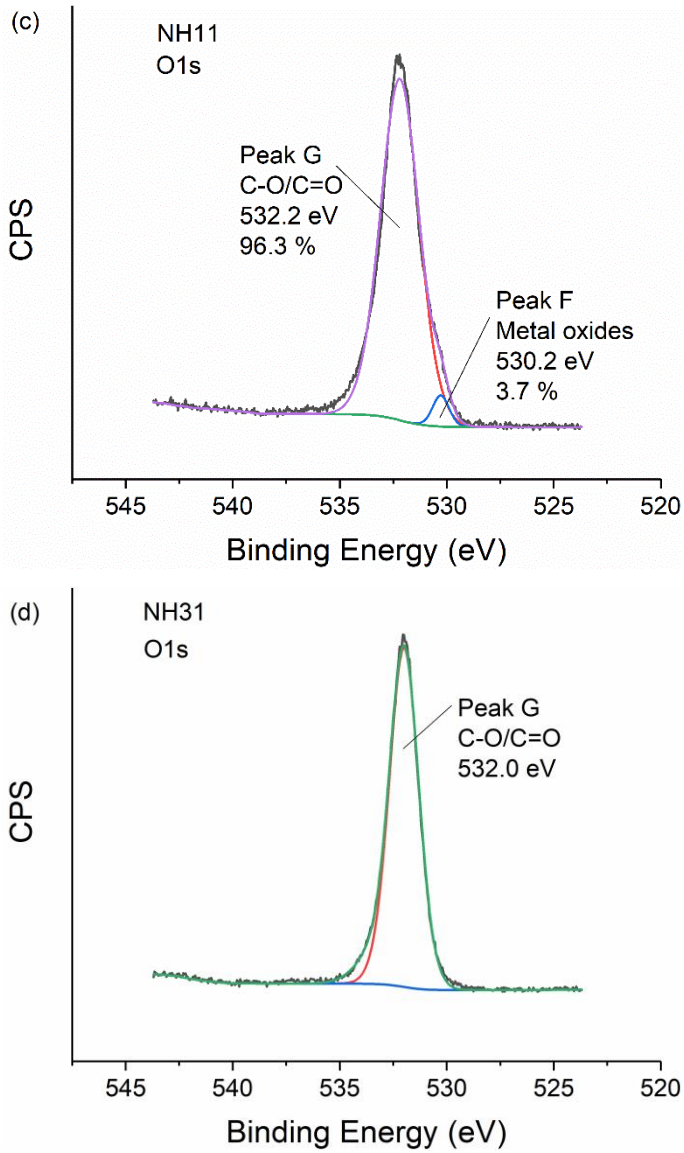


Fig. 4-25 (a) Comparison of high-resolution O1s XPS spectra of GO samples and the deconvoluted spectra of (b) NH13 (c) NH11, and (d) NH31.

5. Fe2p and Cr2p spectra

Fig. 4-26(a-b) show the high-resolution Fe2p and Cr2p XPS spectra of ASP treated GO samples. As compared, the spectra are similar, indicating that the compositions of iron and chromium are similar in the ASP treatments. The XPS spectra of Fe2p and Cr2p are not deconvoluted, but the dominant peaks are covered with light yellow in Fig. 4-26. It is still evident to observe that the

dominant peaks in Fe2p scans are at around 712 eV for $Fe2p_{3/2}$ and 725 eV for $Fe2p_{1/2}$, and the ones in Cr2p scans are at around 577 eV for $Cr2p_{3/2}$ and 587 eV for $Cr2p_{3/2}$. It suggests that these two transition metals are both in oxidised states ($Fe^{2+}$, $Fe^{3+}$, and $Cr^{3+}$) [410, 411], which is according with Peak F in XPS spectra of O1s (Fig. 4-25).

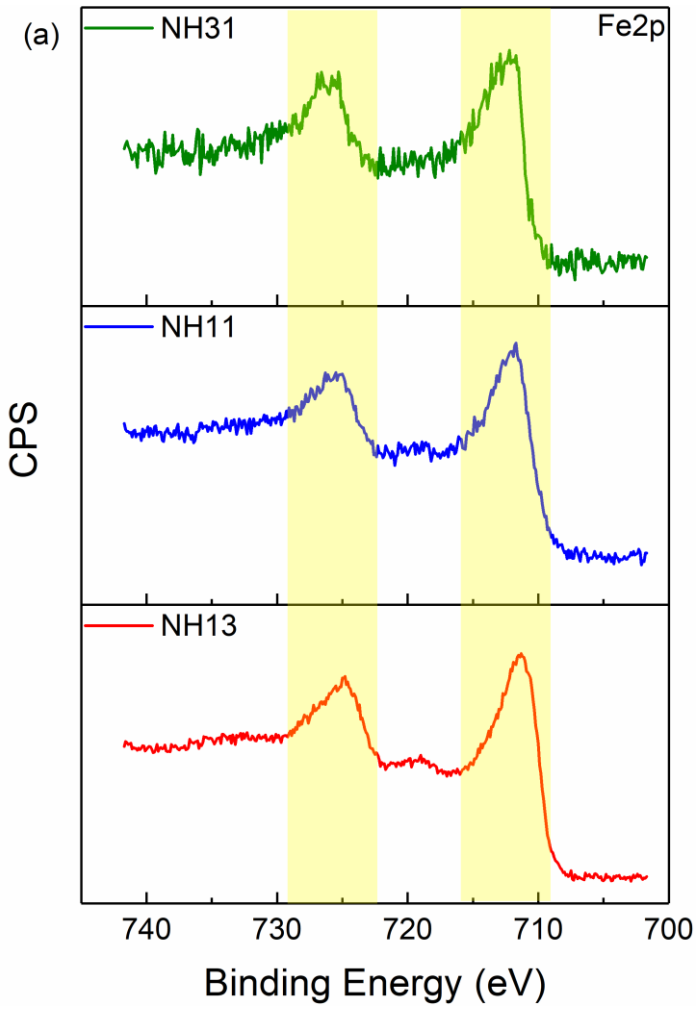

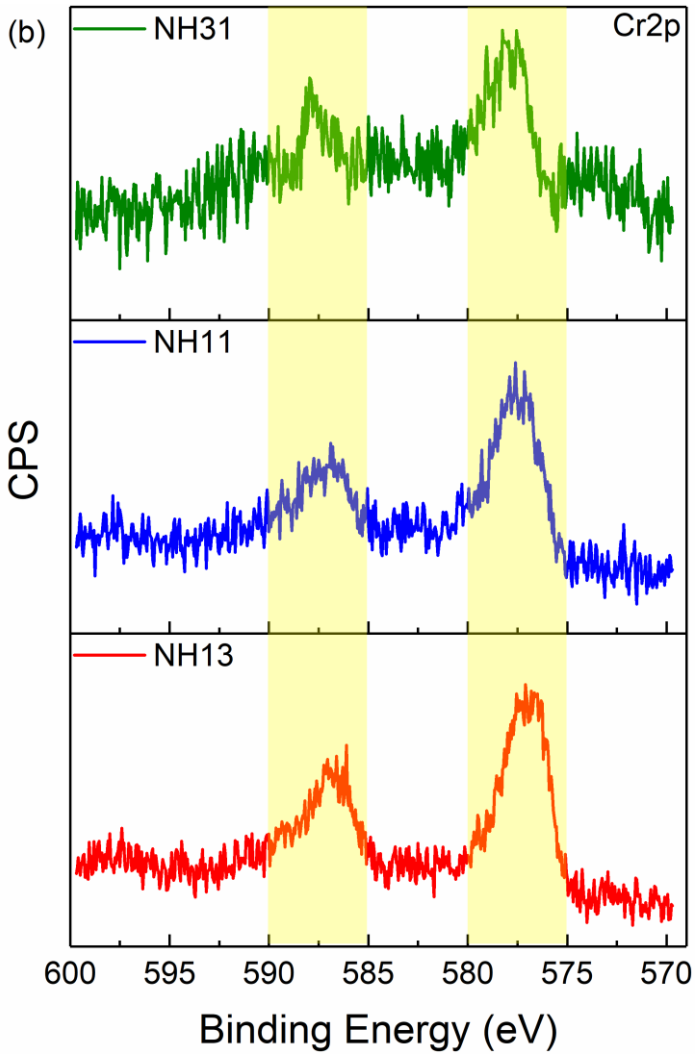


Fig. 4-26 Comparison of high-resolution (a) Fe2p and (b) Cr2p XPS spectra of ASP treated GO samples.

From the XPS results interpreted above, it can be deduced that GO is both reduced and nitrogen doped in ASP treatments using gas mixture of nitrogen and hydrogen, with the best reduction effect being achieved by NH13. With an increasing proportion of hydrogen in gas mixture, the configurations of nitrogen with lower binding energies are more likely to form, and the content of metals deposited on GO also increases. Moreover, the metals (iron and chromium) are mainly in oxidised states.

## 4.5.2 Electrical and electrochemical properties

1. Sheet resistance measurement

Fig. 4-27 shows the sheet resistances of untreated GO, and ASP treated GO using gas mixture of nitrogen and hydrogen in different ratios. It can be seen that the sheet resistances of all ASP treated GO samples are lower than $1\times10^6$ $\Omega$ $sq^{-1}$, an order of magnitude smaller than that of untreated GO, indicating that all the ASP treatments using gas mixture of nitrogen and hydrogen can have an obvious effect on decreasing sheet resistance, regardless of the gas ratio. However, it is also found that among all these three ASP treated GO, NH13 had the lowest sheet resistance, while NH31 the highest. According to the XPS results investigated in Section 4.5.1(Fig. 4-22 to Fig. 4-26), the lower sheet resistance is likely be ascribed to the better reduction effect and the higher content of transition metal oxides.

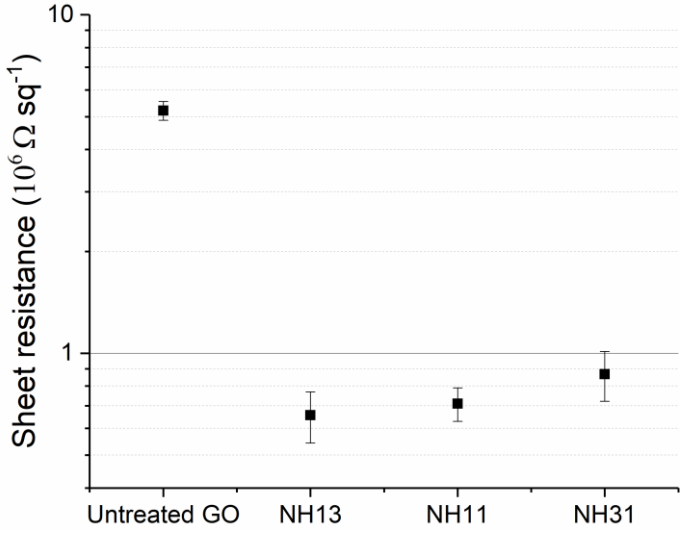


Fig. 4-27 Sheet resistances of untreated and ASP treated GO using gas mixture of nitrogen and hydrogen in different ratios.

2. Electrochemistry tests

(1). CV test

The electrochemical performances of ASP treated GO samples using gas mixture of nitrogen and hydrogen in different ratios are evaluated in CV test at different scan rates, and still, the results are shown in Appendix (Fig. A-2). For all the CV curves of ASP treated GO using gas mixture of nitrogen and hydrogen, the broadening of the capacitive currents is found near 0.8 V, as well as a small hump at around 0.6 V in the negative current section for NH13 and NH11. As discussed in Section 4.2.2, it could be ascribed to the incorporation of transition metal oxides during the ASP treatment.

As compared in Fig. 4-28(a), the broadening of current and hump are more significant in NH13 and NH11, implying that their amount of transition metal oxides is higher than that of NH31, which is consistent of the element content comparison from XPS results in Table 4-8. Also, all these areas of CV curves of three ASP treated GO are larger than that of untreated GO, with NH13 the largest whilst NH31 the smallest. This sequence is the same as the electrical property.

Fig. 4-28(b) displays the capacitances of these GO samples calculated at these scan rates. All the capacitances decrease with the increasing scan rates for all the samples tested, and the capacitances of ASP treated samples using gas mixtures of nitrogen and hydrogen are all much higher than that of untreated

GO.

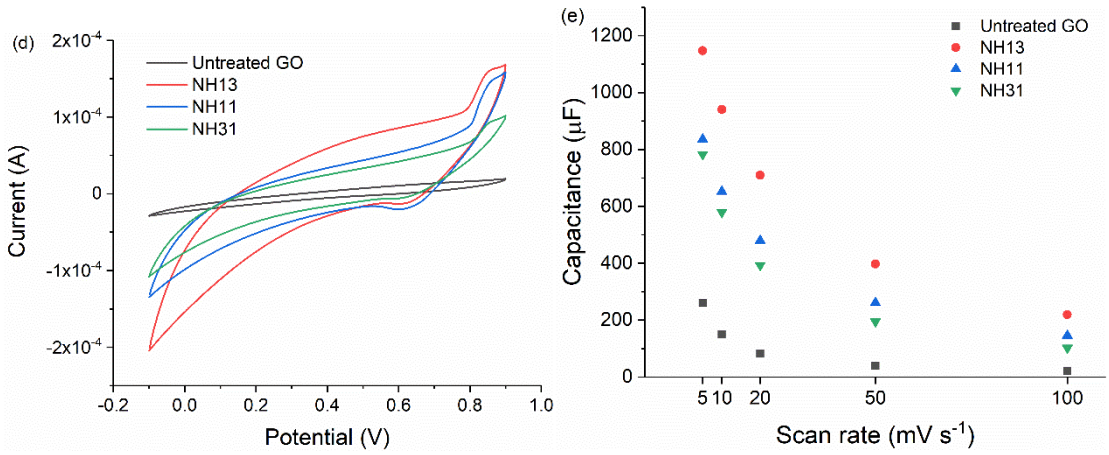


Fig. 4-28 (a) Comparison of CV curves of untreated GO, NH13, NH11 and NH31 at 100 mV $s^{-1}$, and (b) capacitances at different scan rates.

(2). EIS test

EIS test was also conducted to further investigate the electrochemical performance of these GO samples, and Fig. 4-29 shows the Nyquist plots of the EIS results for all the samples. Table 4-9 exhibits some of the parameters of the equivalent circuit fit of the EIS results.

All the ASP treated GO had a much smaller $R_{ct}$ than that of untreated GO, and follow the exact same trend as the capacitance calculated in CV curves, as the smallest $R_{ct}$ belong to NH13. Even for the largest one of NH31, the $R_{ct}$ is only 4.98 kΩ, less than a third of the untreated GO. Also, the ESRs of ASP treated GO using gas mixture of nitrogen and hydrogen are almost the same, all as low as 0.06 kΩ, only a tenth of that of untreated GO. This should be mainly attributed to the lower electrode resistance.

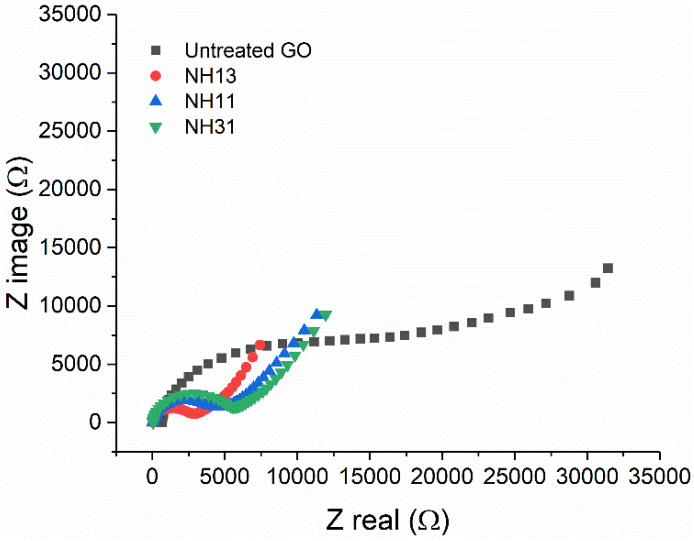


Fig. 4-29 Nyquist plots of untreated GO and ASP treated GO using gas mixture of nitrogen and hydrogen in different ratios.

Table 4-9 Parameters of the equivalent circuit fit of the EIS results

| | ESR (kΩ) | $R_{ct}$ (kΩ) | $Y_o$ ($S \cdot s^{\alpha}$) | α | $W_d$ ($S \cdot s^{1/2}$) | Goodness |
|---|---|---|---|---|---|---|
| **Untreated GO** | 0.64 | 15.82 | $5.60\times10^{-6}$ | 0.89 | $1.26\times10^{-4}$ | $2.70\times10^{-3}$ |
| **NH13** | 0.06 | 2.55 | $4.25\times10^{-6}$ | 0.95 | $5.13\times10^{-4}$ | $0.76\times10^{-3}$ |
| **NH11** | 0.06 | 3.99 | $4.43\times10^{-6}$ | 0.94 | $3.61\times10^{-4}$ | $0.55\times10^{-3}$ |
| **NH31** | 0.06 | 4.98 | $3.85\times10^{-6}$ | 0.96 | $3.76\times10^{-4}$ | $0.61\times10^{-3}$ |

(3). GCD test

GCD test was also conducted for further comparison, and the results are shown in Fig. 4-30. Still similar to those using different gases, these ASP treated GO samples using gas mixture of nitrogen and hydrogen in different gases got the similar charge and discharge lines that are nearly symmetrical, but the charge/discharge plot is not exactly an isosceles triangle, indicating the feasibility for SC application with some pseudo-capacitive characteristics in the electrode. The sequence of charge/discharge time length of all the GO samples follows the same sequence of capacitance and is reversely followed by IR drop. This result once again suggests that the ratio of nitrogen and hydrogen at 1:3

is the most promising one for SC applications. And they all exhibit good cyclic performance, especially NH13.

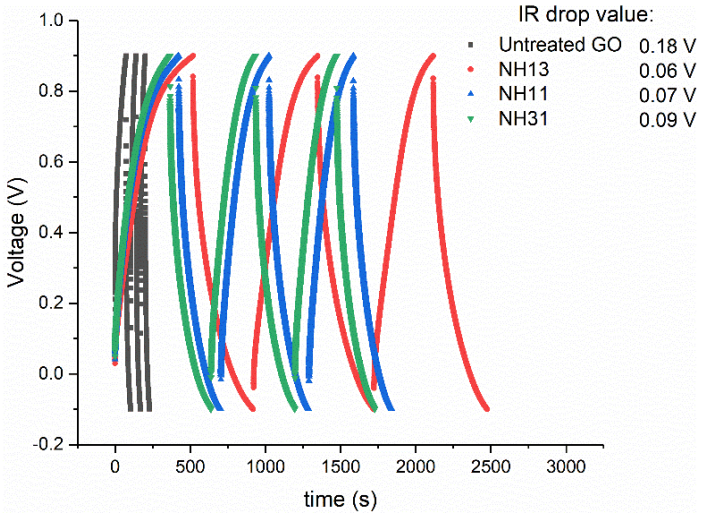


Fig. 4-30 GCD plots of untreated GO and ASP treated GO using gas mixture of nitrogen and hydrogen in different ratios.

Based on all the results above (from Section 4.2 to 4.5), it can be deduced that ASP can reduce GO, with transition metal nanoparticles sputtered from active screen and deposited on GO in the form of oxides. If working gas in ASP treatment is gas mixture of nitrogen and hydrogen, nitrogen doping of GO can also occur simultaneously, with a ratio of 1:3 the best in improving the electrical and electrochemical properties.

## 4.6 Mechanism of ASP Gas Effect

As has been reported in Section 4.4, the properties of ASP treated GO are highly gas composition dependent. For example, ASP treatment using the gas mixture of nitrogen and hydrogen is the most effective in improving both the electrical and electrochemical properties among all the four gas types examined,

while the ASP treatment with a gas mixture of nitrogen and argon revealed the smallest improvement in the electrochemical properties, and even worse electrical properties than untreated GO. Based on these results, it can be deduced that the effectiveness of nitrogen in modifying GO in ASP treatment varied when mixed with different gases.

### 4.6.1 Synergetic Effect of Nitrogen and Hydrogen

As introduced in Section 2.2.2.2, nitrogen doping, through commonly used covalent functionalisation of graphene materials, can modulate the electronic properties of graphene materials. Also, as described in Section 4.5.1, the increase of nitrogen to carbon atomic ratio indicates that GO was successfully doped with nitrogen by ASP treatment. This can therefore explain the improvement of electrochemical properties of GO after ASP treatment using a gas mixture of nitrogen and hydrogen.

Similar to the reduction mechanism discussed above, the mechanism of nitrogen doping in ASP treatment can be attributed to the interactions of active species containing nitrogen with GO. In nitrogen and hydrogen plasma, the active species include protons ($H^+$), nitrogen ions ($N_2^+$ and $N^+$), N-H ions ($NH^+$, $NH_2^+$, $NH_3^+$, $NH_4^+$), excited nitrogen (N*) and hydrogen atoms (H*), activated nitrogen ($N_2$*) and hydrogen molecules ($H_2$*), and radicals of ammonia ($NH_x$*) [412, 413]. Unlike in conventional DC plasma, in ASP, the effective nitrogen mass transfer at the surface of GO occurs in the remote plasma zone [360].

Among all these active species, nitrogen-containing ions collide with the active screen, while some of those activated neutral nitrogen radicals in the form of $N_2$*, N*, $NH_x$*, as well as $N_2$ and $NH_3$ [414] fall onto the GO surface from the active screen mesh, and diffuse into the structure of the graphitic basal plane, thus forming C-N bonding.

The addition of hydrogen in plasma not only plays a role in the reduction of GO, but can also facilitate nitrogen doping effects of ASP [415]. It is already well-established that mixing hydrogen with nitrogen can increase the density of reactive species of nitrogen in plasma. It is known that the dissociation and ionisation energies of hydrogen gas (8.8 eV and 13.1 eV, respectively) are lower than those of nitrogen gas (24.0 eV and 15.6 eV, respectively) [416]. Consequently, more hydrogen ions are generated at a given plasma power and gas pressure, thus increasing the possibility of collisions and the electron density. Accordingly, more nitrogen can then be ionised by the secondary electrons from the cathode [417, 418]. In addition, these hydrogen ions can interact with nitrogen to form ammonia radicals that can also function as nitrogen doping sources, hence enhancing the doping efficiency. Many studies have already confirmed the enhancement of nitrogen ionisation by hydrogen, thus creating more nitrogen ions and nitrogen-containing radicals [419]. Furthermore, the hydrogen plasma can play the role of reducing GO, leaving oxygen vacancies as reactive sites, into which nitrogen tends to incorporate [420].

Notwithstanding the fact that the addition of hydrogen can facilitate the ionisation of nitrogen and increases the density of reactive species of nitrogen, there exists an optimal ratio of nitrogen to hydrogen for the best performance, as too low a proportion of nitrogen means inadequate supply of nitrogen reactive species. Various studies have been carried out to investigate the best ratio, but the results vary greatly [421-424].

Here in this study, the electrical and electrochemical properties of GO treated using different ratios of nitrogen to hydrogen are related to the reduction degree and the nitrogen doping configurations. As evidenced in Section 4.5.1 (Fig. 4-23 and Fig. 4-24), when decreasing the nitrogen to hydrogen ratio, the percentage of Peak B in XPS spectra of C1s (C-O) decreased and the pyridinic N/pyrrolic N of Peak D increased. Recent study have found that the nitrogen doping concentration and configuration can be controlled by the parameters in the doping process [141], and thus it is reasonable to deduce that the concentration and configuration type of nitrogen doped by ASP treatment could be related to the ratio of nitrogen to hydrogen used during the process. However, the mechanism behind the relationship between the ratio of nitrogen to hydrogen in ASP treatment and the nitrogen doping concentration and configuration is still not well understood.

### 4.6.2 Negative Effect of Nitrogen and Argon

As described in Section 4.4.2, when ASP treated using a gas mixture of nitrogen

and argon, the sheet resistance of $N_2$Ar-GO is even higher than that of untreated GO. This means that negative effects on electrical properties of GO arise following ASP treatment using a gas mixture of nitrogen and argon.

In nitrogen and argon plasma, except for the nitrogen gas molecules and argon atoms, there exist nitrogen and argon ions ($N_2^+$, $N^+$, and $Ar^+$) and neutral molecules and atoms at excited states ($N_2$*, N*, and Ar*). When argon is added at a small amount in the plasma, the excited argon atoms can transfer energy to nitrogen molecules via inelastic collisions ($Ar^* + N_2 \rightarrow N_2^* + Ar$), which is the so-called Penning excitation [418]. When the argon content increases, there is another reaction with charge transfer from nitrogen ions to argon ($Ar^* + N_2^+ = N_2 + Ar^+$) [425]. Here in this study, the ratio of nitrogen to argon is 1:3, so both reactions can occur.

In ASP, due to the feature of remote plasma as discussed above, most ions are attracted to the active screen, and the active species that GO samples confront are dominated by excited argon atoms.

In addition, it has also reported that based on the current-voltage characteristics of the discharge that, at low gas pressures, there would be an increase in the electric field when nitrogen is added to argon plasma [426, 427]. Consequently, the ion bombardments on the GO sample from the nitrogen and argon gas mixture plasma, even minimised by the active screen, are still stronger than pure argon plasma. This would cause more defects on the GO treated using a

gas mixture of nitrogen and argon, resulting in the increase of sheet resistance. This is also supported by the electrochemical testing results that that capacitance of nitrogen/argon plasma treated $N_2$Ar-GO is lower than pure argon treated Ar-GO (Fig. 4-19). However, the nitrogen doping effect still played a positive role in this case, and so the electrochemical performance improved, as compared to untreated GO.

# Part III: ASP Metal Sputtering Hybrid Effect

## 4.7 Results of ASP Hybrid Process Combining Modification and Deposition

As explored from Section 4.2 to 4.6, it is found that a small amount of metal nanoparticles from the active screen are sputtered and deposit on GO. To further investigate the sputtering effects of ASP, one more noble metal plate is added as a lid of the active-screen cage, and the relevant results and discussions are displayed from Section 4.7 to 4.10.

In this section, ASP treated GO samples with four types of noble metal as the active-screen lid were compared. The noble metals are silver, palladium, platinum and gold, and the corresponding samples are denoted as GO-Ag, GO-Pd, GO-Pt and GO-Au, respectively. Working gas used is the gas mixture of nitrogen and hydrogen at a ratio of 1:3, and all the other conditions are the same, with a total gas pressure of 0.75 mbar, at a temperature of 100 ℃ for a duration of 1 h.

### 4.7.1 Micro-structure

1. SEM observation and EDS results

Fig. 4-31 are the SEM images in two different magnifications of GO samples after ASP treatments with a noble metal lid. For GO-Ag in Fig. 4-31(a), aggregated particles are separately scattered on the GO film. According to the SEM image of higher magnification shown in Fig. 4-31(b), these aggregated particles are in a size of about one or two microns in diameter. Additionally, it is not surely known of the stains on the low magnificent SEM image of GO-Pt (Fig. 4-31(e)), which are possibly some contaminations during the ASP process.

According to the EDS mapping shown in Fig. 4-32(a-c), the missing signal of silicon indicates that those aggregated particles are at a height of at least one micron. The signals of silver in these corresponding areas prove those particles are metal silver. However, this is only unique for GO-Ag, as for the other three GO samples, few very small particles are observed in the SEM images, as shown in Fig. 4-31(c-h), due to their extremely small sizes of about several or tens of nanometres, but the EDS can detect the existence of the corresponding metal element compositions, as shown in Fig. 4-33(a-c) and the Table 4-10.

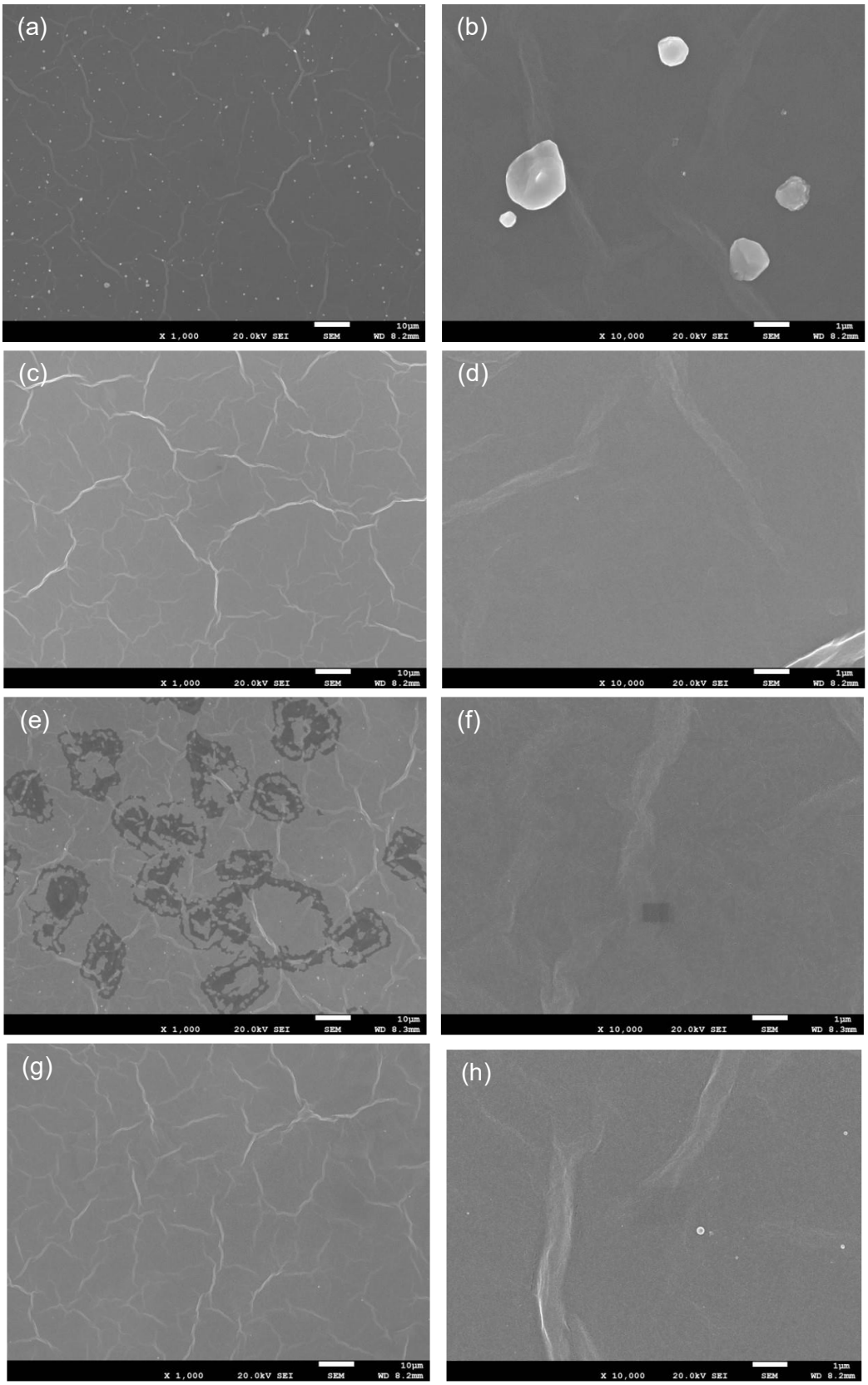


Fig. 4-31 SEM images of (a-b) GO-Ag (c-d) GO-Pd (e-f) GO-Pt and (g-h) GO-Au.

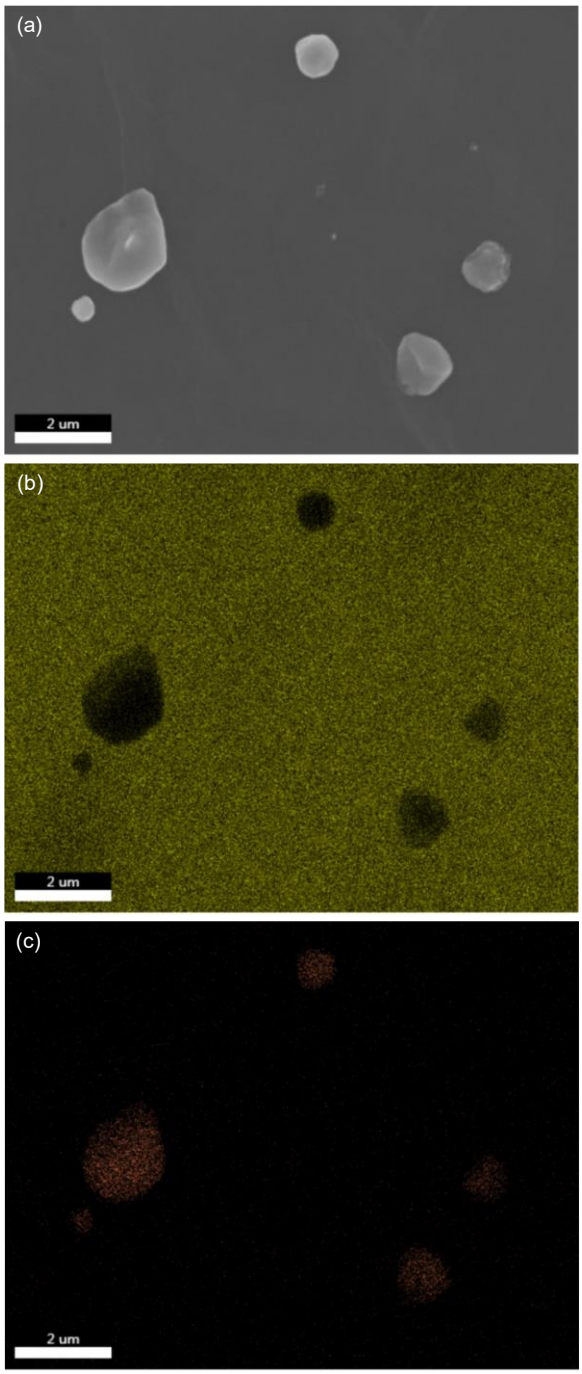


Fig. 4-32 EDS mapping result of GO-Ag (a) image, (b) Si K, (c) Ag L.

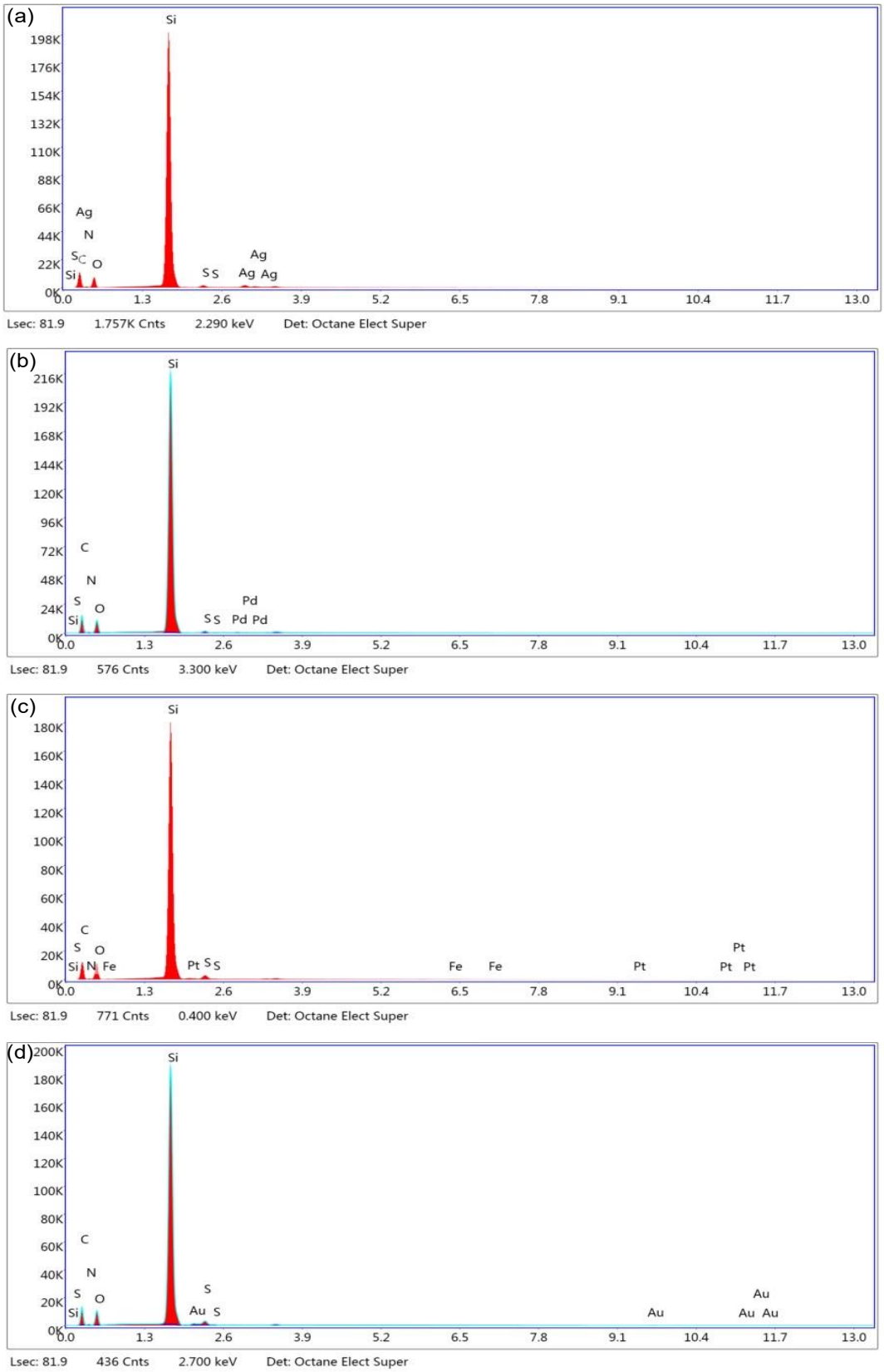


Fig. 4-33 EDS results of (a) GO-Ag, (b) GO-Pd, (c) GO-Pt, and (d) GO-Au.

Table 4-10 Element content weight percentage of GO samples after ASP treatments with a noble metal lid

| | C | N | O | Si | S | Fe | Ag | Pd | Pt | Au |
|---|---|---|---|---|---|---|---|---|---|---|
| **GO-Ag** | 40.73 | 2.48 | 11.48 | 43.32 | 0.61 | / | 1.38 | / | / | / |
| **GO-Pd** | 39.85 | 2.36 | 12.73 | 44.31 | 0.47 | / | / | 0.28 | / | / |
| **GO-Pt** | 41.24 | 1.54 | 15.60 | 39.85 | 1.08 | 0.10 | / | / | 0.59 | / |
| **GO-Au** | 38.99 | 2.34 | 13.91 | 42.00 | 1.25 | / | / | / | / | 1.50 |

2. TEM observation with EDS mapping, HRTEM and SAED

(1). TEM observation with EDS mapping

Fig. 4-34(a-d) are the TEM images and relevant EDS mappings of the GO samples after ASP treatment with different metal lids. Different from SEM images, clusters of different sizes are clearly observed in TEM imaging and are further confirmed by EDS mapping as the corresponding noble metals. Despite the possibility of agglomeration, these noble metals are all in nano-scale, indicating that metals sputtered and deposited on GO film are in loose. Specifically, the clusters of gold are relevantly much larger than the other three noble metals, and hence iron and chromium can be detected in the same area more clearly, suggesting that all types of the metals assemble together, with the noble metals dominating concentration.

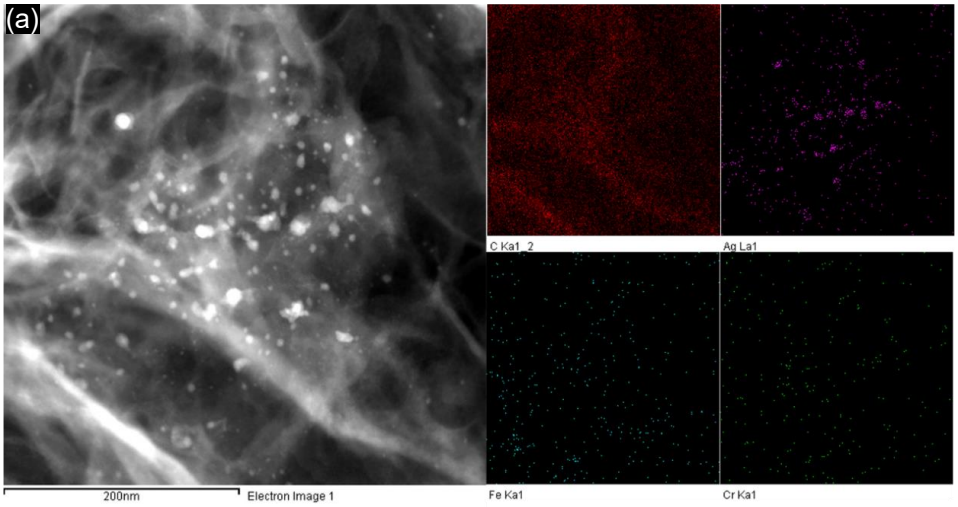
(a)
200nm
Electron Image 1
C Ka1_2
Ag La1
Fe Ka1
Cr Ka1

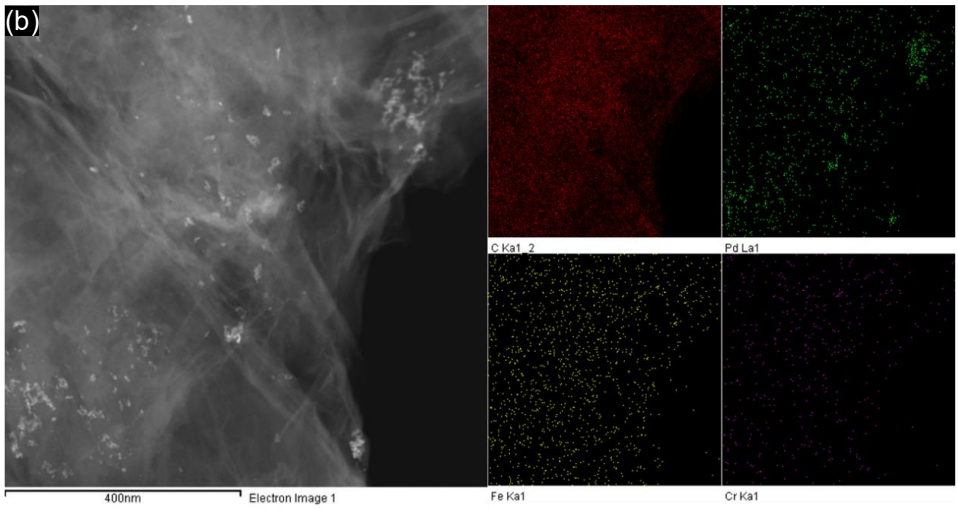
(b)
400nm
Electron Image 1
C Ka1_2
Pd La1
Fe Ka1
Cr Ka1

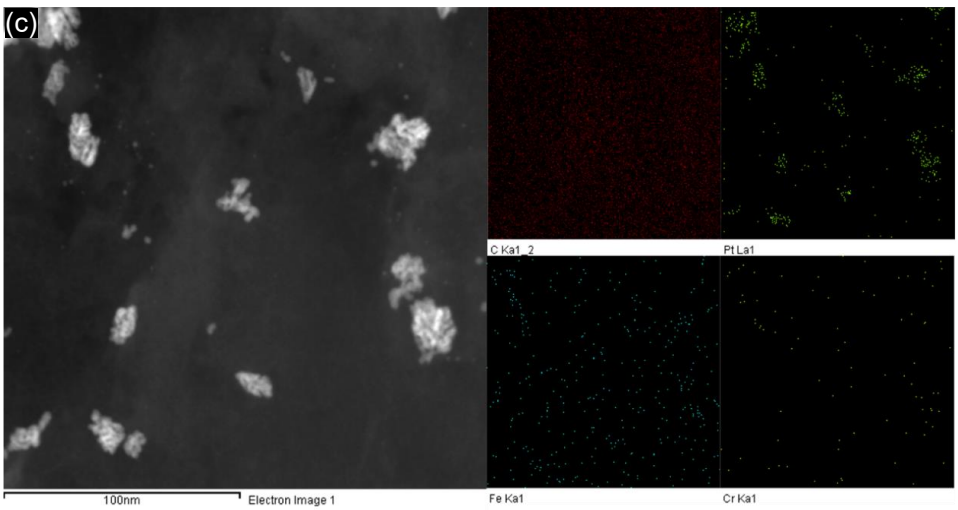
(c)
100nm
Electron Image 1
C Ka1_2
Pt La1
Fe Ka1
Cr Ka1

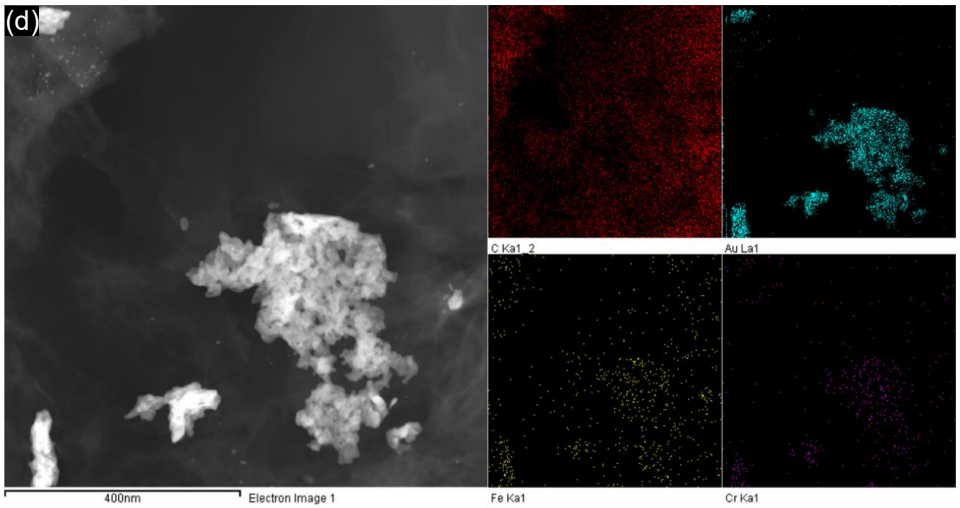


Fig. 4-34 TEM images and relevant EDS mapping of (a) GO-Ag, (b) GO-Pd, (c) GO-Pt, and (d) GO-Au.

(2). TEM with SAED of GO

GO was firstly examined via SAED. Fig. 4-35 is the TEM image of GO-Pt sample, displaying the GO flakes with wrinkles, and the SAED pattern inset shows two rings with distinct six-fold brighter patterns, referring to (100) and (110) planes of graphene film observed from the axes of [001] [428, 429].

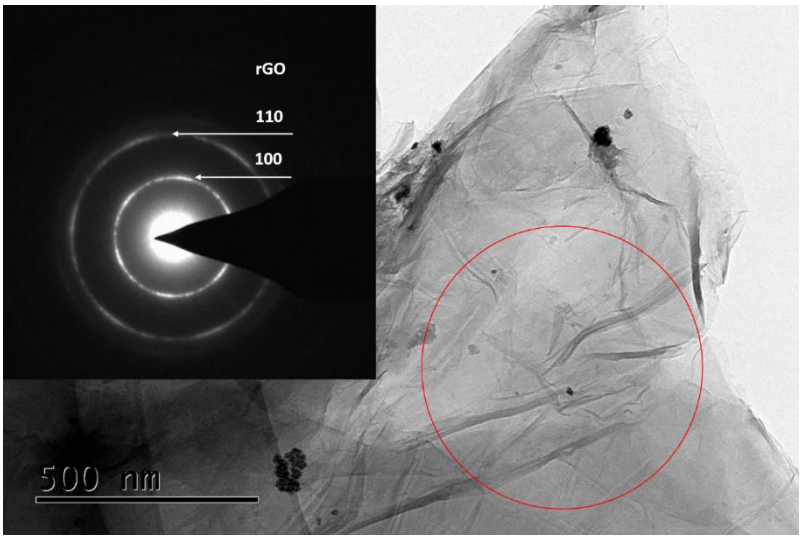


Fig. 4-35 TEM micro-structure of the GO-Pt sample films; inset is SAED pattern from red circle area indicating multi-layered GO diffractions of (100) and (110) rings at B=[001].

(3). HRTEM of silver

Due to the extreme small size of silver particles, poor signals were detected and no SAED pattern of silver is shown here. The lattice assessment of silver particles is displayed in Fig. 4-36. Different from the aggregated silver particles observed in SEM images (Fig. 4-31(a-b)), the silver particles in HRTEM images are quite small, most of which are in extremely fine sizes of 1-2 nm (as circled in Fig. 4-36) with only a few in 3-5 nm diameter. The spacing of the lattice fringe is around 0.238 nm, corresponding to $d_{111}$ of silver [430-432].

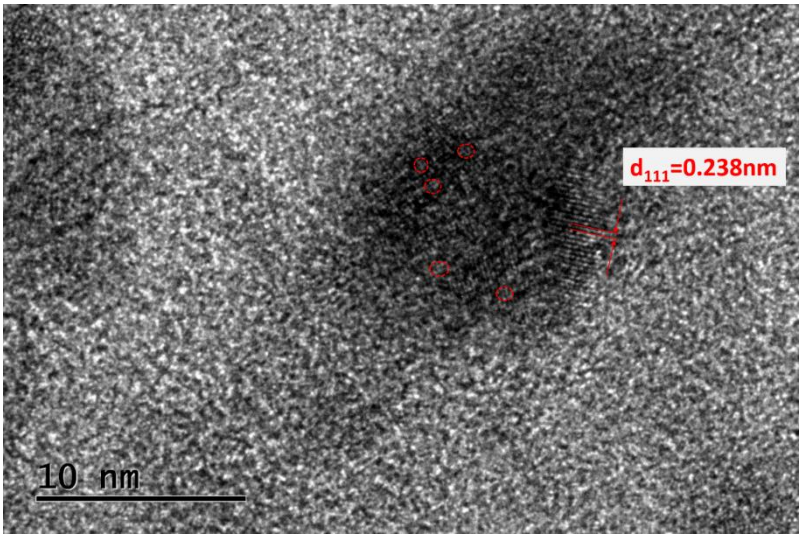


Fig. 4-36 HRTEM of GO-Ag sample.

(4). SAED and HRTEM of palladium

The particles were observed on the GO film, as displayed in TEM image of Fig. 4-37(a), and SAED pattern were obtained from the red circled area in Fig. 4-37(a). Due to plenty of both GO and Pd in this area, the SAED pattern (Fig. 4-37(b)) shows the rings of both spheres of GO, and the *fcc*-structured Pd planes [433, 434]. The HRTEM image of the particles with the same lattice (Fig.

4-37(c)), as circled in red, indicates that the palladium particles are in a size of about 4-7 nm in diameter.

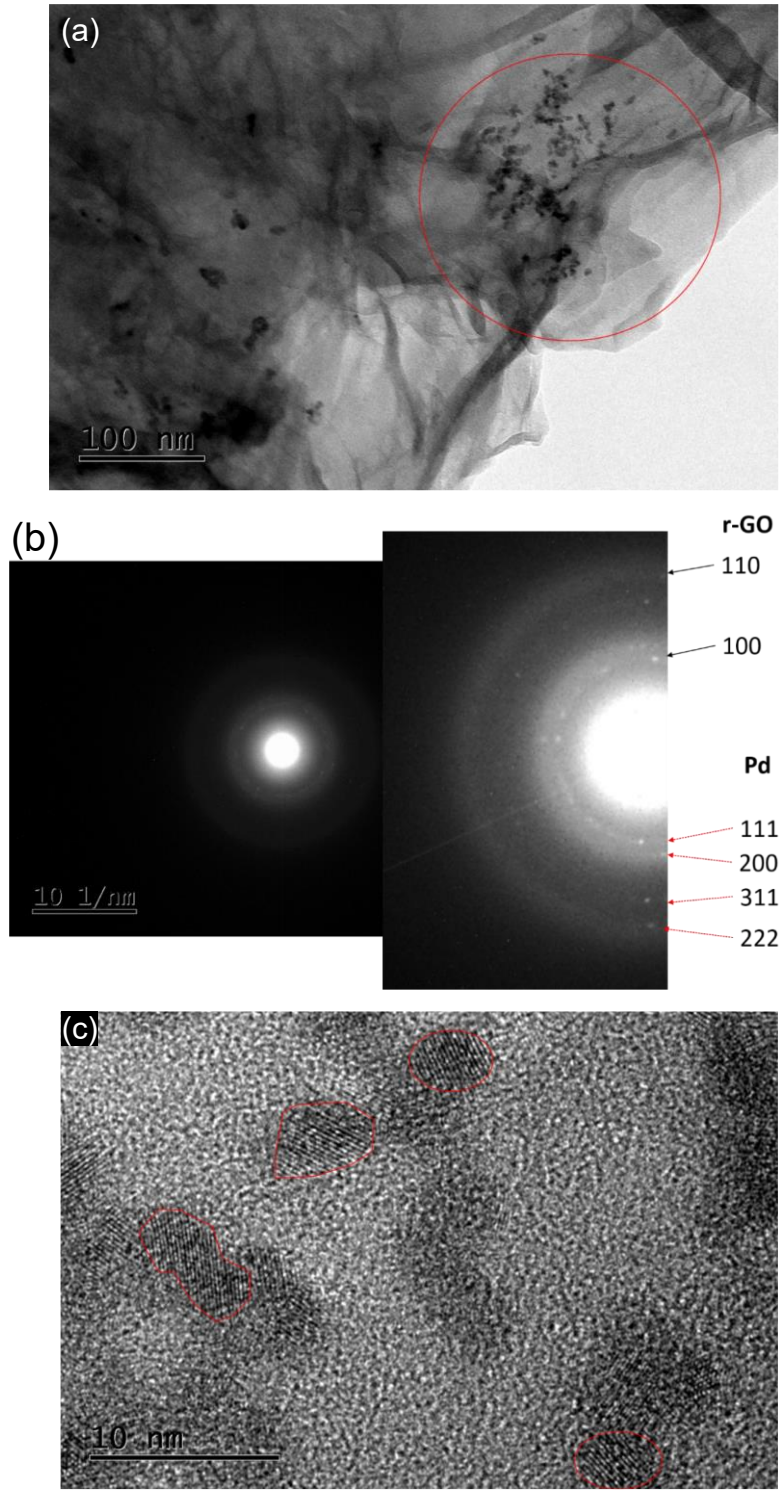


Fig. 4-37 (a)TEM microstructure of the GO-Pd sample; (b) SAED pattern from red circled area in (a); (c) HRTEM image of GO-Pd sample.

(5). SAED and HRTEM of platinum

TEM image of GO-Pt is shown in Fig. 4-38(a). Crystals are observed on GO in various shapes and sizes, as platinum particles agglomerated due to nano-scaled sizes. SAED pattern in Fig. 4-38(b) also exhibits the integration of both GO and platinum. The blurry diffraction rings of GO suggest the multi-layer of GO. The platinum particles in HRTEM (Fig. 4-38(c)) are circled in red here, and their sizes are about 4-6 nm in diameter as well, similar to those of palladium.

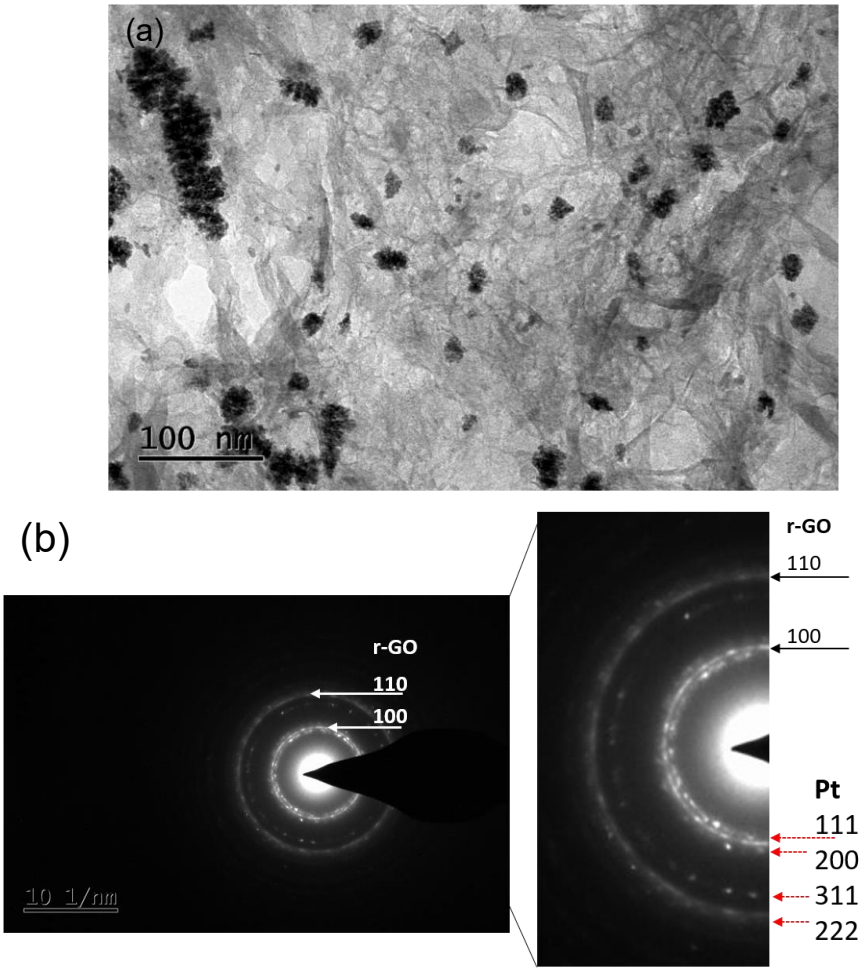

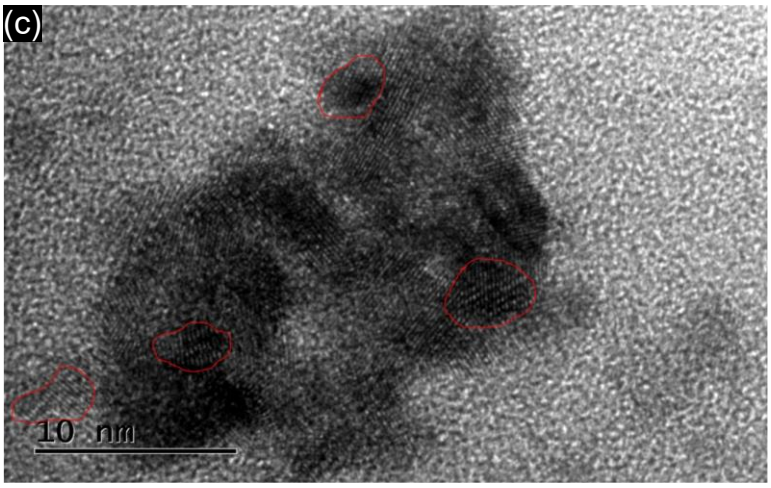


Fig. 4-38 (a)TEM microstructure; (b) SAED pattern; (c) HRTEM image of GO-Pd sample.

(6). SAED and HRTEM of gold

From the TEM image of GO-Au in Fig. 4-39(a), big metal clusters are observed, and its corresponding SAED pattern is shown in Fig. 4-39(b). The (111), (200), (220) and (311) planes indicate the *fcc* lattice structure of gold [435]. From the HRTEM image of GO-Au (Fig. 4-39(c)), particles in the identical lattice fringe, as circled in red, suggest the individual gold particles, and the size are about 10 nm in diameter, much larger than the other three noble metals. This may explain the larger clusters of gold compared to the other three in TEM images.

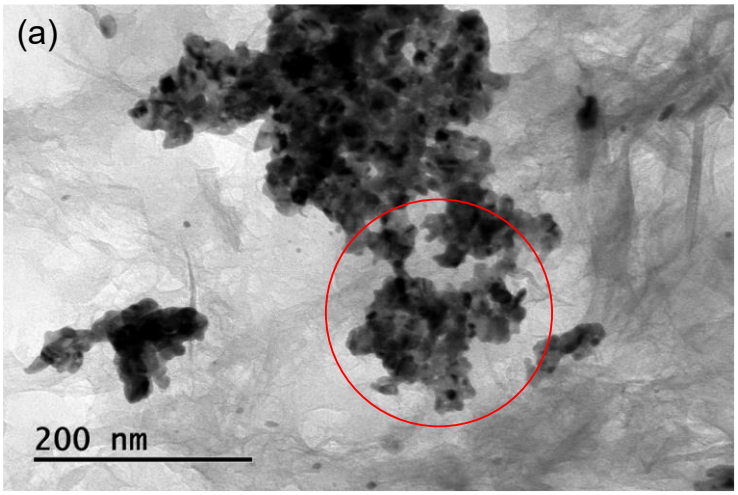

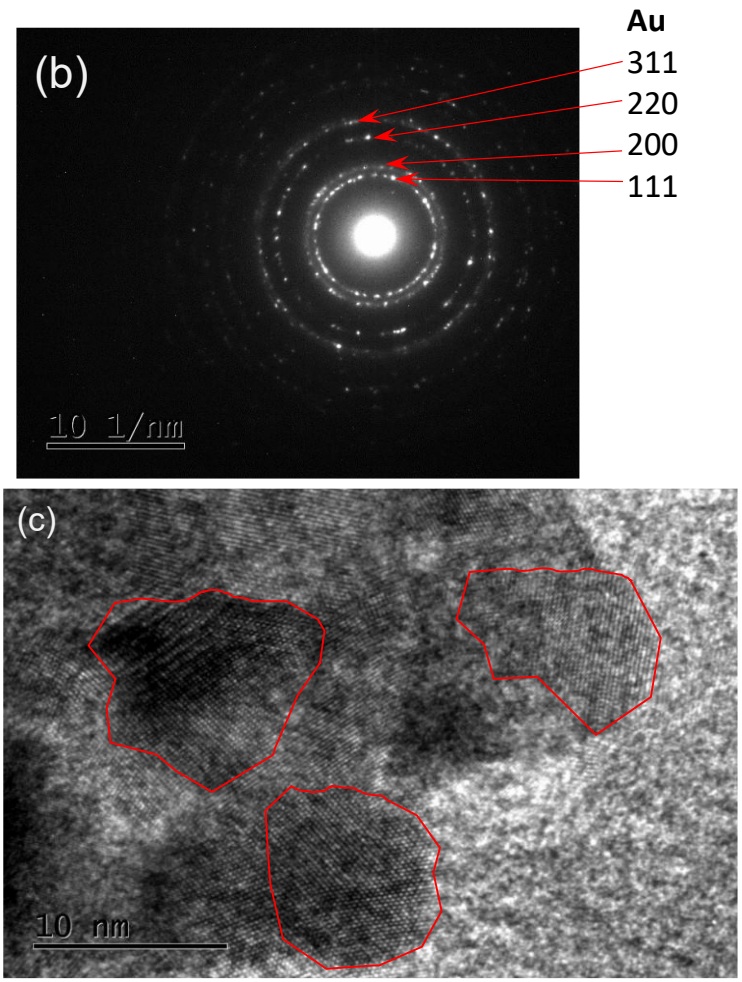


Fig. 4-39 (a)TEM microstructure of the GO-Au sample; (b) SAED pattern from red circled area in (a); (c) HRTEM image of GO-Au sample.

3. Raman spectra

Fig. 4-40 shows the Raman spectra of untreated GO and the GO samples ASP treated with different metal lids. These four Raman spectra are still similar in featuring the dominant D peak and G peak. According to the details of the Raman spectra in Table 4-11, it can be found those of GO-Pd, GO-Pt and GO-Au are almost the same, as FWHM(G) decrease to 81 $cm^{-1}$, $I_D/I_G$ decrease to 0.801 or 0.776, and position of G peak moves to 1602 or 1601 $cm^{-1}$. This suggests that the structure transformation of GO during the ASP process is not

related to the type of these three metals, and the decrease of both $I_D/I_G$ and FWHM(G) are an indication of GO reduction, based on the three-stage model [385].

However, it is not quite the same to GO-Ag, as the $I_D/I_G$ does not decrease and the position of the G peak shifts to 1593 $cm^{-1}$. This is possibly related to the morphology of the metal deposited on the GO film, as that of GO-Ag is unique for its relatively larger size. As to the other three samples, a homogeneous layer is formed on the GO film surface, functioning as a cover or a sheath of the GO film, and it can prevent GO from the possible ion bombardment which may cause damage the structure. However, silver aggregates into big particles, and fails to form the metal layer. Thus, the GO structure gets more damages from the ion bombardment during the ASP process, resulting to the higher $I_D/I_G$.

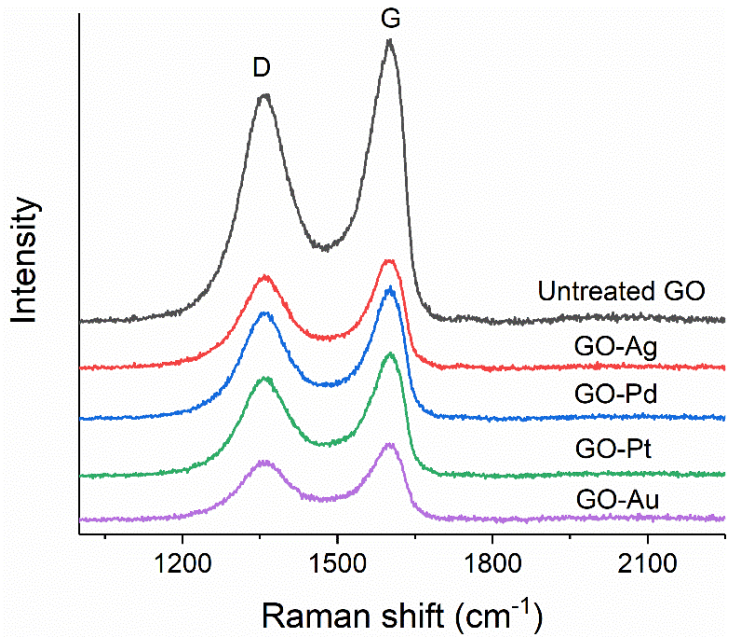


Fig. 4-40 Raman spectra of untreated, ASP treated GO using different metal lids.

Table 4-11 Raman spectra details GO samples after ASP treatment using different metal lids

| | D peak | | G peak | | $I_D/I_G$ |
|---|---|---|---|---|---|
| | Wavelength/$cm^{-1}$ | FWHM/$cm^{-1}$ | Wavelength/$cm^{-1}$ | FWHM/$cm^{-1}$ | |
| **Untreated GO** | 1357 | 139 | 1597 | 92 | 0.858 |
| **GO-Ag** | 1358 | 112 | 1593 | 83 | 0.862 |
| **GO-Pd** | 1357 | 113 | 1602 | 81 | 0.801 |
| **GO-Pt** | 1357 | 115 | 1602 | 81 | 0.801 |
| **GO-Au** | 1363 | 117 | 1601 | 81 | 0.776 |

4. XPS analysis

(1). XPS survey spectra and element contents

Fig. 4-41 shows the XPS survey spectra of the GO samples ASP treated with different noble metal lids. Apart from the basic elements of GO (carbon, nitrogen, oxygen and sulphur) and the metal elements from the stainless steel (iron and chromium), the noble metals corresponding to the extra lid have also been detected, with a noticeable content, especially palladium, platinum and gold. The atomic percentages of each element (excluding sulphur) are listed in Table 4-12. For comparison, the oxygen content of GO-Pd is much lower than the other three GO samples, due to a lower content of metal oxides, as a much lower content of iron detected and even no chromium detected. It is also interesting to notice that, the contents of iron and chromium in GO-Pd and GO-Pt are lower than those of GO-Ag and GO-Au, and chromium is even not detected in GO-Pd. On the other hand, regarding the noble metals, silver is also lower than the other counterparts, possibly related to the big particle size as observed from the morphology in SEM images.

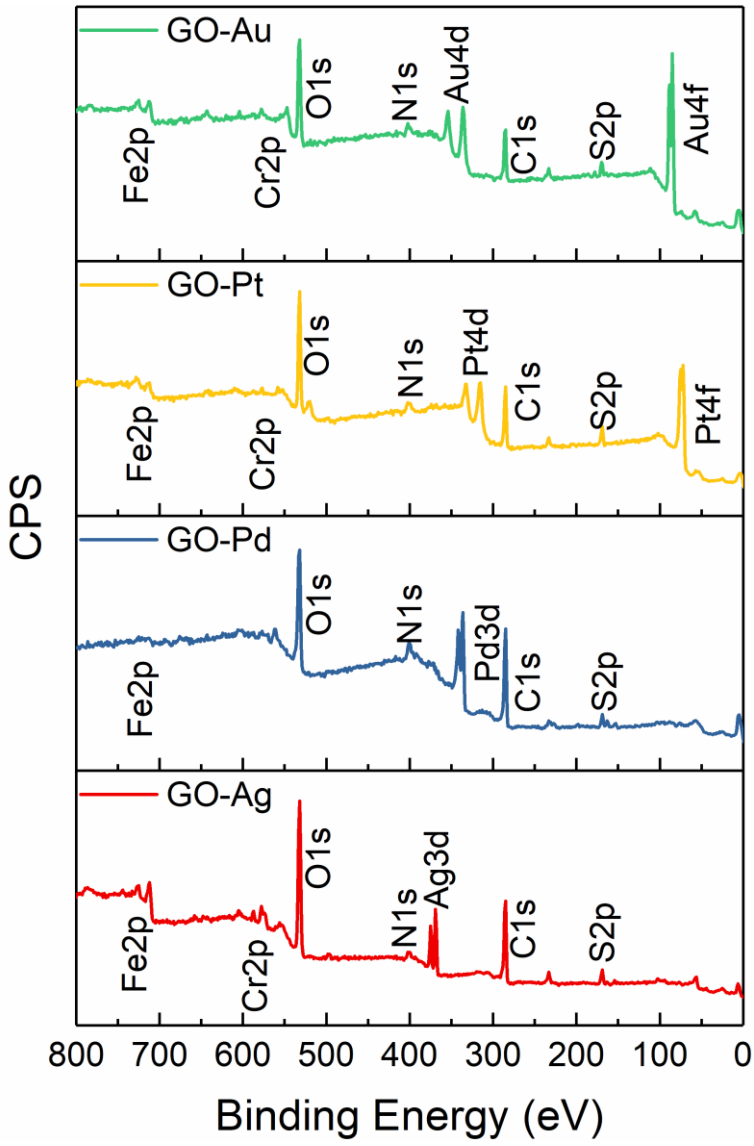


Fig. 4-41 XPS spectra survey of ASP treated GO with different metal lids.

Table 4-12 Atomic percentage of elements detected in ASP treated GO with different metal lids

| | GO-Ag | GO-Pd | GO-Pt | GO-Au |
|---|---|---|---|---|
| **C1s** | 46.14 | 58.38 | 45.34 | 40.23 |
| **O1s** | 40.09 | 27.46 | 37.13 | 37.66 |
| **N1s** | 4.20 | 8.10 | 7.78 | 7.59 |
| **Fe2p** | 5.66 | 0.53 | 1.61 | 5.24 |
| **Cr2p** | 1.65 | / | 0.83 | 1.37 |
| **Ag3d** | 2.26 | / | / | / |
| **Pd3d** | / | 5.53 | / | / |
| **Pt4f** | / | / | 7.31 | / |
| **Au4f** | / | / | / | 7.91 |

(2). C1s spectra

The high-resolution C1s spectra of all the GO samples are compared, as shown in Fig. 4-42. The spectra are similar and can be decomposed into three peaks: Peak A, Peak B, and Peak C, the same as those interpreted in Section 4.5.1 (Fig. 4-23). The deconvolutions of these spectra are shown in Fig. 4-42(b-d).

Comparing the details of the split peaks among these four ASP treated GO, it is found that these four GO samples are almost the same, suggesting that the type of extra noble metal lids has no effect on GO reduction. As to the smaller Peak B in GO-Ag, it should be related to the lower nitrogen content.

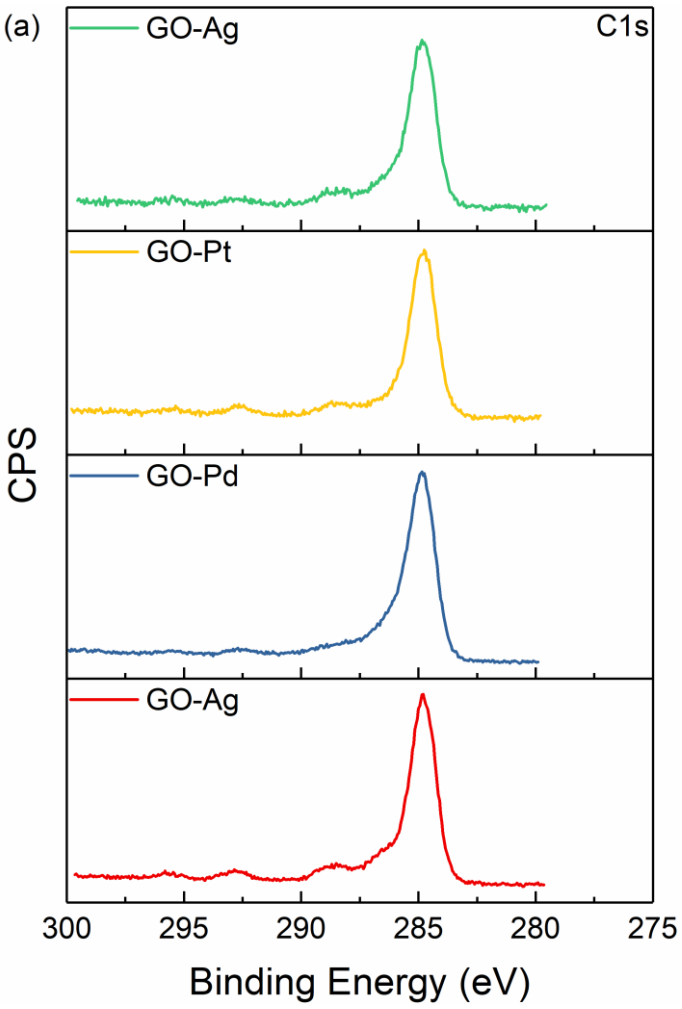

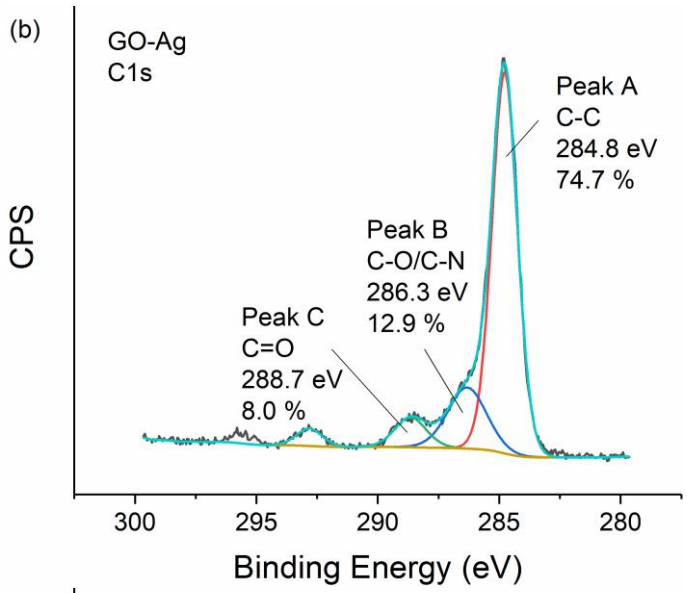
(b)
GO-Ag
C1s
Peak A
C-C
284.8 eV
74.7 %
Peak B
C-O/C-N
286.3 eV
12.9 %
Peak C
C=O
288.7 eV
8.0 %
CPS
300
295
290
285
280
Binding Energy (eV)

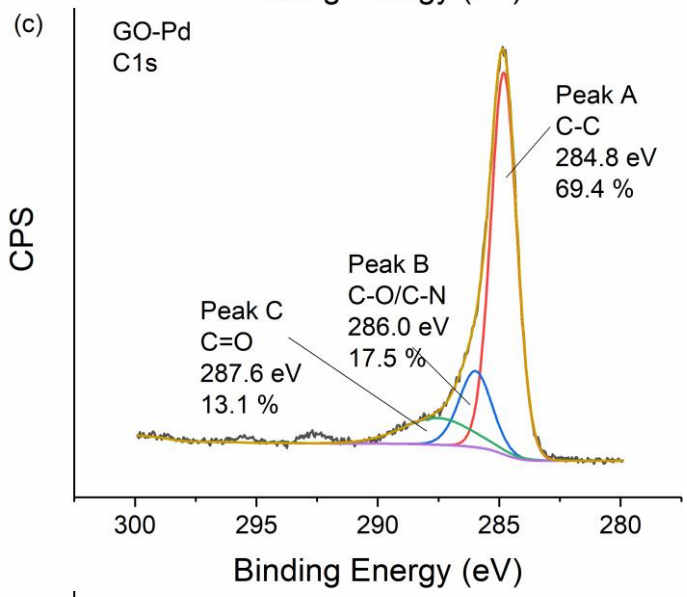
(c)
GO-Pd
C1s
Peak A
C-C
284.8 eV
69.4 %
Peak B
C-O/C-N
286.0 eV
17.5 %
Peak C
C=O
287.6 eV
13.1 %
CPS
300
295
290
285
280
Binding Energy (eV)

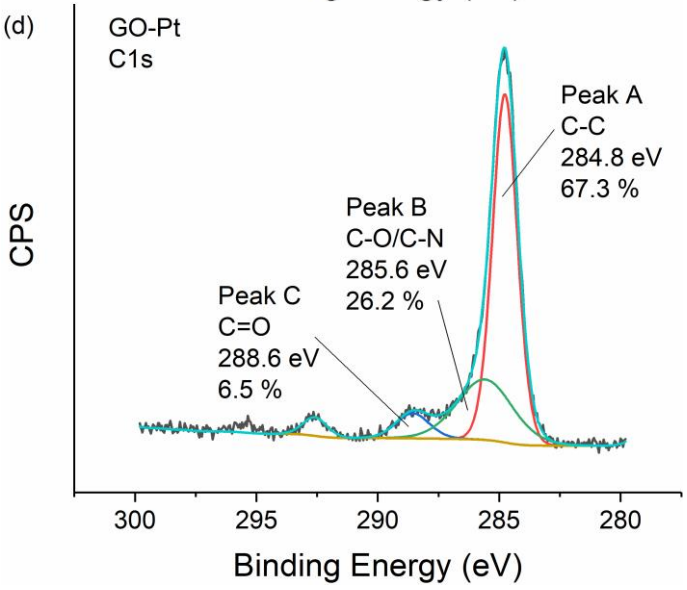
(d)
GO-Pt
C1s
Peak A
C-C
284.8 eV
67.3 %
Peak B
C-O/C-N
285.6 eV
26.2 %
Peak C
C=O
288.6 eV
6.5 %
CPS
300
295
290
285
280
Binding Energy (eV)

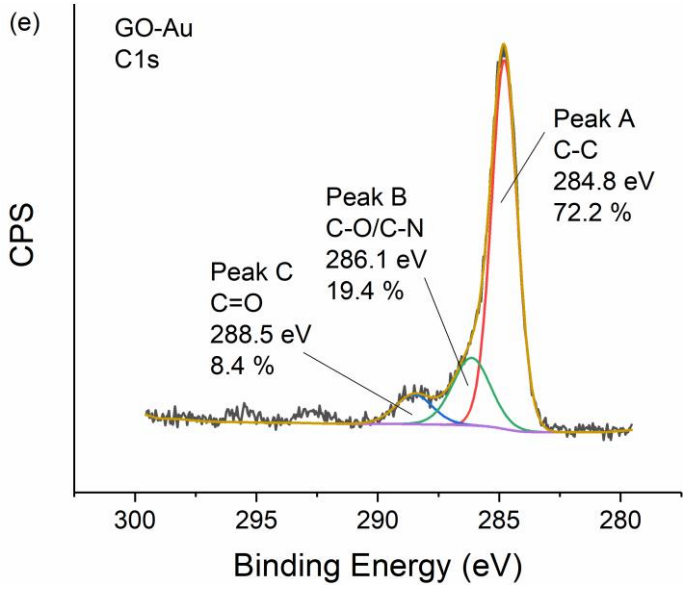


Fig. 4-42 (a) Comparison of high-resolution C1s XPS spectra of GO samples treated using different metal lids and deconvoluted C1s XPS spectra of (b) GO-Ag, (c) GO-Pd, (d) GO-Pt and (e) GO-Au.

(3). N1s spectra

High-resolution N1s spectra are compared as well, as shown in Fig. 4-43(a). However, these spectra are not quite the same. The deconvolution of spectra is shown in Fig. 4-43(b-e), and Pyrrolic N and Graphitic N are resolved in all the spectra, as Peak E and Peak F, respectively. However, Peak D is different in these GO samples. For GO-Pd and GO-Pt, Peak D at 398.2 or 398.5 eV represents Pyridinic N [436], whilst for GO-Ag and GO-Au, Peak D is around 397 eV, which is not related to graphene [437], possibly some metal nitrides [438]. However, it is not known of the reason for the absence of Pyridinic N but the appearance of metal nitrides in these two samples.

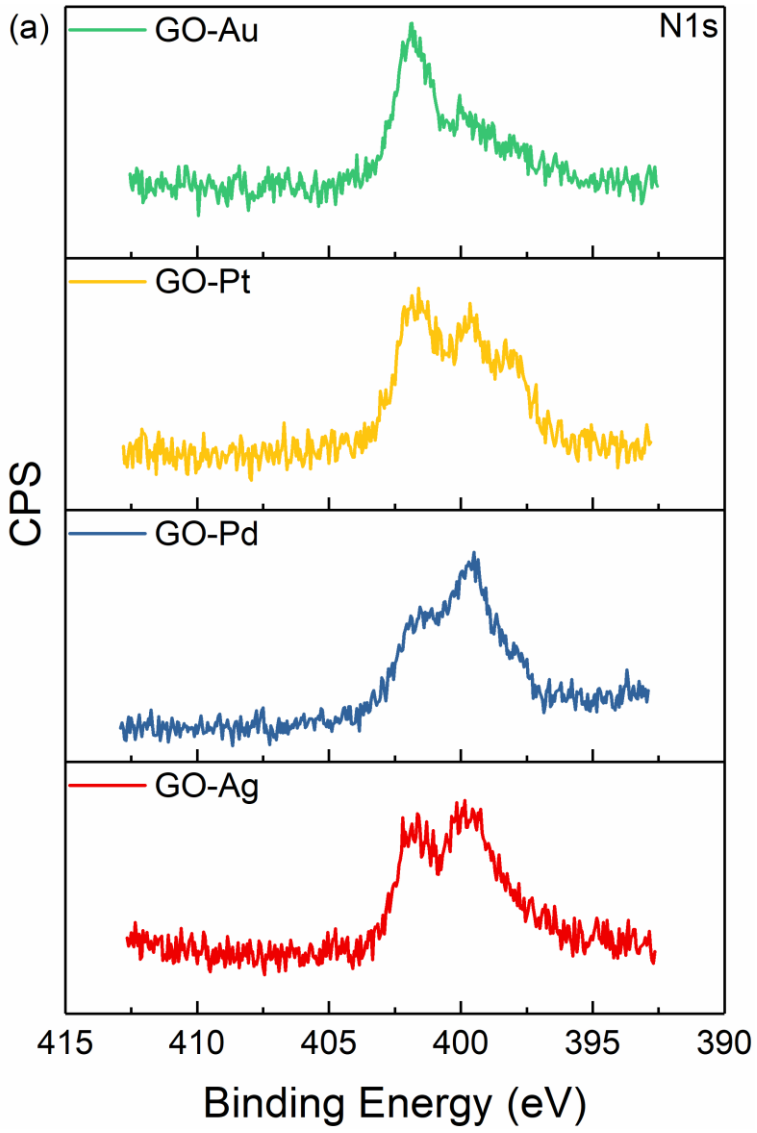
(a)
GO-Au
N1s
GO-Pt
GO-Pd
GO-Ag
CPS
415
410
405
400
395
390
Binding Energy (eV)

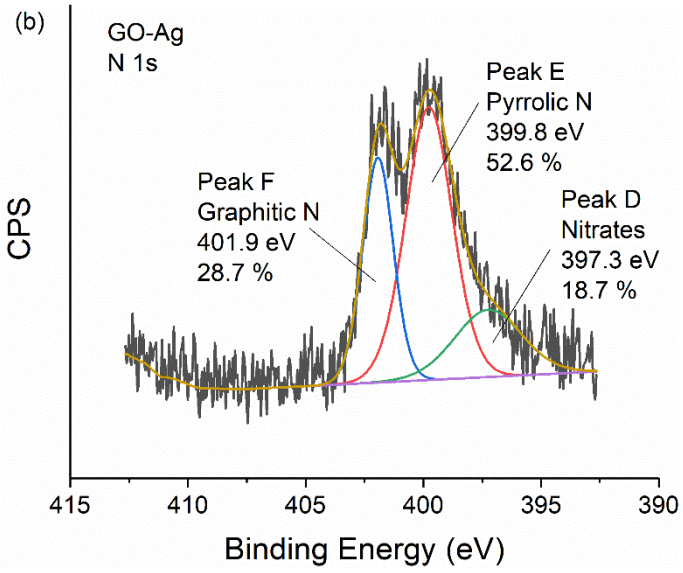
(b)
GO-Ag
N 1s
Peak E
Pyrrolic N
399.8 eV
52.6 %
Peak F
Graphitic N
401.9 eV
28.7 %
Peak D
Nitrates
397.3 eV
18.7 %
CPS
415
410
405
400
395
390
Binding Energy (eV)

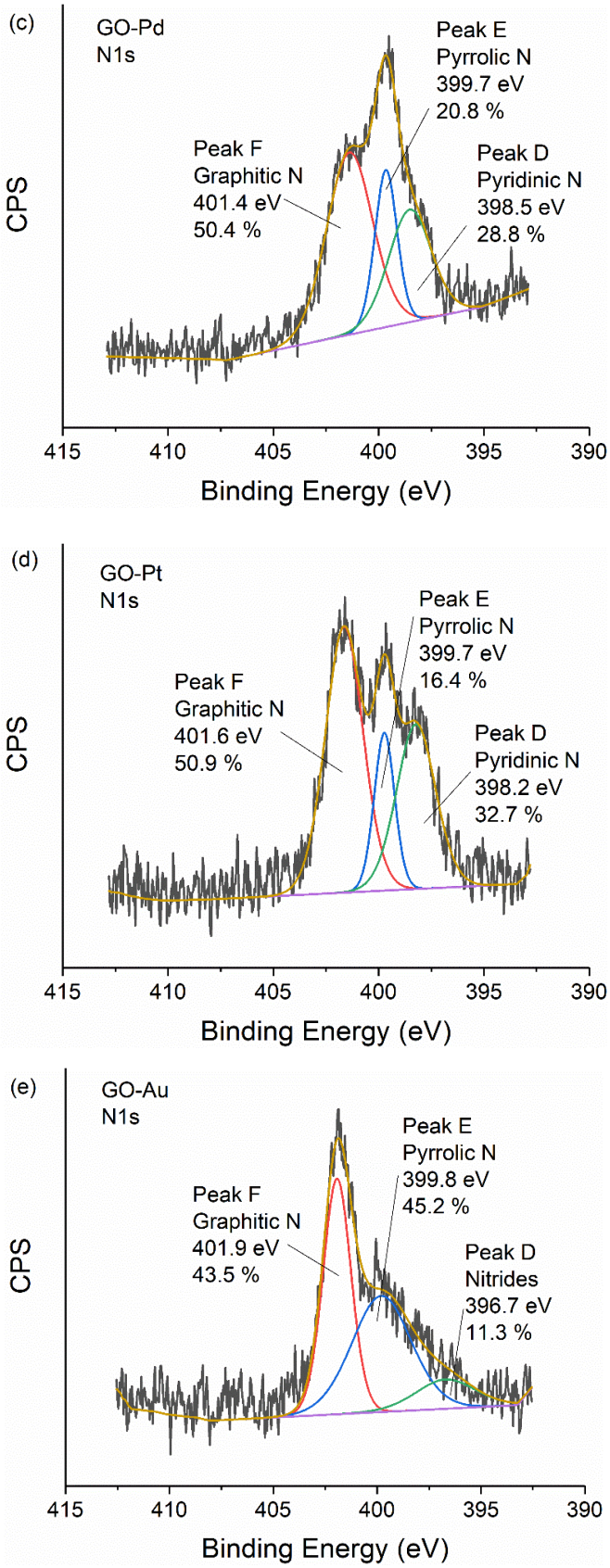


Fig. 4-43 (a) Comparison of high-resolution N1s XPS spectra of GO samples and the deconvoluted XPS spectra of (b) GO-Ag, (c) GO-Pd, (d) GO-Pt and (e) GO-Au.

(4). O1s spectra

Likewise, high-resolution O1s spectra of GO samples after ASP treatments with different metal lids are compared, as shown in Fig. 4-44(a), and the deconvoluted spectra are shown in Fig. 4-44(b-e). However, differences are found in the O1s spectra of these four GO samples.

In GO-Ag and GO-Au, the O1s spectra can be decomposed into three peaks: Peak G, Peak H and Peak I (Fig. 4-44(b, e)). Peak G at around 530 eV represents metal oxides; Peak H at around 532 eV represents oxygen bonding to carbon (C-O and C=O); and Peak I at around 533 eV represents metal hydroxides [439]. It is unique for GO-Ag and GO-Au with the appearance of Peak I, which is not found in all the other samples (NH13, NH11 and NH31 shown in Fig. 4-25, and GO-Pd and GO-Pt shown in Fig. 4-44(c, d)).

For GO-Pd, only Peak H appears. This is due to the extremely low contents of iron and chromium. This also explains the relatively small Peak G in GO-Pt for its evidently smaller content of iron and chromium than those of GO-Ag and GO-Au (Table 4-12).

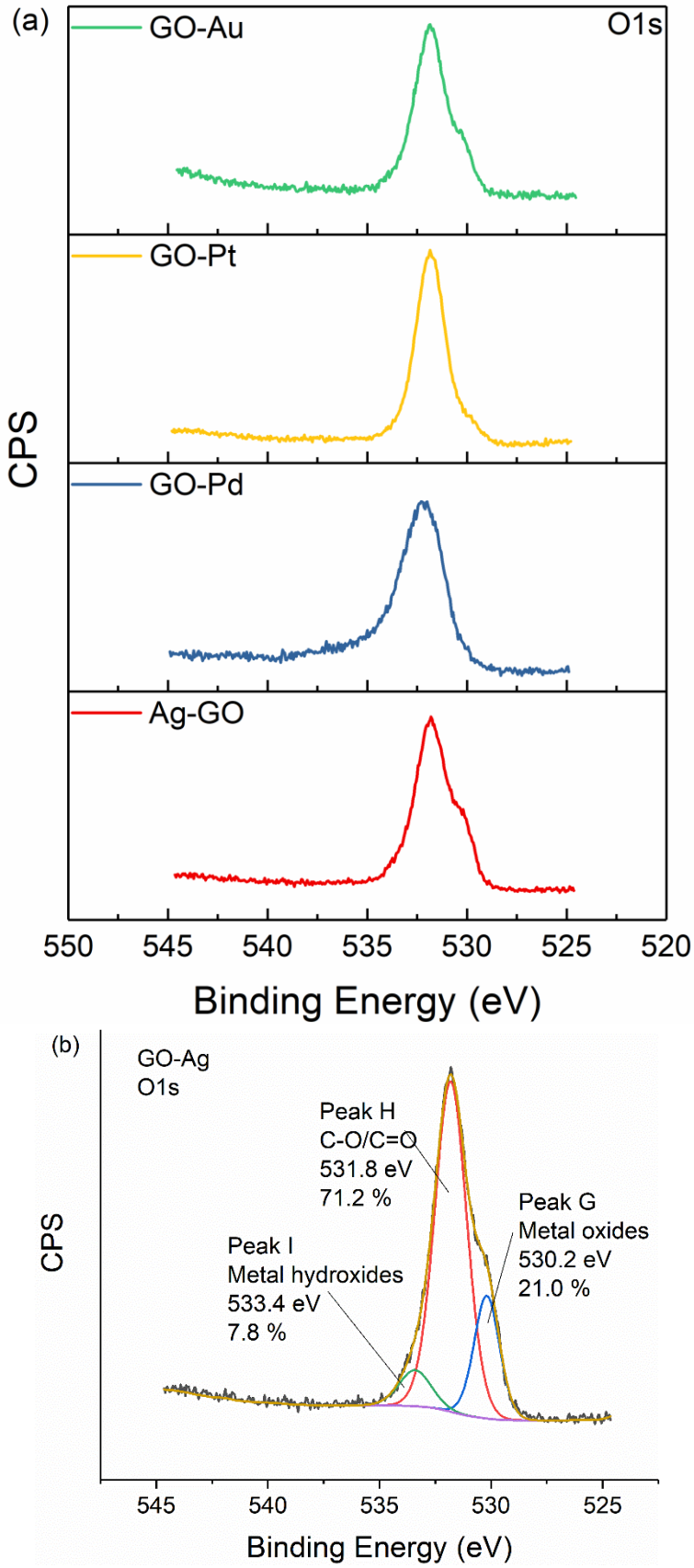
(a)
GO-Au
O1s
GO-Pt
GO-Pd
Ag-GO
CPS
550
545
540
535
530
525
520
Binding Energy (eV)
(b)
GO-Ag
O1s
Peak H
C-O/C=O
531.8 eV
71.2 %
Peak G
Metal oxides
530.2 eV
21.0 %
Peak I
Metal hydroxides
533.4 eV
7.8 %
CPS
545
540
535
530
525
Binding Energy (eV)

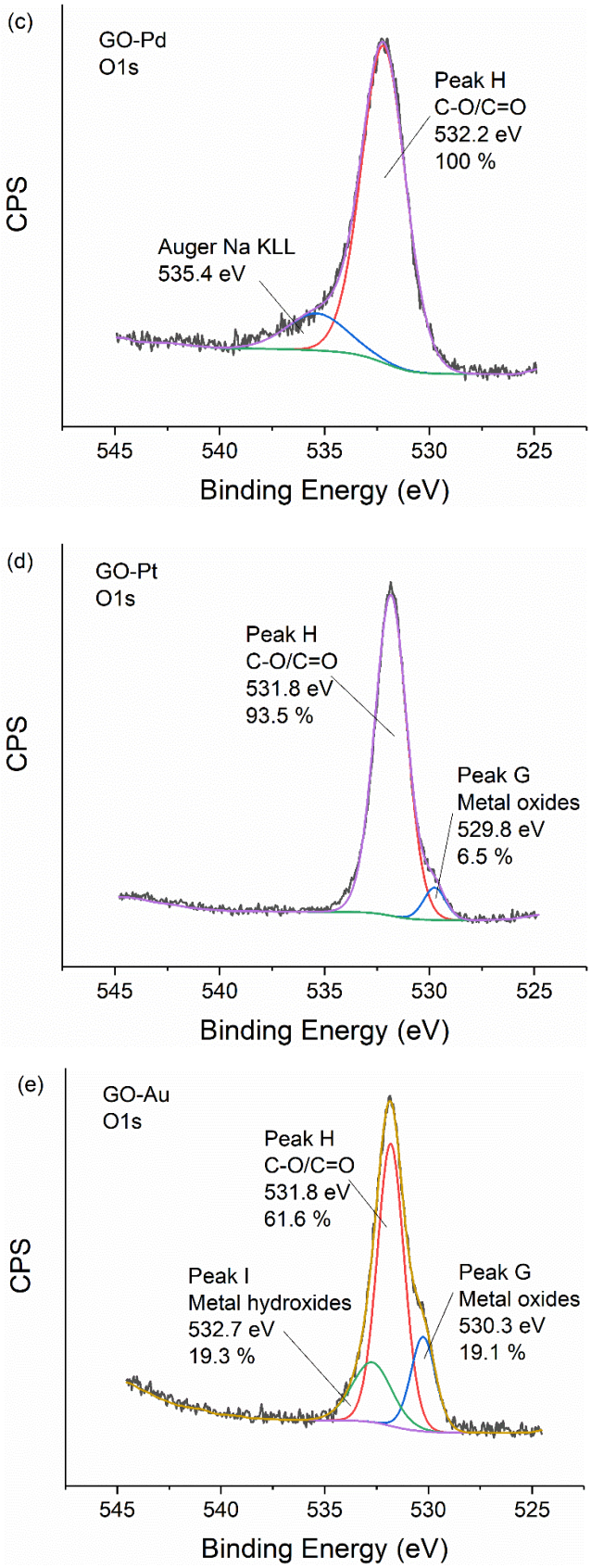


Fig. 4-44 (a) Comparison of high-resolution O1s XPS spectra of GO samples and the deconvoluted XPS spectra of (b) GO-Ag, (c) GO-Pd, (d) GO-Pt and (e) GO-Au.

(5). Fe2p and Cr2p spectra

The high-resolution Fe2p and Cr2p spectra are compared among all the GO samples treated using different metal lids as well. These two spectra are exhibited in Fig. 4-45. and are quite the same as those in Fig. 4-26 interpreted in Section 4.5.1, Therefore, it is still concluded that iron and chromium are both in the form of oxidised states. However, for GO-Ag and GO-Au, according to their corresponding N1s and O1s spectra, nitrides and hydroxides are also included. Due to the extreme low content of Fe and no Cr detected in GO-Pd, the Fe2p spectrum of GO-Pd is not significant, and no Cr2p spectrum is displayed. In addition, the extra peak at around 573.2 eV in GO-Ag results from Ag $3p_{3/2}$.

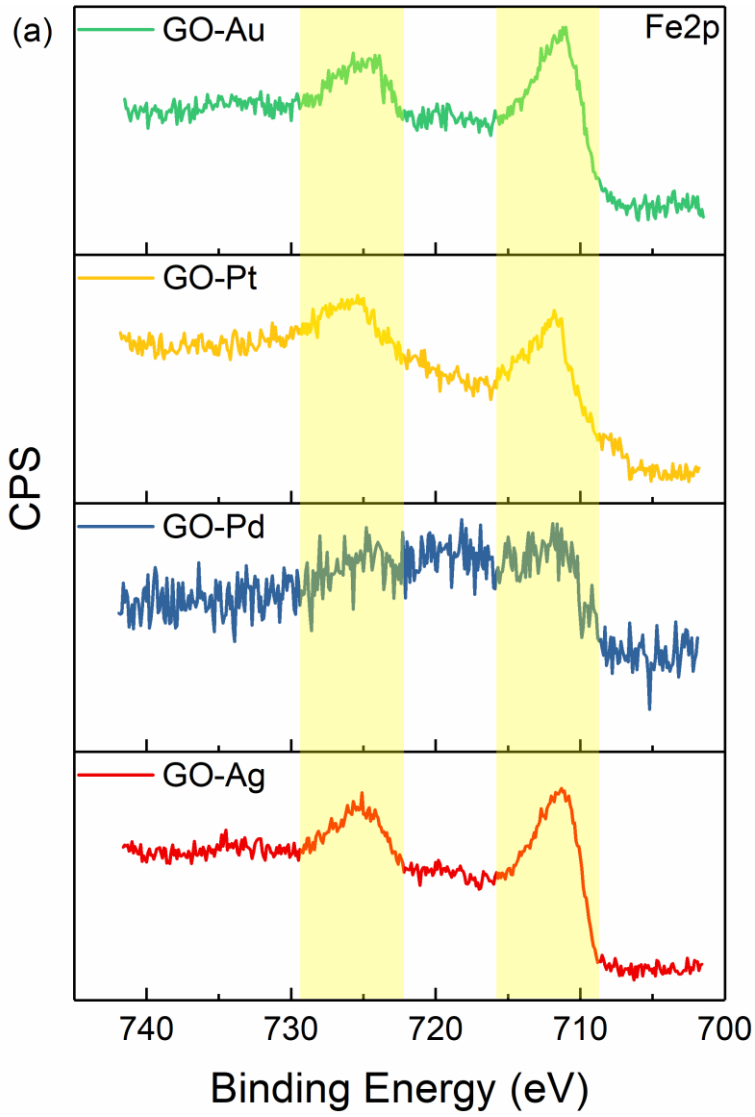
(a)
GO-Au
Fe2p
GO-Pt
GO-Pd
GO-Ag
CPS
740
730
720
710
700
Binding Energy (eV)

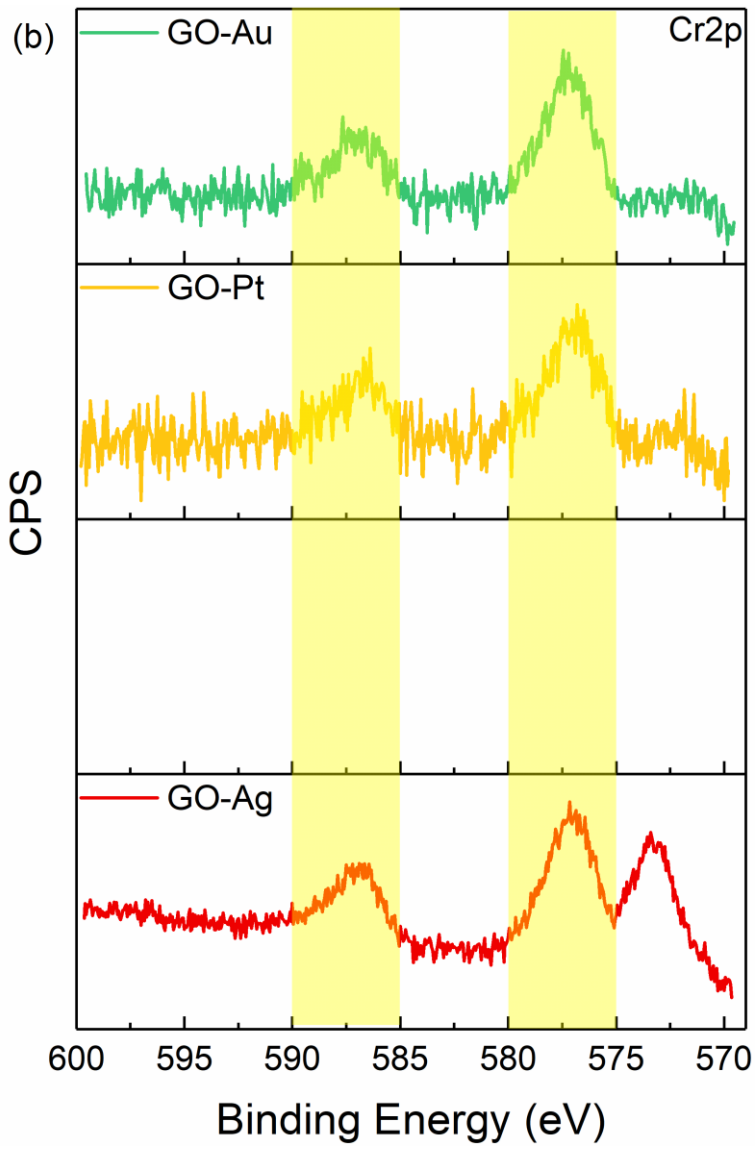


Fig. 4-45 Comparison of high-resolution (a) Fe2p and (b) Cr2p XPS spectra of ASP treated GO samples using different metal lids.

(6). Spectra of the noble metals

Fig. 4-46(a-d) show the high-resolution spectra of the four noble metal elements. As to Ag3d and Au4f, the scans cannot be decomposed. The two peaks in Ag3d level at 368.3 eV for Ag $3d_{5/2}$ and 374.3 eV for Ag $3d_{3/2}$, representing the pure silver metal, and similarly, the two peaks in Au4f level at 84.0 eV for Au $4f_{7/2}$ and 87.9 eV for Au $4f_{5/2}$ are assigned to pure gold metal.

However, in the spectra of Pd3d and Pt4f, native oxides are resolved as well, along with the pure metals. Specifically, in the spectrum of Pd3d (Fig. 4-46(b)), the predominant peaks decomposed at 336.0 eV and 341.2 eV are assigned to the pure palladium metal on carbon material (it may referred to Pd-C, which is discussed in Section 4.10.2) at Pd $3d_{5/2}$ and $3d_{3/2}$, respectively, and the small peaks at 337.3 eV and 342.6 eV are assigned to PdO, while the peaks at 339.3 eV and 344.5 are the satellite peaks [440]. In regard to Pt4f spectrum (Fig. 4-46(c)), the predominant peak at 71.4 eV and 74.7 eV are assigned to the pure platinum metal [441], while another peak at 72.5 eV and 75.8 eV are PtO [442].

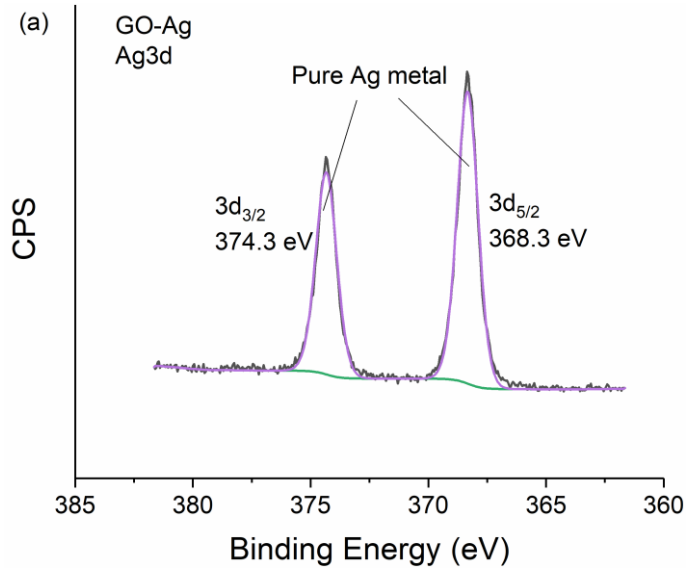

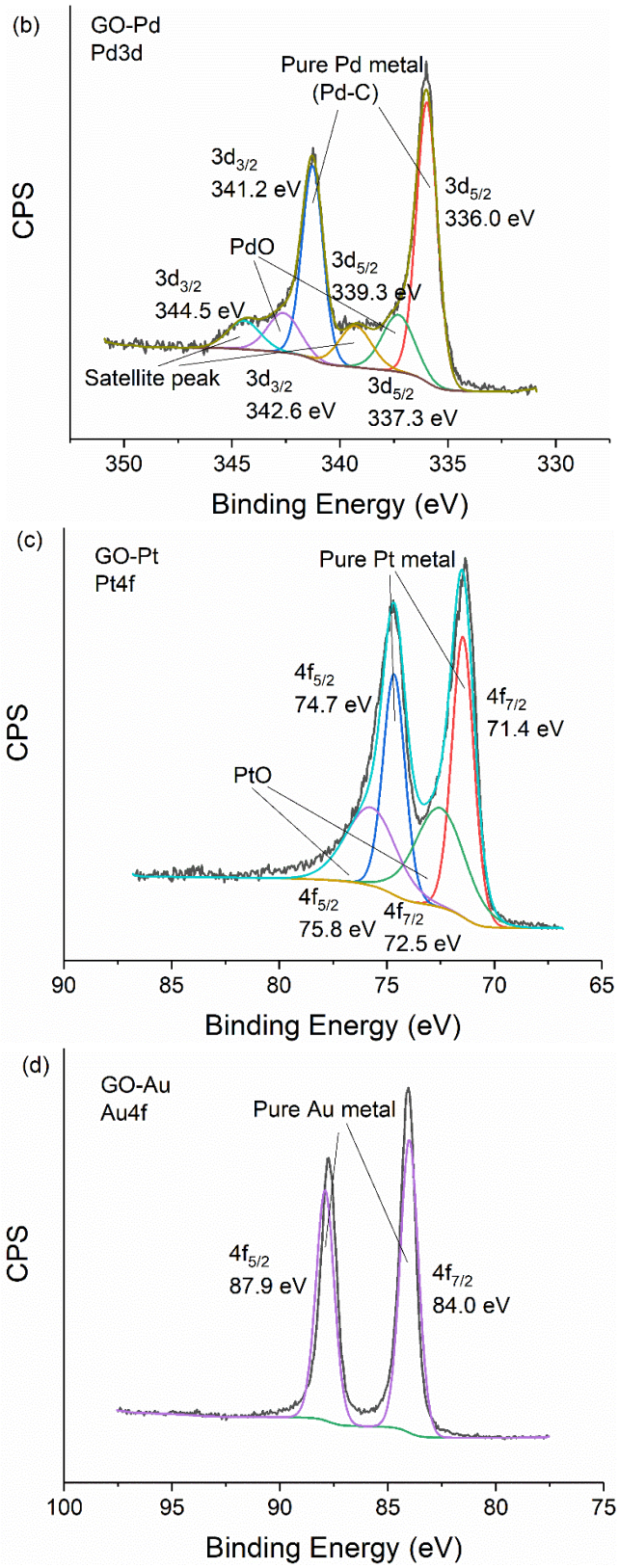


Fig. 4-46 High-resolution (a) Ag3d, (b) Pd3d, (c) Pt4f, and (d) Au4f XPS spectra of the corresponding GO samples.

### 4.7.2 Electrical and electrochemical properties

1. Sheet resistance measurement

Fig. 4-47 displays the sheet resistances of untreated GO and ASP treated GO with different noble metal lids. The sheet resistances of all ASP treated GO samples with noble metal lids can be seen to decrease, but with varying degrees. For GO-Ag and GO-Pd, the sheet resistances decrease to approximately $1.1\times10^{6}$ Ω $sq^{-1}$ and $0.9\times10^{6}$ Ω $sq^{-1}$ , respectively, while the sheet resistance of GO-Pt drops further to $2.0\times10^{4}$ Ω $sq^{-1}$, and even to only $3.4\times10^{2}$ Ω $sq^{-1}$ for GO-Au. These huge differences of sheet resistances among these GO samples indicate that the types of noble metals have a huge impact on the electrical property of GO samples.

Based on the XPS analysis (Fig. 4-41 to Fig. 4-46, as well as Table 4-12), these four GO samples are different in nitrogen doping configurations and the metals deposited on GO. Since the differences in sheet resistances do not accord with the nitrogen doping configurations (GO-Pd and GO-Pt share the same nitrogen doping configurations, but differ greatly in sheet resistance), the electrical properties of these GO samples are mainly related to the deposited metals. The details of the relationships between the deposited metals and the electrical properties are discussed in Section 4.10.2 and Section 4.10.3.

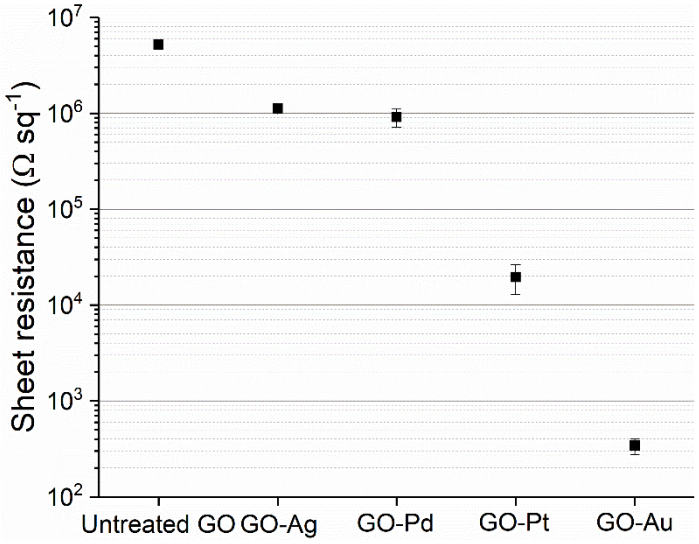


Fig. 4-47 Sheet resistance of untreated GO and ASP treated GO with different metal lids.

2. Electrochemistry tests

(1). CV test

The electrochemical performances of ASP treated GO samples with different noble metal lids are evaluated in CV test at different scan rates, and the results are shown in Appendix (Fig. A-3). However, the CV curves of GO-Au display an abnormal large curve at the scan rate of 100 mV $s^{-1}$, and thus Fig. 4-48 compare the CV curves at a scan rate of both 100 mV $s^{-1}$ and 5 mV $s^{-1}$.

For all the CV curves of ASP treated GO with noble metal lids, the quasi-rectangular shapes indicate their capacitive behaviour [152]. As to GO-Ag and GO-Au, the broadening of the capacitive currents is especially significant near 0.8 V, as well as a small hump at around 0.6 V in the negative current section, which could be owing to the hydroxides that detected in XPS analysis (Fig. 4-44(b, e)), which are more likely to have redox reactions during the CV process.

In the comparison of different GO samples at a scan rate of 100 mV $s^{-1}$ (Fig. 4-48(a)), GO-Au has the largest shape, followed with GO-Pt, GO-Pd and GO-Ag. However, GO-Au becomes the second largest at the scan rate of 5 mV $s^{-1}$, while GO-Pt being the largest, and the other GO samples follow the same sequence as before (Fig. 4-48(b)). Since the CV measurements were tested in the sequence of scan rate 100, 50, 20, 10, 5 mV $s^{-1}$, the deterioration of GO-Au implies that GO-Au is not cyclically stable for the measurements.

Fig. 4-48(c) displays the capacitances of these GO samples calculated at these scan rates. Unlike the other GO samples, the capacitances of GO-Au do not increase with the decreasing of scan rates as expected. The capacitances of GO-Au drop unexpectedly at 50 and 10 mV $s^{-1}$, indicating that after the CV tests at the scan rate of 100 and 20 mV $s^{-1}$, its super-capacitive performance decays. The reason for the phenomenon is unknown, requiring further study. However, all these ASP treated samples with noble metal lids have a higher capacitance than that of untreated GO, but to different degrees. At a scan rate of 100 mV $s^{-1}$, ASP treated GO with the highest capacitance of is GO-Au, and GO-Pt follows, next with GO-Pd and GO-Ag. This sequence is the same as the electrical property.

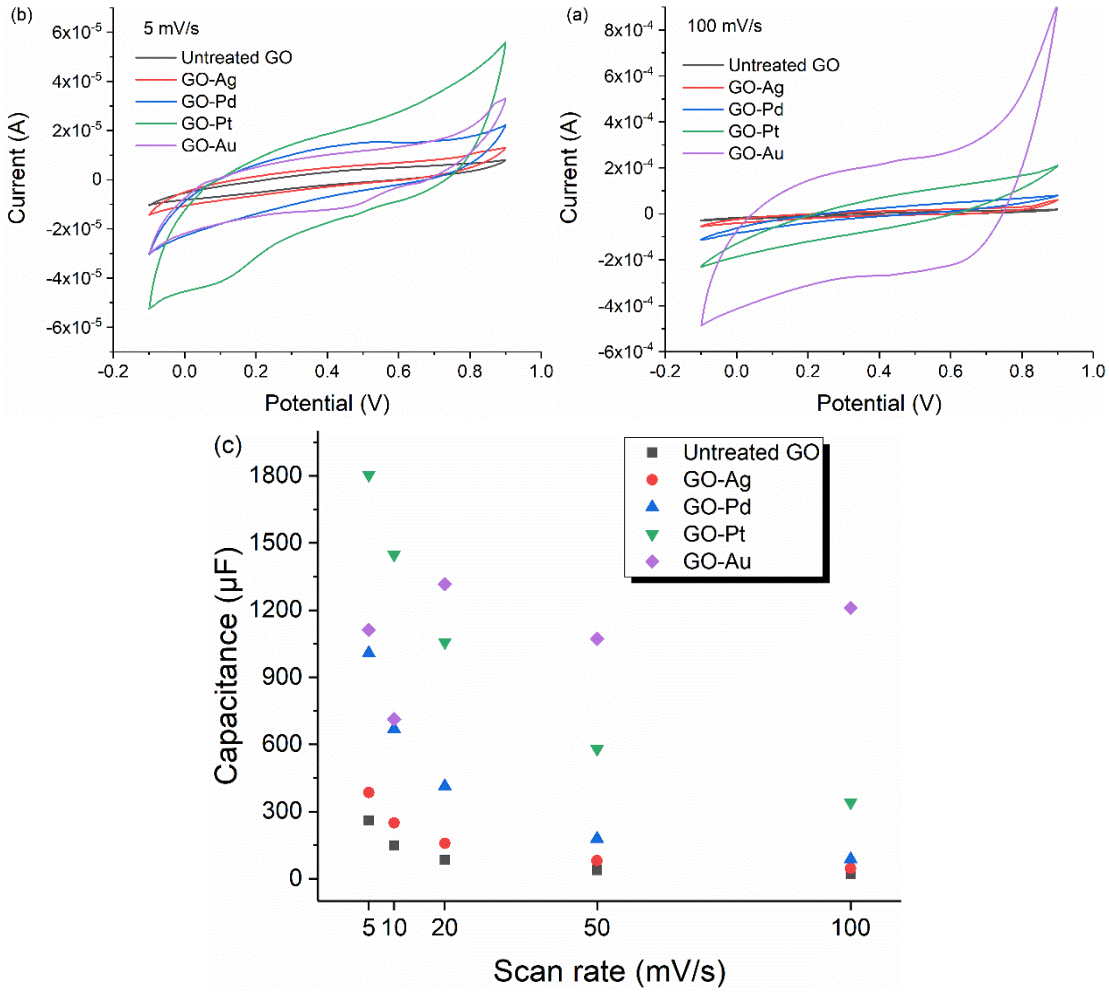


Fig. 4-48 Comparison of CV curves of ASP treated GO with noble metal lids at (a) 100 mV $s^{-1}$ and (b) 5 mV $s^{-1}$, (c) capacitances at different scan rates.

(2). EIS test

EIS tests were also conducted to further investigate the electrochemical performance of these GO samples. Fig. 4-49 shows the Nyquist plots of the EIS results for all the samples, and Table 4-13 exhibits some of the parameters of the equivalent circuit fit of the EIS results.

Since ESR consists of electrode resistance, electrolyte resistance, and contact resistance between electrode and current collector, and the conditions of the electrochemistry tests are the same, the ESR values of these GO samples

should be in corresponding to their sheet resistances, as those of ASP treated GO lower than that of untreated GO, with that of GO-Au the lowest, and that of GO-Pt the second. However, in this case, the ESR of GO-Pd is even larger than that of untreated GO. The deviant of GO-Pd may be owing to the other factors involved.

In regard of $R_{ct}$, all those of ASP treated GO are smaller than that of untreated GO, and follows the exactly same trend as the capacitance calculated in CV curves at the scan rate of 5 mV/s, as the smallest $R_{ct}$ belongs to GO-Pt, which can be as low as only around 0.66 kΩ.

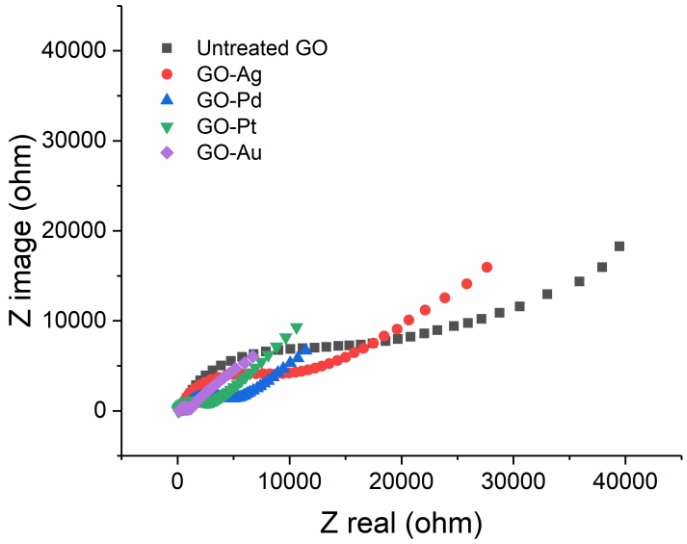


Fig. 4-49 Nyquist plots of untreated GO and ASP treated GO with different noble metal lids.

Table 4-13 Parameters of the equivalent circuit fit of the EIS results

| | ESR (kΩ) | $R_{ct}$ (kΩ) | $Y_o$ ($S \cdot s^{\alpha}$) | α | $W_d$ ($S \cdot s^{1/2}$) | Goodness |
|---|---|---|---|---|---|---|
| **Untreated GO** | 0.64 | 15.82 | $5.60\times10^{-6}$ | 0.89 | $1.26\times10^{-4}$ | $2.70\times10^{-3}$ |
| **GO-Ag** | 0.35 | 8.99 | $5.19\times10^{-6}$ | 0.91 | $1.59\times10^{-4}$ | $1.40\times10^{-3}$ |
| **GO-Pd** | 0.70 | 3.89 | $6.79\times10^{-6}$ | 0.92 | $4.09\times10^{-4}$ | $0.42\times10^{-3}$ |
| **GO-Pt** | 0.20 | 0.66 | $4.49\times10^{-6}$ | 0.94 | $5.73\times10^{-4}$ | $3.65\times10^{-3}$ |
| **GO-Au** | 0.04 | 2.39 | $4.66\times10^{-6}$ | 0.94 | $3.32\times10^{-4}$ | $0.39\times10^{-3}$ |

(3). GCD test

GCD test was also conducted for further comparison, and the results are shown in Fig. 4-50. Still, the charge and discharge lines are nearly symmetrical for all the GO samples, but the charge/discharge plot is not exactly an isosceles triangle, indicating the feasibility for SC application with some pseudocapacitive characteristics in the electrodes. This is particularly true for GO-Au, as there is an inflection point in the discharge process. The sequence of charge/discharge time length of all the GO samples follows the same sequence of capacitance at a scan rate of 5 mV $s^{-1}$, with the longest charge/discharge time of GO-Pt exhibiting the largest capacitance. Conversely, the smallest IR drop for GO-Pt also indicates the smallest internal resistance of GO-Pt. The GCD results once again suggests that GO-Pt is the most promising for SC applications. The cyclic performance of GO-Pt is shown in the next section on duration effect.

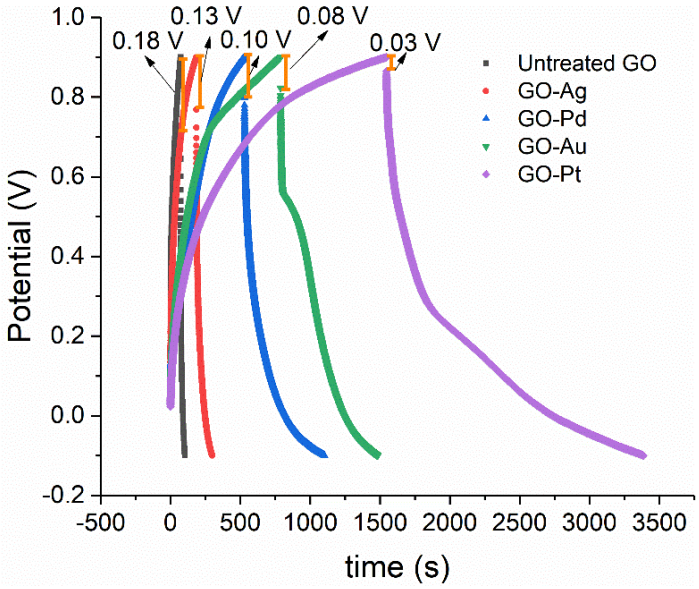


Fig. 4-50 GCD plot of untreated GO and ASP treated GO with different noble metal lids.

## 4.8 Results of Duration Effect on ASP Treatment

From all the characterisations and test results interpreted above, it can be deduced that GO-Pt is the most promising GO samples for the application of SCs. Therefore, GO-Pt treated for different durations were tested to explore the relevant effect on the ASP treatment. The durations are set as 1, 2, and 3 h. All the other conditions are the same, at a total gas pressure of 0.75 mbar using gas mixture of nitrogen and hydrogen in the ratio of 1:3, with temperature at 100 ℃.

### 4.8.1 Micro-structure

1. SEM observation and EDS results

SEM images of GO-Pt treated for three durations are shown in Fig. 4-51(a-f). There is no particle observed in all these SEM images, except for some unknown stains in the GO-Pt treated for one or three hours. This suggest that the form of the platinum nanoparticles deposited on GO-Pt will not alter (such as aggregation like silver in GO-Ag) for an extended duration.

Also, no difference is found in the element content, as listed in Table 4-14, suggesting no composition change in ASP treatment of longer durations.

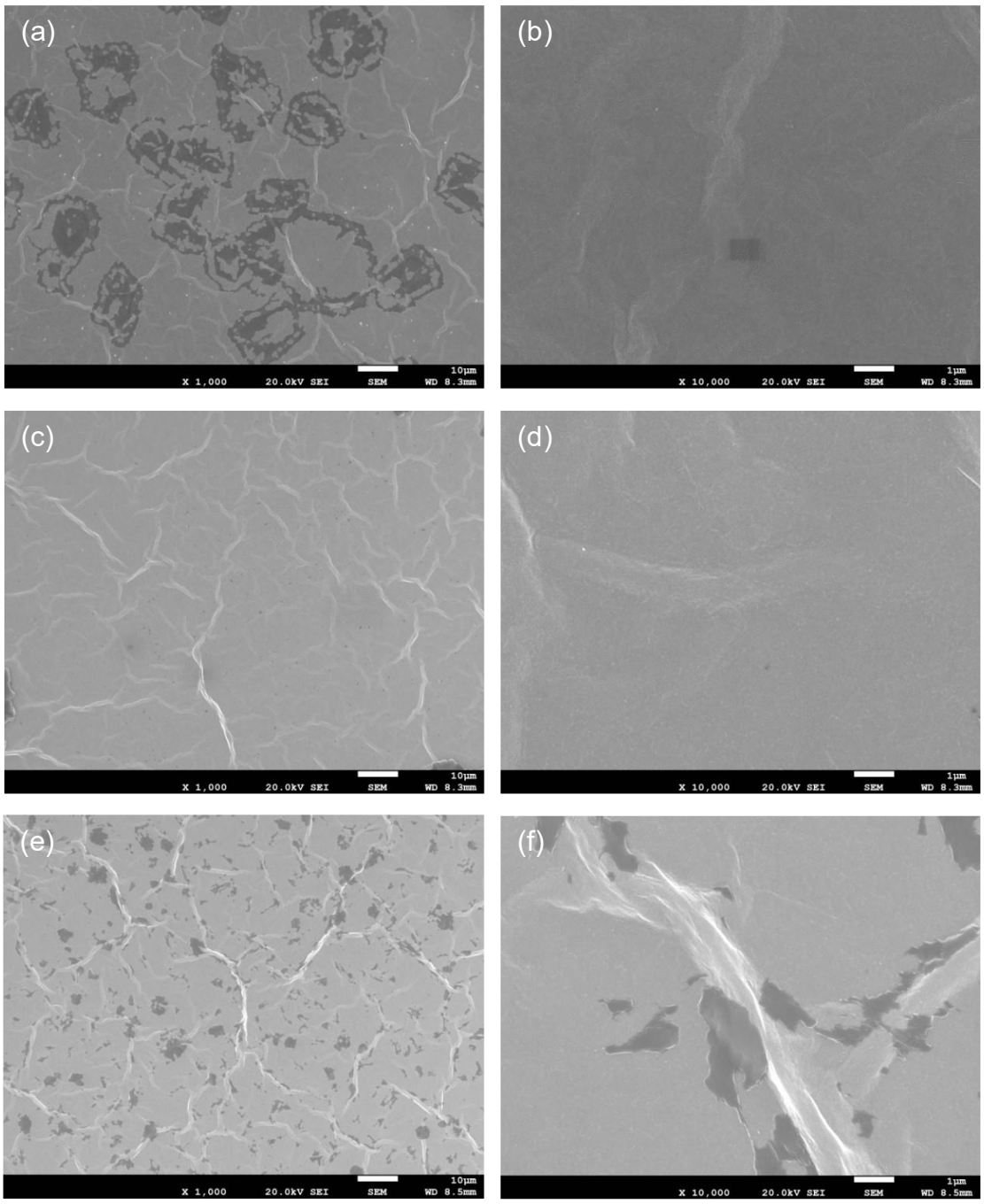


Fig. 4-51 SEM images of GO-Pt for different durations (a-b) 1 h, (c-d) 2 h, and (e-f) 3 h.

Table 4-14 Element content weight percentage of GO-Pt treated for different durations

| | C | N | O | Si | S | Fe | Pt |
|---|---|---|---|---|---|---|---|
| **1 h** | 41.24 | 1.54 | 15.60 | 39.85 | 1.08 | 0.10 | 0.59 |
| **2 h** | 44.01 | 2.81 | 16.46 | 35.60 | 0.80 | / | 0.32 |
| **3 h** | 41.85 | 3.03 | 18.18 | 34.92 | 1.09 | 0.29 | 0.65 |

2. Raman spectra

Fig. 4-52 and Table 4-15 show the Raman spectra of GO-Pt treated for different durations and their corresponding details, respectively. Still, these Raman spectra of GO-Pt treated for the three different durations are close to each other, indicating a longer duration of ASP treatment does not have an impact on the GO structure.

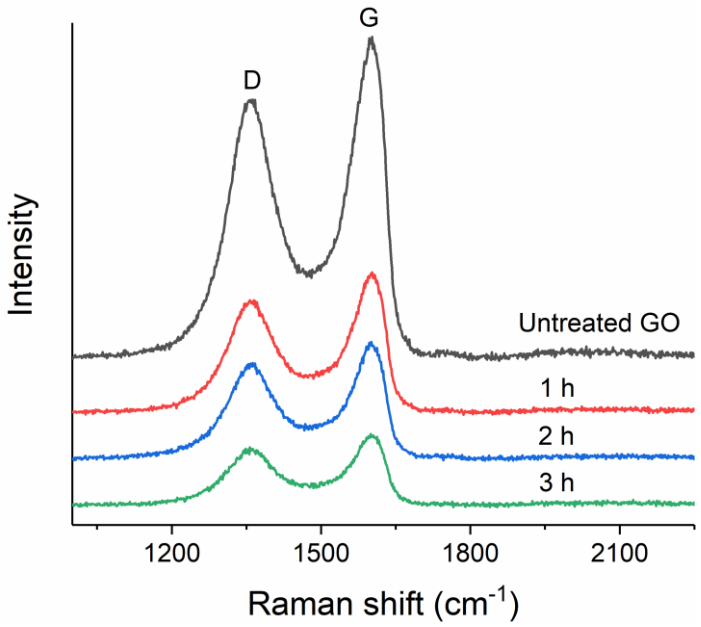


Fig. 4-52 Raman spectra of untreated GO with GO-Pt treated for different durations.

Table 4-15 Raman spectra details of untreated GO and GO-Pt treated for different durations

| | D peak | | G peak | | $I_D/I_G$ |
|---|---|---|---|---|---|
| | Wavelength/$cm^{-1}$ | FWHM/$cm^{-1}$ | Wavelength/$cm^{-1}$ | FWHM/$cm^{-1}$ | |
| **Untreated GO** | 1357 | 139 | 1597 | 92 | 0.858 |
| **1 h** | 1357 | 115 | 1602 | 81 | 0.801 |
| **2 h** | 1363 | 116 | 1601 | 81 | 0.820 |
| **3 h** | 1357 | 115 | 1600 | 83 | 0.810 |

3. XPS analysis

Due to the similarity of all the spectra survey and the high-resolution spectra of

the key elements of GO-Pt treated for different durations, the spectra are shown in Appendix (Fig. A-4 to Fig. A-8). The atomic contents of the elements are displayed in Table 4-16. and the relevant information of the split peaks of C1s, N1s and O1s are listed in Table 4-17.

Table 4-16 Atomic percentages of elements in GO-Pt treated for different durations

| | **1 h** | **2 h** | **3 h** |
|---|---|---|---|
| **C1s** | 45.34 | 54.75 | 53.74 |
| **O1s** | 37.13 | 25.51 | 23.62 |
| **N1s** | 7.78 | 7.32 | 9.39 |
| **Fe2p** | 1.61 | 1.38 | 2.17 |
| **Cr2p** | 0.83 | 1.15 | 1.05 |
| **Pt4f** | 7.31 | 9.89 | 10.03 |

Table 4-17 Binding energies and atomic percentages of split peaks in XPS spectra of C1s, N1s and O1s in GO-Pt treated for different durations

| | **1 h** | | **2 h** | | **3 h** | |
|---|---|---|---|---|---|---|
| | BE*/eV | **% | BE/eV | % | BE/eV | % |
| **Peak A (C-C)** | 284.8 | 67.3 | 284.8 | 76.3 | 284.8 | 80.4 |
| **Peak B (C-O/C-N)** | 285.6 | 26.2 | 285.6 | 18.8 | 286.3 | 13.1 |
| **Peak C (C=O)** | 288.6 | 6.5 | 288.8 | 4.9 | 288.5 | 6.5 |
| **Peak D (Pyridinic N)** | 398.2 | 32.7 | 398.2 | 37.3 | 398.2 | 35.8 |
| **Peak E (Pyrrolic N)** | 399.7 | 16.4 | 399.9 | 19.8 | 399.8 | 15.5 |
| **Peak F (Graphitic N)** | 401.6 | 50.9 | 401.8 | 42.9 | 401.6 | 48.7 |
| **Peak G (Metal oxides)** | 529.8 | 6.5 | 529.9 | 7.0 | 529.7 | 5.7 |
| **Peak H (C-O/C=O)** | 531.8 | 93.5 | 532.0 | 93.0 | 531.8 | 94.3 |

*BE: Binding energy
**%: Atomic percentage

Still, the XPS results are basically close to each other, except a higher content of carbon and a lower content of oxygen in GO-Pt treated for 2 h and 3 h. Correspondingly, as to the spectra deconvolution, Peak A of GO-Pt treated for 2 and 3 h are higher than that of the counterpart treated for only 1 h, and Peak B are accordingly lower (Fig. A-5). This implies that GO-Pt got further reduction

in the second hour of ASP treatment, but the reduction slows down in the third hour. The increase of nitrogen in the third hour is mild, but the doping configurations stay the same (Fig. A-6). Also, a faint increase of metal element contents suggests more metal deposition on GO-Pt, due to the continuous sputtering.

As to high-resolution Fe2p spectra, the peaks of GO-Pt treated for 2 and 3 h get broader than that of the counterpart ASP treated for 1 h, but the broader peak is still assigned to the oxidised states (Fig. A-8). The Cr2p spectra are identical, showing the oxidised state as well (Fig. A-8).

### 4.8.2 Electrical and electrochemical properties

1. Sheet resistance measurement

Fig. 4-53 displays the sheet resistances of GO-Pt treated for different durations. The duration of 0 h denotes the untreated GO. The sheet resistance of GO-Pt treated for 2 h drops to around $2.7\times10^3$ Ω $sq^{-1}$, an order of magnitude lower than that for 1 h. However, the sheet resistance remains almost the same as that of 2 h when the duration reaches 3 h. The trend of the sheet resistances of GO-Pt treated for different durations can be traced to the element content in XPS results. According to the XPS results above, the improvement of sheet resistance is likely to be owing to both GO reduction and the deposited metal layer.

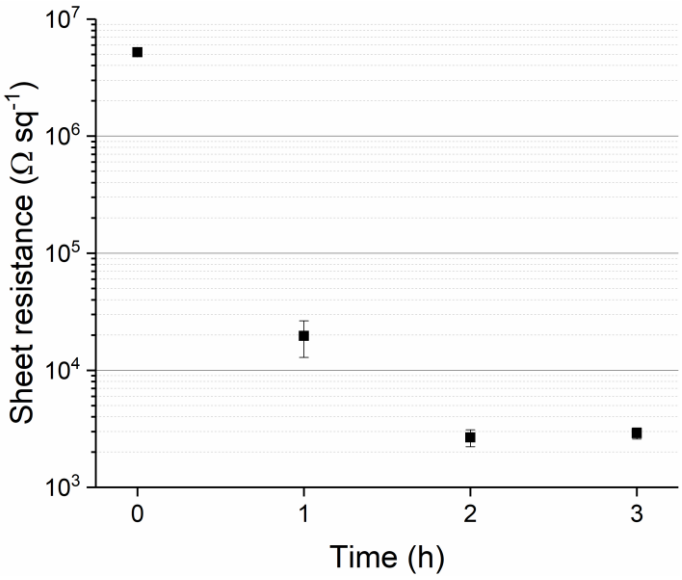


Fig. 4-53 Sheet resistances of GO-Pt treated for different durations.

2. Electrochemistry tests

(1). CV test

The CV curves are displayed in Appendix (Fig. A-9), and the compared CV curves at a scan rate of 100 mV $s^{-1}$ among samples, as well as the capacitances calculated accordingly, are shown in Fig. 4-54.

As expected, the CV curves shows much better quasi-rectangles, and the capacitances get increased with longer durations. It is also noted that the increase of the capacitance from 2 h to 3 h is not as significant as that from 1 h to 2 h. This also accords to trend of sheet resistances.

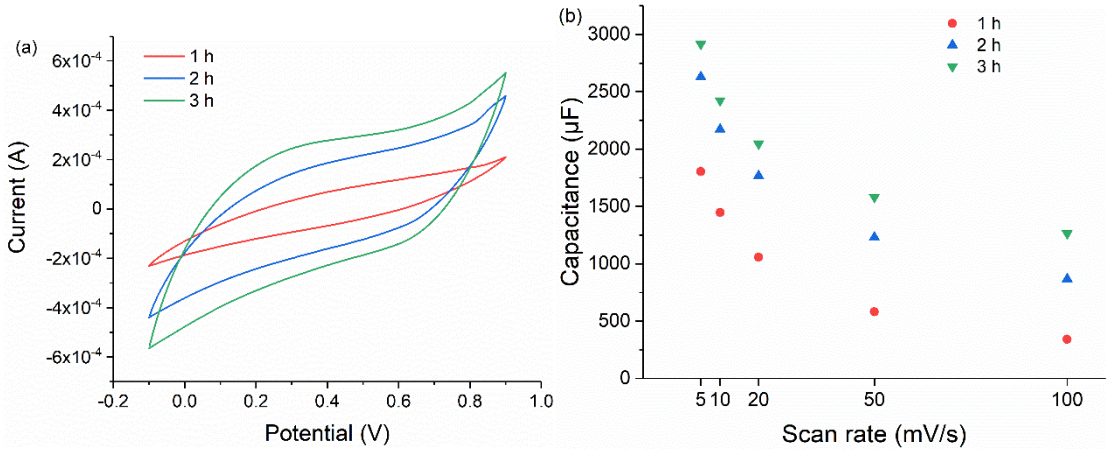


Fig. 4-54 (a) Comparison of CV curves of GO-Pt treated for different durations at 100 mV $s^{-1}$, and (b) capacitances at different scan rates.

(2). EIS test

EIS tests were also conducted to investigate the electrochemical performance of these GO samples, and the results are shown in Fig. 4-55, with some parameters of the equivalent circuit fit of the EIS results in Table 4-18. Still similarly, both ESR and $R_{ct}$ get smaller for longer treatment duration, which is also consistent with that of the lower sheet resistance and higher capacitance.

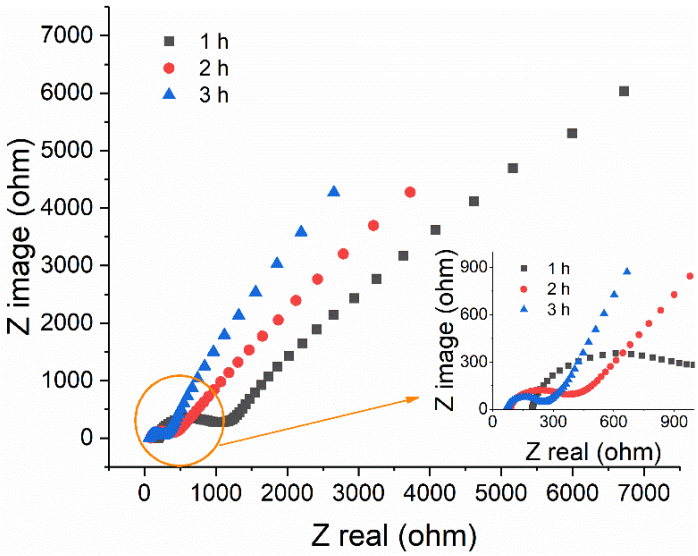


Fig. 4-55 Nyquist plots of GO-Pt treated for different durations.

Table 4-18 Parameters of the equivalent circuit fit of the EIS results of GO-Pt treated for different durations

| | ESR (kΩ) | $R_{ct}$ (kΩ) | $Y_o$ ($S \cdot s^{\alpha}$) | α | $W_d$ ($S \cdot s^{1/2}$) | Goodness |
|---|---|---|---|---|---|---|
| **1 h** | 0.20 | 0.66 | 4.49×10-6 | 0.94 | 5.73×10-4 | 3.65×10-3 |
| **2 h** | 0.09 | 0.23 | 3.85×10-6 | 0.96 | 9.88×10-4 | 7.98×10-3 |
| **3 h** | 0.07 | 0.13 | 2.77×10-6 | 1.00 | 15.40×10-4 | 29.69×10-3 |

(3). GCD test

GCD results are shown in Fig. 4-56. Still, the charge and discharge lines of all the GO-Pt samples shows similar trend, indicating the feasibility for SC application with some pseudocapacitive characteristic in the electrodes.

However, the total GCD time for the one treated for 2 h reaches 6918 s, a little longer than that of the one treated for 3 h of 5668 s, although both share a similar charging time of around 2340 s. This longer discharging time of GO-Pt for 2 h than that of the one treated for 3 h is contrary to the result of capacitance, and the reason is unknown. Still, the IR drop decrease with an increase of the treatment duration, with the lowest of 3 h only about 0.01 V. Also, all the GO-Pt samples for different durations show good cyclic performance, as the deterioration of the charge/discharge time is insignificant.

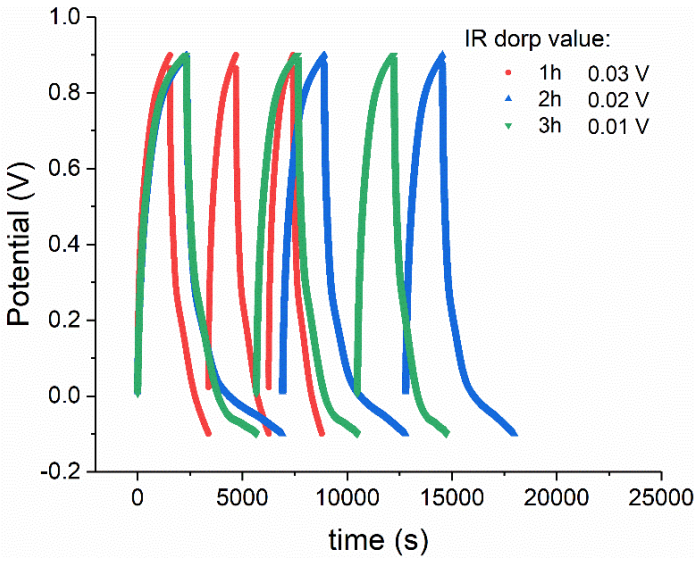


Fig. 4-56 GCD plots of GO-Pt treated for different durations.

## 4.9 Results of Gas Pressure Effect on ASP Treatment

Finally, the effect of gas pressure on ASP is studied, since the gas pressure is one of the significant parameters in plasma treatment, having an impact on the discharge current of plasma and the concentration of the ionised particles. Still, GO-Pt is selected in this section. A pressure of 1.50 mbar is set to compare with GO-Pt treated at 0.75 mbar. The other parameters are the same: using gas mixture of nitrogen and hydrogen in the ration of 1:3, at a temperature of 100 ℃, for a duration of 1 h.

### 4.9.1 Micro-structure

1. SEM observation and EDS results

Fig. 4-57 displays the SEM images of GO-Pt treated at 1.50 mbar and EDS result. The morphology is of no difference with GO-Pt treated at 0.75 mbar (Fig. 4-31(e-f) or Fig. 4-51(a-b)), as no particles can be observed on the GO film.

Still, element platinum can be detected in EDS, but in an extremely low content (Fig. 4-57(c)).

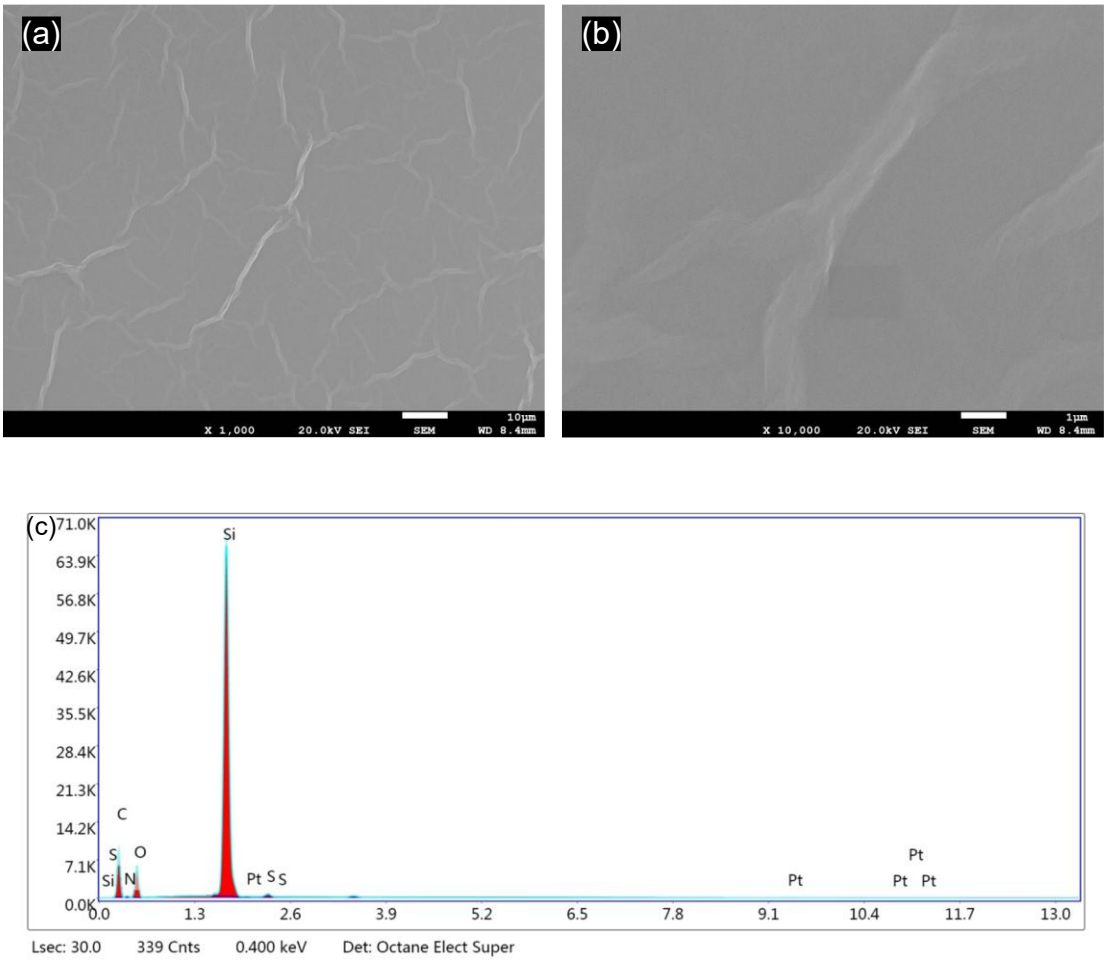


Fig. 4-57 (a, b) SEM images of GO-Pt treated at 1.50 mbar in different magnifications, (c) EDS results of GO-Pt treated at 1.50 mbar.

2. Raman spectra

The Raman spectra of untreated GO and GO-Pt treated at these two gas pressures are shown in Fig. 4-58, and the dominant D and G peaks feature in the Raman spectra. As expected, the two GO-Pt samples share similar Raman spectra results, with a lower FWHM(G) and $I_D/I_G$, as well as an upward moved G peak. Compared to be treated at 0.75 mbar, GO-Pt treated at 1.50 mbar has

a little higher FWHM(G) and $I_D/I_G$, and the G peak increases to 1604 $cm^{-1}$ from 1602 $cm^{-1}$ (Table 4-19). If not considering the effect of deviation, this may imply that more disorders are in GO-Pt treated at 1.50 mbar, with smaller crystalline size, which means poorer plasma effects. This indicates that the gas pressure of 0.75 mbar is more suitable for ASP treatment on GO.

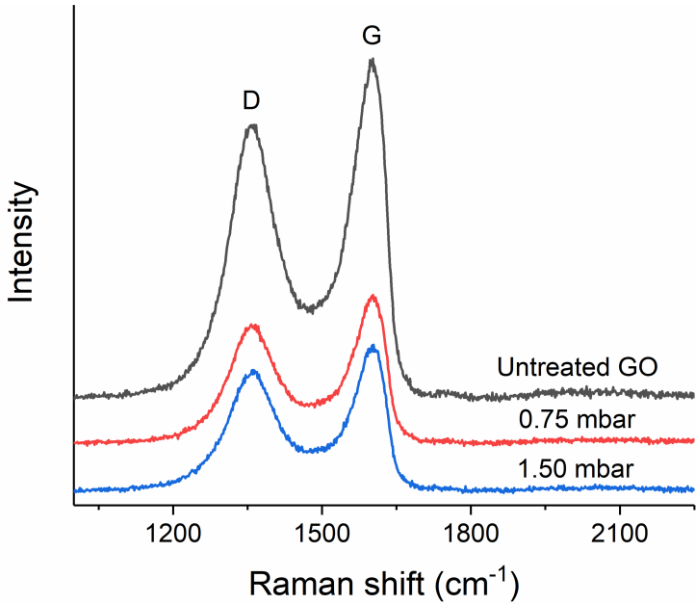


Fig. 4-58 Raman spectra of untreated and GO-Pt treated at different gas pressures.

Table 4-19 Raman spectra details GO-Pt treated at different gas pressures

| | D peak | | G peak | | $I_D/I_G$ |
|---|---|---|---|---|---|
| | Wavelength/$cm^{-1}$ | FWHM/$cm^{-1}$ | Wavelength/$cm^{-1}$ | FWHM/$cm^{-1}$ | |
| **Untreated GO** | 1357 | 139 | 1597 | 92 | 0.858 |
| **0.75 mbar** | 1357 | 115 | 1602 | 81 | 0.801 |
| **1.50 mbar** | 1361 | 116 | 1604 | 82 | 0.826 |

3. XPS analysis

For further comparison, XPS was conducted, and all the spectra figures are shown in Appendix (Fig. A-10 to Fig. A-14), still due to their similarity with those shown before. The atomic contents of the elements are listed in Table 4-20, and

the deconvolution of C1s, N1s and O1s spectra are in Table 4-21.

Table 4-20 Atomic percentages of elements in GO-Pt treated at different gas pressures

| | **0.75 mbar** | **1.50 mbar** |
|---|---|---|
| **C1s** | 45.34 | 56.72 |
| **O1s** | 37.13 | 23.24 |
| **N1s** | 7.78 | 9.92 |
| **Fe2p** | 1.61 | 1.03 |
| **Cr2p** | 0.83 | 0.35 |
| **Pt4f** | 7.31 | 8.74 |

Table 4-21 Binding energies and atomic percentages of split peaks in XPS spectra of C1s, N1s and O1s in GO-Pt treated at different gas pressures

| | **0.75 mbar** | | **1.50 mbar** | |
|---|---|---|---|---|
| | BE*/eV | **% | BE/eV | % |
| **Peak A (C-C)** | 284.8 | 67.3 | 284.8 | 61.0 |
| **Peak B (C-O/C-N)** | 285.6 | 26.2 | 286.0 | 34.0 |
| **Peak C (C=O)** | 288.6 | 6.5 | 288.6 | 5.0 |
| **Peak D (Pyridinic N)** | 398.2 | 32.7 | 398.2 | 29.5 |
| **Peak E (Pyrrolic N)** | 399.7 | 16.4 | 399.7 | 23.4 |
| **Peak F (Graphitic N)** | 401.6 | 50.9 | 401.2 | 47.1 |
| **Peak G (Metal oxides)** | 529.8 | 6.5 | 528.4 | 0.5 |
| **Peak H (C-O/C=O)** | 531.8 | 93.5 | 531.9 | 99.5 |

*BE: Binding energy
**%: Atomic percentage

For GO-Pt treated at 1.50 mbar, compared to the one treated at 0.75 mbar, Peak A is lower and Peak B is higher, which means a poorer reduction effect. As to the lower content of oxygen (Table 4-20), it is due to the lower content of metal oxides, as Peak G is also extremely low, not comparable to that of 0.75 mbar. In the high-resolution Fe2p spectra, there is a more significant peak in light green at a lower binding energy (Fig. A-14(a)), which may represent the pure metal iron. Based on the different oxidisation effect of iron, it is inferred that the oxidisation of metals are possibly occurs during the ASP treatment, and

the oxygen source are the oxygen functional groups removed from GO.

### 4.9.2 Electrical and electrochemical properties

1. Sheet resistance measurement

Fig. 4-59 shows the sheet resistances of GO-Pt treated at different gas pressures. For GO-Pt treated at 1.50 mbar, the sheet resistance is about $4.6\times10^5$ Ω $sq^{-1}$, which is one order of magnitude higher than that of GO-Pt treated at 0.75 mbar ($2.0\times10^4$ Ω $sq^{-1}$), but still lower than the untreated GO. According to the XPS results, the higher sheet resistance of GO-Pt treated at 1.50 mbar than that of GO-Pt treated at 0.75 mbar results from the poorer reduction effect of GO, and possibly also from the metal layer, which is not reflected from the element content in XPS, due to the inaccuracy with insignificant difference. The cause of higher sheet resistance of GO-Pt treated at higher gas pressure will be discussed in detail in Section 4.10.2.

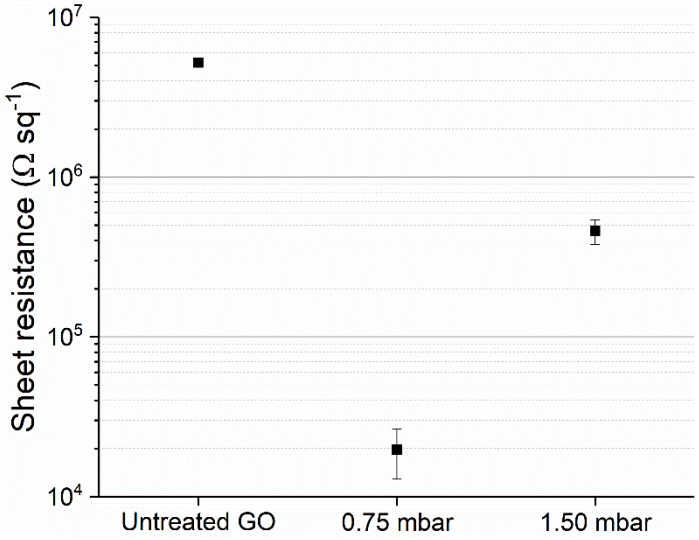


Fig. 4-59 Sheet resistances of GO-Pt treated at different gas pressures.

## 2. Electrochemistry tests

### (1). CV test

The CV curves are shown in Appendix (Fig. A-15), and the CV curves for comparison at a scan rate of 100 mV $s^{-1}$, as well as the capacitances calculated at different scan rates, are shown in Fig. 4-60.

As shown in Fig. A-15, the broadening of the capacitive currents near 0.8 V, as well as a small hump at around 0.6 V in the negative current section were especially significant, and it is more obviously compared to the one of GO-Pt treated at 0.75 mbar, as shown in Fig. 4-60(a). As repeatedly mentioned in Section 4.2.2, it could be ascribed to the incorporation of transition metal oxides during the ASP treatment. However, the capacitance of GO-Pt treated at 1.50 mbar is much lower than that of GO-Pt treated at 0.75 mbar, which agrees with the result of higher sheet resistance.

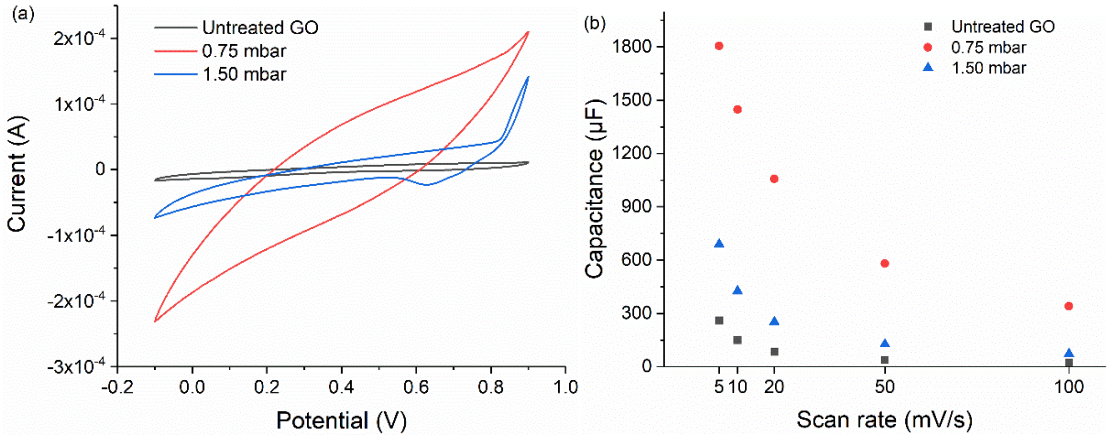


Fig. 4-60 (a) Comparison of CV curves of GO-Pt treated at different gas pressures at 100 mV $s^{-1}$, and (b) capacitances at different scan rates.

(2). EIS test

Fig. 4-61 shows the Nyquist plots of the EIS results for all the samples, and Table 4-22 exhibits some of the parameters of the equivalent circuit fit of the EIS results. Comparable to the capacitance from the CV curves, it is found that the $R_{ct}$ of GO-Pt treated at 1.50 mbar is higher than that of GO-Pt treated at 0.75 mbar, which is also consistent with that of the higher sheet resistance and smaller capacitance.

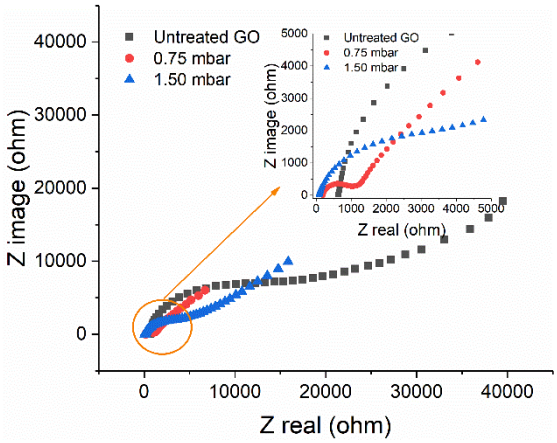


Fig. 4-61 Nyquist plots of GO-Pt treated at different gas pressures.

Table 4-22 Parameters of the equivalent circuit fit of the EIS results of GO-Pt treated at different gas pressures

| | ESR (kΩ) | $R_{ct}$ (kΩ) | $Y_o$ ($S \cdot s^{\alpha}$) | α | $W_d$ ($S \cdot s^{1/2}$) | Goodness |
|---|---|---|---|---|---|---|
| **Untreated GO** | 0.64 | 15.82 | 5.60×10-6 | 0.89 | 1.26×10-4 | 2.70×10-3 |
| **0.75 mbar** | 0.20 | 0.66 | 4.49×10-6 | 0.94 | 5.73×10-4 | 3.65×10-3 |
| **1.50 mbar** | 0.08 | 4.36 | 13.10×10-6 | 0.82 | 2.47×10-4 | 1.50×10-3 |

(3). GCD test

GCD test was also conducted for further comparison, and the results are shown in Fig. 4-62. Still, the charge and discharge lines are nearly symmetrical for all the GO samples, but the charge/discharge plots are not exactly isosceles

triangles, indicating the feasibility for SC application with some pseudocapacitive characteristics in the electrodes. As to GO-Pt treated at 1.50 mbar, the total GCD time is only for 1157 s, much shorter than that of GO-Pt treated at 0.75 mbar, and its IR drop is a little higher than the counterparts. This is consistent with the results of the capacitance from the CV curves, indicating a poorer super-capacitive performance.

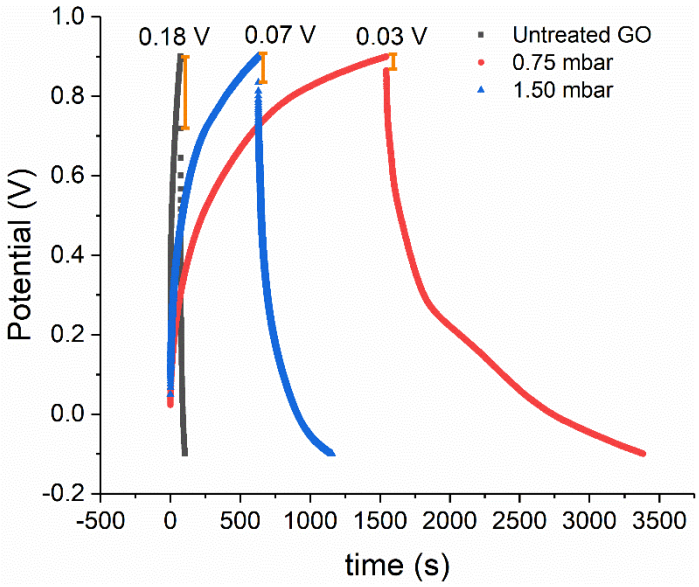


Fig. 4-62 GCD plot of GO-Pt treated at different gas pressures.

# 4.10 Mechanism of Metal Sputtering Effects

## 4.10.1 Metal Sputtering in ASP

Sputtering is a vacuum-based process widely used for thin film deposition, in which atoms or clusters from the source material are ejected in response to ion bombardment and transfer towards the substrate surface with some kinetic energy. These atoms and small clusters deposited on the substrate surface

undergo nucleation and growth, forming a film covered on the substrate. In sputtering techniques, the source material that offers ejected atoms to form films in the sputtering process is termed as the “target”, which is often biased with a negative potential. The positively-charged ions are attracted and move to the negative-charged target as incident ions. When the energy of the incident ions is sufficient enough to exceed the threshold energy, the surface binding energy of the target, atoms and clusters are ejected from the target material [443].

As discussed in Section 2.3.2.4, in the case of ASP, a metal active screen is connected to the cathode and functions as the target. The ions within the plasma bombard the active screen during the ASP treatment and some atoms sputtered off from the screen can deposit on the samples even at a floating potential. This has been evidenced by the traces of iron and chromium detected by XPS from ASP treated GO (Fig. 4-22 and Fig. 4-26).

In Section 4.7, the active screen used for the hybrid plasma modification and deposition of noble metal consisted of both a stainless-steel cage and a noble metal lid positioned on the cage, as described in Fig. 3-1(b). During the hybrid treatment, atoms were sputtered off from the noble metal lid as well as the stainless-steel cage (iron and chromium). The noble metal atoms sputtered off from the top noble metal lid moved through the holes in the stainless-steel mesh lid of the cage and co-deposit with iron and chromium atoms from the stainless-

steel lid on the GO surfaces placed on the worktable at a floating potential within the active screen cage, as shown in Fig. 2-17(c).

There are several factors affecting the sputtering process such as: target material, deposition pressure, discharge voltage and current, distance between target and substrate, precursor gas composition and flow rate, etc. In this study, except for GO-Pt, all other ASP hybrid treatments were conducted under the same plasma processing conditions and hence the discussion in this section is focused on the effect of noble metals.

In this study, the gases used in the hybrid ASP modification with noble metal deposition are a mixture of nitrogen and hydrogen. As they are reactive gases, the sputtering should also be regarded as reactive sputtering, because the gases could react with the metals used during the sputtering [444]. This is supported by the fact that some metal nitrides were detected by the XPS N1s for GO-Ag and GO-Au, as shown in Fig. 4-43.

However, the metal nitrides are in essence iron nitrides and/or chromium nitrides in these samples, as only iron and chromium ions are detected in the XPS spectra of Fe2p and Cr2p (Fig. 4-45); no other noble metal nitrides were detected from the analysis of their corresponding high-resolution XPS (Fig. 4-46). Also, it should be noted that the iron nitrides and/or chromium nitrides did not dominate the composites of the deposition film, as the percentages of the metal nitrides in XPS N1s spectra of GO-Ag and GO-Au are very small, and

are not even detectable in GO-Pd and GO-Pt (Fig. 4-43). The negligible concentrations of metal nitrides in the ASP sputtering deposited layer are possibly due to the mild conditions used (relatively low temperature) [445, 446].

Sputtering yield, the number of target atoms ejected per incident particles, is a very important parameter representing the amount of the target ejected in sputtering. It is known that the value of sputtering yield depends on the target material and the incident particles, and so far, some models and simulations of sputtering yield have been developed, as various equations have been proposed to calculate the value of sputtering yield [447, 448]. Specifically, the sputtering yield is determined by the masses of target atoms and incident ions, the energy of incident ions and the surface binding energy of target material, etc. Given the same sputtering conditions used in this study, the sputtering yield is mainly determined by the metal types, and the sputtering rate of the metal elements used in this study are listed in Table 4-23. The sputtering rate shown in the table is calculated based on the thin film deposition rate at a maximum power density (around 250 W/in$^2$) and distance of 4 inches between source and substrate. Although the sputtering rate shown in the table may differ from the sputtering rate of the noble metal lids used in this research, it provides their relative ranking in sputtering rates. For example, it can be seen from this table that silver possesses the highest sputtering yield among all these six metals, and that the sputtering yield of transition metals iron and chromium are the lowest among these metals.

Table 4-23 Parameters of metal elements

| | Ag | Pd | Pt | Au | Fe | Cr |
|---|---|---|---|---|---|---|
| **Electrical resistance / nΩ·m** | 15.87 | 105.4 | 105 | 22.14 | 96.1 | 125 |
| **Density / g·cm$^{-3}$** | 10.5 | 12.02 | 21.45 | 19.31 | 7.86 | 7.2 |
| ***Sputtering rate / nm·s$^{-1}$** | 38.0 | 27.0 | 20.5 | 32.0 | 18.0 | 18.0 |

*Obtained from: http://www.semicore.com/reference/sputtering-yields-reference

## 4.10.2 Improved Performances of GO-Pt and GO-Au

As reported in Section 4.7, when an extra active-screen lid of noble metal is added on the stainless-steel active screen cage in ASP treatment, it is found that the corresponding noble metal from the added noble metal lid, as well as iron and chromium from the stainless-steel cage were deposited on the surfaces of GO samples.

Enhancement in electrical and electrochemical properties, compared to those of untreated GO and ASP modified GO, and the potential mechanism involved will be discussed in this section, as the hybrid ASP treatments using different noble metal lids exhibited different degrees of the enhancement. Therefore, the sheet resistances and capacitances of the GO samples treated by the hybrid ASP processes with noble metal lids (GO-M, M stands for Ag, Pd, Pt or Au) are first compared with GO samples treated by typical ASP processes without extra noble lid (NGO) using the same gas mixture (viz. the sample $N_2H_2$-GO in Section 4.3 or NH13 in Section 4.5).

As shown in Fig. 4-63(a), the sheet resistances of GO-Pt and GO-Au are superior to NGO, while sheet resistances of GO-Ag and GO-Pd are comparable

with, or even inferior to, NGO. Similarly, the capacitance of GO-Pt is higher than that of NGO, while the capacitances of GO-Ag and GO-Pd are lower (Fig. 4-63(b)). The capacitance of GO-Au is scan rate dependent, the capacitance is much higher than that of NGO at high scan rates (20-100 mV $s^{-1}$), but lower than that of NGO when the scan rate is decreased (5-10 mV $s^{-1}$). These experimental results indicate that different types of the noble metals sputtered and deposited on GO have different or even opposite effects. Thus, questions arise as to the reasons for the different effects of these noble metals on the properties of GO.

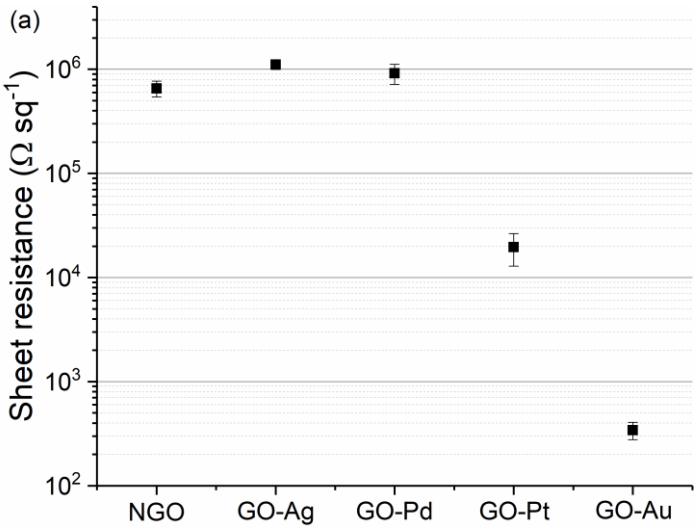

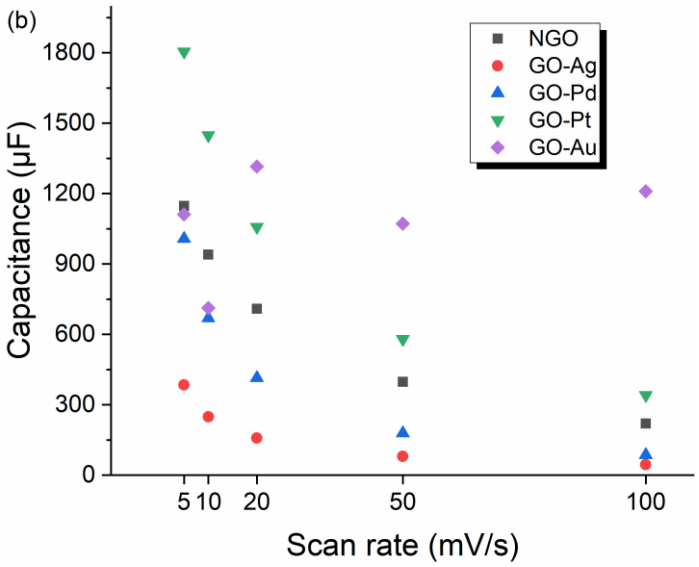


Fig. 4-63 Comparison of NGO with GO deposited with noble metals in (a) sheet resistance and (b) capacitance.

As introduced in Section 2.2.2.3, all these four noble metals have been explored as additives for supercapacitor electrodes to improve the pseudo-capacitance. The performance improvement is attributed to the high conductivity of the noble metal nanoparticles that facilitates the effective transport of electrons [194]. However, here in this study of hybrid ASP treatments, only GO-Pt has met this expectation, while the other three are not (for GO-Ag and GO-Pd), or are not fully (for GO-Au), superior to the typical ASP treated NGO without using the noble metals. Given the fact that the palladium and platinum have the similar electrical resistance (Table 4-23) but GO-Pt significantly outperformed GO-Pd, the reasons for the different effects on capacitance could be related to the different forms of noble metals deposited on the GO surfaces.

When hybridising graphene with metal nanoparticles, the composites can be formed into different structures: encapsulated structure, wrapped structure,

anchored structure, mixed structure, sandwiched structure and layer structure, according to different synthesis process, as shown in Fig. 4-64 [187]. According to the sputtering process of metals in ASP treatment, the metal nanoparticles are deposited on the surface of GO surface. Thus, the structure of the GO-metal composition in this study should be layer structured, as metal nanoparticles would form a loose but well-distributed layer on the GO surface.

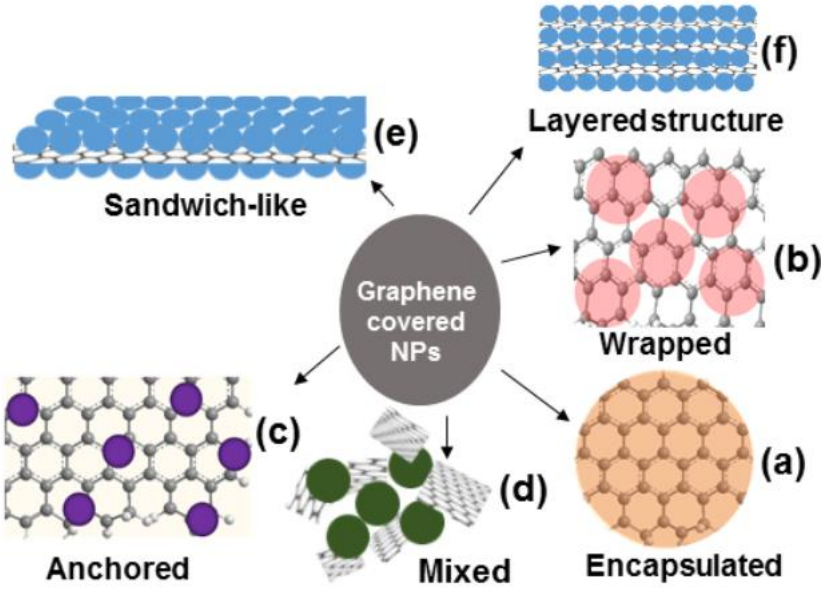


Fig. 4-64 Structures of hybrids of graphene and metal nanoparticles (a) graphene-encapsulated nanoparticles, (b) graphene-wrapped nanoparticles, (c) nanoparticles anchored to graphene sheets, (d) mixed graphene-nanoparticle structure, (e) graphene-nanoparticles sandwich structures, and (f) graphene-nanoparticle layered hybrids [187].

The hybridisation of graphene materials and metal nanoparticles can improve the electrical and electrochemical properties. Considering nanoparticle, the graphene sheets can act as a good host to support the distribution of nanoparticles, and to hinder the agglomeration of nanoparticles. The N-doped reduced GO is a good platform for electron transfer on its own, and act as a

connection for the metal nanoparticles for the enhancement of electrical conductivity [449].

Considering that the deposition of metal (viz. Pt, etc.) nanoparticles is also a type of doping that affects the electronic properties of graphene [450, 451], the metals deposited on graphene act as electrical contacts for applications. According to the experimental studies by Kulshrestha et al., the improvement of electrical performance can be contributed to both the contact improvement between graphene and metals, and the increased interlayer interaction [452]. The increase in interlayer interaction resulted from the doped charge carriers of platinum intercalation. Also, the deposited metals on the surface of graphene sheets can also affect the graphene layers below, as the metal diffuse from the top to the layers below, which can be assisted by defects in the graphene lattice, so that the electrical properties could improve through the vertical tunnelling of the charge carriers.

In relation to the electrochemical performance, although the mechanism of the enhancement by compositing platinum is not fully understood, it could be ascribed to three aspects. The first is the increase of the electrical conductivity by platinum nanoparticles acting as conductive bridges between defect in the graphene lattice for electron transportation [212], and between electrode and electrolyte [215]. Secondly, the deposition of metal nanoparticles can also increase the electrochemically active surface area by intercalating into

interlayers to increase the spacing as a diffusion channel for charge carriers to transfer their charge into the electrode [212], as well as by preventing aggregation of graphene sheets [453], which also contribute to the super-capacitive performance [214]. Thirdly, platinum nanoparticles can also participate into redox reactions to facilitate the ion transport in charge storage, resulting in an increase in higher super-capacitive performance [211]. The latter two reasons can also explain the increasing capacitance from 2 h to 3 h when the resistance remain the same.

As shown in Fig. 4-53 to Fig. 4-56 (Section 4.8), with increasing duration, more platinum can be sputtered out and deposited on GO, and hence doping intensity increase [454], so that the electrical and electrochemical performances are further improved.

Also as depicted in Fig. 4-59 to Fig. 4-62 in Section 4.99, an increase of the gas pressure from 0.75 to 1.5 mbar has a negative effect in the improvement of electrical and electrochemical properties. This can be mainly related to the mean free path, which represents the mean moving distance of a particle before colliding with other particles. An increase of the working gas pressure shortens the mean free path of both electrons and the ions. The electrons with shorter mean free path store less kinetic energy, thus fewer ionised particles are produced at the same temperature, and fewer target metal atoms (platinum atoms in this case) are sputtered off the active screen, and those that do,

possess less energy when reaching GO [455]. Also, the reduced mean free path implies a decrease of the probability of energetic gas atoms and molecules reaching the sample [456], due to the increased possibility of collision between the active species and the sputtered metal atoms [457]. Consequently, the sputtered atoms are more likely to be scattered away from the GO film, hence forming a thinner metal layer on the GO with a higher electrical resistance. Additionally, gas pressure also affects the structure of the deposited metal layer, as an increase of the gas pressure decreases the sputtered particle size and degrades the film crystallinity, which lowers the electrical conductivity of the metal film [457, 458].

Similarly, the increase of gas pressure and the resulting shorter mean free path also account for the poorer reduction effect, as generating fewer ionised and energetic particles that can interact with GO for its reduction.

As shown in Fig. 4-47, the sheet resistance of GO-Au is the lowest among all the GO samples, and the reasons for the decreased sheet resistance should be the same as for GO-Pt. The deposition of gold nanoparticles increased the electrical conductivity of the graphene-based composites via improved contact and the increased interlayer intercalation. Also, the higher electrical conductivity of gold than platinum (Table 4-23) should have contributed to the lower sheet resistances of GO-Au than GO-Pt.

Interestingly, however, the electrochemical performance of GO-Au is highly

scan rate dependent, as evidenced by the fact that the capacitance of GO-Au is the highest at high scan rates of 100, 50 and 20 mV/s, but the capacitance of GO-Au is inferior to GO-Pt and even NGO at low scan rates of 10 and 5 mV/s. The capacitances of GO-Au do not follow the normal increasing trend with the scan rate. This special behaviour of GO-Au is not reported so far in the literature, and the reason remains unknown, which necessitates further study in the future (see Chapter 6).

### 4.10.3 Inferior Performances of GO-Ag and GO-Pd

As shown in Fig. 4-63, whilst GO-Pt and GO-Au showed overall superior capacitance to NGO, both GO-Ag and GO-Pd shared similar inferior performances to NGO. However, the causes for the inferiority of these two are not the same and they are discussed below, respectively.

**1. GO-Ag**

Although pure silver particles initially sputtered from the active screen was also in nano scale, as indicated from the HRTEM in Fig. 4-36, these nano-scaled silver particles tend to aggregate into large particles with a size of about 1-2 microns, as shown in Fig. 4-31(a-b). It is interesting that for all these four noble metals, the phenomenon of aggregation only appears for silver, whilst the other three nano-scaled noble metals sputtered off the active screen deposited uniformly on GO surface without appreciable aggregation, as no large sized particles were observed in SEM imaging (Fig. 4-31(c-h)).

For silver nanoparticles, they are commonly found to aggregate into large particles when conditions allow. For instance, in a study of novel metal-doped ceria-decorated aminated graphene for supercapacitor, silver and platinum were deposited. It was found that the size of platinum nanoparticles were too small to be observed in SEM images, whilst silver nanoparticles aggregated into particles with a size of approximately 100 nm [453]. This is echoed by the recent findings by Li et al. from their work on plasma sputtering and deposition of silver and platinum on nanocarbon fibres [17]. In a research by Gao et al., the particle size of silver increased to 1 μm when the ratio of silver precursor to GO increased to 2:1 [459].

Although the reason for the silver aggregation is not fully understood, it is possibly related to the lowest density (atomic mass) but highest sputtering rate of silver among these four noble metals used in the research (Table 4-23). When the particles arrive at the substrate after sputtering with different energy, the adatom mobility varies, as a particle with low energy tends to stick to the region where it arrives due to its low mobility and inability to overcome the diffusion barrier, while a particle with higher energy has higher mobility [460]. Since sputtering is a process of momentum transfer, silver with the lowest atomic mass will gain the highest energy during the sputtering, and thus be more mobile than the other metals, and tends to reduce the surface free energy via aggregation (lower surface area o volume ratio) in their motion on the substrate. The highest sputtering rate (38 nm/s) of silver may also contribute to

its aggregation into large particles as more silver will be sputtered from the silver lid and then deposited on GO surfaces for a given sputtering period as compared with other three deposited noble metals.

The relatively poor performance of GO-Ag with large silver particles is supported by other researchers finding that the silver particles can only benefit the electrical performance when distributed uniformly on graphene films [459, 212]. It is also reported that in the cases of hybrids of graphene and silver with improved electrical and electrochemical performances, the silver particles should be distributed on graphene sheets in nano scale [200, 199]. Here in this case, the silver nanoparticles aggregated into large particles, which is likely to be the reason of poor electrical and electrochemical properties.

**2. GO-Pd**

When graphene is adsorbed on metals, according to their binding energies (energies per carbon atom required to remove the graphene sheet from the metal surface) and equilibrium separations (separation in the *z* direction between the carbon atoms of the graphene sheet and the relaxed positions of the topmost metal layer), metals can be divided into two categories: weakly bonded metals of which the binding energy is mostly less than 0.04 eV/carbon atom and equilibrium separation is approximately 0.33 nm, such as Au, Pt, Cu, Ag, and Al; and strongly bonded metals of which the binding energy is mostly over 0.1 eV/carbon atom and equilibrium separation shorter than 0.23 nm, such

as Pd, Ni, and Co [461, 462].

For those weakly interacted metals, the contact or bonding between graphene and metals can be viewed as physio-adsorption, and the linear π-band dispersion of graphene is preserved, so that charges can transfer between graphene and metals, due to the equilibration of the chemical potentials [461].

However, for strongly interacting metals, the $p_z$ states of graphene and *d* states of metals are hybridised, forming chemical bonds, hence metal carbides form, especially at defective sites [463, 464].

With regard to palladium, as one of the strongly interacted metal, its deposition on the graphene surface also results to a chemical reaction at the interface of carbon and palladium [465]. The formation of Pd-C is also confirmed in Section 4.7.1(Fig. 4-46(b)), where the high-resolution XPS spectra of Pd3d is located at 336.0 eV, 1.0 eV higher than pristine bulk palladium, representing the bonding of Pd-C [466]. Also, in the XPS spectra of Pd3d, the peak is fully at 336.0 eV without peak split at 335.0 eV, meaning that the layer of palladium is thin enough that all the palladium sputtered are formed into Pd-C in this study, without any bulk palladium above.

Due to the formation of palladium carbide, the graphitic structure is damaged, affecting the free electron transportation in π-band. Also, the resistivity of thin sheet of PdC is much higher than bulk palladium, with the value being three

orders of magnitude higher than bulk palladium when the thickness is in the range of 100-250 nm, and still two orders of magnitude higher when the thickness exceeded 250 nm [467]. Since palladium and platinum share close electrical resistances (Table 4-23) and PdC was formed in GO-Pd, it can be deduced that the sheet resistance of GO-Pd should be two or three orders of magnitude higher than that of GO-Pt, which is fully supported by the experimental results shown in Section 4.7.2 (Fig. 4-47).

# Chapter 5 Conclusions

Active-screen plasma (ASP) treatment has been applied on graphene oxide (GO) throughout this research, and the effects of ASP on GO reduction, nitrogen doping, and metal deposition have been explored. The micro-structures and compositions of GO before and after ASP treatments have been characterised, and the electrical and electrochemical properties have been evaluated. The main conclusions are summarised as follows:

## I. ASP GO reduction

(1). GO can be effectively reduced via ASP treatment, using either argon or hydrogen as the working gas.

(2). ASP treated GO exhibits better electrical and electrochemical properties than annealed GO. The sheet resistance of ASP treated GO is about one order of magnitude lowered to that of untreated GO, and capacitance increase to 3.5 times that of untreated GO.

## II. ASP GO nitrogen doping

(3). GO can be reduced and nitrogen doped simultaneously via ASP treatment using gas mixture of nitrogen and hydrogen, with 1:3 the best ratio of N/C for reduction and performance improvement.

(4). The nitrogen doping configuration is related to the ratio of gas mixture, and when the ratio of N/C is 1:3, the configuration include: pyridinic N, pyrrolic N and graphitic N, while pyridinic N is absent when the ratio is

1:1 or 3:1. Overall, there is a tendency of forming nitrogen configuration with lower binding energies when ASP treated using gas mixture with a higher proportion of hydrogen.

(5). When GO reduction and nitrogen doping is ASP treated at the optimal gas ratio, the electrical and electrochemical property are further enhanced, compared to reduction only, with the capacitance around 4.4 times that of untreated GO.

(6). ASP treatment using a gas mixture of nitrogen and argon has a negative effect on the electrical properties, and the sheet resistance after ASP treatment is much higher than that of untreated GO.

**III. Combined ASP modification and metal hybridisation**

(7). When ASP treating GO, metals from the active screen are sputtered simultaneously, and deposit on GO surface, forming a GO-based hybrid. This effect is more obviously shown when a piece of noble metal plate is added as an extra lid of active screen cage.

(8). The iron and chromium sputtered from the stainless-steel active screen are in the form of oxides, as well as possibly a small quantity of hydroxides and nitrides. The noble metals are mainly in the form pure metal, but a small amount of palladium oxide and platinum oxide are also formed.

(9). For GO-Ag composites, it is unique that the silver aggregates into large particles in a size of 1-2 microns, separately scattered on the GO

surface. The hybridisation with silver cannot further improve the electrical and electrochemical properties.

(10). For GO-Pd composites, apart from the PdO formed, the majority of pure palladium is chemically bonded to carbon, and the hybridisation cannot contribute to the electrical or electrochemical properties.

(11). For GO-Pt composites, platinum nanoparticles are homogeneously distributed in the form of pure platinum, as well as a minority as metal oxides. The electrical and electrochemical properties are greatly enhanced, with its super-capacitive performance being the best among all the GO hybrids.

(12). For GO-Au composites, the electrical property was the best among all the GO hybrids. However, the capacitance of GO-Au exhibits dependence on scan rate.

**IV. ASP optimal condition**

(13). When treatment duration is extended from 1 h to 2 h, GO is better reduced, with more metals theoretically deposited, and the properties improve. However, when the duration increases to 3 h, the improvement slows down.

(14). ASP treatment at a gas pressure of 0.75 mbar is better than that of 1.50 mbar in GO reduction and metal sputtering, as well as the resulting electrical and electrochemical properties.

# Chapter 6 Future work

The present project has clearly shown that ASP treatment can effectively reduce and functionalise GO. Based on all the results interpreted and discussed above, to fully explore the potential of ASP on GO materials, some topics are proposed below for further studies.

- **Further condition optimisation**

  As known, a variety of parameters can influence the effect of plasma treatment. In this study, only working gas type and gas ratio of mixture, treatment duration and gas pressure were investigated. Apart from these, there are many other conditions that worth exploring, such as voltage and current, applied bias, distance between active screen and GO sample, etc. Furthermore, the hollow cathode effect can also be incorporated in treatments for future studies when the additional target lid is added above the original active screen with changing spacing, therefore allowing overlapping of the negative plasma glow-discharge regions.

  In addition, a suitable processing condition for a deposition of silver nanoparticles without aggregation is also imperative for its specific applications.

- **Further super-capacitive performance evaluation and supercapacitor fabrication**

In this study, the super-capacitive performances are evaluated through CV, EIS and GCD tests. Except for these tests, the stability of the super-capacitive performance through cyclic charging/discharging, and evaluation of energy and power densities, should also be taken into consideration. After the optimisation of treatment conditions, and an overall performance evaluation, a real supercapacitor should be fabricated for comprehensive assessment, so that ASP treatment on GO can be applied into practical use.

Additionally, the phenomenon of scan rate-dependent capacitance of GO-Au also warrants further detailed study.

- **Evaluation on performances for other applications**

  As stated, nitrogen-doped graphene materials, and graphene-metal hybrids have great potential for a variety of applications. This thesis only focuses on the electrochemical property tests for supercapacitor applications. The performances of ASP treated GO for other applications, such as electrocatalysts, sensors and so on, are also worth evaluation, so that the potential of ASP treated GO can be fully exploited.

  Apart from all the potential applications which are mentioned in Literature Review, this technique also opens the path towards potential for new applications based on the hybridisation of graphene and metal nanoparticles. For example, GO-Ag for anti-bacterial materials, GO-Au and

GO-Ag for surface-enhanced Raman scattering, and GO-Pt, GO-Pd and GO-Au for catalysts.

# References


1. Zhu Y, Murali S, Cai W, et al (2010) Graphene and Graphene Oxide: Synthesis, Properties, and Applications. Adv Mater 22:3906–3924. https://doi.org/10.1002/adma.201001068

2. Lotya M, Hernandez Y, King PJ, et al (2009) Liquid Phase Production of Graphene by Exfoliation of Graphite in Surfactant/Water Solutions. J Am Chem Soc 131:3611–3620. https://doi.org/10.1021/ja807449u

3. Lotya M, King PJ, Khan U, et al (2010) High-Concentration, Surfactant-Stabilized Graphene Dispersions. ACS Nano 4:3155–3162. https://doi.org/10.1021/nn1005304

4. Chen D, Feng H, Li J (2012) Graphene oxide: Preparation, functionalization, and electrochemical applications. Chem. Rev. 112:6027–6053

5. Babaev AA, Zobov ME, Kornilov DY, et al (2018) Optical and Electrical Properties of Graphene Oxide. Opt Spectrosc 125:1014–1018. https://doi.org/10.1134/S0030400X18120032

6. Gasnier A, Pedano ML, Rubianes MD, Rivas GA (2013) Graphene paste electrode: Electrochemical behavior and analytical applications for the quantification of NADH. Sensors Actuators, B Chem 176:921–926. https://doi.org/10.1016/j.snb.2012.09.092

7. Wang H, Maiyalagan T, Wang X (2012) Review on recent progress in nitrogen-doped graphene: Synthesis, characterization, and its potential applications. ACS Catal 2:781–794. https://doi.org/10.1021/cs200652y

8. Yadav R, Dixit CK (2017) Synthesis, characterization and prospective applications of nitrogen-doped graphene: A short review. J Sci Adv Mater Devices 2:141–149. https://doi.org/10.1016/j.jsamd.2017.05.007

9. Pei S, Cheng HM (2012) The reduction of graphene oxide. Carbon N Y 50:3210–3228. https://doi.org/10.1016/j.carbon.2011.11.010

10. Singh G, Botcha VD, Sutar DS, et al (2014) Near room temperature reduction of graphene oxide Langmuir-Blodgett monolayers by hydrogen plasma. Phys Chem Chem Phys 16:11708–11718. https://doi.org/10.1039/c4cp00875h

11. Lin YP, Ksari Y, Prakash J, et al (2014) Nitrogen-doping processes of graphene by a versatile plasma-based method. Carbon N Y 73:216–224. https://doi.org/10.1016/j.carbon.2014.02.057

12. Khan M, Tahir MN, Adil SF, et al (2015) Graphene based metal and metal oxide nanocomposites: synthesis, properties and their applications. J Mater Chem A 3:18753–18808. https://doi.org/10.1039/c5ta02240a

13. Wang Q, Song M, Chen C, et al (2012) Synthesis of graphene-based Pt nanoparticles by a one-step in situ plasma approach under mild conditions. Appl Phys Lett 101:. https://doi.org/10.1063/1.4737421

14. Spies HJ, Biermann H, Burlacov I, Börner K (2013) Active screen plasma nitriding. Adv Mater Process 171:66–68. https://doi.org/10.1179/174329409X439032

15. Corujeira Gallo S, Dong H (2011) EBSD and AFM observations of the microstructural changes induced by low temperature plasma carburising on AISI 316. Appl Surf Sci 258:608–613. https://doi.org/10.1016/j.apsusc.2011.06.158

16. Corujeira Gallo S, Li X, Fütterer K, et al (2017) Carbon Nanofibers Functionalized with Active Screen Plasma-Deposited Metal Nanoparticles for Electrical Energy Storage Devices. ACS Appl Mater Interfaces 9:23195–23201. https://doi.org/10.1021/acsami.7b05567

17. Li Z, Qi S, Liang Y, et al (2018) Plasma surface functionalization of carbon nanofibres with silver, palladium and platinum nanoparticles for cost-effective and high-performance supercapacitors. Micromachines 10:. https://doi.org/10.3390/mi10010002

18. Moseley PT, Rand DAJ, Davidson A, Monahov B (2018) Understanding the functions of carbon in the negative active-mass of the lead–acid battery: A review of progress. J Energy Storage 19:272–290. https://doi.org/10.1016/j.est.2018.08.003

19. Hirsch A (2010) The era of carbon allotropes. Nat Mater 9:868–871. https://doi.org/10.1038/nmat2885

20. Kroto HW, Heath JR, O'Brien SC, et al (1985) C60: Buckminsterfullerene. Nature 318:162–163. https://doi.org/10.1038/318162a0

21. Iijima S (1991) Helical microtubules of graphitic carbon. Nature 354:56–58. https://doi.org/10.1038/354056a0

22. Novoselov KS, Geim AK, Morozov S V, et al (2004) Electric field in atomically thin carbon films. Science (80- ) 306:666–669. https://doi.org/10.1126/science.1102896

23. Hummers WS, Offeman RE (1958) Preparation of Graphitic Oxide. J Am Chem Soc 80:1339–1339. https://doi.org/10.1021/ja01539a017

24. Marcano DC, Kosynkin D V, Berlin JM, et al (2010) Improved Synthesis of Graphene Oxide. ACS Nano 4:4806–4814. https://doi.org/10.1021/nn1006368

25. Zhang Y, Zhang L, Zhou C (2013) Review of Chemical Vapor Deposition of Graphene and Related Applications. Acc Chem Res 46:2329–2339. https://doi.org/10.1021/ar300203n

26. Schäffel F (2013) The Atomic Structure of Graphene and Its Few-layer Counterparts

27. Liu F, Ming P, Li J (2007) Ab initio calculation of ideal strength and phonon instability of graphene under tension. Phys Rev B - Condens Matter Mater Phys 76:1–7. https://doi.org/10.1103/PhysRevB.76.064120

28. Lee C, Wei X, Kysar JW, Hone J (2008) Measurement of the Elastic Properties and Intrinsic Strength of Monolayer Graphene. Science (80- ) 321:385–388. https://doi.org/10.1126/science.1157996

29. Gómez-Navarro C, Burghard M, Kern K (2008) Elastic Properties of Chemically Derived Single Graphene Sheets. Nano Lett 8:2045–2049. https://doi.org/10.1021/nl801384y

30. Poot M, Van Der Zant HSJ (2008) Nanomechanical properties of few-layer graphene membranes. Appl Phys Lett 92:. https://doi.org/10.1063/1.2857472

31. Frank IW, Tanenbaum DM, Van Der Zande AM, McEuen PL (2007) Mechanical properties of suspended graphene sheets. J Vac Sci Technol B Microelectron Nanom Struct 25:2558–2561. https://doi.org/10.1116/1.2789446

32. Balandin AA, Ghosh S, Bao W, et al (2008) Superior Thermal Conductivity of Single-Layer Graphene. Nano Lett 8:902–907. https://doi.org/10.1021/nl0731872

33. Faugeras C, Faugeras B, Orlita M, et al (2010) Thermal conductivity of graphene in corbino membrane geometry. ACS Nano 4:1889–1892. https://doi.org/10.1021/nn9016229

34. Castro Neto AH, Guinea F, Peres NMR, et al (2009) The electronic properties of graphene. Rev Mod Phys 81:109–162. https://doi.org/10.1103/RevModPhys.81.109

35. Morozov S V., Novoselov KS, Katsnelson MI, et al (2008) Giant intrinsic carrier mobilities in graphene and its bilayer. Phys Rev Lett 100:11–14. https://doi.org/10.1103/PhysRevLett.100.016602

36. Chen W, Chen S, Dong CQ, et al (2007) Surface transfer p-type doping of epitaxial graphene. J Am Chem Soc 129:10418–10422. https://doi.org/10.1021/ja071658g

37. Iqbal MZ, Siddique S, Iqbal MW, Eom J (2013) Formation of p-n junction with stable p-doping in graphene field effect transistors using deep UV irradiation. J Mater Chem C 1:3078–3083. https://doi.org/10.1039/c3tc30232f

38. Iqbal MZ, Anwar N, Siddique S, et al (2017) Formation of pn-junction with stable n-doping in graphene field effect transistors using e-beam irradiation. Opt Mater (Amst) 69:254–258. https://doi.org/10.1016/j.optmat.2017.04.041

39. Cooper DR, D'Anjou B, Ghattamaneni N, et al (2012) Experimental Review of Graphene. ISRN Condens Matter Phys 2012:1–56. https://doi.org/10.5402/2012/501686

40. Yoon HJ, Jun DH, Yang JH, et al (2011) Carbon dioxide gas sensor using a graphene sheet. Sensors Actuators, B Chem 157:310–313. https://doi.org/10.1016/j.snb.2011.03.035

41. Cadore AR, Mania E, Alencar AB, et al (2018) Enhancing the response of NH3 graphene-sensors by using devices with different graphene-substrate distances. Sensors Actuators, B Chem 266:438–446. https://doi.org/10.1016/j.snb.2018.03.164

42. Qi S, Zhao B, Tang H, Jiang X (2015) Determination of ascorbic acid, dopamine, and uric acid by a novel electrochemical sensor based on pristine graphene. Electrochim Acta 161:395–402. https://doi.org/10.1016/j.electacta.2015.02.116

43. Keeley GP, O'Neill A, Holzinger M, et al (2011) DMF-exfoliated graphene for electrochemical NADH detection. Phys Chem Chem Phys 13:7747–7750. https://doi.org/10.1039/c1cp20060g

44. Li X, Zhu Y, Cai W, et al (2009) Transfer of Large-Area Graphene Films for High-Performance Transparent Conductive Electrodes. Nano Lett 9:4359–4363. https://doi.org/10.1021/nl902623y

45. Casaluci S, Gemmi M, Pellegrini V, et al (2016) Graphene-based large area dye-sensitized solar cell modules. Nanoscale 8:5368–5378. https://doi.org/10.1039/C5NR07971C

46. Raccichini R, Varzi A, Passerini S, Scrosati B (2015) The role of graphene for electrochemical energy storage. Nat Mater 14:271–279. https://doi.org/10.1038/nmat4170

47. Shao Y, El-Kady MF, Wang LJ, et al (2015) Graphene-based materials for flexible supercapacitors. Chem. Soc. Rev. 44:3639–3665

48. Guo P, Song H, Chen X (2009) Electrochemical performance of graphene nanosheets as anode material for lithium-ion batteries. Electrochem commun 11:1320–1324. https://doi.org/10.1016/j.elecom.2009.04.036

49. Choi HJ, Jung SM, Seo JM, et al (2012) Graphene for energy conversion and storage in fuel cells and supercapacitors. Nano Energy 1:534–551

50. Tozzini V, Pellegrini V (2013) Prospects for hydrogen storage in graphene. Phys Chem Chem Phys 15:80–89. https://doi.org/10.1039/c2cp42538f

51. Gao W, Alemany LB, Ci L, Ajayan PM (2009) New insights into the structure and reduction of graphite oxide. Nat Chem 1:403–408. https://doi.org/10.1038/nchem.281

52. Sun L (2019) Structure and synthesis of graphene oxide. Chinese J Chem Eng 27:2251–2260. https://doi.org/10.1016/j.cjche.2019.05.003

53. Krueger M, Berg S, Stone D, et al (2011) Drop-casted self-assembling graphene oxide membranes for scanning electron microscopy on wet and dense gaseous samples. ACS Nano 5:10047–10054. https://doi.org/10.1021/nn204287g

54. Kang J, Shin D, Bae S, Hong BH (2012) Graphene transfer: Key for applications. Nanoscale 4:5527–5537. https://doi.org/10.1039/c2nr31317k

55. Eda G, Chhowalla M (2010) Chemically derived graphene oxide: Towards large-area thin-film electronics and optoelectronics. Adv. Mater. 22:2392–2415

56. Paci JT, Belytschko T, Schatz GC (2007) Computational studies of the structure, behavior upon heating and mechanical properties of graphite oxide. J Phys Chem C 111:18099–18111. https://doi.org/10.1021/jp075799g

57. Suk JW, Piner RD, An J, Ruoff RS (2010) Mechanical properties of monolayer graphene oxide. ACS Nano 4:6557–6564. https://doi.org/10.1021/nn101781v

58. Kang SH, Fang TH, Hong ZH, Chuang CH (2013) Mechanical properties of free-standing graphene oxide. Diam Relat Mater 38:73–78. https://doi.org/10.1016/j.diamond.2013.06.016

59. Liu L, Zhang J, Zhao J, Liu F (2012) Mechanical properties of graphene oxides. Nanoscale 4:5910–5916. https://doi.org/10.1039/c2nr31164j

60. Mu X, Wu X, Zhang T, et al (2014) Thermal transport in graphene oxide - From ballistic extreme to amorphous limit. Sci Rep 4:1–9. https://doi.org/10.1038/srep03909

61. Chen J, Li L (2020) Thermal Conductivity of Graphene Oxide: A Molecular Dynamics Study. JETP Lett 112:117–121. https://doi.org/10.1134/S0021364020140015

62. Chen J, Li L (2020) Effect of oxidation degree on the thermal properties of graphene oxide. J Mater Res Technol 9:13740–13748. https://doi.org/10.1016/j.jmrt.2020.09.092

63. Yang Y, Cao J, Wei N, et al (2019) Thermal conductivity of defective graphene oxide: A molecular dynamic study. Molecules 24:. https://doi.org/10.3390/molecules24061103

64. Mattevi C, Eda G, Agnoli S, et al (2009) Evolution of electrical, chemical, and structural properties of transparent and conducting chemically derived graphene thin films. Adv Funct Mater 19:2577–2583. https://doi.org/10.1002/adfm.200900166

65. Rao S, Upadhyay J, Polychronopoulou K, et al (2018) Reduced Graphene Oxide: Effect of Reduction on Electrical Conductivity. J Compos Sci 2:25. https://doi.org/10.3390/jcs2020025

66. Park H, Lim S, Nguyen D Du, Suk JW (2019) Electrical measurements of thermally reduced graphene oxide powders under pressure. Nanomaterials 9:1–11. https://doi.org/10.3390/nano9101387

67. Kang SH, Fang TH, Hong ZH (2013) Electrical and mechanical properties of graphene oxide on flexible substrate. J Phys Chem Solids 74:1783–1793. https://doi.org/10.1016/j.jpcs.2013.07.009

68. Choi YR, Yoon YG, Choi KS, et al (2015) Role of oxygen functional groups in graphene oxide for reversible room-temperature NO2 sensing. Carbon N Y 91:178–187. https://doi.org/10.1016/j.carbon.2015.04.082

69. Singh RK, Kumar R, Singh DP (2016) Graphene oxide: Strategies for synthesis, reduction and frontier applications. RSC Adv. 6:64993–65011

70. Huang XM, Liu LZ, Zhou S, Zhao JJ (2020) Physical properties and device applications of graphene oxide. Front Phys 15:. https://doi.org/10.1007/s11467-019-0937-9

71. Wu SY, An SSA, Hulme J (2015) Current applications of graphene oxide in nanomedicine. Int J Nanomedicine 10:9–24. https://doi.org/10.2147/IJN.S88285

72. Dideikin AT, Vul' AY (2019) Graphene oxide and derivatives: The place in graphene family. Front. Phys. 6

73. Venugopal G, Krishnamoorthy K, Mohan R, Kim SJ (2012) An investigation of the electrical transport properties of graphene-oxide thin films. Mater Chem Phys 132:29–33. https://doi.org/10.1016/j.matchemphys.2011.10.040

74. Long MQ, Tang L, Wang D, et al (2009) Theoretical predictions of size-dependent carrier mobility and polarity in graphene. J Am Chem Soc 131:17728–17729. https://doi.org/10.1021/ja907528a

75. De S, Coleman JN (2010) Are there fundamental limitations on the sheet resistance and transmittance of thin graphene films? ACS Nano 4:2713–2720. https://doi.org/10.1021/nn100343f

76. Bae S, Kim H, Lee Y, et al (2010) Roll-to-roll production of 30-inch graphene films for transparent electrodes. Nat Nanotechnol 5:574–578. https://doi.org/10.1038/nnano.2010.132

77. Han TH, Lee Y, Choi MR, et al (2012) Extremely efficient flexible organic light-emitting diodes with modified graphene anode. Nat Photonics 6:105–110. https://doi.org/10.1038/nphoton.2011.318

78. Gomez De Arco L, Zhang Y, Schlenker CW, et al (2010) Continuous, highly flexible, and transparent graphene films by chemical vapor deposition for organic photovoltaics. ACS Nano 4:2865–2873. https://doi.org/10.1021/nn901587x

79. Wakihara M (2001) Recent developments in lithium ion batteries. Mater Sci Eng R Reports 33:109–134. https://doi.org/10.1016/S0927-796X(01)00030-4

80. Mohamed N, Allam NK (2020) Recent advances in the design of cathode materials for Li-ion batteries. RSC Adv. 10:21662–21685

81. Kucinskis G, Bajars G, Kleperis J (2013) Graphene in lithium ion battery cathode materials: A review. J Power Sources 240:66–79. https://doi.org/10.1016/j.jpowsour.2013.03.160

82. Cai X, Lai L, Shen Z, Lin J (2017) Graphene and graphene-based composites as Li-ion battery electrode materials and their application in full cells. J Mater Chem A 5:15423–15446. https://doi.org/10.1039/c7ta04354f

83. Wang Y, Song Y, Xia Y (2016) Electrochemical capacitors: Mechanism, materials, systems, characterization and applications. Chem Soc Rev 45:5925–5950. https://doi.org/10.1039/c5cs00580a

84. Libich J, Máca J, Vondrák J, et al (2018) Supercapacitors: Properties and applications. J Energy Storage 17:224–227. https://doi.org/10.1016/j.est.2018.03.012

85. Pal B, Yang S, Ramesh S, et al (2019) Electrolyte selection for supercapacitive devices: A critical review. Nanoscale Adv 1:3807–3835. https://doi.org/10.1039/c9na00374f

86. Bonaccorso F, Colombo L, Yu G, et al (2015) Graphene, related two-dimensional crystals, and hybrid systems for energy conversion and storage. Science (80-. ). 347

87. Lemine AS, Zagho MM, Altahtamouni TM, Bensalah N (2018) Graphene a promising electrode material for supercapacitors-A review. Int J Energy Res 42:4284–4300. https://doi.org/10.1002/er.4170

88. Ke Q, Wang J (2016) Graphene-based materials for supercapacitor electrodes – A review. J Mater 2:37–54. https://doi.org/10.1016/j.jmat.2016.01.001

89. Yang H, Kannappan S, Pandian AS, et al (2017) Graphene supercapacitor with both high power and energy density. Nanotechnology 28:. https://doi.org/10.1088/1361-6528/aa8948

90. Poonam, Sharma K, Arora A, Tripathi SK (2019) Review of supercapacitors: Materials and devices. J Energy Storage 21:801–825. https://doi.org/10.1016/j.est.2019.01.010

91. Nandi D, Mohan VB, Bhowmick AK, Bhattacharyya D (2020) Metal/metal oxide decorated graphene synthesis and application as supercapacitor: a review. J Mater Sci 55:6375–6400. https://doi.org/10.1007/s10853-020-04475-z

92. Li Y, Zhang S, Ni Y (2016) Graphene sheets stacked polyacrylate latex composites for ultraefficient electromagnetic shielding. Mater Res Express 3:. https://doi.org/10.1088/2053-1591/3/7/075012

93. Zhang Y, Huang Y, Zhang T, et al (2015) Broadband and tunable high-performance microwave absorption of an ultralight and highly compressible graphene foam. Adv Mater 27:2049–2053. https://doi.org/10.1002/adma.201405788

94. Kumar R, Oh JH, Kim HJ, et al (2015) Nanohole-Structured and Palladium-Embedded 3D Porous Graphene for Ultrahigh Hydrogen Storage and CO Oxidation Multifunctionalities. ACS Nano 9:7343–7351. https://doi.org/10.1021/acsnano.5b02337

95. Fakorede O, Feger Z, Ibrahim H, et al (2016) Ice protection systems for wind turbines in cold climate: characteristics, comparisons and analysis. Renew Sustain Energy Rev 65:662–675. https://doi.org/10.1016/j.rser.2016.06.080

96. Karim N, Zhang M, Afroj S, et al (2018) Graphene-based surface heater for de-icing applications. RSC Adv 8:16815–16823. https://doi.org/10.1039/c8ra02567c

97. Mucsi V, Ayub AS, Muhammad-Sukki F, et al (2020) Lightning protection methods for wind turbine blades: An alternative approach. Appl Sci 10:. https://doi.org/10.3390/app10062130

98. Papageorgiou DG, Kinloch IA, Young RJ (2017) Mechanical properties of graphene and graphene-based nanocomposites. Prog Mater Sci 90:75–127. https://doi.org/10.1016/j.pmatsci.2017.07.004

99. Sreenivasulu B, Ramji BR, Nagaral M (2018) A Review on Graphene Reinforced Polymer Matrix Composites. Mater Today Proc 5:2419–2428. https://doi.org/10.1016/j.matpr.2017.11.021

100. Young RJ, Liu M, Kinloch IA, et al (2018) The mechanics of reinforcement of polymers by graphene nanoplatelets. Compos Sci Technol 154:110–116. https://doi.org/10.1016/j.compscitech.2017.11.007

101. Papageorgiou DG, Li Z, Liu M, et al (2020) Mechanisms of mechanical reinforcement by graphene and carbon nanotubes in polymer nanocomposites. Nanoscale 12:2228–2267. https://doi.org/10.1039/c9nr06952f

102. Gao Z, Zhu J, Rajabpour S, et al (2020) Graphene reinforced carbon fibers. Sci Adv 6:1–11. https://doi.org/10.1126/sciadv.aaz4191

103. Song P, Cao Z, Cai Y, et al (2011) Fabrication of exfoliated graphene-based polypropylene nanocomposites with enhanced mechanical and thermal properties. Polymer (Guildf) 52:4001–4010. https://doi.org/10.1016/j.polymer.2011.06.045

104. Zhang P, Li Z, Zhang S, Shao G (2018) Recent Advances in Effective Reduction of Graphene Oxide for Highly Improved Performance Toward Electrochemical Energy Storage. Energy Environ Mater 1:5–12. https://doi.org/10.1002/eem2.12001

105. Compton OC, Jain B, Dikin DA, et al (2011) Chemically active reduced graphene oxide with tunable C/O ratios. ACS Nano 5:4380–4391. https://doi.org/10.1021/nn1030725

106. Dong L, Yang J, Chhowalla M, Loh KP (2017) Synthesis and reduction of large sized graphene oxide sheets. Chem Soc Rev 46:7306–7316. https://doi.org/10.1039/c7cs00485k

107. Li X, Biswas S, Drzal LT (2013) High temperature vacuum annealing and hydrogenation modification of exfoliated graphite nanoplatelets. J Eng (United Kingdom) 2013:. https://doi.org/10.1155/2013/638576

108. Schniepp HC, Li JL, McAllister MJ, et al (2006) Functionalized single graphene sheets derived from splitting graphite oxide. J Phys Chem B 110:8535–8539. https://doi.org/10.1021/jp060936f

109. Vallés C, David Núñez J, Benito AM, Maser WK (2012) Flexible conductive graphene paper obtained by direct and gentle annealing of graphene oxide paper. Carbon N Y 50:835–844. https://doi.org/10.1016/j.carbon.2011.09.042

110. Acik M, Lee G, Mattevi C, et al (2011) The role of oxygen during thermal reduction of graphene oxide studied by infrared absorption spectroscopy. J Phys Chem C 115:19761–19781. https://doi.org/10.1021/jp2052618

111. Yang D, Velamakanni A, Bozoklu G, et al (2009) Chemical analysis of graphene oxide films after heat and chemical treatments by X-ray photoelectron and Micro-Raman spectroscopy. Carbon N Y 47:145–152. https://doi.org/10.1016/j.carbon.2008.09.045

112. Sengupta I, Chakraborty S, Talukdar M, et al (2018) Thermal reduction of graphene oxide: How temperature influences purity. J Mater Res 33:4113–4122. https://doi.org/10.1557/jmr.2018.338

113. Zhao B, Liu P, Jiang Y, et al (2012) Supercapacitor performances of thermally reduced graphene oxide. J Power Sources 198:423–427. https://doi.org/10.1016/j.jpowsour.2011.09.074

114. Wang X, Li L, Wang Y, et al (2013) Application of reduced graphene oxide and carbon nanotube modified electrodes for measuring the enzymatic activity of alcohol dehydrogenase. Food Chem 138:2195–2200. https://doi.org/10.1016/j.foodchem.2012.11.137

115. Huang TY, Huang JH, Wei HY, et al (2013) RGO/SWCNT composites as novel electrode materials for electrochemical biosensing. Biosens Bioelectron 43:173–179. https://doi.org/10.1016/j.bios.2012.10.047

116. Shin HJ, Kim KK, Benayad A, et al (2009) Efficient reduction of graphite oxide by sodium borohydride and its effect on electrical conductance. Adv Funct Mater 19:1987–1992. https://doi.org/10.1002/adfm.200900167

117. Muda MR, Ramli MM, Isa SSM, et al (2017) Fundamental study of reduction graphene oxide by sodium borohydride for gas sensor application. AIP Conf Proc 1808:. https://doi.org/10.1063/1.4975267

118. Zhao J, Pei S, Ren W, et al (2010) Efficient preparation of large-area graphene oxide sheets for transparent conductive films. ACS Nano 4:5245–5252. https://doi.org/10.1021/nn1015506

119. Moon IK, Lee J, Ruoff RS, Lee H (2010) Reduced graphene oxide by chemical graphitization. Nat Commun 1:1–6. https://doi.org/10.1038/ncomms1067

120. Stankovich S, Dikin DA, Piner RD, et al (2007) Synthesis of graphene-based nanosheets via chemical reduction of exfoliated graphite oxide. Carbon N Y 45:1558–1565. https://doi.org/10.1016/j.carbon.2007.02.034

121. Park S, Hu Y, Hwang JO, et al (2012) Chemical structures of hydrazine-treated graphene oxide and generation of aromatic nitrogen doping. Nat Commun 3:. https://doi.org/10.1038/ncomms1643

122. Guex LG, Sacchi B, Peuvot KF, et al (2017) Experimental review: Chemical reduction of graphene oxide (GO) to reduced graphene oxide (rGO) by aqueous chemistry. Nanoscale 9:9562–9571. https://doi.org/10.1039/c7nr02943h

123. Pei S, Zhao J, Du J, et al (2010) Direct reduction of graphene oxide films into highly conductive and flexible graphene films by hydrohalic acids. Carbon N Y 48:4466–4474. https://doi.org/10.1016/j.carbon.2010.08.006

124. Zhang J, Yang H, Shen G, et al (2010) Reduction of graphene oxide vial-ascorbic acid. Chem Commun 46:1112–1114. https://doi.org/10.1039/b917705a

125. De Silva KKH, Huang HH, Joshi RK, Yoshimura M (2017) Chemical reduction of graphene oxide using green reductants. Carbon N. Y. 119:190–199

126. Fernández-Merino MJ, Guardia L, Paredes JI, et al (2010) Vitamin C Is an Ideal Substitute for Hydrazine in the Reduction of Graphene Oxide Suspensions. J Phys Chem C 114:6426–6432. https://doi.org/10.1021/jp100603h

127. Chen W, Yan L, Bangal PR (2010) Preparation of graphene by the rapid and mild thermal reduction of graphene oxide induced by microwaves. Carbon N Y 48:1146–1152. https://doi.org/10.1016/j.carbon.2009.11.037

128. Voiry D, Yang J, Kupferberg J, et al (2016) High-quality graphene via microwave reduction of solution-exfoliated graphene oxide. Science (80- ) 353:1413–1416. https://doi.org/10.1126/science.aah3398

129. Cote LJ, Cruz-Silva R, Huang J (2009) Flash reduction and patterning of graphite oxide and its polymer composite. J Am Chem Soc 131:11027–11032. https://doi.org/10.1021/ja902348k

130. Zhang Y, Guo L, Wei S, et al (2010) Direct imprinting of microcircuits on graphene oxides film by femtosecond laser reduction. Nano Today 5:15–20. https://doi.org/10.1016/j.nantod.2009.12.009

131. Ding YH, Zhang P, Zhuo Q, et al (2011) A green approach to the synthesis of reduced graphene oxide nanosheets under UV irradiation. Nanotechnology 22:. https://doi.org/10.1088/0957-4484/22/21/215601

132. Shaw Yong Toh, Kee Shyuan Loh, Siti Kartom Kamarudin WRWD (2014) Graphene production via electrochemical reduction of graphene oxide: Synthesis and characterisation. Chem Eng J 148:422–434. https://doi.org/10.1002/ceat200800213

133. Lindfors T, Österholm A, Kauppila J, Pesonen M (2013) Electrochemical reduction of graphene oxide in electrically conducting poly(3,4-ethylenedioxythiophene) composite films. Electrochim Acta 110:428–436. https://doi.org/10.1016/j.electacta.2013.03.070

134. Liu H, Liu Y, Zhu D (2011) Chemical doping of graphene. J Mater Chem 21:3335–3345. https://doi.org/10.1039/c0jm02922j

135. Guo B, Fang L, Zhang B, Gong JR (2011) Graphene Doping: A Review. Insciences J 1:80–89. https://doi.org/10.5640/insc.010280

136. Wang Y, Shao Y, Matson DW, et al (2010) Nitrogen-doped graphene and its application in electrochemical biosensing. ACS Nano 4:1790–1798. https://doi.org/10.1021/nn100315s

137. Wei D, Liu Y, Wang Y, et al (2009) Synthesis of n-doped graphene by chemical vapor deposition and its electrical properties. Nano Lett 9:1752–1758. https://doi.org/10.1021/nl803279t

138. Schiros T, Nordlund D, Pálová L, et al (2012) Connecting dopant bond type with electronic structure in n-doped graphene. Nano Lett 12:4025–4031. https://doi.org/10.1021/nl301409h

139. Usachov D, Fedorov A, Vilkov O, et al (2014) The chemistry of imperfections in N-graphene. Nano Lett 14:4982–4988. https://doi.org/10.1021/nl501389h

140. Shen W, Wang C, Xu Q, et al (2015) Nitrogen-doping-induced defects of a carbon coating layer facilitate Na-storage in electrode materials. Adv Energy Mater 5:. https://doi.org/10.1002/aenm.201400982

141. Granzier-Nakajima T, Fujisawa K, Anil V, et al (2019) Controlling nitrogen doping in graphene with atomic precision: Synthesis and characterization. Nanomaterials 9:1–18. https://doi.org/10.3390/nano9030425

142. Jalili S, Vaziri R (2011) Study of the electronic properties of Li-intercalated nitrogen doped graphite. Mol Phys 109:687–694. https://doi.org/10.1080/00268976.2010.547523

143. Li X, Tang T, Li M, He X (2015) Nitrogen-doped graphene films from simple photochemical doping for n-type field-effect transistors. Appl Phys Lett 106:. https://doi.org/10.1063/1.4905342

144. Chang DW, Lee EK, Park EY, et al (2013) Nitrogen-doped graphene nanoplatelets from simple solution edge-functionalization for n-type field-effect transistors. J Am Chem Soc 135:8981–8988. https://doi.org/10.1021/ja402555n

145. Reddy ALM, Srivastava A, Gowda SR, et al (2010) Synthesis of nitrogen-doped graphene films for lithium battery application. ACS Nano 4:6337–6342. https://doi.org/10.1021/nn101926g

146. Wu ZS, Ren W, Xu L, et al (2011) Doped graphene sheets as anode materials with superhigh rate and large capacity for lithium ion batteries. ACS Nano 5:5463–5471. https://doi.org/10.1021/nn2006249

147. Wang X, Lv L, Cheng Z, et al (2016) High-Density Monolith of N-Doped Holey Graphene for Ultrahigh Volumetric Capacity of Li-Ion Batteries. Adv Energy Mater 6:1–7. https://doi.org/10.1002/aenm.201502100

148. Lu Y, Huang Y, Zhang M, Chen Y (2014) Nitrogen-doped graphene materials for supercapacitor applications. J. Nanosci. Nanotechnol. 14:1134–1144

149. Kumar NA, Baek JB (2015) Doped graphene supercapacitors. Nanotechnology 26:. https://doi.org/10.1088/0957-4484/26/49/492001

150. Sahu V, Grover S, Tulachan B, et al (2015) Heavily nitrogen doped, graphene supercapacitor from silk cocoon. Electrochim Acta 160:244–253. https://doi.org/10.1016/j.electacta.2015.02.019

151. Balaji SS, Elavarasan A, Sathish M (2016) High performance supercapacitor using N-doped graphene prepared via supercritical fluid processing with an oxime nitrogen source. Electrochim Acta 200:37–45. https://doi.org/10.1016/j.electacta.2016.03.150

152. Elessawy NA, El Nady J, Wazeer W, Kashyout AB (2019) Development of High-Performance Supercapacitor based on a Novel Controllable Green Synthesis for 3D Nitrogen Doped Graphene. Sci Rep 9:1–10. https://doi.org/10.1038/s41598-018-37369-x

153. Jiang F, Zhang J, Li N, et al (2019) Nitrogen-doped graphene prepared by thermal annealing of fluorinated graphene oxide as supercapacitor electrode. J Chem Technol Biotechnol 94:3530–3537. https://doi.org/10.1002/jctb.6147

154. Kumar MP, Raju MM, Arunchander A, et al (2016) Nitrogen Doped Graphene as Metal Free Electrocatalyst for Efficient Oxygen Reduction Reaction in Alkaline Media and Its Application in Anion Exchange Membrane Fuel Cells. J Electrochem Soc 163:F848–F855. https://doi.org/10.1149/2.0541608jes

155. Gao X, Wang L, Ma J, et al (2017) Facile preparation of nitrogen-doped graphene as an efficient oxygen reduction electrocatalyst. Inorg Chem Front 4:1582–1590. https://doi.org/10.1039/c7qi00387k

156. Dumont JH, Martinez U, Artyushkova K, et al (2019) Nitrogen-Doped Graphene Oxide Electrocatalysts for the Oxygen Reduction Reaction. ACS Appl Nano Mater 2:1675–1682. https://doi.org/10.1021/acsanm.8b02235

157. Shao Y, Jiang Z, Zhang Q, Guan J (2019) Progress in Nonmetal-Doped Graphene Electrocatalysts for the Oxygen Reduction Reaction. ChemSusChem 12:2133–2146. https://doi.org/10.1002/cssc.201900060

158. Lu X, Wang D, Ge L, et al (2018) Enriched graphitic N in nitrogen-doped graphene as a superior metal-free electrocatalyst for the oxygen reduction reaction. New J Chem 42:19665–19670. https://doi.org/10.1039/c8nj04857f

159. Lemes G, Sebastián D, Pastor E, Lázaro MJ (2019) N-doped graphene catalysts with high nitrogen concentration for the oxygen reduction reaction. J Power Sources 438:. https://doi.org/10.1016/j.jpowsour.2019.227036

160. Sheng ZH, Zheng XQ, Xu JY, et al (2012) Electrochemical sensor based on nitrogen doped graphene: Simultaneous determination of ascorbic acid, dopamine and uric acid. Biosens Bioelectron 34:125–131. https://doi.org/10.1016/j.bios.2012.01.030

161. Fan H, Li Y, Wu D, et al (2012) Electrochemical bisphenol A sensor based on N-doped graphene sheets. Anal Chim Acta 711:24–28. https://doi.org/10.1016/j.aca.2011.10.051

162. Lv R, Li Q, Botello-Méndez AR, et al (2012) Nitrogen-doped graphene: Beyond single substitution and enhanced molecular sensing. Sci Rep 2:1–8. https://doi.org/10.1038/srep00586

163. Wu ZL, Gao MX, Wang TT, et al (2014) A general quantitative pH sensor developed with dicyandiamide N-doped high quantum yield graphene quantum dots. Nanoscale 6:3868–3874. https://doi.org/10.1039/c3nr06353d

164. Liu N, Tian H, Schwartz G, et al (2014) Large-area, transparent, and flexible infrared photodetector fabricated using P-N junctions formed by N-doping chemical vapor deposition grown graphene. Nano Lett 14:3702–3708. https://doi.org/10.1021/nl500443j

165. Liu Q, Yu C, He Z, et al (2018) Chemical vapor deposition graphene of high mobility by gradient growth method on an 4H-SiC (0 0 0 1) substrate. Appl Surf Sci 454:68–73. https://doi.org/10.1016/j.apsusc.2018.05.131

166. Zhang C, Fu L, Liu N, et al (2011) Synthesis of nitrogen-doped graphene using embedded carbon and nitrogen sources. Adv Mater 23:1020–1024. https://doi.org/10.1002/adma.201004110

167. Bleu Y, Barnier V, Christien F, et al (2019) Dynamics of carbon diffusion and segregation through nickel catalyst, investigated by in situ XPS, during growth of nitrogen doped graphene. Carbon N Y 155:410–420. https://doi.org/10.1016/j.carbon.2019.08.084

168. Deng D, Pan X, Yu L, et al (2011) Toward N-doped graphene via solvothermal synthesis. Chem Mater 23:1188–1193. https://doi.org/10.1021/cm102666r

169. Xing Z, Ju Z, Zhao Y, et al (2016) One-pot hydrothermal synthesis of Nitrogen-doped graphene as high-performance anode materials for lithium ion batteries. Sci Rep 6:1–10. https://doi.org/10.1038/srep26146

170. Pham TV, Kim JG, Jung JY, et al (2019) High Areal Capacitance of N-Doped Graphene Synthesized by Arc Discharge. Adv Funct Mater 29:1–9. https://doi.org/10.1002/adfm.201905511

171. Zhou Y, Wang N, Muhammad J, et al (2019) Graphene nanoflakes with optimized nitrogen doping fabricated by arc discharge method as highly efficient absorbers toward microwave absorption. Carbon N Y 148:204–213. https://doi.org/10.1016/j.carbon.2019.03.034

172. Zhao P, Li W, Wang G, et al (2014) Facile hydrothermal fabrication of nitrogen-doped graphene/Fe2O3 composites as high performance electrode materials for supercapacitor. J Alloys Compd 604:87–93. https://doi.org/10.1016/j.jallcom.2014.03.106

173. Sun L, Wang L, Tian C, et al (2012) Nitrogen-doped graphene with high nitrogen level via a one-step hydrothermal reaction of graphene oxide with urea for superior capacitive energy storage. RSC Adv 2:4498–4506. https://doi.org/10.1039/c2ra01367c

174. Chen X, Oh W Da, Hu ZT, et al (2018) Enhancing sulfacetamide degradation by peroxymonosulfate activation with N-doped graphene produced through delicately-controlled nitrogen functionalization via tweaking thermal annealing processes. Appl Catal B Environ 225:243–257. https://doi.org/10.1016/j.apcatb.2017.11.071

175. Sheng ZH, Shao L, Chen JJ, et al (2011) Catalyst-free synthesis of nitrogen-doped graphene via thermal annealing graphite oxide with melamine and its excellent electrocatalysis. ACS Nano 5:4350–4358. https://doi.org/10.1021/nn103584t

176. Cui L, Chen X, Liu B, et al (2018) Highly Conductive Nitrogen-Doped Graphene Grown on Glass toward Electrochromic Applications. ACS Appl Mater Interfaces 10:32622–32630. https://doi.org/10.1021/acsami.8b11579

177. Shinde SM, Kano E, Kalita G, et al (2016) Grain structures of nitrogen-doped graphene synthesized by solid source-based chemical vapor deposition. Carbon N Y 96:448–453. https://doi.org/10.1016/j.carbon.2015.09.086

178. Liang X, Zhong J, Shi Y, et al (2015) Hydrothermal synthesis of highly nitrogen-doped few-layer graphene via solid-gas reaction. Mater Res Bull 61:252–258. https://doi.org/10.1016/j.materresbull.2014.09.088

179. Shazali SS, Amiri A, Mohd Zubir MN, et al (2018) Facile hydrothermal method for synthesizing nitrogen-doped graphene nanoplatelets using aqueous ammonia: dispersion, stability in solvents and thermophysical performances. Mater Res Express 5:035042. https://doi.org/10.1088/2053-1591/aab527

180. Chen P, Yang JJ, Li SS, et al (2013) Hydrothermal synthesis of macroscopic nitrogen-doped graphene hydrogels for ultrafast supercapacitor. Nano Energy 2:249–256. https://doi.org/10.1016/j.nanoen.2012.09.003

181. Liu Q, Guo B, Rao Z, et al (2013) Strong two-photon-induced fluorescence from photostable, biocompatible nitrogen-doped graphene quantum dots for cellular and deep-tissue imaging. Nano Lett 13:2436–2441. https://doi.org/10.1021/nl400368v

182. Liu C, Zhang L, Liu R, et al (2016) Hydrothermal synthesis of N-doped TiO2 nanowires and N-doped graphene heterostructures with enhanced photocatalytic properties. J Alloys Compd 656:24–32. https://doi.org/10.1016/j.jallcom.2015.09.211

183. Zhang S, Gao H, Huang M, Zhou J (2017) One-step hydrothermal synthesis of nitrogen doping graphene based cobalt oxide and its supercapacitive properties. J Alloys Compd 705:801–805. https://doi.org/10.1016/j.jallcom.2017.02.169

184. Li XJ, Yu XX, Liu JY, et al (2012) Synthesis of nitrogen-doped graphene via thermal annealing graphene with urea. Chinese J Chem Phys 25:325–329. https://doi.org/10.1088/1674-0068/25/03/325-329

185. Zheng B, Chen TW, Xiao FN, et al (2013) KOH-activated nitrogen-doped graphene by means of thermal annealing for supercapacitor. J Solid State Electrochem 17:1809–1814. https://doi.org/10.1007/s10008-013-2101-8

186. Li D, Duan X, Sun H, et al (2017) Facile synthesis of nitrogen-doped graphene via low-temperature pyrolysis: The effects of precursors and annealing ambience on metal-free catalytic oxidation. Carbon N Y 115:649–658. https://doi.org/10.1016/j.carbon.2017.01.058

187. Jana A, Scheer E, Polarz S (2017) Synthesis of graphene-transition metal oxide hybrid nanoparticles and their application in various fields. Beilstein J Nanotechnol 8:688–714. https://doi.org/10.3762/bjnano.8.74

188. Majumdar D, Maiyalagan T, Jiang Z (2019) Recent Progress in Ruthenium Oxide-Based Composites for Supercapacitor Applications. ChemElectroChem 6:4343–4372. https://doi.org/10.1002/celc.201900668

189. Soin N, Roy SS, Mitra SK, et al (2012) Nanocrystalline ruthenium oxide dispersed Few Layered Graphene (FLG) nanoflakes as supercapacitor electrodes. J Mater Chem 22:14944–14950. https://doi.org/10.1039/c2jm31226c

190. Yan J, Fan Z, Wei T, et al (2010) Fast and reversible surface redox reaction of graphene-MnO2 composites as supercapacitor electrodes. Carbon N Y 48:3825–3833. https://doi.org/10.1016/j.carbon.2010.06.047

191. Singu BS, Yoon KR (2019) Exfoliated graphene-manganese oxide nanocomposite electrode materials for supercapacitor. J Alloys Compd 770:1189–1199. https://doi.org/10.1016/j.jallcom.2018.08.145

192. Shi W, Zhu J, Sim DH, et al (2011) Achieving high specific charge capacitances in Fe3O 4/reduced graphene oxide nanocomposites. J Mater Chem 21:3422–3427. https://doi.org/10.1039/c0jm03175e

193. Ma Z, Huang X, Dou S, et al (2014) One-pot synthesis of Fe2O3 nanoparticles on nitrogen-doped graphene as advanced supercapacitor electrode materials. J Phys Chem C 118:17231–17239. https://doi.org/10.1021/jp502226j

194. Yan Y, Wang T, Li X, et al (2017) Noble metal-based materials in high-performance supercapacitors. Inorg Chem Front 4:33–51. https://doi.org/10.1039/c6qi00199h

195. Sawangphruk M, Suksomboon M, Kongsupornsak K, et al (2013) High-performance supercapacitors based on silver nanoparticle-polyaniline-graphene nanocomposites coated on flexible carbon fiber paper. J Mater Chem A 1:9630–9636. https://doi.org/10.1039/c3ta12194a

196. Shao Y, Wang H, Zhang Q, Li Y (2013) High-performance flexible asymmetric supercapacitors based on 3D porous graphene/MnO2 nanorod and graphene/Ag hybrid thin-film electrodes. J Mater Chem C 1:1245–1251. https://doi.org/10.1039/c2tc00235c

197. Kalambate PK, Dar RA, Karna SP, Srivastava AK (2015) High performance supercapacitor based on graphene-silver nanoparticles-polypyrrole nanocomposite coated on glassy carbon electrode. J Power Sources 276:262–270. https://doi.org/10.1016/j.jpowsour.2014.11.130

198. Reddy KR, Alonso-Marroquin F (2017) Graphene oxide functionalized with silver nanoparticles as conducting electrodes for solar cells and electrochemical energy storage devices. AIP Conf Proc 1856:. https://doi.org/10.1063/1.4985555

199. Khamlich S, Khamliche T, Dhlamini MS, et al (2017) Rapid microwave-assisted growth of silver nanoparticles on 3D graphene networks for supercapacitor application. J Colloid Interface Sci 493:130–137. https://doi.org/10.1016/j.jcis.2017.01.020

200. Dhibar S, Das CK (2017) Silver nanoparticles decorated polypyrrole/graphene nanocomposite: A potential candidate for next-generation supercapacitor electrode material. J Appl Polym Sci 134:1–14. https://doi.org/10.1002/app.44724

201. Jiao S, Li T, Xiong C, et al (2019) A facile method to prepare silver doped graphene combined with polyaniline for high performances of filter paper based flexible electrode. Nanomaterials 9:. https://doi.org/10.3390/nano9101434

202. Ankamwar B, Das P, Sur UK (2016) Graphene–gold nanoparticle-based nanocomposites as an electrode material in supercapacitors. Indian J Phys 90:391–397. https://doi.org/10.1007/s12648-015-0765-x

203. Yu Z, Sun S, Huang M (2016) Electrodeposition of gold nanoparticles on electrochemically reduced graphene oxide for high performance supercapacitor electrode materials. Int J Electrochem Sci 11:3643–3650. https://doi.org/10.20964/110448

204. Sahoo G, Sarkar N, Sahu D, Swain SK (2017) Nano gold decorated reduced graphene oxide wrapped polymethylmethacrylate for supercapacitor applications. RSC Adv 7:2137–2150. https://doi.org/10.1039/c6ra26930c

205. Bahar N, Ekinci D (2020) Hollow porous gold nanoparticle/reduced graphene oxide composite films for electrochemical supercapacitor applications. Electrochim Acta 337:135844. https://doi.org/10.1016/j.electacta.2020.135844

206. Dar RA, Giri L, Karna SP, Srivastava AK (2016) Performance of palladium nanoparticle-graphene composite as an efficient electrode material for electrochemical double layer capacitors. Electrochim Acta 196:547–557. https://doi.org/10.1016/j.electacta.2016.02.197

207. Toth PS, Velický M, Slater TJA, et al (2017) Hydrogen evolution and capacitance behavior of Au/Pd nanoparticle-decorated graphene heterostructures. Appl Mater Today 8:125–131. https://doi.org/10.1016/j.apmt.2017.07.008

208. Gupta VK, Fakhri A, Agarwal S, Naji M (2018) Palladium oxide nanoparticles supported on reduced graphene oxide and gold doped: Preparation, characterization and electrochemical study of supercapacitor electrode. J Mol Liq 249:61–65. https://doi.org/10.1016/j.molliq.2017.11.016

209. Kalambate PK, Rawool CR, Karna SP, Srivastava AK (2019) Nitrogen-doped graphene/palladium nanoparticles/porous polyaniline ternary composite as an efficient electrode material for high performance supercapacitor. Mater Sci Energy Technol 2:246–257. https://doi.org/10.1016/j.mset.2018.12.005

210. Higgins D, Zamani P, Yu A, Chen Z (2016) The application of graphene and its composites in oxygen reduction electrocatalysis: A perspective and review of recent progress. Energy Environ. Sci. 9:357–390

211. Zhang D, Zhang X, Chen Y, et al (2012) Supercapacitor electrodes with especially high rate capability and cyclability based on a novel Pt nanosphere and cysteine-generated graphene. Phys Chem Chem Phys 14:10899–10903. https://doi.org/10.1039/c2cp41051f

212. Zhang Q, Zhang Y, Gao Z, et al (2013) A facile synthesis of platinum nanoparticle decorated graphene by one-step γ-ray induced reduction for high rate supercapacitors. J Mater Chem C 1:321–328. https://doi.org/10.1039/c2tc00078d

213. Ghouri ZK, Barakat NAM, Saud PS, et al (2016) Supercapacitors based on ternary nanocomposite of TiO2&Pt@graphenes. J Mater Sci Mater Electron 27:3894–3900. https://doi.org/10.1007/s10854-015-4239-x

214. Golikand AN, Bagherzadeh M, Shirazi Z (2017) Evaluation of the Polyaniline Based Nanocomposite Modified with Graphene Nanosheet, Carbon Nanotube, and Pt Nanoparticle as a Material for Supercapacitor. Electrochim Acta 247:116–124. https://doi.org/10.1016/j.electacta.2017.07.011

215. Sha R, Badhulika S (2017) Binder free platinum nanoparticles decorated graphene-polyaniline composite film for high performance supercapacitor application. Electrochim Acta 251:505–512. https://doi.org/10.1016/j.electacta.2017.08.140

216. Tancredi P, Moscoso Londoño O, Rivas Rojas PC, et al (2018) Step-by-step synthesis of iron-oxide nanoparticles attached to graphene oxide: A study on the composite properties and architecture. Mater Res Bull 107:255–263. https://doi.org/10.1016/j.materresbull.2018.08.003

217. Gonzalez-Rodriguez R, Campbell E, Naumov A (2019) Multifunctional graphene oxide/iron oxide nanoparticles for magnetic targeted drug delivery dual magnetic resonance/ fluorescence imaging and cancer sensing. PLoS One 14:1–18. https://doi.org/10.1371/journal.pone.0217072

218. Huang J, Zhang L, Chen B, et al (2010) Nanocomposites of size-controlled gold nanoparticles and graphene oxide: Formation and applications in SERS and catalysis. Nanoscale 2:2733–2738. https://doi.org/10.1039/c0nr00473a

219. Ren W, Fang Y, Wang E (2011) A binary functional substrate for enrichment and ultrasensitive SERS spectroscopic detection of folic acid using graphene oxide/Ag nanoparticle hybrids. ACS Nano 5:6425–6433. https://doi.org/10.1021/nn201606r

220. Kumari S, Sharma P, Yadav S, et al (2020) A Novel Synthesis of the Graphene Oxide-Silver (GO-Ag) Nanocomposite for Unique Physiochemical Applications. ACS Omega 5:5041–5047. https://doi.org/10.1021/acsomega.9b03976

221. Zhu C, Guo S, Zhai Y, Dong S (2010) Layer-by-layer self-assembly for constructing a graphene/platinum nanoparticle three-dimensional hybrid nanostructure using ionic liquid as a linker. Langmuir 26:7614–7618. https://doi.org/10.1021/la904201j

222. Shen X, Wu J, Bai S, Zhou H (2010) One-pot solvothermal syntheses and magnetic properties of graphene-based magnetic nanocomposites. J Alloys Compd 506:136–140. https://doi.org/10.1016/j.jallcom.2010.06.158

223. Wang C, Feng C, Gao Y, et al (2011) Preparation of a graphene-based magnetic nanocomposite for the removal of an organic dye from aqueous solution. Chem Eng J 173:92–97. https://doi.org/10.1016/j.cej.2011.07.041

224. Geng Z, Lin Y, Yu X, et al (2012) Highly efficient dye adsorption and removal: A functional hybrid of reduced graphene oxide-Fe 3O 4 nanoparticles as an easily regenerative adsorbent. J Mater Chem 22:3527–3535. https://doi.org/10.1039/c2jm15544c

225. Thy LTM, Thuong NH, Tu TH, et al (2019) Synthesis of magnetic iron oxide/graphene oxide nanocomposites for removal of cadmium ions from water. Adv Nat Sci Nanosci Nanotechnol 10:. https://doi.org/10.1088/2043-6254/ab1b79

226. Tian L, Zhuang Q, Li J, et al (2012) The production of self-assembled Fe 2O 3-graphene hybrid materials by a hydrothermal process for improved Li-cycling. Electrochim Acta 65:153–158. https://doi.org/10.1016/j.electacta.2012.01.034

227. Orfanakis G, Patila M, Catzikonstantinou A V., et al (2018) Hybrid nanomaterials of magnetic iron nanoparticles and graphene oxide as matrices for the immobilization of β-glucosidase: Synthesis, characterization, and biocatalytic properties. Front Mater 5:1–11. https://doi.org/10.3389/fmats.2018.00025

228. Ghasemi S, Hosseini SR, Kazemi Z (2018) Electrophoretic preparation of graphene-iron oxide nanocomposite as an efficient Pt-free counter electrode for dye-sensitized solar cell. J Solid State Electrochem 22:245–253. https://doi.org/10.1007/s10008-017-3741-x

229. Guo A-M, Sun Q (2006) Decorating Graphene Sheets with Gold Nanoparticles. Anal Bioanal Chem i:946–951. https://doi.org/10.1002/adma.201302950

230. Jasuja K, Berry V (2009) Implantation and growth of dendritic gold nanostructures on graphene derivatives: Electrical property tailoring and Raman enhancement. ACS Nano 3:2358–2366. https://doi.org/10.1021/nn900504v

231. Goncalves G, Marques PAAP, Granadeiro CM, et al (2009) Surface modification of graphene nanosheets with gold nanoparticles: The role of oxygen moieties at graphene surface on gold nucleation and growth. Chem Mater 21:4796–4802. https://doi.org/10.1021/cm901052s

232. Huang X, Li S, Wu S, et al (2012) Graphene oxide-templated synthesis of ultrathin or tadpole-shaped Au nanowires with alternating hcp and fcc domains. Adv Mater 24:979–983. https://doi.org/10.1002/adma.201104153

233. Thirumalraj B, Rajkumar C, Chen SM, Palanisamy S (2017) One-Pot Green Synthesis of Graphene Nanosheets Encapsulated Gold Nanoparticles for Sensitive and Selective Detection of Dopamine. Sci Rep 7:1–11. https://doi.org/10.1038/srep41213

234. Chen W, Shen J, Chen S, et al (2019) Synthesis of graphene quantum dot-stabilized gold nanoparticles and their application. RSC Adv 9:21215–21219. https://doi.org/10.1039/c9ra02758k

235. Zhou X, Huang X, Qi X, et al (2009) In situ synthesis of metal nanoparticles on single-layer graphene oxide and reduced graphene oxide surfaces. J Phys Chem C 113:10842–10846. https://doi.org/10.1021/jp903821n

236. Zhu M, Chen P, Liu M (2011) Graphene oxide enwrapped Ag/AgX (X = Br, Cl) nanocomposite as a highly efficient visible-light plasmonic photocatalyst. ACS Nano 5:4529–4536. https://doi.org/10.1021/nn200088x

237. Lu G, Li H, Liusman C, et al (2011) Surface enhanced Raman scattering of Ag or Au nanoparticle-decorated reduced graphene oxide for detection of aromatic molecules. Chem Sci 2:1817–1821. https://doi.org/10.1039/c1sc00254f

238. Zheng L, Zhang G, Zhang M, et al (2012) Preparation and capacitance performance of Ag-graphene based nanocomposite. J Power Sources 201:376–381. https://doi.org/10.1016/j.jpowsour.2011.11.026

239. Li Y, Gao W, Ci L, et al (2010) Catalytic performance of Pt nanoparticles on reduced graphene oxide for methanol electro-oxidation. Carbon N Y 48:1124–1130. https://doi.org/10.1016/j.carbon.2009.11.034

240. Vinayan BP, Nagar R, Ramaprabhu S (2012) Synthesis and investigation of mechanism of platinum-graphene electrocatalysts by novel co-reduction techniques for proton exchange membrane fuel cell applications. J Mater Chem 22:25325–25334. https://doi.org/10.1039/c2jm33894g

241. Liu Z, Duan X, Cheng H, et al (2015) Synthesis of platinum/graphene composites by a polyol method: The role of graphite oxide precursor surface chemistry. Carbon N Y 89:93–101. https://doi.org/10.1016/j.carbon.2015.03.022

242. Li N, Wang Z, Zhao K, et al (2010) Graphene-Pd composite as highly active catalyst for the Suzuki-Miyaura coupling reaction. J Nanosci Nanotechnol 10:6748–6751. https://doi.org/10.1166/jnn.2010.2638

243. Yang J, Tian C, Wang L, et al (2012) In situ reduction, oxygen etching, and reduction using formic acid: An effective strategy for controllable growth of monodisperse palladium nanoparticles on graphene. Chempluschem 77:301–307. https://doi.org/10.1002/cplu.201100058

244. Scheuermann GM, Rumi L, Steurer P, et al (2009) Palladium nanoparticles on graphite oxide and its functionalized graphene derivatives as highly active catalysts for the Suzuki-Miyaura coupling reaction. J Am Chem Soc 131:8262–8270. https://doi.org/10.1021/ja901105a

245. Li Y, Fan X, Qi J, et al (2010) Palladium nanoparticle-graphene hybrids as active catalysts for the Suzuki reaction. Nano Res 3:429–437. https://doi.org/10.1007/s12274-010-0002-z

246. Moussa S, Abdelsayed V, Samy El-Shall M (2011) Laser synthesis of Pt, Pd, CoO and Pd-CoO nanoparticle catalysts supported on graphene. Chem Phys Lett 510:179–184. https://doi.org/10.1016/j.cplett.2011.05.026

247. Lu LM, Li HB, Qu F, et al (2011) In situ synthesis of palladium nanoparticle-graphene nanohybrids and their application in nonenzymatic glucose biosensors. Biosens Bioelectron 26:3500–3504. https://doi.org/10.1016/j.bios.2011.01.033

248. Marinoiu A, Raceanu M, Andrulevicius M, et al (2020) Low-cost preparation method of well dispersed gold nanoparticles on reduced graphene oxide and electrocatalytic stability in PEM fuel cell. Arab J Chem 13:3585–3600. https://doi.org/10.1016/j.arabjc.2018.12.009

249. Li J, Liu CY (2010) Ag/Graphene heterostructures: Synthesis, characterization and optical properties. Eur J Inorg Chem 1244–1248. https://doi.org/10.1002/ejic.200901048

250. Lu X, Qi H, Zhang X, et al (2011) Highly dispersive Ag nanoparticles on functionalized graphene for an excellent electrochemical sensor of nitroaromatic compounds. Chem Commun 47:12494–12496. https://doi.org/10.1039/c1cc15697g

251. Xin Y, Liu JG, Zhou Y, et al (2011) Preparation and characterization of Pt supported on graphene with enhanced electrocatalytic activity in fuel cell. J Power Sources 196:1012–1018. https://doi.org/10.1016/j.jpowsour.2010.08.051

252. Zhang Z, Chen H, Xing C, et al (2011) Sodium citrate: A universal reducing agent for reduction / decoration of graphene oxide with au nanoparticles. Nano Res 4:599–611. https://doi.org/10.1007/s12274-011-0116-y

253. Choi DH, Hong JE, Jung Y, et al (2019) Synthesis of gold nanoparticles supported at graphene derivatives using green reductants and evaluation of their catalytic activity in 4-nitrophenol reduction. Gold Bull 52:165–174. https://doi.org/10.1007/s13404-019-00258-w

254. Sun S, Wu P (2011) Competitive surface-enhanced Raman scattering effects in noble metal nanoparticle-decorated graphene sheets. Phys Chem Chem Phys 13:21116–21120. https://doi.org/10.1039/c1cp22727k

255. Sidorov AN, Sławiński GW, Jayatissa AH, et al (2012) A surface-enhanced Raman spectroscopy study of thin graphene sheets functionalized with gold and silver nanostructures by seed-mediated growth. Carbon N Y 50:699–705. https://doi.org/10.1016/j.carbon.2011.09.030

256. Cobos M, De-La-pinta I, Quindós G, et al (2020) Graphene oxide–silver nanoparticle nanohybrids: Synthesis, characterization, and antimicrobial properties. Nanomaterials 10:. https://doi.org/10.3390/nano10020376

257. Gong F, Wang H, Wang ZS (2011) Self-assembled monolayer of graphene/Pt as counter electrode for efficient dye-sensitized solar cell. Phys Chem Chem Phys 13:17676–17682. https://doi.org/10.1039/c1cp22542a

258. Cuong L Van, Thinh ND, Nghia LTT, et al (2020) Synthesis of platinum/reduced graphene oxide composite pastes for fabrication of cathodes in dye-sensitized solar cells with screen-printing technology. Inorg Chem Commun 118:108033. https://doi.org/10.1016/j.inoche.2020.108033

259. Fu C, Kuang Y, Huang Z, et al (2010) Electrochemical co-reduction synthesis of graphene/Au nanocomposites in ionic liquid and their electrochemical activity. Chem Phys Lett 499:250–253. https://doi.org/10.1016/j.cplett.2010.09.055

260. Liu S, Wang J, Zeng J, et al (2010) “Green” electrochemical synthesis of Pt/graphene sheet nanocomposite film and its electrocatalytic property. J Power Sources 195:4628–4633. https://doi.org/10.1016/j.jpowsour.2010.02.024

261. Chen C, Long MC, Wu H, Cai WM (2013) One-step synthesis of Pt nanoparticles/reduced graphene oxide composite with enhanced electrochemical catalytic activity. Sci China Chem 56:354–361. https://doi.org/10.1007/s11426-012-4702-y

262. Hu Y, Jin J, Wu P, et al (2010) Graphene-gold nanostructure composites fabricated by electrodeposition and their electrocatalytic activity toward the oxygen reduction and glucose oxidation. Electrochim Acta 56:491–500. https://doi.org/10.1016/j.electacta.2010.09.021

263. Arif M, Heo K, Lee BY, et al (2011) Metallic nanowire-graphene hybrid nanostructures for highly flexible field emission devices. Nanotechnology 22:. https://doi.org/10.1088/0957-4484/22/35/355709

264. Yao Z, Zhu M, Jiang F, et al (2012) Highly efficient electrocatalytic performance based on Pt nanoflowers modified reduced graphene oxide/carbon cloth electrode. J Mater Chem 22:13707–13713. https://doi.org/10.1039/c2jm31683h

265. Huang X, Zhou X, Wu S, et al (2010) Reduced graphene oxide-templated photochemical synthesis and in situ assembly of Au nanodots to orderly patterned Au nanodot chains. Small 6:513–516. https://doi.org/10.1002/smll.200902001

266. Chen J, Zheng X, Wang H, Zheng W (2011) Graphene oxide-Ag nanocomposite: In situ photochemical synthesis and application as a surface-enhanced Raman scattering substrate. Thin Solid Films 520:179–185. https://doi.org/10.1016/j.tsf.2011.07.012

267. Min S, Lu G (2012) Dye-cosensitized graphene/Pt photocatalyst for high efficient visible light hydrogen evolution. Int J Hydrogen Energy 37:10564–10574. https://doi.org/10.1016/j.ijhydene.2012.04.072

268. Yin Z, He Q, Huang X, et al (2012) Real-time DNA detection using Pt nanoparticle-decorated reduced graphene oxide field-effect transistors. Nanoscale 4:293–297. https://doi.org/10.1039/c1nr11149c

269. Park G, Lee KG, Lee SJ, et al (2011) Synthesis of graphene-gold nanocomposites via sonochemical reduction. J Nanosci Nanotechnol 11:6095–6101. https://doi.org/10.1166/jnn.2011.4446

270. Guo S, Wen D, Zhai Y, et al (2010) Platinum nanoparticle ensemble-on-graphene hybrid nanosheet: One-pot, rapid synthesis, and used as new electrode material for electrochemical sensing. ACS Nano 4:3959–3968. https://doi.org/10.1021/nn100852h

271. Kundu P, Nethravathi C, Deshpande PA, et al (2011) Ultrafast microwave-assisted route to surfactant-free ultrafine Pt nanoparticles on graphene: Synergistic co-reduction mechanism and high catalytic activity. Chem Mater 23:2772–2780. https://doi.org/10.1021/cm200329a

272. Wen Z, Yang S, Liang Y, et al (2010) The improved electrocatalytic activity of palladium/graphene nanosheets towards ethanol oxidation by tin oxide. Electrochim Acta 56:139–144. https://doi.org/10.1016/j.electacta.2010.09.032

273. Siamaki AR, Khder AERS, Abdelsayed V, et al (2011) Microwave-assisted synthesis of palladium nanoparticles supported on graphene: A highly active and recyclable catalyst for carbon-carbon cross-coupling reactions. J Catal 279:1–11. https://doi.org/10.1016/j.jcat.2010.12.003

274. Shi M, Liu W, Zhao D, et al (2014) Synthesis of palladium nanoparticles supported on reduced graphene oxide-tungsten carbide composite and the investigation of its performance for electrooxidation of formic acid. J Solid State Electrochem 18:1923–1932. https://doi.org/10.1007/s10008-014-2440-0

275. Brinkley KW, Burkholder M, Siamaki AR, et al (2015) The continuous synthesis and application of graphene supported palladium nanoparticles: A highly effective catalyst for Suzuki-Miyaura cross-coupling reactions. Green Process Synth 4:241–246. https://doi.org/10.1515/gps-2015-0021

276. Khalil I, Julkapli NM, Yehye WA, et al (2016) Graphene-gold nanoparticles hybrid-synthesis, functionalization, and application in a electrochemical and surface-enhanced raman scattering biosensor

277. Liu X, Mao J, Liu P, Wei X (2010) Fabrication of metal-graphene hybrid materials by electroless deposition. Carbon N Y 49:477–483. https://doi.org/10.1016/j.carbon.2010.09.044

278. Giovanni M, Poh HL, Ambrosi A, et al (2012) Noble metal (Pd, Ru, Rh, Pt, Au, Ag) doped graphene hybrids for electrocatalysis. Nanoscale 4:5002–5008. https://doi.org/10.1039/c2nr31077e

279. Park Y, Koo JY, Kim S, Choi HC (2019) Spontaneous Formation of Gold Nanoparticles on Graphene by Galvanic Reaction through Graphene. ACS Omega 4:18423–18427. https://doi.org/10.1021/acsomega.9b02691

280. Garg K, Papponen P, Johansson A, et al (2020) Preparation of graphene nanocomposites from aqueous silver nitrate using graphene oxide’s peroxidase-like and carbocatalytic properties. Sci Rep 10:1–13. https://doi.org/10.1038/s41598-020-61929-9

281. Abdolhosseinzadeh S, Sadighikia S, Alkan Gürsel S (2018) Scalable Synthesis of Sub-Nanosized Platinum-Reduced Graphene Oxide Composite by an Ultraprecise Photocatalytic Method. ACS Sustain Chem Eng 6:3773–3782. https://doi.org/10.1021/acssuschemeng.7b04148

282. Tang X, Haddad PA, Mager N, et al (2019) Chemically deposited palladium nanoparticles on graphene for hydrogen sensor applications. Sci Rep 9:1–11. https://doi.org/10.1038/s41598-019-40257-7

283. Robert J. Goldston and Paul H. Rutherford (1995) Introduction to plasma physics. IOP Publishing Ltd.

284. J. Reece Roth (1995) Industrial Plasma Engineering, Volume 1: Principles. Institute of Physics Publishing

285. Xu Z, Xiong FF (2017) Plasma Surface Metallurgy. Springer Singapore, Singapore

286. Szabó D, Schlabach S (2014) Microwave Plasma Synthesis of Materials—From Physics and Chemistry to Nanoparticles: A Materials Scientist's Viewpoint. Inorganics 2:468–507. https://doi.org/10.3390/inorganics2030468

287. Tendero C, Tixier C, Tristant P, et al (2006) Atmospheric pressure plasmas: A review. Spectrochim Acta - Part B At Spectrosc 61:2–30. https://doi.org/10.1016/j.sab.2005.10.003

288. Dudeck M, André P, Kaminska A, Lino Da Silva M (2012) Thermodynamics equilibrium and non equilibrium of plasma flows. IOP Conf Ser Mater Sci Eng 29:. https://doi.org/10.1088/1757-899X/29/1/012005

289. Kuzelev M V., Mkheidze GP, Rukhadze AA, et al (1999) Electron Beam Generated Plasmas: Theory, Experiments, Applications. Adv Technol Based Wave Beam Gener Plasmas 391–428. https://doi.org/10.1007/978-94-017-0633-9_18

290. Danehkar A (2018) Electron beam-plasma interaction and electron-acoustic solitary waves in a plasma with suprathermal electrons. Plasma Phys Control Fusion 60:. https://doi.org/10.1088/1361-6587/aabc40

291. Chu PK, Chen JY, Wang LP, Huang N (2002) Plasma-surface modification of biomaterials. Mater Sci Eng R 36:143–206. https://doi.org/10.1016/S0927-796X(02)00004-9

292. Bogaerts A, Neyts EC (2018) Plasma Technology: An Emerging Technology for Energy Storage. ACS Energy Lett 3:1013–1027. https://doi.org/10.1021/acsenergylett.8b00184

293. Lu W, Abbas Y, Mustafa MF, et al (2019) A review on application of dielectric barrier discharge plasma technology on the abatement of volatile organic compounds. Front Environ Sci Eng 13:. https://doi.org/10.1007/s11783-019-1108-5

294. Kogelschatz U (2003) Dielectric-Barrier Discharges: Their History, Discharge Physics, and Industrial Applications. Plasma Chem Plasma Process 23:1–36. https://doi.org/10.1023/A

295. Winter J, Brandenburg R, Weltmann KD (2015) Atmospheric pressure plasma jets: An overview of devices and new directions. Plasma Sources Sci Technol 24:64001. https://doi.org/10.1088/0963-0252/24/6/064001

296. Alotaibi F, Tung TT, Nine MJ, et al (2018) Scanning atmospheric plasma for ultrafast reduction of graphene oxide and fabrication of highly conductive graphene films and patterns. Carbon N Y 127:113–121. https://doi.org/10.1016/j.carbon.2017.10.075

297. Penkov O V., Khadem M, Lim WS, Kim DE (2015) A review of recent applications of atmospheric pressure plasma jets for materials processing. J Coatings Technol Res 12:225–235. https://doi.org/10.1007/s11998-014-9638-z

298. Gudmundsson JT, Hecimovic A (2017) Foundations of DC plasma sources. Plasma Sources Sci Technol 26:. https://doi.org/10.1088/1361-6595/aa940d

299. Muhl S, Pérez A (2015) The use of hollow cathodes in deposition processes: A critical review. Thin Solid Films 579:174–198. https://doi.org/10.1016/j.tsf.2015.02.066

300. Aghajani H, Behrangi S (2017) Active Screen Plasma Nitriding. In: Plasma Nitriding of Steels. Springer International Publishing, Cham, pp 127–159

301. Corujeira Gallo S, Li X, Dong H (2012) Dry sliding wear of active screen plasma carburised austenitic stainless steel. Tribol Lett 45:153–160. https://doi.org/10.1007/s11249-011-9875-6

302. Liang Y, Li X, Semitekolos D, et al (2020) Enhanced properties of PAN-derived carbon fibres and resulting composites by active screen plasma

surface functionalisation. Plasma Process Polym. https://doi.org/10.1002/ppap.201900252

303. Corujeira Gallo S, Charitidis C, Dong H (2017) Surface functionalization of carbon fibers with active screen plasma. J Vac Sci Technol A Vacuum, Surfaces, Film 35:021404. https://doi.org/10.1116/1.4974913

304. Gómez-Navarro C, Weitz RT, Bittner AM, et al (2007) Electronic transport properties of individual chemically reduced graphene oxide sheets. Nano Lett 7:3499–3503. https://doi.org/10.1021/nl072090c

305. Baraket M, Walton SG, Wei Z, et al (2010) Reduction of graphene oxide by electron beam generated plasmas produced in methane/argon mixtures. Carbon N. Y. 48:3382–3390

306. Lambert TN, Luhrs CC, Chavez CA, et al (2010) Graphite oxide as a precursor for the synthesis of disordered graphenes using the aerosol-through-plasma method. Carbon N Y 48:4081–4089. https://doi.org/10.1016/j.carbon.2010.07.015

307. Cardinali M, Valentini L, Fabbri P, Kenny JM (2011) Radiofrequency plasma assisted exfoliation and reduction of large-area graphene oxide platelets produced by a mechanical transfer process. Chem Phys Lett 508:285–288. https://doi.org/10.1016/j.cplett.2011.04.065

308. Li T, Patel T, Banerjee I, et al (2015) Plasma treated graphene oxide films: structural and electrical studies. J Mater Sci Mater Electron 26:4810–4815. https://doi.org/10.1007/s10854-015-3122-0

309. Lee SW, Mattevi C, Chhowalla M, Sankaran RM (2012) Plasma-assisted reduction of graphene oxide at low temperature and atmospheric pressure for flexible conductor applications. J Phys Chem Lett 3:772–777. https://doi.org/10.1021/jz300080p

310. Krishnamoorthy K, Ananth A, Mok YS, Kim SJ (2014) Plasma Assisted Synthesis of Graphene Nanosheets and Their Supercapacitor Applications. Sci Adv Mater 6:349–353. https://doi.org/10.1166/sam.2014.1722

311. Bodik M, Zahoranova A, Micusik M, et al (2017) Fast low-temperature plasma reduction of monolayer graphene oxide at atmospheric pressure. Nanotechnology 28:. https://doi.org/10.1088/1361-6528/aa60ef

312. Dey A, Krishnamurthy S, Bowen J, et al (2018) Plasma Jet Printing and in Situ Reduction of Highly Acidic Graphene Oxide. ACS Nano

12:5473–5481. https://doi.org/10.1021/acsnano.8b00903

313. Chandana L, Ghosal P, Challapalli S (2016) Improved Solar Cell Performance of High Quality Plasma Reduced Graphene Oxide. Plasma Process Polym 13:929–936. https://doi.org/10.1002/ppap.201600007

314. Senthilnathan J, Yoshimura M (2017) Low energy liquid plasma for direct reduction and formation of rGO-aminopyridine hybrid for electrical and environmental applications. J Hazard Mater 340:26–35. https://doi.org/10.1016/j.jhazmat.2017.06.061

315. Bo Z, Qian J, Han ZJ, et al (2015) Note: Rapid reduction of graphene oxide paper by glow discharge plasma. Rev Sci Instrum 86:2013–2016. https://doi.org/10.1063/1.4919732

316. Li J, Chen C, Wei J, et al (2014) Enhanced electrochemical performance of reduced graphene oxides by H2/Ar plasma treatment. J Phys Chem C 118:28440–28447. https://doi.org/10.1021/jp509182g

317. Bo Z, Zhu W, Tu X, et al (2014) Instantaneous reduction of graphene oxide paper for supercapacitor electrodes with unimpeded liquid permeation. J Phys Chem C 118:13493–13502. https://doi.org/10.1021/jp5037734

318. Kim M, Kahng YH, Kim YJ, et al (2013) Optical endpoint detection for plasma reduction of graphene oxide. AIP Adv 3:. https://doi.org/10.1063/1.4795240

319. Muhammad Hafiz S, Ritikos R, Whitcher TJ, et al (2014) A practical carbon dioxide gas sensor using room-temperature hydrogen plasma reduced graphene oxide. Sensors Actuators, B Chem 193:692–700. https://doi.org/10.1016/j.snb.2013.12.017

320. Homola T, Pospíšil J, Krumpolec R, et al (2018) Atmospheric Dry Hydrogen Plasma Reduction of Inkjet-Printed Flexible Graphene Oxide Electrodes. ChemSusChem 11:941–947. https://doi.org/10.1002/cssc.201702139

321. Banerjee I, Mahapatra SK, Pal C, et al (2018) Effect of plasma power on reduction of printable graphene oxide thin films on flexible substrates. Mater Res Express 5:056405. https://doi.org/10.1088/2053-1591/aac04e

322. Cheng M, Yang R, Zhang L, et al (2012) Restoration of graphene from graphene oxide by defect repair. Carbon N Y 50:2581–2587. https://doi.org/10.1016/j.carbon.2012.02.016

323. Chiang WH, Lin TC, Li YS, et al (2016) Toward bandgap tunable graphene oxide nanoribbons by plasma-assisted reduction and defect restoration at low temperature. RSC Adv 6:2270–2278. https://doi.org/10.1039/c5ra21537d

324. Yang C, Gong J, Zeng P, et al (2018) Fast room-temperature reduction of graphene oxide by methane/argon plasma for flexible electronics. Appl Surf Sci 452:481–486. https://doi.org/10.1016/j.apsusc.2018.04.272

325. Obata S, Sato M, Akada K, Saiki K (2018) High degree reduction and restoration of graphene oxide on SiO2 at low temperature via remote Cu-assisted plasma treatment. Nanotechnology 29:245603. https://doi.org/10.1088/1361-6528/aab73e

326. McManus JB, Hennessy A, Cullen CP, et al (2017) Controlling Defect and Dopant Concentrations in Graphene by Remote Plasma Treatments. Phys Status Solidi Basic Res 254:1–6. https://doi.org/10.1002/pssb.201700214

327. Akada K, Terasawa TO, Imamura G, et al (2014) Control of work function of graphene by plasma assisted nitrogen doping. Appl Phys Lett 104:1–5. https://doi.org/10.1063/1.4870424

328. Zeng JJ, Lin YJ (2014) Tuning the work function of graphene by nitrogen plasma treatment with different radio-frequency powers. Appl Phys Lett 104:. https://doi.org/10.1063/1.4882159

329. Ding D, Song ZL, Cheng ZQ, et al (2014) Plasma-assisted nitrogen doping of graphene-encapsulated Pt nanocrystals as efficient fuel cell catalysts. J Mater Chem A 2:472–477. https://doi.org/10.1039/c3ta14054g

330. Imran Jafri R, Rajalakshmi N, Ramaprabhu S (2010) Nitrogen doped graphene nanoplatelets as catalyst support for oxygen reduction reaction in proton exchange membrane fuel cell. J Mater Chem 20:7114–7117. https://doi.org/10.1039/c0jm00467g

331. Amirfakhri SJ, Binny D, Meunier JL, Berk D (2014) Investigation of hydrogen peroxide reduction reaction on graphene and nitrogen doped graphene nanoflakes in neutral solution. J Power Sources 257:356–363. https://doi.org/10.1016/j.jpowsour.2014.01.114

332. Dou S, Tao L, Huo J, et al (2016) Etched and doped Co9S8/graphene hybrid for oxygen electrocatalysis. Energy Environ Sci 9:1320–1326. https://doi.org/10.1039/c6ee00054a

333. Sim U, Yang TY, Moon J, et al (2013) N-doped monolayer graphene catalyst on silicon photocathode for hydrogen production. Energy Environ Sci 6:3658–3664. https://doi.org/10.1039/c3ee42106f

334. Kirubaharan CJ, Santhakumar K, Gnana Kumar G, et al (2015) Nitrogen doped graphene sheets as metal free anode catalysts for the high performance microbial fuel cells. Int J Hydrogen Energy 40:13061–13070. https://doi.org/10.1016/j.ijhydene.2015.06.025

335. Li S, Zhao X, Gang R, et al (2020) Doping Nitrogen into Q-Graphene by Plasma Treatment toward Peroxidase Mimics with Enhanced Catalysis. Anal Chem 92:5152–5157. https://doi.org/10.1021/acs.analchem.9b05645

336. Yen HF, Horng YY, Hu MS, et al (2015) Vertically aligned epitaxial graphene nanowalls with dominated nitrogen doping for superior supercapacitors. Carbon N Y 82:124–134. https://doi.org/10.1016/j.carbon.2014.10.042

337. Yang CH, Kuok FH, Liao CY, et al (2017) Flexible reduced graphene oxide supercapacitor fabricated using a nitrogen DC-pulse atmospheric-pressure plasma jet. Mater Res Express 4:. https://doi.org/10.1088/2053-1591/aa5ed5

338. Jeong HM, Lee JW, Shin WH, et al (2011) Nitrogen-doped graphene for high-performance ultracapacitors and the importance of nitrogen-doped sites at basal planes. Nano Lett 11:2472–2477. https://doi.org/10.1021/nl2009058

339. Chien HH, Cheng YC, Hao YC, et al (2018) Nitrogen DC-pulse atmospheric-pressure-plasma jet (APPJ)-processed reduced graphene oxide (rGO)‑carbon black (CB) nanocomposite electrodes for supercapacitor applications. Diam Relat Mater 88:23–31. https://doi.org/10.1016/j.diamond.2018.06.019

340. Hsu AR, Chien HH, Liao CY, et al (2018) Scan-mode atmospheric-pressure plasma jet processed reduced graphene oxides for quasi-solid-state gel-electrolyte supercapacitors. Coatings 8:. https://doi.org/10.3390/coatings8020052

341. Fan CF, Chien YC, Hsu CC, et al (2020) Flexible reduced graphene oxide supercapacitors processed using atmospheric-pressure plasma jet under various temperatures adjusted by flow rate and jet-substrate distance. Mater Res Express 7:. https://doi.org/10.1088/2053-1591/ab59a2

342. Duan L, Zhao L, Cong H, et al (2019) Plasma Treatment for Nitrogen-Doped 3D Graphene Framework by a Conductive Matrix with Sulfur for High-Performance Li–S Batteries. Small 15:1–8. https://doi.org/10.1002/smll.201804347

343. Baraket M, Stine R, Lee WK, et al (2012) Aminated graphene for DNA attachment produced via plasma functionalization. Appl Phys Lett 100:. https://doi.org/10.1063/1.4711771

344. Lavanya J, Subbiah A, Neogi S, Gomathi N (2018) Direct electron transfer of hemoglobin at nitrogen incorporated reduced graphene oxide obtained by radio frequency ammonia plasma treatment. Sensors Actuators, B Chem 255:536–543. https://doi.org/10.1016/j.snb.2017.08.047

345. Jothi L, Neogi S, Jaganathan S kumar, Nageswaran G (2018) Simultaneous determination of ascorbic acid, dopamine and uric acid by a novel electrochemical sensor based on N2/Ar RF plasma assisted graphene nanosheets/graphene nanoribbons. Biosens Bioelectron 105:236–242. https://doi.org/10.1016/j.bios.2018.01.040

346. Zhou HP, Ye X, Huang W, et al (2019) Wearable, Flexible, Disposable Plasma-Reduced Graphene Oxide Stress Sensors for Monitoring Activities in Austere Environments. ACS Appl Mater Interfaces 11:15122–15132. https://doi.org/10.1021/acsami.8b22673

347. Soin N, Sinha Roy S, Roy S, et al (2011) Enhanced and stable field emission from in situ nitrogen-doped few-layered graphene nanoflakes. J Phys Chem C 115:5366–5372. https://doi.org/10.1021/jp110476m

348. Zhao CX, Zhang Y, Deng SZ, et al (2016) Surface nitrogen functionality for the enhanced field emission of free-standing few-layer graphene nanowalls. J Alloys Compd 672:433–439. https://doi.org/10.1016/j.jallcom.2016.01.265

349. Tamilarasan P, Ramaprabhu S (2015) Sub-ambient carbon dioxide adsorption properties of nitrogen doped graphene. J Appl Phys 117:. https://doi.org/10.1063/1.4917205

350. Qin S, Xu Q (2017) Room temperature ferromagnetism in N2plasma treated graphene oxide. J Alloys Compd 692:332–338. https://doi.org/10.1016/j.jallcom.2016.09.055

351. Hernández SC, Bezares FJ, Robinson JT, et al (2013) Controlling the local chemical reactivity of graphene through spatial functionalization. Carbon N Y 60:84–93. https://doi.org/10.1016/j.carbon.2013.03.059

352. Park SH, Chae J, Cho MH, et al (2014) High concentration of nitrogen doped into graphene using N2 plasma with an aluminum oxide buffer layer. J Mater Chem C 2:933–939. https://doi.org/10.1039/c3tc31773k

353. Neustroev EP, Burtseva EK, Soloviev BD, et al (2018) Modification of graphene oxide films by radiofrequency N2 plasma. Nanotechnology 29:144002. https://doi.org/10.1088/1361-6528/aaabe3

354. Lin YP, Ksari Y, Aubel D, et al (2016) Efficient and low-damage nitrogen doping of graphene via plasma-based methods. Carbon N Y 100:337–344. https://doi.org/10.1016/j.carbon.2015.12.094

355. Sakulsermsuk S, Singjai P, Chaiwong C (2016) Influence of plasma process on the nitrogen configuration in graphene. Diam Relat Mater 70:211–218. https://doi.org/10.1016/j.diamond.2016.11.001

356. Robert Bigras G, Glad X, Martel R, et al (2018) Treatment of graphene films in the early and late afterglows of N 2 plasmas: comparison of the defect generation and N-incorporation dynamics. Plasma Sources Sci Technol 27:. https://doi.org/10.1088/1361-6595/aaedfd

357. Bertóti I, Mohai M, László K (2015) Surface modification of graphene and graphite by nitrogen plasma: Determination of chemical state alterations and assignments by quantitative X-ray photoelectron spectroscopy. Carbon N Y 84:185–196. https://doi.org/10.1016/j.carbon.2014.11.056

358. Mohai M, Bertóti I (2016) Modification of graphene-oxide surface in nitrogen and argon glow discharge plasma. Surf Interface Anal 48:461–464. https://doi.org/10.1002/sia.5929

359. Rybin M, Pereyaslavtsev A, Vasilieva T, et al (2016) Efficient nitrogen doping of graphene by plasma treatment. Carbon N Y 96:196–202. https://doi.org/10.1016/j.carbon.2015.09.056

360. Dias A, Bundaleski N, Tatarova E, et al (2016) Production of N-graphene by microwave N2-Ar plasma. J Phys D Appl Phys 49:. https://doi.org/10.1088/0022-3727/49/5/055307

361. Chi YW, Hu CC, Huang KP, et al (2016) Manipulation of defect density and nitrogen doping on few-layer graphene sheets using the plasma methodology for electrochemical applications. Electrochim Acta 221:144–153. https://doi.org/10.1016/j.electacta.2016.10.093

362. Yanilmaz A, Tomak A, Akbali B, et al (2017) Nitrogen doping for facile and effective modification of graphene surfaces. RSC Adv 7:28383–28392. https://doi.org/10.1039/c7ra03046k

363. Bundaleska N, Bundaleski N, Dias A, et al (2018) Microwave N2-Ar plasmas applied for N-graphene post synthesis. Mater Res Express 5:095605. https://doi.org/10.1088/2053-1591/aad7e9

364. M. Santhosh N, Filipič G, Kovacevic E, et al (2020) N-Graphene Nanowalls via Plasma Nitrogen Incorporation and Substitution: The Experimental Evidence. Nano-Micro Lett 12:. https://doi.org/10.1007/s40820-020-0395-5

365. Lu G, Mao S, Park S, et al (2009) Facile, noncovalent decoration of graphene oxide sheets with nanocrystals. Nano Res 2:192–200. https://doi.org/10.1007/s12274-009-9017-8

366. Yamazaki K, Maehara Y, Lee CC, et al (2018) Atomic Structure and Local Electronic States of Single Pt Atoms Dispersed on Graphene. J Phys Chem C 122:27292–27300. https://doi.org/10.1021/acs.jpcc.8b04529

367. Xu W, Wang X, Zhou Q, et al (2012) Low-temperature plasma-assisted preparation of graphene supported palladium nanoparticles with high hydrodesulfurization activity. J Mater Chem 22:14363–14368. https://doi.org/10.1039/c2jm16479e

368. Wan T-H, Chiu Y-F, Chen C-W, et al (2016) Atmospheric-Pressure Plasma Jet Processed Pt-Decorated Reduced Graphene Oxides for Counter-Electrodes of Dye-Sensitized Solar Cells. Coatings 6:44. https://doi.org/10.3390/coatings6040044

369. Wei Y, Zuo X, Li X, et al (2014) Dry plasma synthesis of graphene oxide-Ag nanocomposites: A simple and green approach. Mater Res Bull 53:145–150. https://doi.org/10.1016/j.materresbull.2014.02.015

370. Dao VD, Jung SH, Kim JS, et al (2015) AuNP/graphene nanohybrid prepared by dry plasma reduction as a low-cost counter electrode material for dye-sensitized solar cells. Electrochim Acta 156:138–146. https://doi.org/10.1016/j.electacta.2014.12.109

371. Yang C, Yu Y, Xie Y, et al (2019) One-step synthesis of size-tunable gold nanoparticles/reduced graphene oxide nanocomposites using argon plasma and their applications in sensing and catalysis. Appl Surf Sci 473:83–90. https://doi.org/10.1016/j.apsusc.2018.12.125

372. Wang Y, Zhang K, Wang R, et al (2019) Plasma jet printing for preparation of N-doped graphene electrode. J Mater Sci Mater Electron 8944–8954. https://doi.org/10.1007/s10854-019-01222-2

373. Li J, Chen C, Zhang R, Wang X (2015) Nanoscale zero-valent iron particles supported on reduced graphene oxides by using a plasma technique and their application for removal of heavy-metal ions. Chem - An Asian J 10:1410–1417. https://doi.org/10.1002/asia.201500242

374. Liu T, Cui Z, Liu Y, Bai X (2019) In-situ fabrication of ultrafine Pd supported on nitrogen-doped reduced graphene oxide via nitrogen glow discharge plasma for catalytic reduction of 4-Nitrophenol. Appl Catal A Gen 588:117278. https://doi.org/10.1016/j.apcata.2019.117278

375. Li X, Zhang BW, Yan X, et al (2019) Fe,N-doped graphene prepared by NH3 plasma with a high performance for oxygen reduction reaction. Catal Today 337:97–101. https://doi.org/10.1016/j.cattod.2019.04.032

376. Meyer JC, Eder F, Kurasch S, et al (2012) Accurate measurement of electron beam induced displacement cross sections for single-layer graphene. Phys Rev Lett 108:1–6. https://doi.org/10.1103/PhysRevLett.108.196102

377. Cho Y, Yang J, Lam D Van, et al (2014) Transmission Electron Microscopy Specimen Preparation for Layer-area Graphene by a Direct Transfer Method. Appl Microsc 44:133–137. https://doi.org/10.9729/am.2014.44.4.133

378. Rabchinskii MK, Dideikin AT, Kirilenko DA, et al (2018) Facile reduction of graphene oxide suspensions and films using glass wafers. Sci Rep 8:1–11. https://doi.org/10.1038/s41598-018-32488-x

379. Li L, Li G (2020) Multi-bit biomemory based on chitosan: Graphene oxide nanocomposite with wrinkled surface. Micromachines 11:1–13. https://doi.org/10.3390/mi11060580

380. Deng S, Berry V (2016) Wrinkled, rippled and crumpled graphene: An overview of formation mechanism, electronic properties, and applications. Mater Today 19:197–212. https://doi.org/10.1016/j.mattod.2015.10.002

381. Lee KT, Lu SY (2012) Porous FTO thin layers created with a facile one-step Sn 4+-based anodic deposition process and their potential applications in ion sensing. J Mater Chem 22:16259–16268. https://doi.org/10.1039/c2jm33060a

382. Ghrairi N, Bouaicha M (2012) Structural, morphological, and optical properties of TiO2 thin films synthesized by the electro phoretic deposition technique. Nanoscale Res Lett 7:1–17. https://doi.org/10.1186/1556-276X-7-1

383. Johra FT, Lee JW, Jung WG (2014) Facile and safe graphene preparation on solution based platform. J Ind Eng Chem 20:2883–2887. https://doi.org/10.1016/j.jiec.2013.11.022

384. Siburian R, Sihotang H, Lumban Raja S, et al (2018) New route to synthesize of graphene nano sheets. Orient J Chem 34:182–187. https://doi.org/10.13005/ojc/340120

385. Ferrari AC, Basko DM (2013) Raman spectroscopy as a versatile tool for studying the properties of graphene. Nat. Nanotechnol. 8:235–246

386. Al-Gaashani R, Najjar A, Zakaria Y, et al (2019) XPS and structural studies of high quality graphene oxide and reduced graphene oxide prepared by different chemical oxidation methods. Ceram Int 45:14439–14448. https://doi.org/10.1016/j.ceramint.2019.04.165

387. Sonia FJ, Kalita H, Aslam M, Mukhopadhyay A (2017) Correlations between preparation methods, structural features and electrochemical Li-storage behavior of reduced graphene oxide. Nanoscale 9:11303–11317. https://doi.org/10.1039/c7nr03348f

388. Malard LM, Pimenta MA, Dresselhaus G, Dresselhaus MS (2009) Raman spectroscopy in graphene. Phys Rep 473:51–87. https://doi.org/10.1016/j.physrep.2009.02.003

389. Ferrari AC, Robertson J (2000) Interpretation of Raman spectra of disordered and amorphous carbon. Phys Rev B 61:14095–14107. https://doi.org/10.1103/PhysRevB.61.14095

390. Ferrari AC (2007) Raman spectroscopy of graphene and graphite: Disorder, electron-phonon coupling, doping and nonadiabatic effects. Solid State Commun 143:47–57. https://doi.org/10.1016/j.ssc.2007.03.052

391. Hulman M (2014) Raman spectroscopy of graphene. Graphene Prop Prep Characterisation Devices 156–183. https://doi.org/10.1533/9780857099334.2.156

392. Ferrari AC, Rodil SE, Robertson J, et al (2003) Interpretation of infrared and Raman spectra of amorphous carbon nitrides. Phys Rev B - Condens Matter Mater Phys 67:1–20. https://doi.org/10.1103/PhysRevB.67.155306

393. Saha D, Li Y, Bi Z, et al (2014) Studies on supercapacitor electrode material from activated lignin-derived mesoporous carbon. Langmuir 30:900–910. https://doi.org/10.1021/la404112m

394. Mei BA, Munteshari O, Lau J, et al (2018) Physical Interpretations of Nyquist Plots for EDLC Electrodes and Devices. J Phys Chem C 122:194–206. https://doi.org/10.1021/acs.jpcc.7b10582

395. Taberna PL, Simon P, Fauvarque JF (2003) Electrochemical Characteristics and Impedance Spectroscopy Studies of Carbon-Carbon Supercapacitors. J Electrochem Soc 150:A292. https://doi.org/10.1149/1.1543948

396. Kakaei K, Hamidi M, Kakaei N (2019) Simultaneous electro-synthesis of polyaniline graphene nanocomposite in dilute graphene oxide as dopant and aniline by electrochemical method and its high specific capacitance. Mater Res Express 6:. https://doi.org/10.1088/2053-1591/ab2312

397. Zohuri B, Fathi N (2015) Thermal Radiation. In: Thermal-Hydraulic Analysis of Nuclear Reactors. Springer International Publishing, Cham, pp 325–346

398. Jung I, Dikin DA, Piner RD, Ruoff RS (2008) Tunable electrical conductivity of individual graphene oxide sheets reduced at “Low” temperatures. Nano Lett 8:4283–4287. https://doi.org/10.1021/nl8019938

399. Chen J, Shi X, Qi S, et al (2015) Reducing and multiple-element doping of graphene oxide using active screen plasma treatments. Carbon N Y 95:338–346. https://doi.org/10.1016/j.carbon.2015.08.046

400. Alam SN, Sharma N, Kumar L (2017) Synthesis of Graphene Oxide (GO) by Modified Hummers Method and Its Thermal Reduction to Obtain Reduced Graphene Oxide (rGO)*. Graphene 06:1–18. https://doi.org/10.4236/graphene.2017.61001

401. Anthony B (1989) In situ cleaning of silicon substrate surfaces by remote plasma-excited hydrogen. J Vac Sci Technol B Microelectron Nanom Struct 7:621. https://doi.org/10.1116/1.584805

402. Chen L, Zhang X, Huang L, Lei L (2010) Post-plasma catalysis for methane partial oxidation to methanol: Role of the copper-promoted iron oxide catalyst. Chem Eng Technol 33:2073–2081. https://doi.org/10.1002/ceat.201000092

403. Kumar NA, Nolan H, McEvoy N, et al (2013) Plasma-assisted simultaneous reduction and nitrogen doping of graphene oxide nanosheets. J Mater Chem A 1:4431–4435. https://doi.org/10.1039/c3ta10337d

404. Mousavi H, Moradian R (2011) Nitrogen and boron doping effects on the electrical conductivity of graphene and nanotube. Solid State Sci 13:1459–1464. https://doi.org/10.1016/j.solidstatesciences.2011.03.008

405. Ganguly A, Sharma S, Papakonstantinou P, Hamilton J (2011) Probing the Thermal Deoxygenation of Graphene Oxide Using High-Resolution In Situ X-ray-Based Spectroscopies. J Phys Chem C 115:17009–17019. https://doi.org/10.1021/jp203741y

406. Zhao M, Cao Y, Liu X, et al (2014) Effect of nitrogen atomic percentage on N+-bombarded MWCNTs in cytocompatibility and hemocompatibility. Nanoscale Res Lett 9:1–9. https://doi.org/10.1186/1556-276X-9-142

407. Hu X, Ma M, Zeng M, et al (2014) Supercritical carbon dioxide anchored Fe3O4 nanoparticles on graphene foam and lithium battery performance. ACS Appl Mater Interfaces 6:22527–22533. https://doi.org/10.1021/am5066255

408. Zhang N, Yan X, Huang Y, et al (2017) Electrostatically Assembled Magnetite Nanoparticles/Graphene Foam as a Binder-Free Anode for Lithium Ion Battery. Langmuir 33:8899–8905. https://doi.org/10.1021/acs.langmuir.7b01519

409. Alam K, Sim Y, Yu J-H, et al (2019) In-situ Deposition of Graphene Oxide Catalyst for Efficient Photoelectrochemical Hydrogen Evolution Reaction Using Atmospheric Plasma. Materials (Basel) 13:12. https://doi.org/10.3390/ma13010012

410. Liu Q, Hu S, Yang Z, et al (2019) Green synthesis of composite graphene aerogels with robust magnetism for effective water remediation. Materials (Basel) 12:. https://doi.org/10.3390/ma1224106

411. Ngamou PHT, Ivanova ME, Herwartz C, et al (2015) Tailoring the structure and gas permeation properties of silica membranes via binary metal oxides doping. RSC Adv 5:82717–82725. https://doi.org/10.1039/c5ra15783h

412. Body T, Cousens S, Kirby J, Corr C (2018) A volume-averaged model of nitrogen-hydrogen plasma chemistry to investigate ammonia production in a plasma-surface-interaction device. Plasma Phys Control Fusion 60:. https://doi.org/10.1088/1361-6587/aab740

413. Perillo R, Chandra R, Akkermans GRA, et al (2018) Studying the influence of nitrogen seeding in a detached-like hydrogen plasma by means of numerical simulations. Plasma Phys Control Fusion 60:. https://doi.org/10.1088/1361-6587/aad703

414. Suzuki A, Asahina S (2014) Dependence of composition of stable molecules in N2-H2 plasmas on nitrogen gas flow rate ratio measured using a quartz sensor. Jpn J Appl Phys 53:. https://doi.org/10.7567/JJAP.53.11RC03

415. Ogawa D, Kato M, Mori J, Nakamura K (2014) Dispersion of multi-walled carbon nanotube in tetrahydrofuran functionalized with Ar/O2, Ar/N2, and Ar/N2/H2 plasma. Surf Coatings Technol 258:605–607. https://doi.org/10.1016/j.surfcoat.2014.08.029

416. Mohammadzadeh R, Akbari A, Drouet M (2014) Microstructure and wear properties of AISI M2 tool steel on RF plasma nitriding at different N2-H2 gas compositions. Surf Coatings Technol 258:566–573. https://doi.org/10.1016/j.surfcoat.2014.08.036

417. Hirohata Y, Tsuchiya N, Hino T (2001) Effect of mixing of hydrogen into nitrogen plasma. Appl Surf Sci 169–170:612–616. https://doi.org/10.1016/S0169-4332(00)00799-6

418. Borisyuk Y V., Oreshnikova NM, Mozgrin D V., et al (2016) Pulse-periodic abnormal glow discharge in nitrogen, argon, hydrogen and their mixtures. J Phys Conf Ser 747:. https://doi.org/10.1088/1742-6596/747/1/012019

419. Kim YM, Kim JU, Han JG (2002) Investigation on the pulsed DC plasma nitriding with optical emission spectroscopy. Surf Coatings Technol 151:227–232. https://doi.org/10.1016/S0257-8972(01)01601-2

420. Ryu S, Wang Y, Ricard A, et al (2019) The role of hydrogen in the nitriding of anatase TiO2 films in the N2-H2 microwave afterglows. Surf Coatings Technol 364:341–346. https://doi.org/10.1016/j.surfcoat.2019.03.011

421. Lin JF, Chen KW, Xie JQ, et al (2007) Effects of implantation temperature and volume flow rate ratio of nitrogen and hydrogen on nitrogen concentration distribution, mechanical properties, fatigue life, fracture toughness, and tribological behavior of plasma-nitrided P20, 718 and 420 steels. Surf Coatings Technol 201:5912–5924. https://doi.org/10.1016/j.surfcoat.2006.10.043

422. Lepienski CM, Nascimento FC, Foerster CE, et al (2008) Glow discharge nitriding in AISI 304 at different nitrogen-hydrogen atmospheres: Structural, mechanical and tribological properties. Mater Sci Eng A 489:201–206. https://doi.org/10.1016/j.msea.2007.12.012

423. Song L, Peng T, Zhao X, Hu J (2018) Effect of nitrogen hydrogen ratio on plasma nitriding for 38CrMoAl. Acta Metall Slovaca 24:229–233. https://doi.org/10.12776/ams.v24i3.1155

424. Lima SC, Hinrichs R, Vasconcellos MAZ (2019) The influence of nitrogen to hydrogen ratio and temperature on thickness and phase composition in plasma nitrided Ti-6AL-4V. Rev Mater 24:. https://doi.org/10.1590/S1517-707620190001.0607

425. Qayyum A, Zeb S, Naveed MA, et al (2007) Optical emission spectroscopy of Ar-N2 mixture plasma. J Quant Spectrosc Radiat Transf 107:361–371. https://doi.org/10.1016/j.jqsrt.2007.02.008

426. Dyatko NA, Ionikh YZ, Meshchanov A V., et al (2010) Specific features of the current-voltage characteristics of diffuse glow discharges in Ar:N2 mixtures. Plasma Phys Reports 36:1040–1064. https://doi.org/10.1134/S1063780X10120056

427. Dyatko NA, Ionikh YZ, Napartovich AP (2019) Influence of nitrogen admixture on plasma characteristics in a DC argon glow discharge and in afterglow. Atoms 7:. https://doi.org/10.3390/atoms7010013

428. Huang PY, Ruiz-Vargas CS, Van Der Zande AM, et al (2011) Grains and grain boundaries in single-layer graphene atomic patchwork quilts. Nature 469:389–392. https://doi.org/10.1038/nature09718

429. Singh S, Rathi K, Pal K (2018) Synthesis, characterization of graphene oxide wrapped silicon carbide for excellent mechanical and damping performance for aerospace application. J Alloys Compd 740:436–445. https://doi.org/10.1016/j.jallcom.2017.12.069

430. Hofmeister H, Tan GL, Dubiel M (2005) Shape and internal structure of silver nanoparticles embedded in glass. J Mater Res 20:1551–1562. https://doi.org/10.1557/JMR.2005.0197

431. Khan MAM, Kumar S, Ahamed M, et al (2011) Structural and thermal studies of silver nanoparticles and electrical transport study of their thin films. Nanoscale Res Lett 6:1–8. https://doi.org/10.1186/1556-276X-6-434

432. Khan MJ, Shameli K, Sazili AQ, et al (2019) Rapid green synthesis and characterization of silver nanoparticles arbitrated by curcumin in an alkaline medium. Molecules 24:. https://doi.org/10.3390/molecules24040719

433. Zhang D, Jin C, Tian H, et al (2017) An: In situ TEM study of the surface oxidation of palladium nanocrystals assisted by electron irradiation. Nanoscale 9:6327–6333. https://doi.org/10.1039/c6nr08763a

434. Vats T, Dutt S, Kumar R, Siril PF (2016) Facile synthesis of pristine graphene-palladium nanocomposites with extraordinary catalytic activities using swollen liquid crystals. Sci Rep 6:1–11. https://doi.org/10.1038/srep33053

435. Umamaheswari C, Lakshmanan A, Nagarajan NS (2018) Green synthesis, characterization and catalytic degradation studies of gold nanoparticles against congo red and methyl orange. J Photochem Photobiol B Biol 178:33–39. https://doi.org/10.1016/j.jphotobiol.2017.10.017

436. Susi T, Pichler T, Ayala P (2015) X-ray photoelectron spectroscopy of graphitic carbon nanomaterials doped with heteroatoms. Beilstein J Nanotechnol 6:177–192. https://doi.org/10.3762/bjnano.6.17

437. Usachov D, Vilkov O, Grüneis A, et al (2011) Nitrogen-Doped Graphene: Efficient Growth, Structure, and Electronic Properties. Nano Lett 11:5401–5407. https://doi.org/10.1021/nl2031037

438. Jiang Y, Zhang X, Mehedi A Al, et al (2015) A method to evaluate α ″-Fe 16 N 2 volume ratio in FeN bulk material by XPS. Mater Res Express 2:116103. https://doi.org/10.1088/2053-1591/2/11/116103

439. Miyakawa M, Nakata M, Tsuji H, Fujisaki Y (2018) Simple and reliable direct patterning method for carbon-free solution-processed metal oxide TFTs. Sci Rep 8:1–9. https://doi.org/10.1038/s41598-018-31134-w

440. Guerrero-Ortega LPA, Ramírez-Meneses E, Cabrera-Sierra R, et al (2019) Pd and Pd@PdO core–shell nanoparticles supported on Vulcan carbon XC-72R: comparison of electroactivity for methanol electro-oxidation reaction. J Mater Sci 54:13694–13714. https://doi.org/10.1007/s10853-019-03843-8

441. Khumalo ZM, Topić M, Blumenthal M, et al (2020) In-situ study of platinum reaction with oxygen contaminated silicon layer. Nucl Instruments Methods Phys Res Sect B Beam Interact with Mater Atoms 467:27–32. https://doi.org/10.1016/j.nimb.2020.02.001

442. Smirnov MY, Kalinkin A V., Bukhtiyarov VI (2007) X-ray photoelectron spectroscopic study of the interaction of supported metal catalysts with NOx. J Struct Chem 48:1053–1060. https://doi.org/10.1007/s10947-007-0170-1

443. Westwood WD (1988) Sputter Deposition Processes. MRS Bull 13:46–51. https://doi.org/10.1557/S0883769400063697

444. Kinbara A, Kusano E, Kondo I (1998) Fundamentals of plasma and sputtering processes. Vacuum 51:475–478. https://doi.org/10.1016/s0042-207x(98)00237-1

445. Rissanen L, Neubauer M, Lieb KP, Schaaf P (1998) The new cubic iron-nitride phase FeN prepared by reactive magnetron sputtering. J Alloys Compd 274:74–82. https://doi.org/10.1016/S0925-8388(98)00594-5

446. Rissanen L, Schaaf P, Neubauer M, et al (1999) The production of the new cubic FeN phase by reactive magnetron sputtering. Appl Surf Sci 138–139:261–265. https://doi.org/10.1016/S0169-4332(98)00404-8

447. Sigmund P (1969) Theory of Sputtering. I. Sputtering Yield of Amorphous and Polycrystalline Targets. Phys Rev 184:383–416. https://doi.org/10.1103/PhysRev.184.383

448. Yamamura Y, Tawara H (1996) Energy dependence of ion-induced sputtering yields from monatomic solids at normal incidence. At Data Nucl Data Tables 62:149–253. https://doi.org/10.1006/adnd.1996.0005

449. Yu A, Park HW, Davies A, et al (2011) Free-standing layer-by-layer hybrid thin film of graphene-MnO2 nanotube as anode for lithium ion batteries. J Phys Chem Lett 2:1855–1860. https://doi.org/10.1021/jz200836h

450. Iqbal MW, Singh AK, Iqbal MZ, Eom J (2012) Raman fingerprint of doping due to metal adsorbates on graphene. J Phys Condens Matter 24:. https://doi.org/10.1088/0953-8984/24/33/335301

451. Sundaram RS, Steiner M, Chiu HY, et al (2011) The graphene-gold interface and its implications for nanoelectronics. Nano Lett 11:3833–3837. https://doi.org/10.1021/nl201907u

452. Kulshrestha N, Misra A, Koratkar N, Misra DS (2013) Electrical transport and breakdown in graphene multilayers loaded with electron beam induced deposited platinum. ACS Appl Mater Interfaces 5:3424–3430. https://doi.org/10.1021/am400489y

453. Kumar R, Agrawal A, Nagarale RK, Sharma A (2016) High Performance Supercapacitors from Novel Metal-Doped Ceria-Decorated Aminated Graphene. J Phys Chem C 120:3107–3116. https://doi.org/10.1021/acs.jpcc.5b09062

454. Iqbal MW, Iqbal MZ, Khan MF, et al (2014) Modification of the structural and electrical properties of graphene layers by Pt adsorbates. Sci Technol Adv Mater 15:. https://doi.org/10.1088/1468-6996/15/5/055002

455. Chaoumead A, Sung YM, Kwak DJ (2012) The effects of RF sputtering power and gas pressure on structural and electrical properties of ITiO thin film. Adv Condens Matter Phys 2012:. https://doi.org/10.1155/2012/651587

456. Qiu H, Wang F, Wu P, et al (2002) Structural and electrical properties of Cu films deposited on glass by DC magnetron sputtering. Vacuum 66:447–452. https://doi.org/10.1016/S0042-207X(02)00169-0

457. Chan KY, Teo BS (2006) Atomic force microscopy (AFM) and X-ray diffraction (XRD) investigations of copper thin films prepared by dc magnetron sputtering technique. Microelectronics J 37:1064–1071. https://doi.org/10.1016/j.mejo.2006.04.008

458. Chan KY, Teo BS (2007) Effect of Ar pressure on grain size of magnetron sputter-deposited Cu thin films. IET Sci Meas Technol 1:87–90. https://doi.org/10.1049/iet-smt:20060110

459. Gao R, Hu N, Yang Z, et al (2013) Paper-like graphene-Ag composite films with enhanced mechanical and electrical properties. Nanoscale Res Lett 8:32. https://doi.org/10.1186/1556-276x-8-32

460. Mahieu S, Ghekiere P, Depla D, De Gryse R (2006) Biaxial alignment in sputter deposited thin films. Thin Solid Films 515:1229–1249. https://doi.org/10.1016/j.tsf.2006.06.027

461. Khomyakov PA, Giovannetti G, Rusu PC, et al (2009) First-principles study of the interaction and charge transfer between graphene and metals. Phys Rev B - Condens Matter Mater Phys 79:1–12. https://doi.org/10.1103/PhysRevB.79.195425

462. Gong C, Lee G, Shan B, et al (2010) First-principles study of metal–graphene interfaces. J Appl Phys 108:123711. https://doi.org/10.1063/1.3524232

463. Boukhvalov DW, Katsnelson MI (2009) Destruction of graphene by metal adatoms. Appl Phys Lett 95:023109. https://doi.org/10.1063/1.3160551

464. Lahiri J, Batzill M (2010) Graphene destruction by metal-carbide formation: An approach for patterning of metal-supported graphene. Appl Phys Lett 97:1–4. https://doi.org/10.1063/1.3464173

465. Gong C, McDonnell S, Qin X, et al (2014) Realistic Metal–Graphene Contact Structures. ACS Nano 8:642–649. https://doi.org/10.1021/nn405249n

466. Bi C, Feng C, Miao T, et al (2015) Understanding the effect of ultrathin AuPd alloy shells of irregularly shaped Au@AuPd nanoparticles with high-index facets on enhanced performance of ethanol oxidation. Nanoscale 7:20105–20116. https://doi.org/10.1039/c5nr06035d

467. Spoddig D, Schindler K, Rödiger P, et al (2007) Transport properties and growth parameters of PdC and WC nanowires prepared in a dual-beam microscope. Nanotechnology 18:. https://doi.org/10.1088/0957-4484/18/49/495202

# Appendix

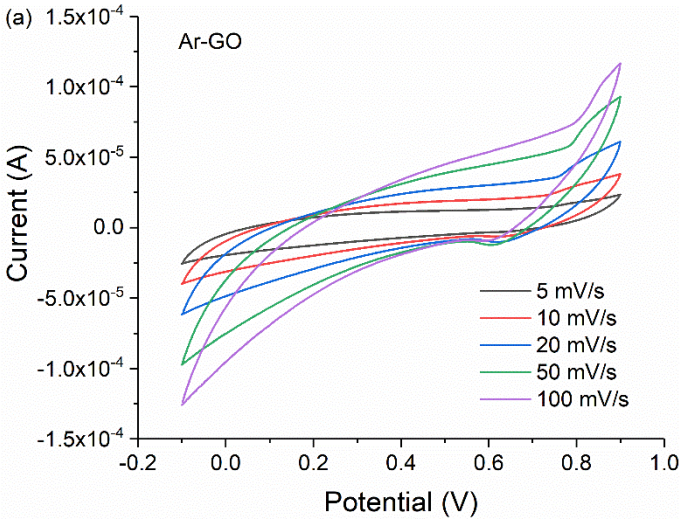
(a)
Ar-GO
Current (A)
Potential (V)
5 mV/s
10 mV/s
20 mV/s
50 mV/s
100 mV/s

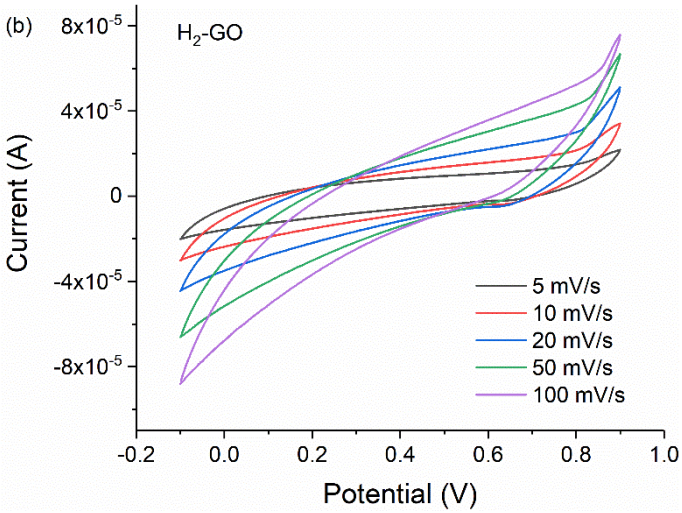
(b)
H2-GO
Current (A)
Potential (V)
5 mV/s
10 mV/s
20 mV/s
50 mV/s
100 mV/s

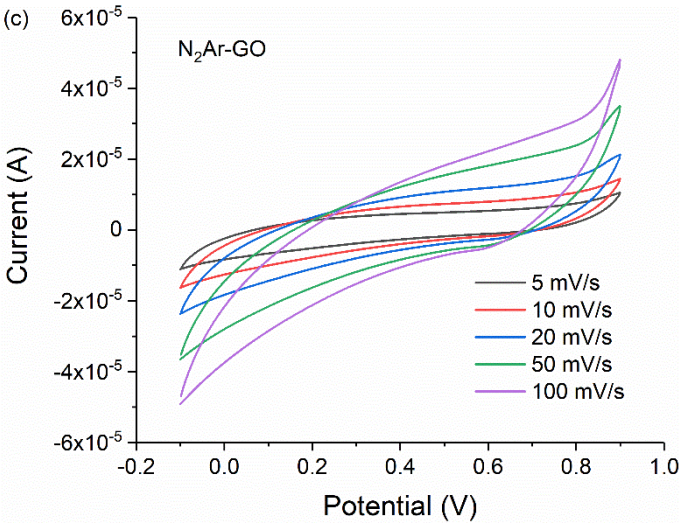
(c)
N2Ar-GO
Current (A)
Potential (V)
5 mV/s
10 mV/s
20 mV/s
50 mV/s
100 mV/s

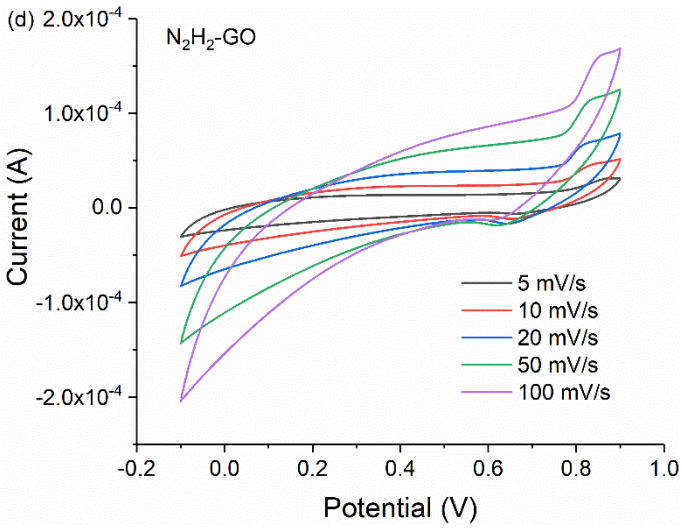


Fig. A-1 CV curves of (a) Ar-GO (b) $H_2$-GO (c) $N_2$Ar-GO (d) $N_2H_2$-GO.

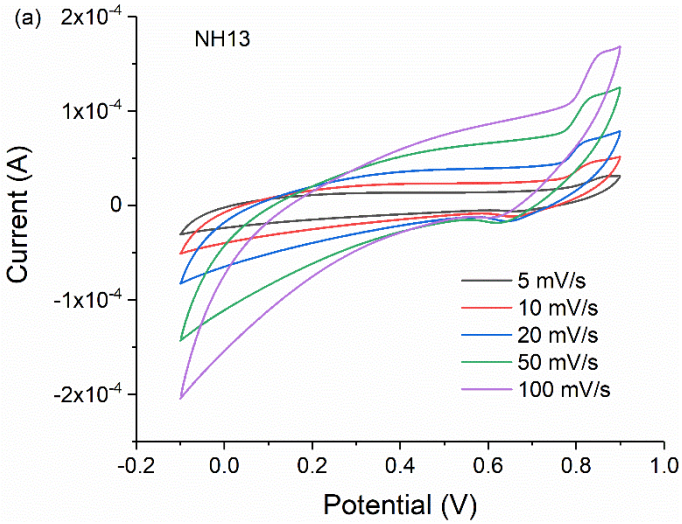


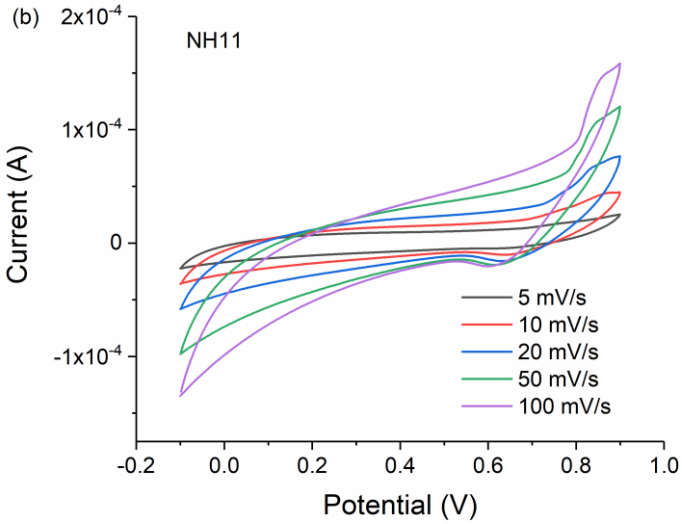

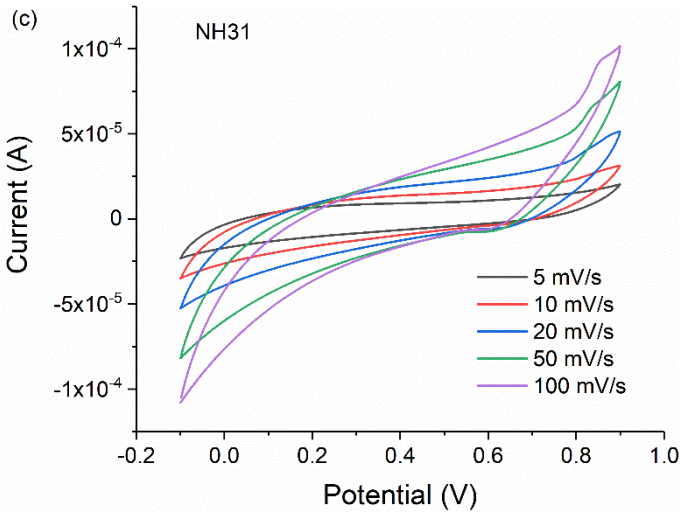


Fig. A-2 CV curves of (a) NH13 (b) NH11 (c) NH31. And (a) is the same one as Fig. X(d).

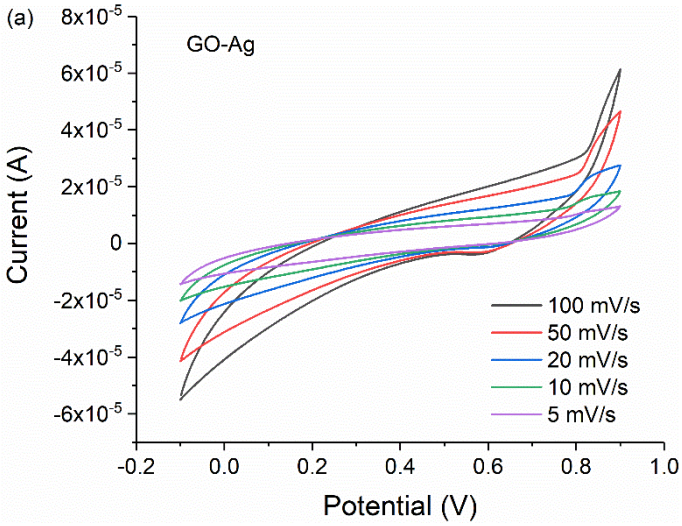


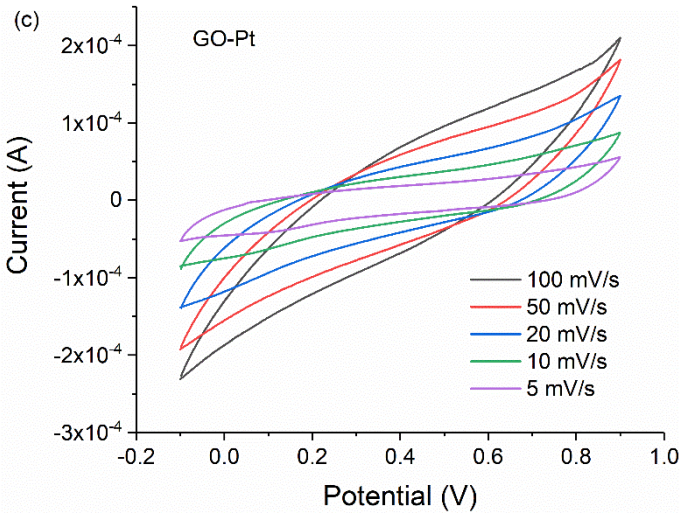

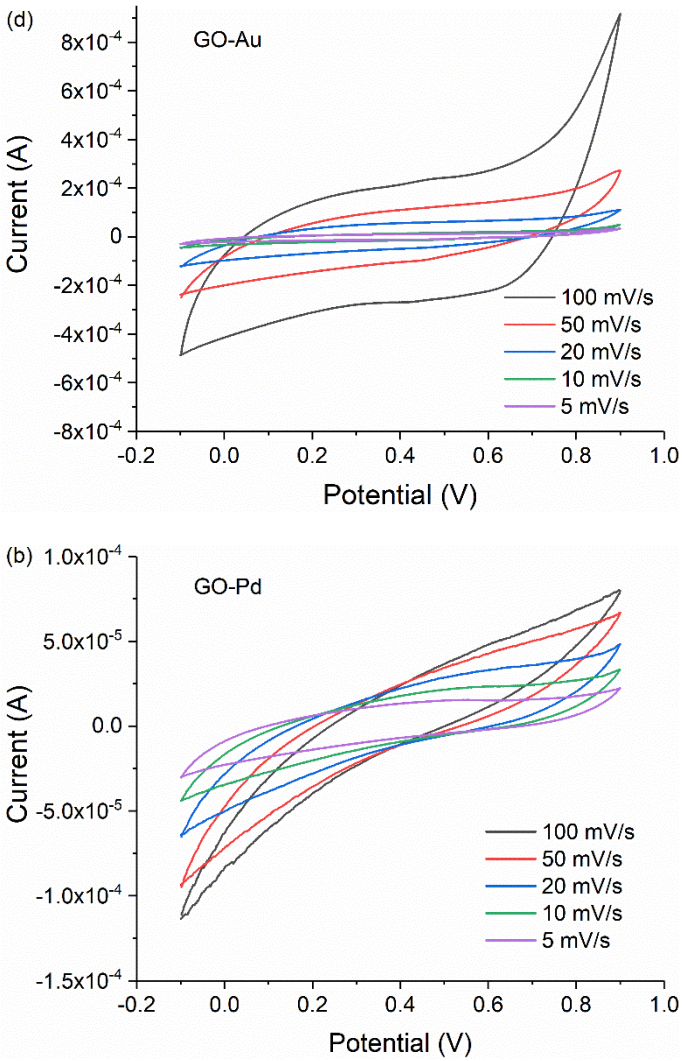


Fig. A-3 CV curves of (a) GO-Ag (b) GO-Pd (c) GO-Pt (d) GO-Au.

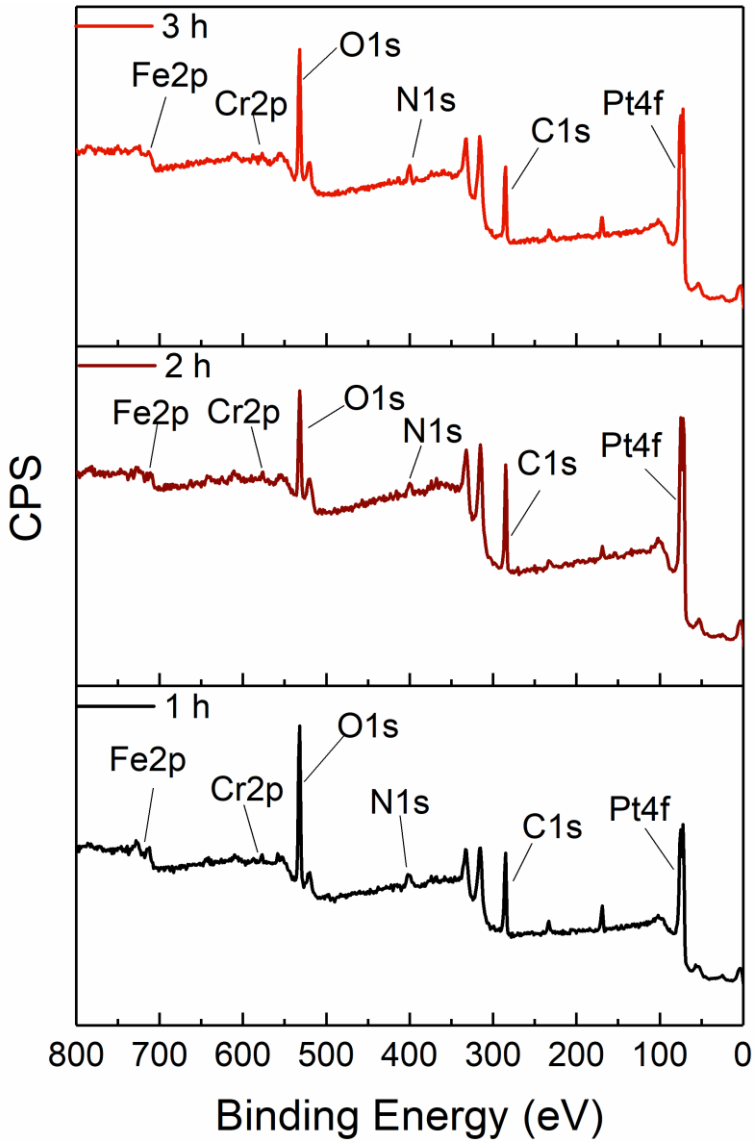


Fig. A-4 XPS spectra survey of GO-Pt treated for different durations.

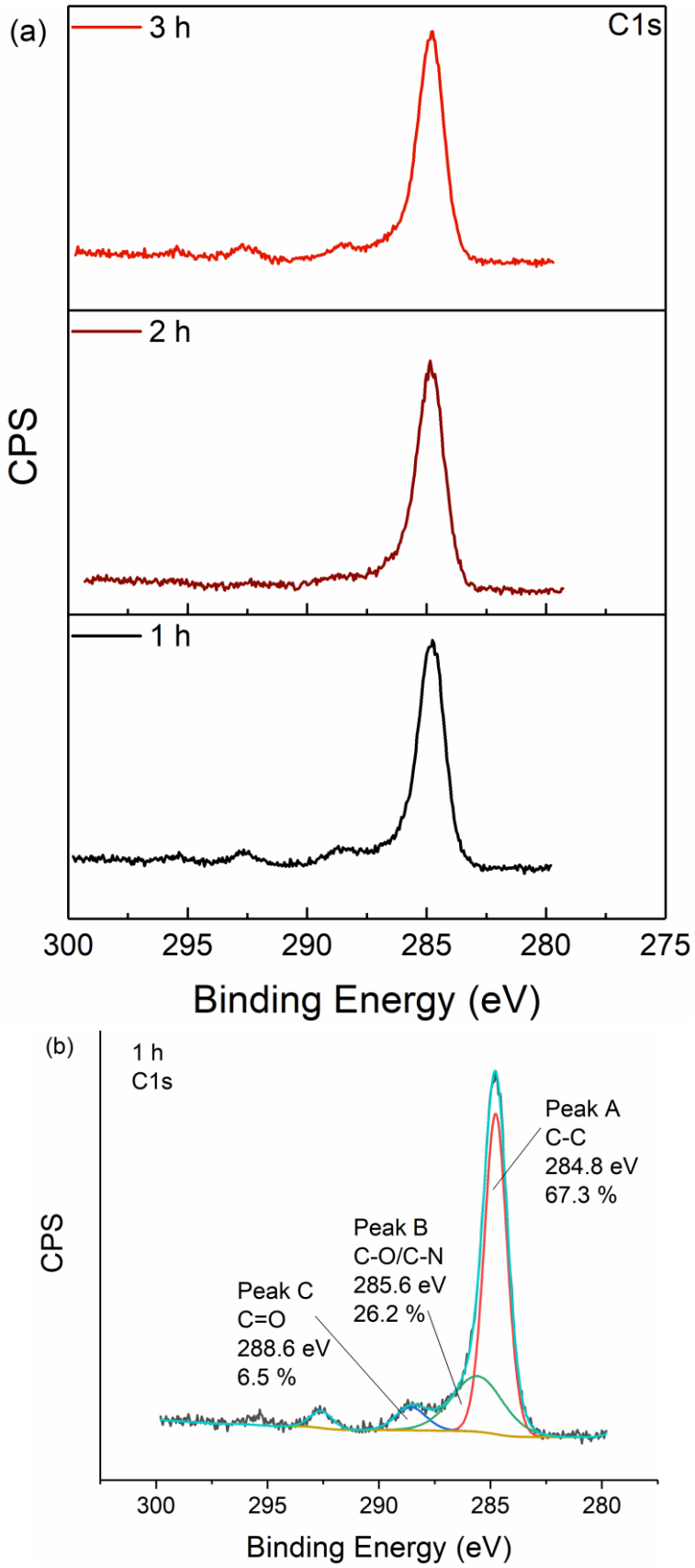
(a)
3 h
C1s
2 h
1 h
CPS
300
295
290
285
280
275
Binding Energy (eV)
(b)
1 h
C1s
Peak A
C-C
284.8 eV
67.3 %
Peak B
C-O/C-N
285.6 eV
26.2 %
Peak C
C=O
288.6 eV
6.5 %
CPS
300
295
290
285
280
Binding Energy (eV)

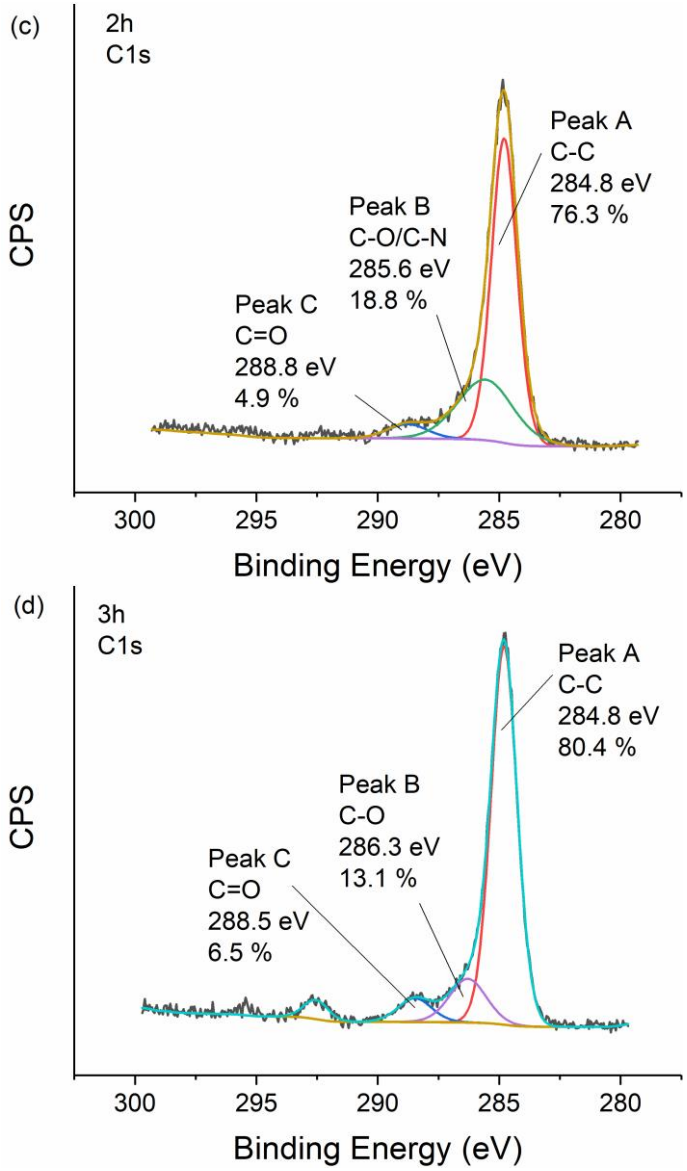


Fig. A-5 (a) Comparison of high-resolution C1s XPS spectra of GO-Pt samples and the deconvoluted XPS spectra of GO-Pt treated for (b) 1 h, (c) 2 h, and (d) 3 h.

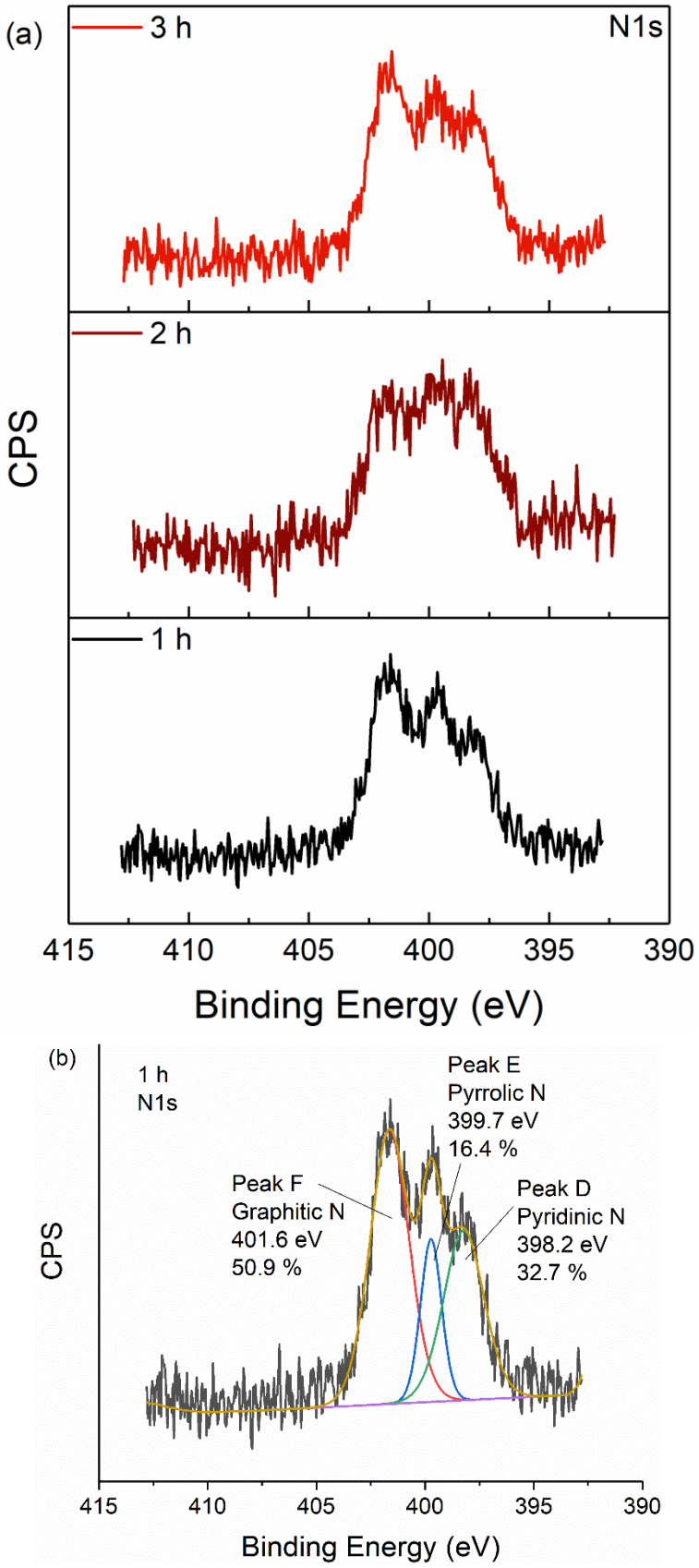
(a)
3 h
N1s
2 h
1 h
CPS
415
410
405
400
395
390
Binding Energy (eV)
(b)
1 h
N1s
Peak E
Pyrrolic N
399.7 eV
16.4 %
Peak F
Graphitic N
401.6 eV
50.9 %
Peak D
Pyridinic N
398.2 eV
32.7 %
CPS
415
410
405
400
395
390
Binding Energy (eV)

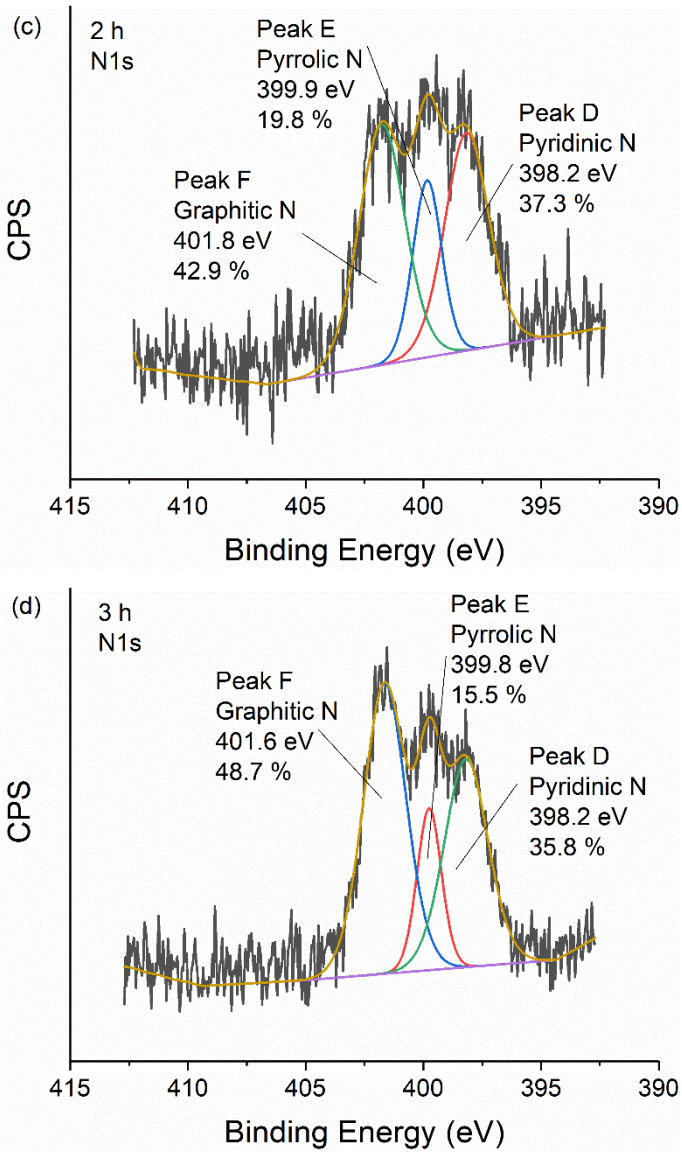


Fig. A-6 (a) Comparison of high-resolution N1s XPS spectra of GO-Pt samples and the deconvoluted XPS spectra of GO-Pt treated for (b) 1 h, (c) 2 h, and (d) 3 h.

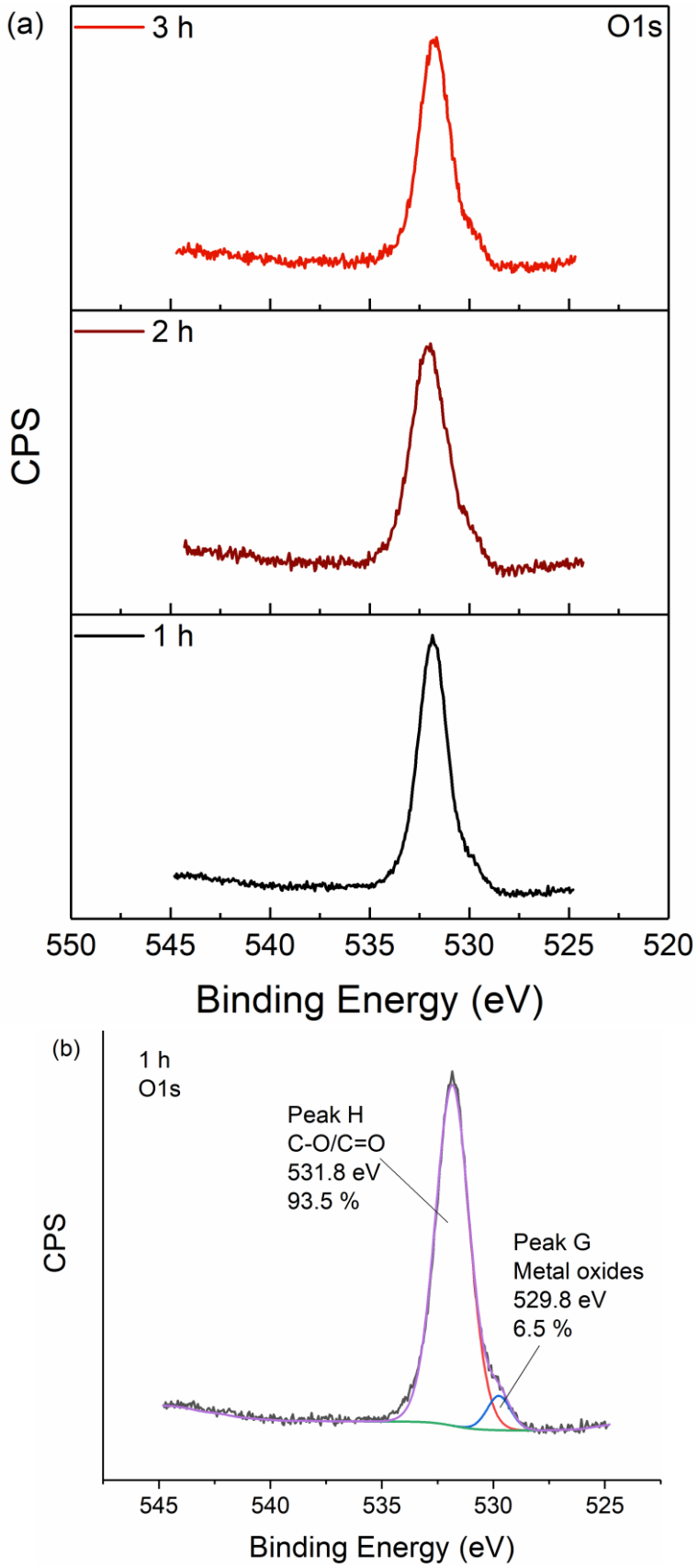
(a)
3 h
O1s
2 h
1 h
CPS
550
545
540
535
530
525
520
Binding Energy (eV)
(b)
1 h
O1s
Peak H
C-O/C=O
531.8 eV
93.5 %
Peak G
Metal oxides
529.8 eV
6.5 %
CPS
545
540
535
530
525
Binding Energy (eV)

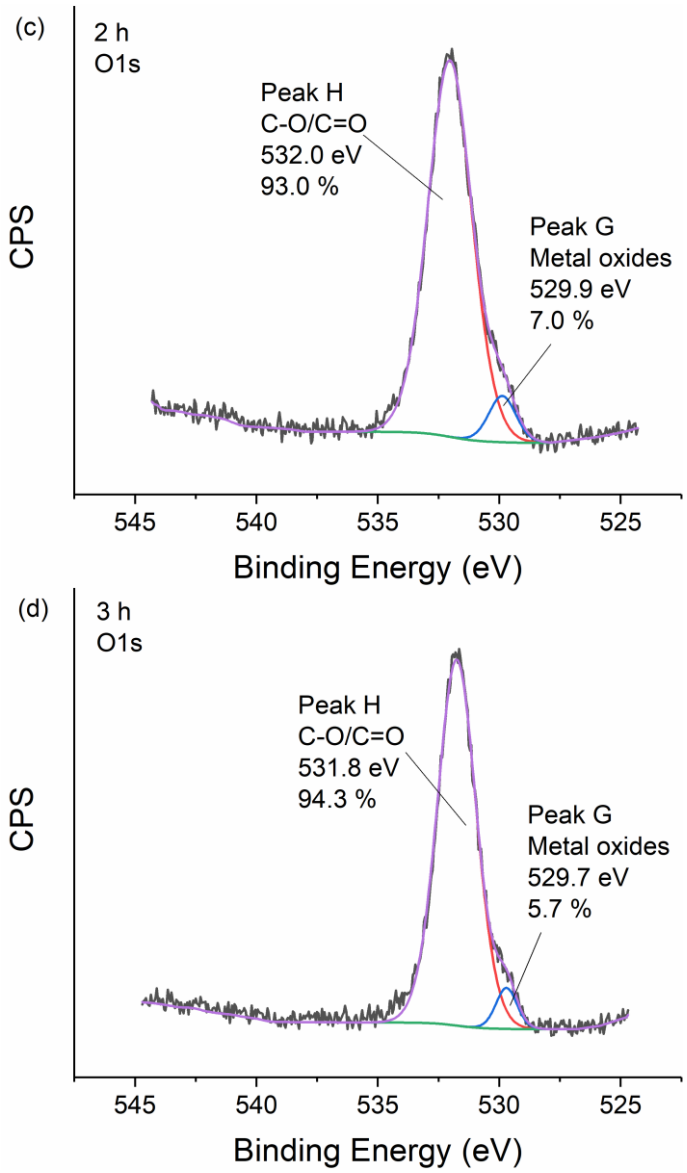


Fig. A-7 (a) Comparison of high-resolution O1s XPS spectra of GO-Pt samples and the deconvoluted XPS spectra of GO-Pt treated for (b) 1 h, (c) 2 h, and (d) 3 h.

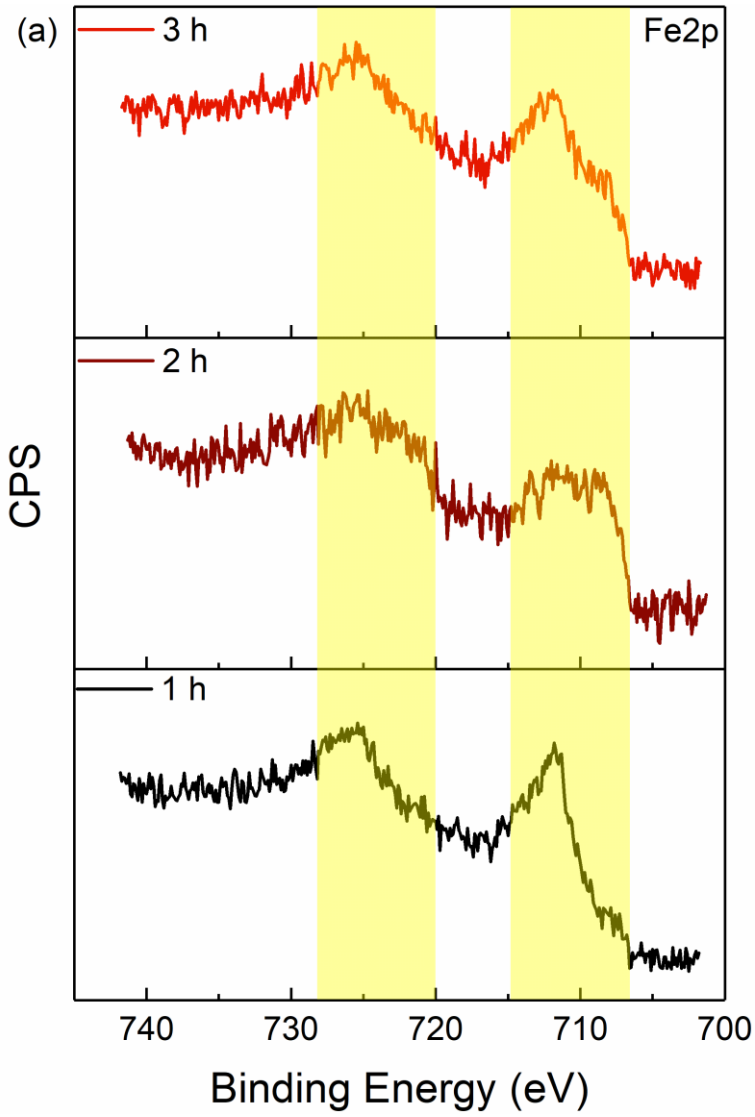
(a)
3 h
Fe2p
2 h
1 h
CPS
740
730
720
710
700
Binding Energy (eV)

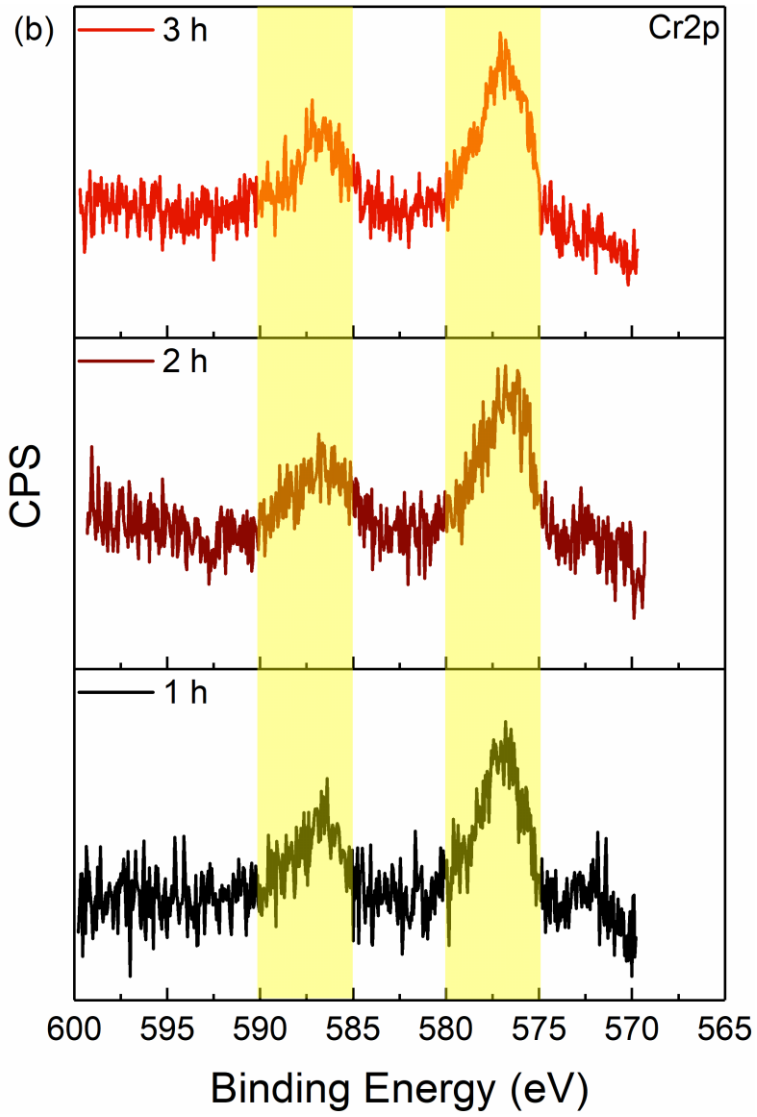
(b)
3 h
Cr2p
2 h
1 h
CPS
600
595
590
585
580
575
570
565
Binding Energy (eV)

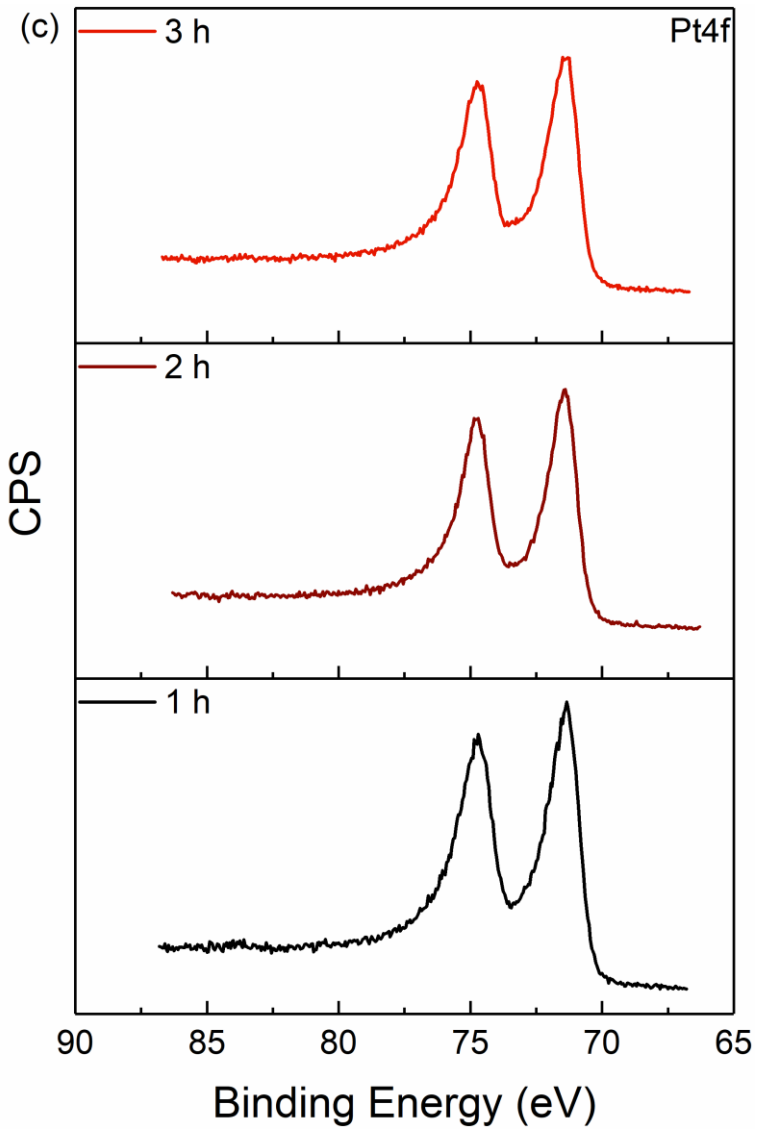


Fig. A-8 Comparison of high-resolution (a) Fe2p, (b) Cr2p, and (c) Pt4f XPS spectra of GO-Pt samples treated for different durations.

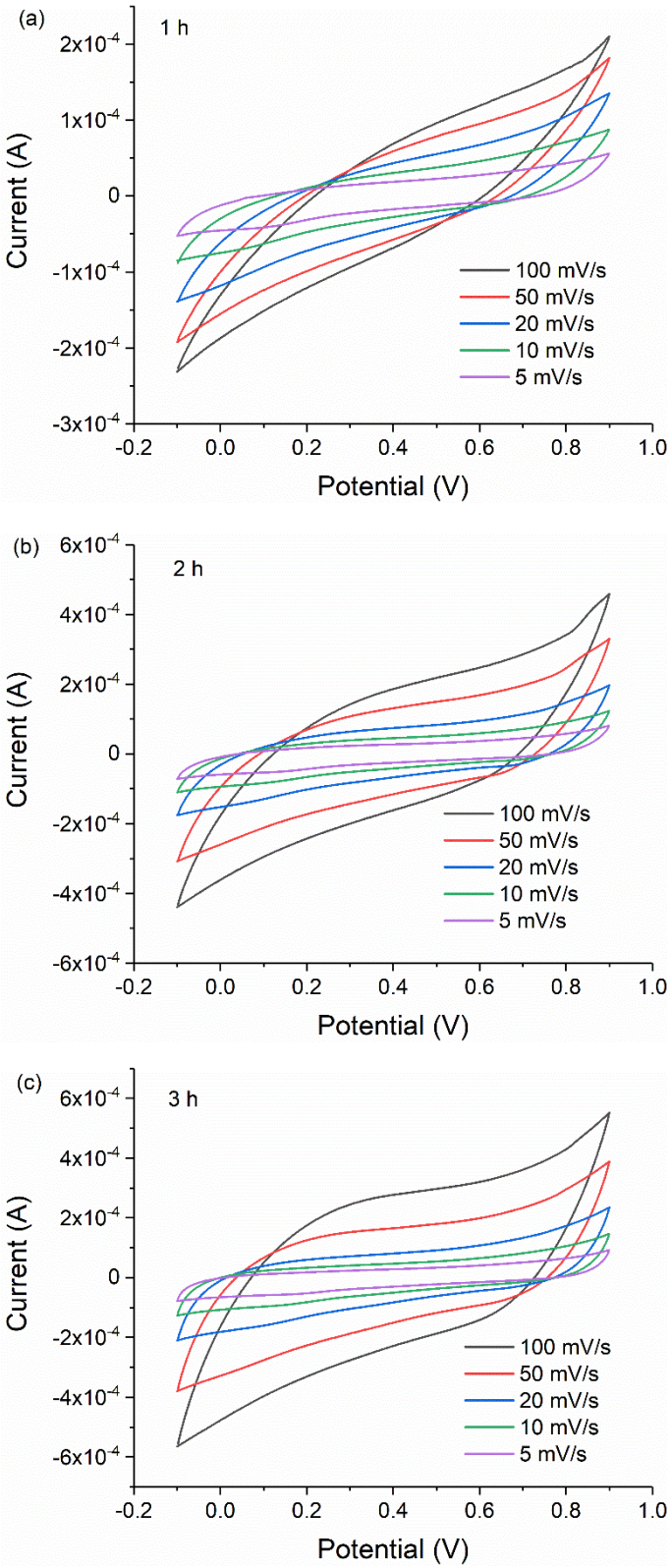


Fig. A-9 CV curves of GO-Pt treated for (a) 1 h (b) 2 h (c) 3 h.

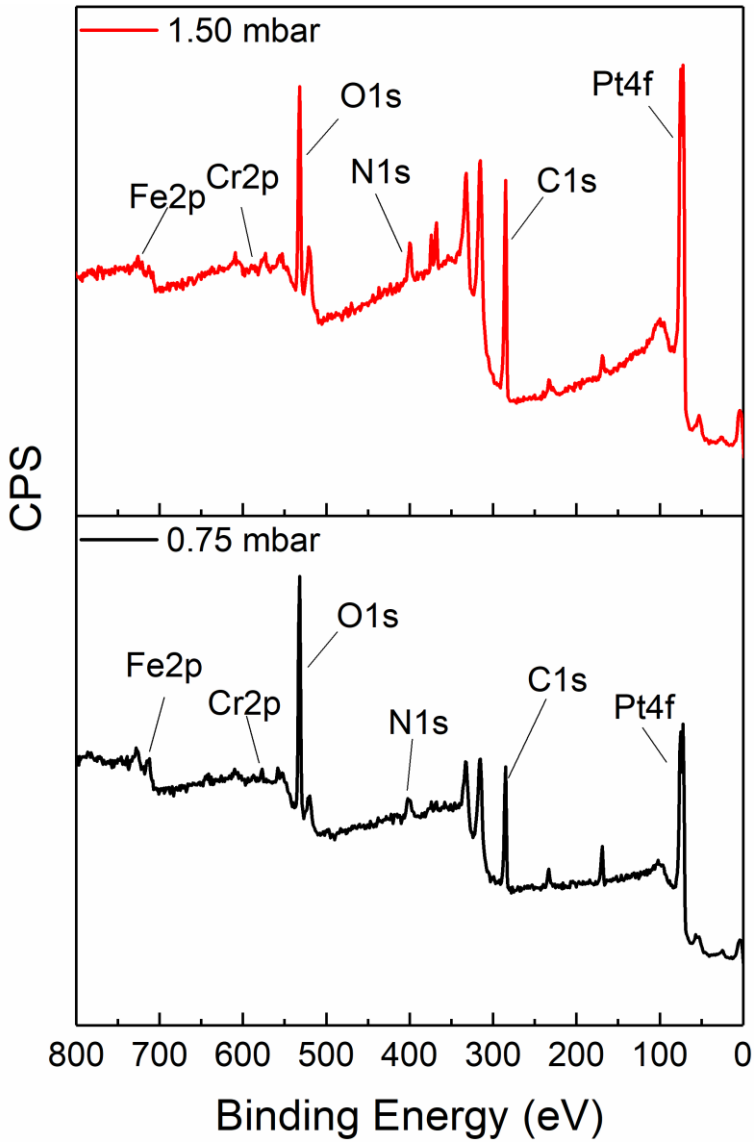


Fig. A-10 XPS spectra survey of GO-Pt treated at different gas pressures.

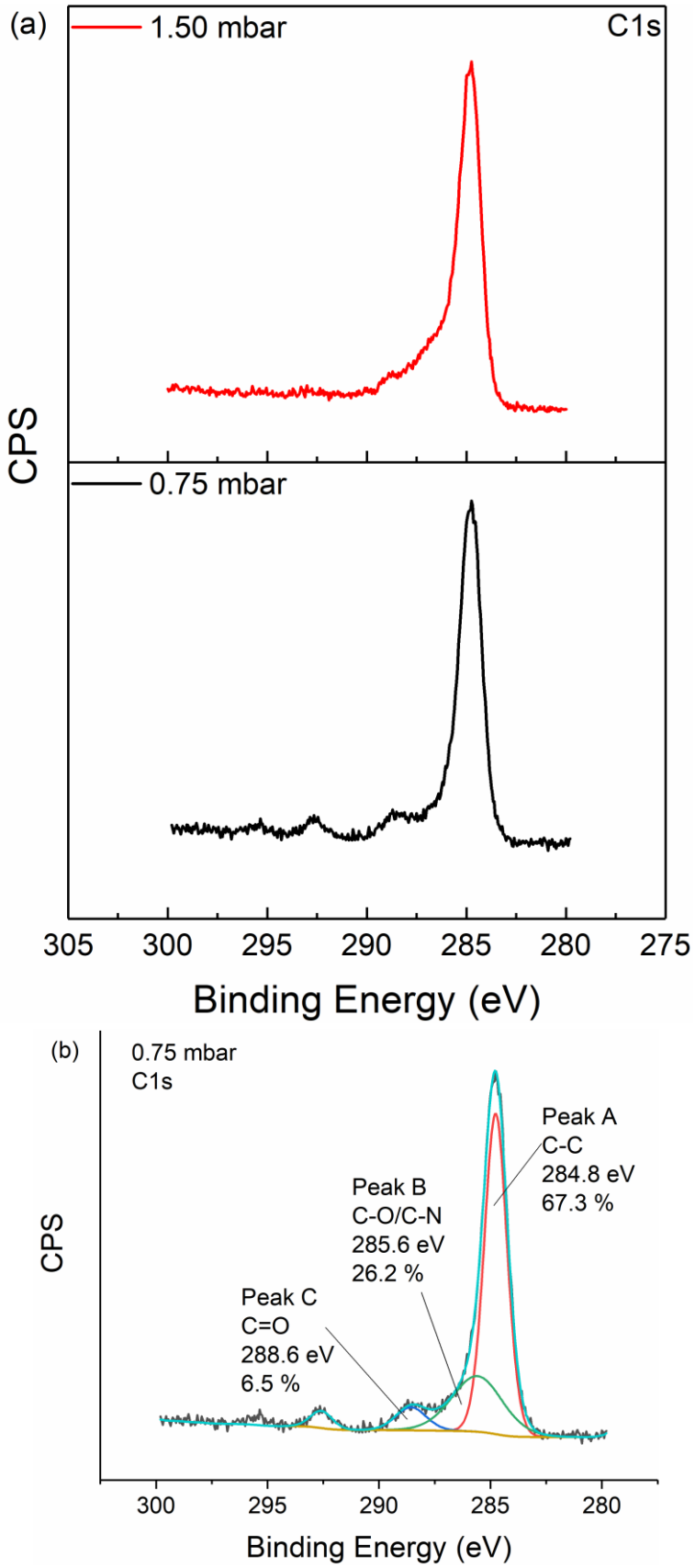
(a)
1.50 mbar
C1s
CPS
0.75 mbar
305
300
295
290
285
280
275
Binding Energy (eV)
(b)
0.75 mbar
C1s
Peak A
C-C
284.8 eV
67.3 %
Peak B
C-O/C-N
285.6 eV
26.2 %
Peak C
C=O
288.6 eV
6.5 %
CPS
300
295
290
285
280
Binding Energy (eV)

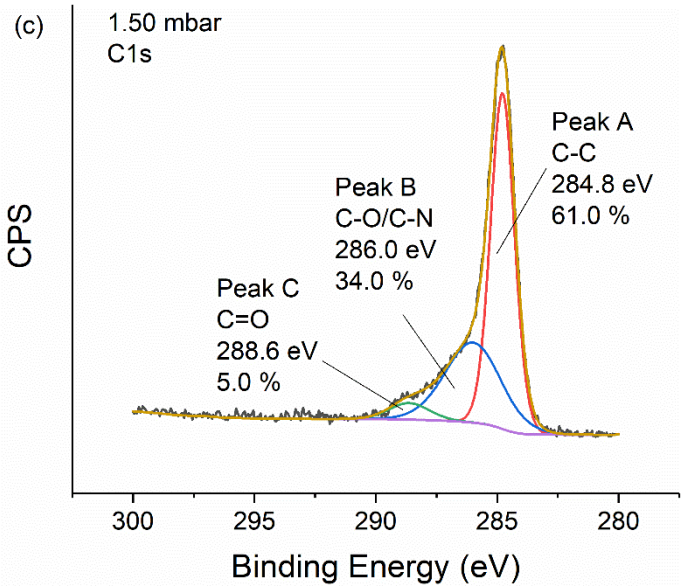


Fig. A-11 (a) Comparison of high-resolution C1s XPS spectra of GO-Pt samples and the deconvoluted XPS spectra of GO-Pt treated at (b) 0.75 mbar, and (c) 1.5 mbar.

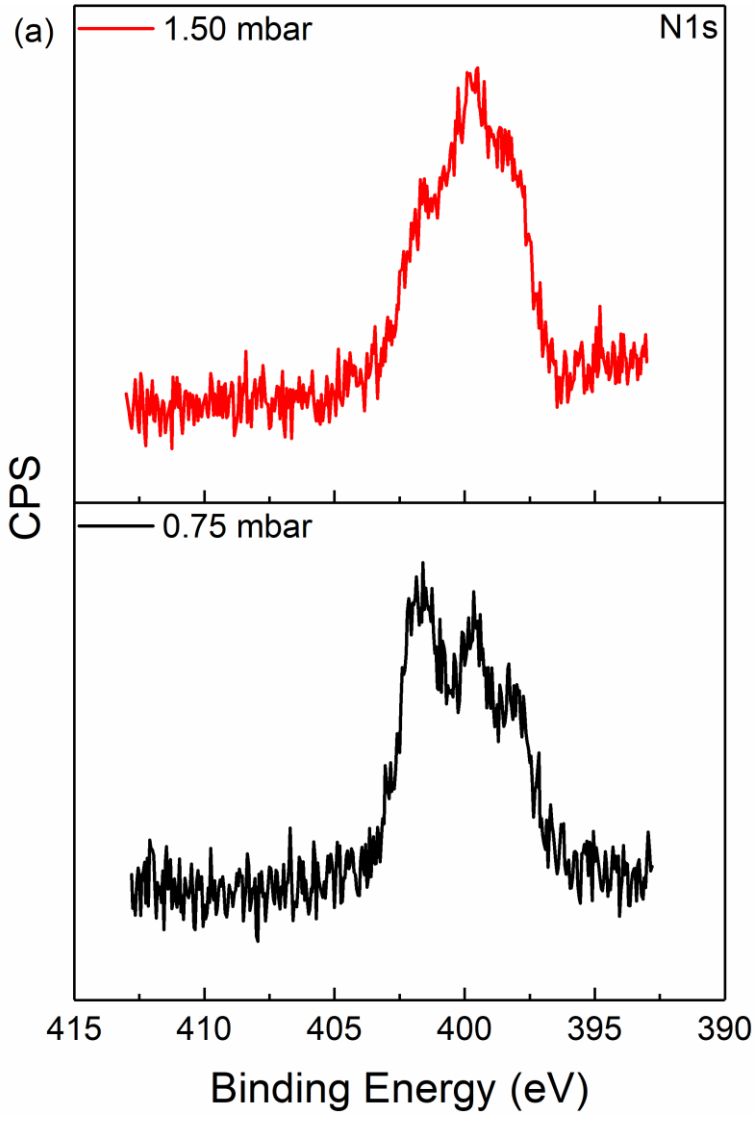

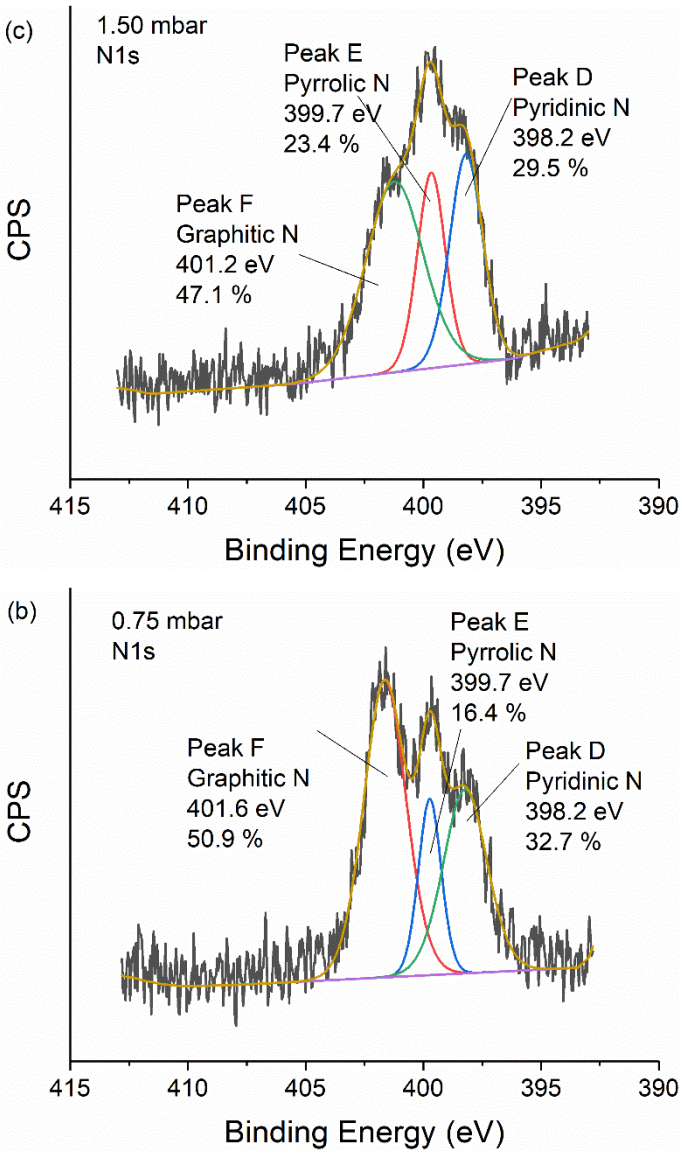


Fig. A-12 (a) Comparison of high-resolution N1s XPS spectra GO-Pt samples and the deconvoluted XPS spectra of GO-Pt treated at (b) 0.75 mbar, and (c) 1.5 mbar.

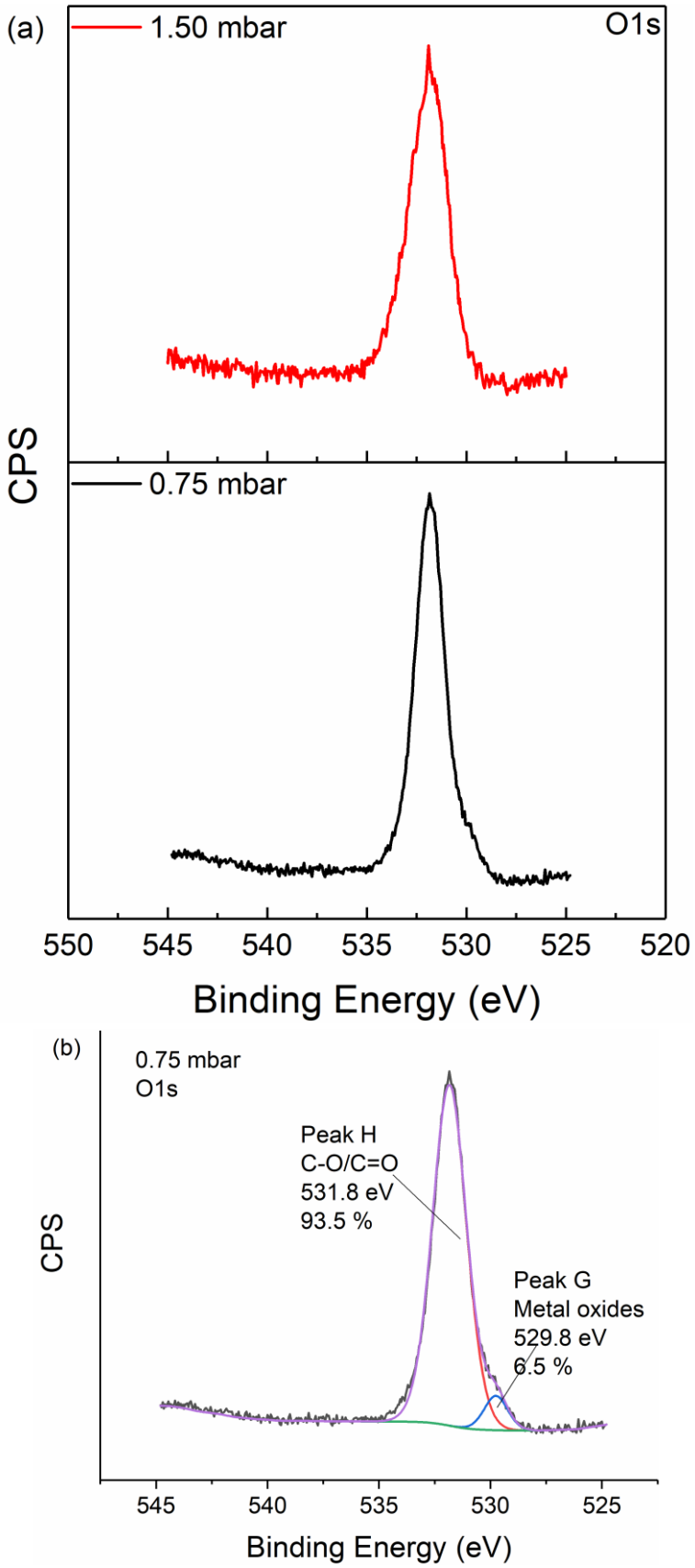
(a)
1.50 mbar
O1s
0.75 mbar
CPS
550
545
540
535
530
525
520
Binding Energy (eV)
(b)
0.75 mbar
O1s
Peak H
C-O/C=O
531.8 eV
93.5 %
Peak G
Metal oxides
529.8 eV
6.5 %
CPS
545
540
535
530
525
Binding Energy (eV)

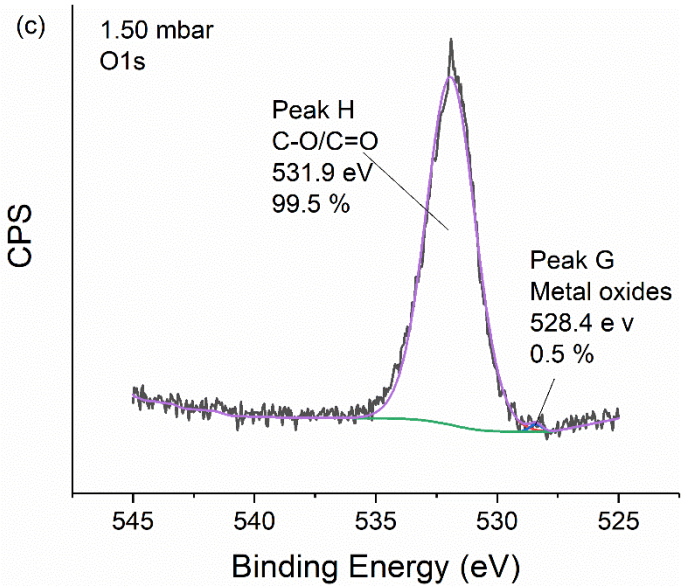


Fig. A-13 (a) Comparison of high-resolution O1s XPS spectra of GO-Pt samples and the deconvoluted XPS spectra of GO-Pt treated at (b) 0.75 mbar, and (c) 1.5 mbar.

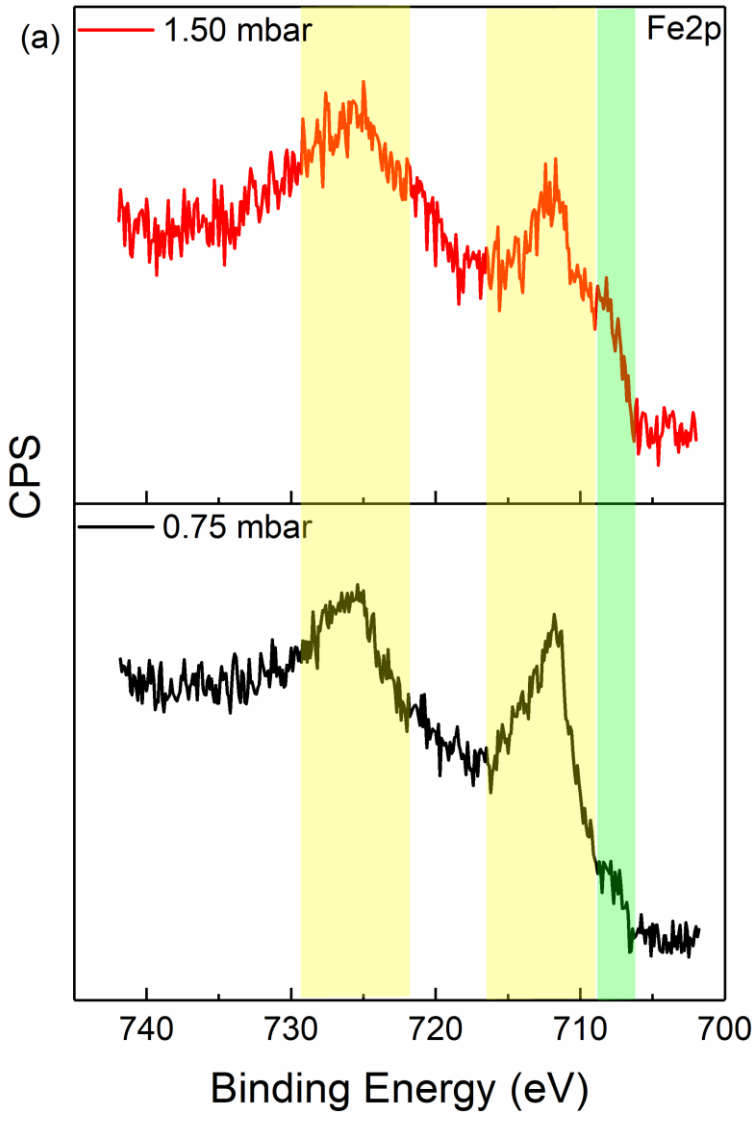

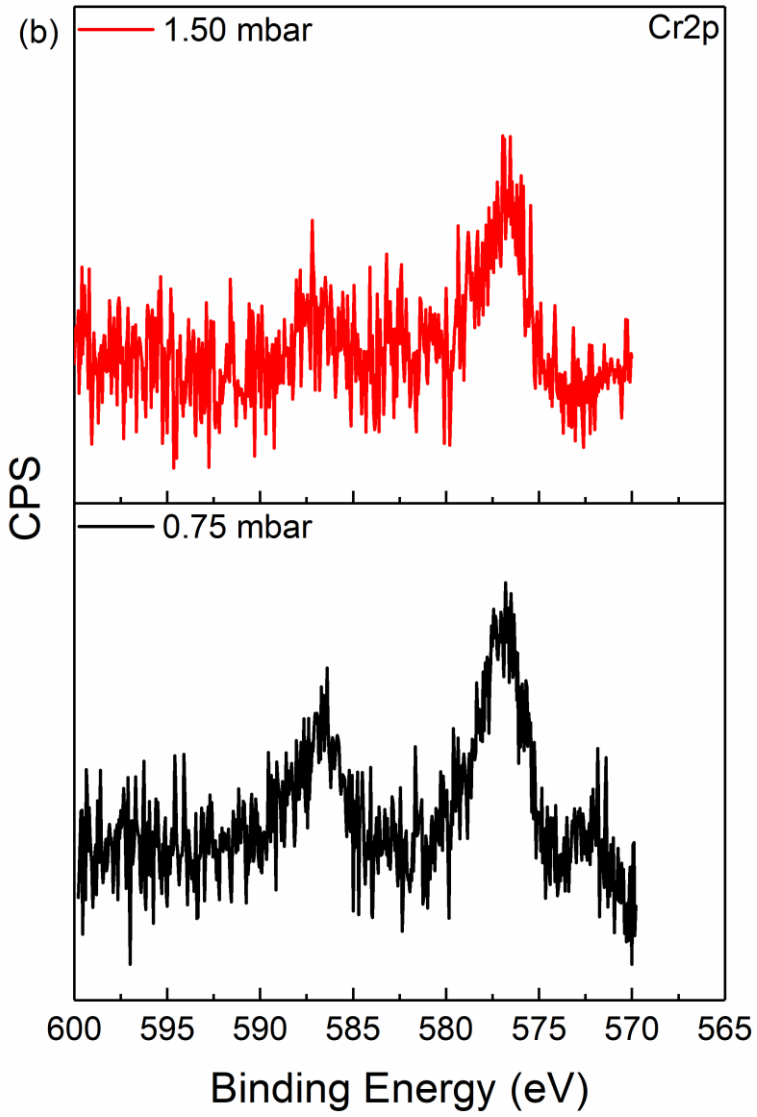
(b)
1.50 mbar
Cr2p
CPS
0.75 mbar
600
595
590
585
580
575
570
565
Binding Energy (eV)

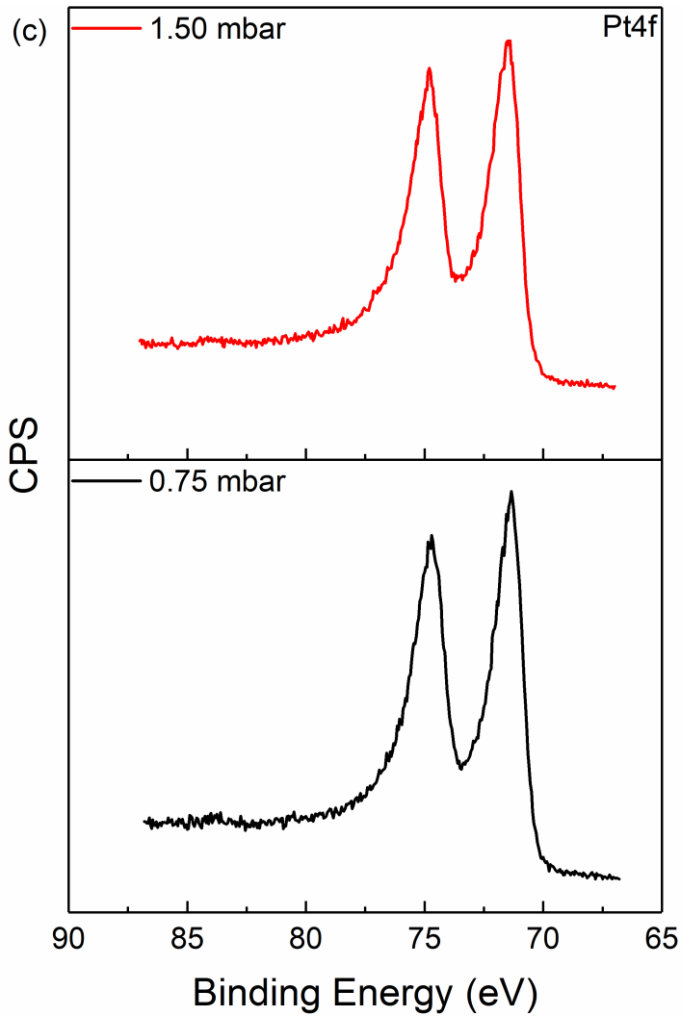


Fig. A-14 Comparison of high-resolution (a) Fe2p, (b) Cr2p, and (c) Pt4f XPS spectra of GO-Pt samples treated at different gas pressures.

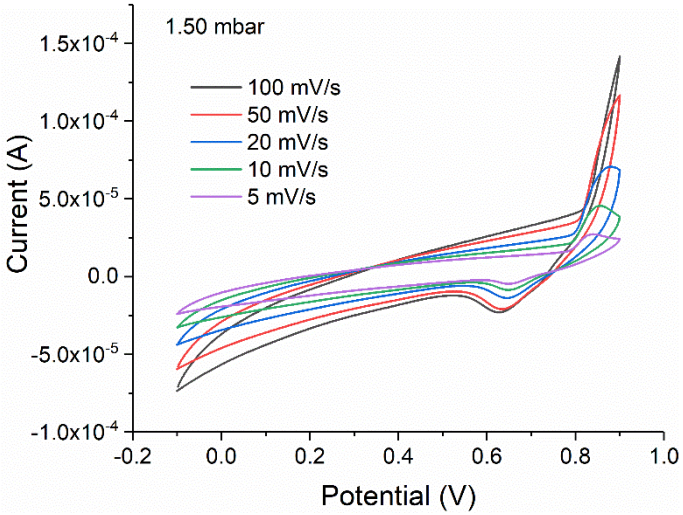


Fig. A-15 CV curves of GO-Pt treated at 1.50 mbar.